

# Enabling Continuous Blood Pressure Estimation on Artifact Contaminated Recordings Applying a Novel Pulse Wave Signal Quality Detector

vorgelegt von Dipl.-Ing. Maik Pflugradt  
geboren in Berlin

von der Fakultät IV – Elektrotechnik und Informatik der Technischen Universität  
Berlin zur Erlangung des akademischen Grades

Doktor der Ingenieurwissenschaften  
- Dr.-Ing. -

genehmigte Dissertation

Promotionsausschuss:

Vorsitzender: Prof. Dr.-Ing. C. Gühmann, TU Berlin

Gutachter: Prof. Dr.-Ing. R. Orglmeister, TU Berlin

Gutachter: Prof. Dr.-Ing. K. Mylvaganam, University College of Southeast Norway

Gutachter: Priv.-Doz. Dr. med. E. Wellnhofer, Deutsches Herzzentrum Berlin

Tag der wissenschaftlichen Aussprache: 15.12.2017

Berlin 2018



---

To my wonderful family.



# Abstract

The universe of home-monitoring and unobtrusive longtime measurements has experienced a remarkable development in the past years. Smart and cheap recording devices interconnected to body sensor networks have emerged in a great variety, promoting features such as on-line signal processing, low power consumption and high data rates. These hardware systems provide a novel platform for ambitious medical applications, thereby broadening the possibilities of related treatments and diagnostics. One field of operation that significantly profits from this technological process involves multimodal pulse wave analysis, which is exploited in innovative procedures such as continuous blood pressure estimation. These methods can yield invaluable insights into the cardiovascular state, especially in unsupervised settings. On the other hand, ambulatory records incorporating electrocardiography and pulse wave signals have to cope with external influences, including motion artifacts, and pathophysiological incidents, such as ectopic beats. If left unattended, automatic signal processing routines can be severely hampered, resulting in infeasible outputs that impede further evaluations. To tackle those issues in an attempt to support pulse wave analysis procedures in difficult environments, this thesis deals with different aspects of signal quality, ranging from hardware considerations to algorithmic implementations concentrating on the detection and suppression of different kinds of signal distortions.

In the scope of the conducted efforts, an improved wireless body sensor network was developed, which features competitive properties including an accurate synchronization mechanism based on Bluetooth, capable and rich frontends equipped with additional acceleration sensors and a well balanced trade-off regarding processing power and overall power consumption. Further, a novel signal quality estimator for photoplethysmographic signals is realized, which outperforms existing methods and is executable on battery driven devices with reduced computational capabilities. Thanks to its convincing detection qualities, pulse wave related recordings were shown to remain applicable in noisy measurement environments, as periods of decreased signal quality are reliably discarded. Especially artifact prone methods such as blood pressure estimation routines profit from the presented achievements, becoming more robust in ambulatory measurement settings again. The proposed signal quality discrimination stage is further complemented by a multimodal ectopic beat detector, which accounts for physiological abnormalities that are known to have a serious impact on pulse wave processing as well. Finally, preliminary results of a novel hand movement recognition and an improved pulse wave artifact suppression approach are presented, providing powerful tools to further increase the robustness of ubiquitous pulse wave monitoring.



# Kurzfassung

Die Möglichkeiten nicht überwachter Langzeitmessungen im Homemonitoring Bereich haben in den letzten Jahren eine beachtliche Entwicklung vollzogen. Vor allem die zunehmende preisgünstige Verfügbarkeit elektronischer Komponenten hat deutlich zur Verbreitung drahtlos vernetzter Sensornetzwerke beigetragen, die mit steigender Leistungsfähigkeit bei ständig kleiner werdendem Strombedarf aufwarten. Durch solche intelligenten Hardware-Systeme finden auch komplexere Applikationen eine Plattform, welche die Anwendungsgebiete medizinischer Behandlungen und Überwachungen beträchtlich ausweiten. Insbesondere multimodale Ansätze wie die durch das EKG getriggerte Pulswellenanalyse profitieren von den neuen technischen Möglichkeiten, die auch bei den Methoden der kontinuierlichen Blutdruckschätzung genutzt werden. Vor allem ambulante Langzeitmessungen können hier neue und wertvolle Einblicke in den kardiovaskulären Zustand bieten. Auf der anderen Seite haben automatisierte Auswerteverfahren nicht überwachter Messungen mit größeren Problemen, verursacht durch Signalartefakte oder physiologische Abnormalitäten, wie beispielsweise dem vermehrten Auftreten von Extrasystolen, zu kämpfen, wodurch deutliche Qualitätseinbußen zu erwarten sind. Die vorliegende Arbeit beschäftigt sich daher mit neuen Lösungsansätzen zur zuverlässigen Erkennung und Unterdrückung der oben genannten Störeinflüsse bei automatisierten Pulswellenanalysen.

Zur stabilen Gewinnung der verschiedenen Pulswellenparameter wurde ein neues, drahtloses Sensornetzwerk zur synchronen Erfassung mehrkanaliger Biosignale entworfen, welches eine hochgenaue Synchronisation auf Basis des Bluetooth Standards, reduzierten Strombedarf und mannigfaltige analoge und digitale Sensorfrontends vorweisen kann. Den Hauptneuwert dieser Arbeit stellt anschließend ein neuer Ansatz zur Qualitätsschätzung von pulsatilen Signalen dar, welcher bisherige Methoden in den Punkten Klassifikationsqualität, Rechenaufwand und praktischer Anwendbarkeit deutlich überlegen ist. Der bedeutende Mehrwert für die Pulswellenanalyse wurde am Beispiel der Anwendung kontinuierlicher Blutdruckschätzer auf gestörte Datensätze gezeigt, die durch die robuste Diskriminierung der Signalqualität zuverlässige Resultate liefern. Des Weiteren werden verbesserte Methoden zur Erkennung von Extrasystolen, zur Klassifikation von Handbewegungen sowie zur Unterdrückung von Pulswellenartefakten vorgestellt, die die Auswertung von nicht überwachten Aufzeichnungen unter schwierigen Messbedingungen zusätzlich unterstützen.



# Contents

<b>Nomenclature</b>	<b>xi</b>
<b>1 Introduction</b>	<b>1</b>
1.1 Multimodal Measurements of Vital Parameters in Longtime Recordings . . .	1
1.2 Structure and Concrete Aims of the Thesis . . . . .	3
<b>2 Cardiovascular Backgrounds and Important Measurement Methods</b>	<b>7</b>
2.1 Cardiovascular System . . . . .	7
2.1.1 Electrocardiography . . . . .	8
2.1.2 Measurement of Blood Pressure . . . . .	11
2.1.3 Photoplethysmography . . . . .	13
2.2 Non-Invasive Blood Pressure Estimation . . . . .	17
2.2.1 Pulse Wave Velocity Considerations . . . . .	17
2.2.1.1 Pulse Wave Velocity Backgrounds . . . . .	17
2.2.1.2 PWV Measurements . . . . .	20
2.2.1.3 PWV Parameters and Influencing Factors . . . . .	21
2.2.2 Blood Pressure Estimation Models . . . . .	23
2.3 Blood Pressure Measurements for Diagnosing Orthostatic Hypotension . . .	29
<b>3 Acquisition of Vital Parameters</b>	<b>33</b>
3.1 ECG Acquisition . . . . .	33
3.2 PPG Acquisition . . . . .	34
3.3 Body Sensor Networks . . . . .	35
3.4 A Novel Robust Body Sensor Network . . . . .	38
3.4.1 Architectural Overview . . . . .	38
3.4.2 Sensors . . . . .	40
3.4.3 Clock Synchronization . . . . .	46
3.5 Database . . . . .	50
<b>4 Enhanced Pulse Wave Discrimination with OPRA</b>	<b>55</b>
4.1 Determination of PAT and PTT . . . . .	56
4.2 ECG Signal Quality Detection . . . . .	60
4.3 Pulse Wave Signal Quality . . . . .	62
4.3.1 Overview of Currently Published Methods . . . . .	62
4.3.2 A Novel On-line Applicable Approach: OPRA . . . . .	67
4.3.2.1 Mathematical Preliminaries . . . . .	69

4.3.2.2	OPRA - On-line Pulse Reliability Analysis . . . . .	74
4.3.3	Performance Evaluation . . . . .	82
4.3.3.1	OPRA Parameter Trimming . . . . .	84
4.3.3.2	Performance Comparison . . . . .	85
4.4	Ectopic Beat Detection . . . . .	87
4.4.1	Established Ectopic Beat Detection Approaches . . . . .	90
4.4.2	A Novel Multimodal Ectopic Beat Detection Method . . . . .	94
<b>5</b>	<b>Artifact Suppression for Pulse Wave Signals</b>	<b>105</b>
5.1	PPG Artifact Reduction . . . . .	105
5.1.1	Methods Currently in Use . . . . .	106
5.1.2	Enhanced PPG Artifact Reduction by Blind Source Separation . . . . .	111
5.1.2.1	Motion Reference Data . . . . .	111
5.1.2.2	ICA Artifact Elimination Framework . . . . .	112
5.1.2.3	Performance Evaluation . . . . .	112
5.1.3	Hand Movement Detection . . . . .	116
<b>6</b>	<b>Unsupervised Blood Pressure Estimation Based on PAT Measurements</b>	<b>119</b>
6.1	BPE Performance on Clean Signals . . . . .	119
6.2	BPE Performance on Artifact Contaminated Signals . . . . .	122
6.3	BPE Performance During Ectopic Beats . . . . .	124
<b>7</b>	<b>Conclusion</b>	<b>129</b>
7.1	Major Contributions of This Work . . . . .	129
7.2	Limitations and Unsolved Issues . . . . .	130
7.3	Future Works and Outlook . . . . .	132
<b>8</b>	<b>Appendix</b>	<b>133</b>
8.1	Tables . . . . .	133
8.2	Performance Measures . . . . .	141
8.3	Additional Information . . . . .	143
	<b>Acknowledgements</b>	<b>145</b>
	<b>Figures</b>	<b>148</b>
	<b>Tables</b>	<b>150</b>
	<b>Bibliography</b>	<b>151</b>





# Nomenclature

## Notations

$c_{ij}$	Covariance of random variables $x_i$ and $x_j$
$\mathbf{C}_x$	Covariance matrix of $\mathbf{x}$
$E \langle \cdot \rangle$	Expectation operator
$m_{x_k}$	Mean value of random variable $x_k$
$\mathbf{m}_x$	Vector of mean values of $\mathbf{x}$
$n_{cal}$	Number of epochs during OPRA calibration
$p_x(x)$	Probability density of $\mathbf{x}$
$s$	PPG signal
$SpO_2$	Oxygen Saturation
$\mathbf{W}(k)$	Weight matrix at epoch $k$
$\mathbf{w}_i$	The $i$ -th weight vector in gradient ascent algorithms
$x$	Random variable
$\mathbf{x}$	Vector of random variables
$y_i$	The $i$ -th neural network output
$z_k$	The $k$ -th principal component

## Roman Symbols

$A$	Area	$\text{m}^2$
$c$	Speed of pulse wave in the arteries	$\text{m s}^{-1}$
$C$	Compliance	$\text{m}^3 \text{Pa}^{-1}$
$C_A$	Area compliance	$\text{m}^2 \text{Pa}^{-1}$
$C_D$	Diameter compliance	$\text{m Pa}^{-1}$
$C_{Dist}$	Distensibility	$1/\text{Pa}$

## Contents

---

$D$	Diameter	m
$E$	Young's modulus	$\text{N m}^{-2}$
$E_{inc}$	Incremental Young's modulus	$\text{N m}^{-2}$
$e_a$	Absolute SBP estimation error	$\text{N m}^{-2}$
$e_r$	Relative SBP estimation error	
$EL$	Elasticity	$\text{Pa m}^{-3}$
$F$	Force	$\text{kg m s}^{-2}$
$h$	Vessel wall thickness	m
$K$	Bulk modulus	Pa
$l$	Length	m
$P$	Pressure	$\text{N m}^{-2}$
$r$	Radius	m
$RR$	RR-Interval, time between two consecutive R-Peaks	s
$t$	Time	s
$v_{pulse}$	Pulse wave propagation speed	$\text{m s}^{-1}$
$V$	Volume	$\text{m}^3$
<b>Greek Symbols</b>		
$\zeta$	Pressure constant in Young's modulus equation of best fit	$\text{m}^2 \text{N}^{-1}$
$\gamma$	Learning rate in gradient ascent algorithms	
$\epsilon$	Mechanical strain	
$\eta$	OPRA calibration phase weight update threshold	
$\lambda_k$	The k-th eigenvalue of $\mathbf{C}_x$	
$\sigma_x$	Variance of x	
$\theta$	OPRA classification phase weight update threshold	
$\phi$	Stress	$\text{N m}^{-2}$
$\rho$	Blood density	$\text{kg m}^{-3}$

**Abbreviations:**

<b>AAMI</b>	Advancement of Medical Instrumentation	<b>FET</b>	Field Effect Transistor
<b>ABI</b>	Ankle Brachial Index	<b>FFT</b>	Fast Fourier Transform
<b>AC</b>	Alternating Current	<b>FIR</b>	Finite Impulse Response
<b>ACC</b>	Acceleration	<b>FPR</b>	False Positive Rate
<b>ACY</b>	Accuracy	<b>HFC</b>	High Frequency Component
<b>ABP</b>	Arterial Blood Pressure	<b>HPE</b>	Heart Rate Pulse Rate Error
<b>ADC</b>	Analog-to-Digital-Converter	<b>HR</b>	Heart Rate
<b>AES</b>	Advanced Encryption Standard	<b>HRV</b>	Heart Rate Variability
<b>ANC</b>	Adaptive Noise Cancellation	<b>I2C</b>	Inter Integrated Circuit
<b>ANN</b>	Artificial Neural Network	<b>ICA</b>	Independent Component Analysis
<b>AT</b>	Applanation Tonometry	<b>ICT</b>	Isovolumetric Contraction Time
<b>AI</b>	Augmentation Index	<b>ICU</b>	Intensive Care Unit
<b>AV</b>	Atrioventricular	<b>IEGM</b>	Intracardiac Electrogram
<b>BP</b>	Blood Pressure	<b>IMG</b>	Impedancemyogram
<b>bpm</b>	Beats Per Minute	<b>ISM</b>	Industrial, Scientific and Medical
<b>BPE</b>	Blood Pressure Estimation	<b>JADE</b>	Joint Approximate Diagonalization of Eigenmatrices
<b>BSN</b>	Body Sensor Network	<b>LED</b>	Light-Emitting Diode
<b>BSS</b>	Blind Source Separation	<b>LD</b>	Linear Discrimination
<b>BT</b>	Bluetooth	<b>LDA</b>	Linear Discrimination Analysis
<b>CC</b>	Correlation Coefficient	<b>LDO</b>	Low Dropout Regulator
<b>CCR</b>	Capture Compare Register	<b>LFC</b>	Low Frequency Component
<b>CPU</b>	Central Processing Unit	<b>MAP</b>	Mean Arterial Pressure
<b>CRC</b>	Cyclic Redundancy Check	<b>MAPRE</b>	Mean Absolute Pulse Rate Error
<b>CVS</b>	Cardiovascular State	<b>MEMS</b>	Micro Electro-Mechanical Systems
<b>DBP</b>	Diastolic Blood Pressure	<b>MIMIC</b>	Multiparameter Intelligent Monitoring in Intensive Care
<b>DAC</b>	Digital-Analog-Converter	<b>MLP</b>	Multilayer Perceptron
<b>DC</b>	Direct Current	<b>MRI</b>	Magnet Resonance Imaging
<b>DVP</b>	Digital Volume Pulse	<b>MSE</b>	Mean Squared Error
<b>EB</b>	Ectopic Beat	<b>NB</b>	Naive Bayes
<b>ECG</b>	Electrocardiogram	<b>OH</b>	Orthostatic Hypotension
<b>EEG</b>	Electroencephalogram	<b>OPRA</b>	On-line Pulse Reliability Analysis
<b>EMG</b>	Electromyogram		
<b>EV</b>	Eigenvector		
<b>FAT</b>	File Allocation Table		

<b>PAT</b>	Pulse Arrival Time	<b>SA</b>	Sinoatrial
<b>PC</b>	Principal Component	<b>SGA</b>	Stochastic Gradient Ascent
<b>PCA</b>	Principal Component Analysis	<b>SBP</b>	Systolic Blood Pressure
<b>PCB</b>	Printed Circuit Board	<b>SLP</b>	Single Layer Perceptron
<b>PCG</b>	Phonocardiogram	<b>SNR</b>	Signal to Noise Ratio
<b>PEP</b>	Pre-Ejection Period	<b>SOBI</b>	Second Order Blind Identification
<b>PhyCh15</b>	PhysioNet Challenge 2015		
<b>PNN</b>	Probabilistic Neural Network	<b>SPI</b>	Serial Peripheral Interface
<b>PPG</b>	Photoplethysmogram	<b>SQI</b>	Signal Quality Index
<b>PR</b>	Pulse Rate	<b>SRAM</b>	Static Random Access Memory
<b>PRC</b>	Precision	<b>STD</b>	Standard Deviation
<b>PTT</b>	Pulse Transit Time	<b>STFT</b>	Short Time Fourier Transform
<b>PWA</b>	Pulse Wave Analysis	<b>SVEB</b>	Supraventricular Ectopic Beat
<b>PWV</b>	Pulse Wave Velocity	<b>SVD</b>	Singular Value Decomposition
<b>RAM</b>	Random Access Memory	<b>SVM</b>	Support Vector Machine
<b>RAS</b>	Relative Amplitude of Secondary peak	<b>TPR</b>	True Positive Rate
<b>ROC</b>	Receiver Operator Characteristic	<b>UART</b>	Universal Asynchronous Receiver Transmitter
<b>RLS</b>	Recursive Least Squares	<b>VEB</b>	Ventricular Ectopic Beat
<b>rBSN</b>	robust Body Sensor Network	<b>WBAN</b>	Wireless Body Area Network
<b>RI</b>	Reflection Index	<b>WBSN</b>	Wireless Body Sensor Network
<b>RMSE</b>	Root Mean Squared Error	<b>WT</b>	Wavelet

# 1 Introduction

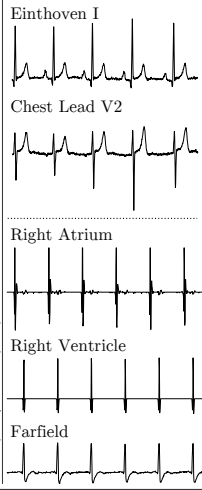
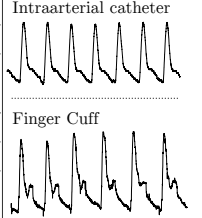
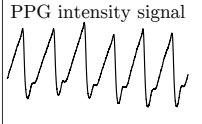
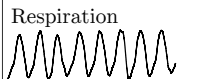
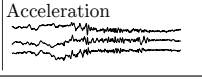
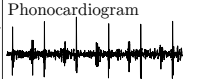
## 1.1 Multimodal Measurements of Vital Parameters in Longtime Recordings

Continuous monitoring of cardiovascular biosignals such as the electrocardiogram (ECG), arterial blood pressure (ABP), the photoplethysmogram (PPG) or respirational activity - to name only four examples - has become an inevitable standard in various clinical applications. In the first place, these signals provide a detailed picture of the hemodynamic state since a wide range of underlying mechanisms are already well understood, allowing associations between signal variations and corresponding activities in the organism. Moreover, vital parameters such as heart rate (HR), breathing frequency or even arterial oxygen saturation can be derived by non-invasive measurements, which have in fact revolutionized the possibilities of medical treatments.

Due to the ongoing miniaturization and increasing performance of electronic devices, along with continuously decreasing costs and overall power consumption, ambulatory surveillance of the cardiovascular state (CVS) has gained significant attraction in the last decades. Table 1.1 gives a superficial overview of the most prevalent biosignals with brief notes on measurements and related features. Obviously, unobtrusive monitoring in everyday situations can reveal much more information when compared to limited visits to the doctor's office where only sporadic pathological events or long-term anomalies will be investigated.

Unsupervised recordings, on the other hand, introduce serious problems such as motion artifacts and missing knowledge of environmental conditions. The interpretation of data acquired in such situations therefore is challenging for both the trained physician as well as automatic signal processing approaches. Whereas there are well established and robust measures such as the ECG (acquired with reliable wet electrode-skin interfaces), other recordings including EEG, PCG or pulse wave related signals (e.g. ABP and PPG) are very prone to signal distortions and partly require expert supervision during the respective measurements. To date, methods involving pulse wave analysis (PWA) are therefore considerably limited in their applications in difficult measurement environments, as they rely on accurate evaluation of the acquired signals. Extracting waveform features, such as peaks and valleys or even more sophisticated morphological properties, becomes impossible when the expected physiological pulse shape is distorted. Although literature contributions on PWA methods have clearly increased, works dealing with signal quality are

**Table 1.1:** Overview on common biosignals with related measurements and features.

signal	measurements	signal extracts	interpretation, features, events
ECG	<p>Surface ECG: Einthoven I-III, chest leads V1-V6 typically electrode-skin contact based on wet or dry electrodes Also researched in the past years: non-contact (capacitive coupling, sensing electromagnetic activity)</p> <p>Invasive measurements: Intracardiac Electrogram (IEGM). Electrophysiology catheter electrodes placed near cardiac muscle cells. Implants: Pacemaker and implantable defibrillator electrodes (bipolar leads in right atrium or right ventricle), Farfield channels measuring potential between electrode tip and implant case.</p>	 <p>Einthoven I Chest Lead V2 Right Atrium Right Ventricle Farfield</p>	<p>Primary application: Detection of myocardial arrhythmia such as atrial fibrillation, supraventricular and ventricular tachycardia, bundle branch blocks, asystolies and bradycardiac events including AV blocks or sick sinus syndrome to name just a few. Secondary applications: Heart rate variability, respirational activity, biometric recognition.</p> <p>Implants: Arrhythmia detection and analysis, measurement of conduction times (AV delays, bundle branch blocks, . . . ) refractory periods, therapies including pacing, cardiac resynchronization therapy.</p>
ABP	<p>Arterial blood pressure: Invasive interface: canula placed in the lumen of an artery and connected to a pressure transducer. Continuous measure. Non-invasive ABP recordings: Cuff measurements based on auscultatory or oscillometric principles (intermittent), arterial tonometry (pressure sensors placed on skin above arteries, continuous)</p>	 <p>Intraarterial catheter Finger Cuff</p>	<p>Main applications: Hemodynamic surveillance especially during anesthesia, decreased ABP can reveal information on anesthetic depth, hypovolemia, dehydration, hypoxia, hypothermia.</p> <p>Monitoring of hypo-/hypertension.</p>
PPG	<p>Non-invasive photoplethysmographic measurements. Transmission mode, reflectance mode typically applied at extremities like finger, toe or earlobe.</p>	 <p>PPG intensity signal</p>	<p>Pulse rate detection, arterial oxygen saturation (<math>SaO_2</math>) extraction, pulse contour and morphology analysis (affected by vasodilation/vasoconstriction), respirational activity</p>
resp	<p>Inductive belts, resistive belts, piezo, thermistor</p>	 <p>Respiration</p>	<p>Respiration frequency, estimation of breath volume, important measure in sleep medicine, apnea monitoring</p>
ACC	<p>Typically realized as micro electro-mechanical systems (MEMS) providing bi- and tri-axial acceleration recordings.</p>	 <p>Acceleration</p>	<p>Activity, posture, motion recognition. Discrimination of behavioural patterns. Reference to tackle motion artifacts.</p>
PCG	<p>Phonocardiogram: Monitoring of additional heart activity including valve closings using a microphone.</p>	 <p>Phonocardiogram</p>	<p>Measurement of cardiac timing intervals. Estimation of pulmonary arterial pressure.</p>
EEG	<p>Electroencephalogram electrical impulse activity in the brain.</p>	 <p>EEG</p>	<p>Assists diagnosis of neurological problems (headache, seizure disorders, degenerative brain disease, epilepsy). Applied in sleep medicine to detect apnea and arousals.</p>
EMG	<p>Electromyogram Surface EMG (standard wet electrodes) or intramuscular EMG (monopolar or concentric needle electrodes).</p>	 <p>EMG</p>	<p>Typically applied in nerve conduction studies.</p>
TEMP	<p>Temperature. Simple oral, rectal or oesophageal measures to more sophisticated devices like ingestible sensors.</p>		<p>Body core temperature to detect thermal illness. Applications in sports (deep sea diving) or general anesthesia monitoring.</p>
Echo	<p>Ultrasound measures (based on acoustic transducers), various modes (amplitude, brightness, Doppler-effect exploits, . . . )</p>	 <p>Sonography</p>	<p>Sonography covers measures of various tissues of the body with a wide field of applications. Experts are required during measurements.</p>
IMG	<p>Impedance AC/DC</p>	-	<p>Endocrine activity, emotion, blood volume</p>

still rather sparse. When it comes to on-line applicability and implementation considerations on small battery driven devices, current proposals are not satisfactory with respect to the high requirements of unsupervised PWA. In consequence, published results regarding the extraction of physiological parameters such as pulse rate (PR), respirational activity, oxygen saturation or blood pressure related attributes remain uncertain when reapplied in unguided recordings with unforeseeable external influences.

In particular, blood pressure (BP) records and PWA derived BP parameters are regarded as relevant sources for analyzing the CVS and related malfunctioning. Hyper- and hypotension are considered responsible for serious heart diseases and are linked to high mortality, elevating BP related cardiovascular properties in the focus of many diagnostics and treatments. Unfortunately, non-invasive blood pressure monitoring still poses a significant challenge, promoting novel approaches as BP estimation based on pulse contour analysis or transit time measurements. Continuous and non-occlusive blood pressure estimation (BPE) would serve as a path-breaking contribution especially with reference to diagnostic tools observing autonomic regulation. Blood pressure estimation based on PWA models has been attracting the scientific community for several decades, with many published results that appear very promising already, thereby approaching the ultimate goal of continuous BP estimation. However, the reported achievements have been validated on data acquired in well defined measurement environments only. Regarding public databases, most records have a clinical background, therefore containing high quality signals that are well suited for automatic evaluation. On the other side, when applying the published methods to signals acquired in ambulatory settings, it turns out that the efficacy of PWA applications significantly degrades, prohibiting reproductions of the earlier reported performance values. Artifacts of any kind, and especially those caused by motion, can be seen as the major factor responsible for complications in automatic signal processing approaches, limiting the range of ambulatory monitoring possibilities and respective treatments.

## **1.2 Structure and Concrete Aims of the Thesis**

This thesis will concern itself with the complex universe of ambulatory biosignal acquisition and aims to tackle the introduced challenges of unsupervised recordings regarding PWA related applications. The following topics are focused in the single chapters of this work.

### **Pulse Wave Analysis, Physiological Backgrounds and Considered Applications**

In order to depict the difficulties of non-invasive pulse wave recordings, which will motivate the aspects researched in this work, chapter 2 provides a very compact overview of the cardiovascular basics of the human organism. Section 2.1 therefore introduces the electromechanical mechanism of the heart and relating aspects of electrocardiography. The pulsatile propagation of the blood in the systemic cycle, as a direct consequence of the

periodic muscle contraction in the myocardium, can be measured by pressure and volume changes at different sites of the arteries. Thus, section 2.1.2 and 2.1.3 give a short summary of the most important aspects concerning blood pressure and photoplethysmography. As PWA does not only reveal information on cardiac activity but also provides indicative data on vessel characteristics and hemodynamic regulations in general, deeper examinations like morphology evaluation or pulse transit time (PTT) detection received increased scientific attention. A very prominent topic in current research projects is dealing with the introductory mentioned link between arterial blood pressure and PTT. Section 2.2 provides a more thorough insight into the current findings of blood pressure estimation by depicting basic models and published BPE approaches along with their performance reports. Moreover, section 2.2 illustrates the most important PTT associations and also presents established pulse derived parameters.

Reliable extraction of pulse wave parameters would contribute an influential enhancement in numerous medical fields. One example are geriatric units, which have a deeper interest in hemodynamic parameters (especially blood pressure), to monitor age dependent changes of cardiovascular properties. Although hypertension is considered a substantial cardiovascular state for developing various cardiac diseases, the exact opposite - hypotension - also should come under the physician's attention requiring immediate treatment. Decreasing BP is often a byproduct of orthostatic dysregulation and in this context commonly referred to as orthostatic hypotension (OH). Detecting OH is not as easy as it seems because the most widespread definitions for positive diagnosis are based on BP thresholds during and after orthostatic challenge. However, standard non-invasive BP measurements, as will also be explored in more detail in section 2.1.2, are known to influence the subject under test, which might introduce inaccuracies regarding the diagnostic results. Furthermore, exact timings are difficult to maintain and continuous measurement methods are not well suited in practical situations. Thus, OH diagnostics and therapies might significantly benefit from a more reliable and robust extraction of relating parameters as presented in this thesis. Section 2.3 will give a compressed introduction on OH backgrounds, current diagnostic ideas and unsolved challenges.

### **rBSN - A Novel Body Sensor Network Implementation**

A significant part of this work then concentrates on unsupervised acquisition of multichannel biosignals, which is dealt with in chapter 3. First, the very basic methodologies of ECG and PPG signal acquisition are briefly touched upon in section 3.1 and 3.2 respectively. As a lot of hardware systems proposing Body Sensor Networks (BSN) for multimodal signal acquisition have been published in recent literature, a thorough investigation is conducted next in section 3.3. It turns out, that it is hard to meet the tight requirements of unobtrusive and unsupervised longtime measurements in difficult environments. Therefore, a novel and robust BSN system (termed rBSN) was developed in conjunction with this work, which is designed for clinical as well as ambulatory environments and can be seen as one major contribution of this thesis. In addition, the system provides the flexibility

needed for adjustments in elaborated scientific experiments. The architectural rBSN details, including the specific sensors along with their improved analog and digital frontends, are presented in section 3.4, which also introduces a novel synchronization mechanism based on the Bluetooth (BT) standard. Moreover, this section presents the details of all clinical and laboratory field studies, which were conducted within the scope of this thesis.

### **OPRA - Pulse Wave Signal Quality Detection**

Although unsupervised longtime measurements might allow broader physiological insights, they also introduce considerable difficulties due to the changing external circumstances. As mentioned earlier, the PPG is known to be liable towards motion artifacts and prone to numerous environmental influences, often resulting in unreliable evaluations. Thus, the PPG can be seen as a limiting factor in applications as PTT extraction and therefore requires careful handling in automatic processing routines, which is the focus of chapter 4. Section 4.1 will start with a detailed overview of pulse wave velocity (PWV) extraction based on pulse transit- and pulse arrival times (PAT). Moreover, different extraction techniques are discussed and compared to each other with respect to their general robustness. Section 4.2 briefly depicts ECG signal quality aspects whereas section 4.3 concerns itself with a deep investigation of pulse wave signal quality issues. First, published signal quality detectors are illuminated to particularly point out their strengths and shortcomings. It appears that none of the analyzed methods achieves satisfactory results in all considered categories such as classifying performance, computational complexity, manual calibration and others. Consequently, this work presents a novel light-weight signal quality estimator, which outperforms the current methods and significantly contributes to reliable PWV applications in difficult environments and reveals its strength in on-line applicability and adaptive behaviour for different kinds of signal morphologies. The development of this algorithm constitutes the second major achievement of this thesis.

### **Ectopic Beat Detection**

Next to external conditions affecting the quality of respective recordings, physiological abnormalities such as cardiac arrhythmia can also negatively influence medical evaluation. With reference to PWV practices again, ectopic beat detection is - unfortunately - a widely neglected issue and indeed requires careful attention in automatic approaches. Section 4.4 presents different signal processing advances for automatic extrasystole detection and further proposes a novel approach incorporating multimodal features, that improve even more the sensitivity and specificity of the ectopic beat classifier.

### **Artifact Suppression in Pulse Wave Signals**

Artifact suppression in pulsatile signals is another important field, which perceived a lot of contributions in recent research. Although one has to be very cautious in interpreting artifact cleaned signals, this work also explores common noise cancellation methods and

presents preliminary results of a promising approach in section 5.1, which exploits movement information by means of blind source separation (BSS). As different kinds of motion lead to different shapes of artifacts, section 5.1.3 further presents a reliable hand movement detector based on features derived from the rBSN sensors' onboard accelerometers, which can be used to further support decisions relating to proper artifact treatment.

### **Influence of Pulse Wave Signal Quality and Ectopic Beats on Blood Pressure Estimation Methods**

Finally, chapter 6 will demonstrate the benefits of the accomplished results in practical applications, by evaluating different BPE approaches combined with the proposed signal quality detection and ectopic beat marker. It will be shown that a reliable pulse quality indication can contribute to trustworthy outcomes of blood pressure estimation methods, sorting out inappropriate PAT/PTT samples in real-time and working on battery driven devices. Different BPE models proposed in literature are implemented and tested upon mixed databases, which contain periods of major signal quality degradations as well as increased occurrences of ectopic beats that would significantly hamper approaches under test.

All results are summarized in Chapter 7, which finishes with a critical review not only highlighting the presented achievements but also pointing out identified limitations and unresolved aspects. Last but not least, possible future works are pointed out in a short outlook.

## 2 Cardiovascular Backgrounds and Important Measurement Methods

### 2.1 Cardiovascular System

To keep itself alive, a cell basically needs oxygen and glucose used in a biochemical process to produce energy, water and carbon dioxide, which is known as aerobic respiration. The body organ supply of dissolved oxygen in the blood and further nutrients is carefully regulated by the circulatory system, which is essentially controlled by the rhythmic contractions of the heart. Figure 2.2 provides the heart's general structure, depicting the atrium and ventricle on each side of the myocardium. Being delivered by the venous system of the body, oxygen depleted blood is collected in the right atrium at the beginning of a normal cardiac cycle. It then passes the right atrioventricular valve where it enters the right ventricle, from where it is eventually pushed through the pulmonary valve into the lungs. Inside the lungs, oxygen diffuses to the blood whereas carbon dioxide diffuses to the lungs. The lung is basically composed of the primary bronchi, giving rise to multiple bronchioles with several alveolar ducts ending in alveolar sacs, which themselves contain so-called alveoli where the actual gas exchange happens. As mentioned before, oxygen enters the blood by the process of diffusion, which is defined as the net movement of particles from an area of higher partial pressure to a region of lower partial pressure. Diffusion is known to occur only in distances of less than 1 mm, so that it can principally take place between the cells of the capillary and the cells of the alveoli, which are as near as  $0.5\ \mu\text{m}$  to each other. Compared to pulmonary arterial blood, the air in the alveoli provides a much higher partial pressure of oxygen and a lower partial pressure of carbon dioxide leading to a pressure gradient that causes the diffusion to take place. It should be mentioned that gases are barely soluble in blood which itself is a suspension of particles (cells and macromolecules) in an aqueous fluid. However, the red blood cells contain hemoglobin molecules, which provide a binding mechanism to transport oxygen as depicted in the right hand side of figure 2.1. A single hemoglobin molecule contains four heme (containing iron) and four globin units (polypeptide chains). As one hem and one globin molecule together can carry one molecule of oxygen, each hemoglobin molecule can bind four molecules of oxygen. Oxygenated hemoglobin is bright red while a deoxygenated hemoglobin is dark red, explaining the different colors of arterial and venous blood. Once the hemoglobin has bound the first oxygen molecule, its affinity towards further oxygen molecules is increased, leading to a sigmoid shape of the dissociation curve as illustrated in left part of figure 2.1.

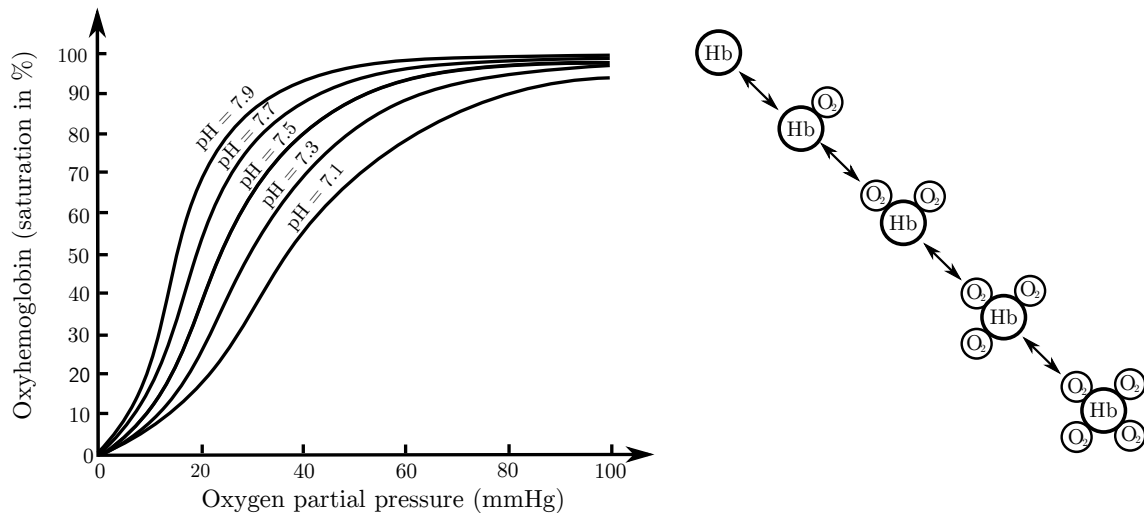


**Figure 2.1: left)** Oxyhemoglobin dissociation curve showing relation between partial pressure of oxygen and maximum percentage of saturated hemoglobin (oxygen saturation). The sigmoid shape describes the affinity of hemoglobin for oxygen, which also depends on carbon dioxide concentration, pH value and temperature [324].

**right)** Hemoglobin molecules (Hb) found in red blood cells. Each hemoglobin molecule can carry up to four  $O_2$  molecules. Deoxygenated hemoglobin is dark red whereas its color becomes much brighter when fully oxygenated, a phenomenon which is exploited in optical and non-invasive oxygen saturation measurements.

The oxygenated blood is then returned by the pulmonary veins and collected in the left atrium, which passes the blood into the left ventricle from where it is forced into all arterial vessels supplying the body organs. This periodic mechanism is realized by a sequence of electrically triggered and synchronized muscle contractions resulting in mechanical forces to transport the blood fluid throughout the whole system. The details of such a cardiac cycle are shortly discussed in the following subsection.

### 2.1.1 Electrocardiography

Since Willem Einthoven's invention of the electrocardiograph, which was awarded the Nobel Prize in 1924, the ECG has rapidly become a recognized medical tool in the diagnosis of cardiovascular diseases. In addition to the Einthoven ECG leads I, II and III, the American Heart Association and the Cardiac Society of Great Britain defined the standard positions and wiring of the chest leads V1 - V6 in 1938 [16]. Four years later, Emanuel Goldberger introduced the augmented limb leads aVR, aVL and aVF, which are used as unipolar leads with respect to an indifferent electrode similar to that, which was defined earlier by Frank Wilson (now known as Wilson Central Terminal). To date, these 12 leads still form the standard electrocardiogram that is used in modern clinical applications. The following part gives a brief overview of the electrical mechanism governing the morphological shape of the ECG recorded by body surface electrodes.

Basically, there are two states of single muscle cells in the myocardium: Mechanical

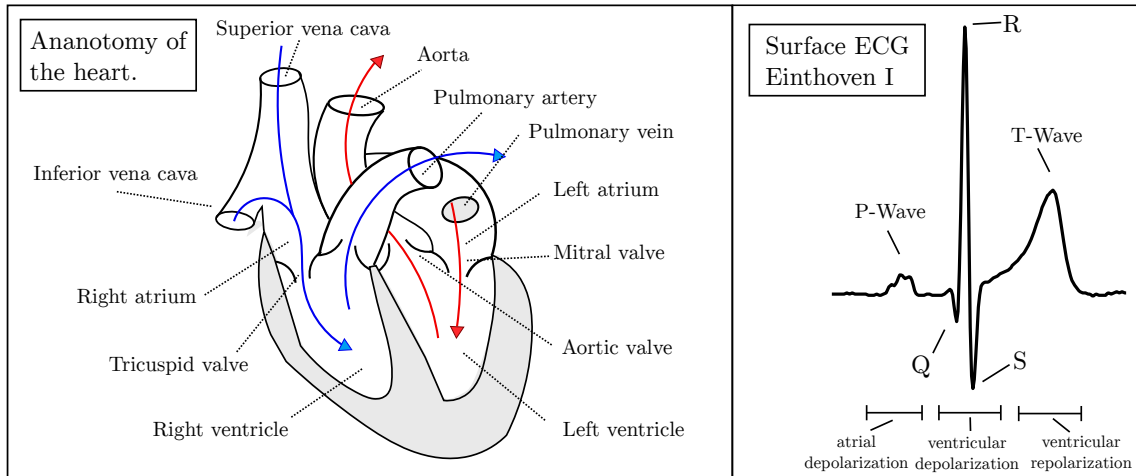


**Figure 2.2:** *left*) Principle structure of the human heart. At the end of the systemic circulation, oxygen depleted blood enters the right atrium and passes the right ventricle (blue line). From there it is pumped into the pulmonary arteries leading to the pulmonary circuit where the gas exchange takes place inside the lungs. Oxygen saturated blood then returns to the left atrium and ventricle (red line) where the next cycle begins with the following contraction. *right*) Surface ECG trace during cardiac cycle.

contraction and mechanical relaxation. Contraction is triggered by electrical depolarization, where the cell membrane potential rapidly changes from  $-90$  mV to  $20$  mV in approximately  $1$  ms. This is also referred to as the initial phase of the cardiac action potential. This rapid change in voltage leads to depolarization of the neighboring cells, causing an electrical impulse to spread from cell to cell throughout the myocardium. After depolarization, the cell membrane potential slowly returns to its resting state, which is known as repolarization. The surface ECG actually gives a piece of information on the current flowing in the intra- and extracellular fluid, which is a direct result of the potential changes generated by the millions of action potentials inside the cardiac cells. Thus, it is possible to derive temporal as well as spatial information by evaluating the morphological shape of the surface ECG. More precisely, individual cells of the myocardium and conduction system may be regarded as current dipole sources, whose three dimensional vector describes the dipoles' time varying position, orientation and magnitude. All relating vectors are summarized to a dominant vector, which describes the direction of the electrical wavefront. The surface ECG is proportional to the projection of the dominant vector onto the respective lead vector.

The origin of the electrical impulse is found in the sinoatrial node (SA node), which contains groups of pacemaker cells with a self triggering ability, and is situated in the upper part of the right atrium. The heart with its conduction cells can be seen as a whole conduction system on which the electrical wavefront is propagated. At the very beginning of a cardiac cycle, all cells are at rest, which results in the isoelectric line of the ECG. Once the SA node has triggered, both atria begin to depolarize with a dominant vector pointing downwards toward the AV node, provoking a small positive ECG peak known as P-Wave. The impulse then moves ahead through the atrioventricular node where it is significantly delayed by

the local muscle tissue before it reaches the bundle of His and eventually the ventricular chambers. Due to the low muscle mass, this part is not visible in the ECG. Nonetheless, the slowed conduction allows for a proper filling of the ventricles, which contract when the wavefront is conducted through the Purkinje fibers, which form an extensive and fast network on the inner ventricular walls. The ongoing and much faster ventricular depolarization first produces a peak with negative polarity in the ECG (Q-Wave), as the associated vector points away from the exploring electrode. The left ventricle walls contain much more muscle mass, which is the reason why this part takes longer to depolarize and forces the dominant vector to gradually point towards the exploring electrode producing the fiducial ECG peak (R-Peak). At the same time, the atria are already repolarizing, which is, however, not visible in the ECG as it is completely masked by the depolarization activity of the ventricles. When the depolarization of the ventricular chamber is completely terminated, the vector points away from the electrode (S-Peak) and the ECG begins to return to the isoelectric line again. The ventricular repolarization then produces a clearly visible wave of positive polarity, also known as T-Wave. Figure 2.2 provides a coarse overview of the heart's anatomy and depicts the presented ECG wave components. It should be noted that the specific shape of the ECG waveform (morphology and polarity) completely depends on the respective electrode position, underlining the importance of correct electrode placements in standard ECG applications.

Nonetheless, this well structured mechanism might be disturbed by several pathophysiological influences. The electrical wavefront propagation can be inhibited or completely blocked. In case of a sinoatrial block, for example, the electrical impulse is blocked on its way towards the atria. In such situations, the AV node can adopt its function as secondary pacemaker stimulating the ventricles at lower heart rates. The AV node is then often referred to as ectopic pacemaker. Such dysfunctions in the conduction system can be treated by implantable pacemakers, which are configured to resynchronize the rhythmical cardiac contraction.

Deviations of electrical timings in the conduction system might occasionally occur and do not have to be considered as pathophysiological in all cases. Commonly witnessed incidents are premature QRS complexes, which are referred to as extrasystoles or ectopic beats (EB). A supraventricular ectopic beat (SVEB) has its origin in one of the two atria. Depending on the exact location, the P-Wave might be normal, inverted or even missing, whereas the QRS complex is expected to preserve a normal morphology as the electrical impulse takes the normal way through the AV node. When the ectopic focus is located in the ventricle, the extrasystole is labeled as ventricular ectopic beat (VEB). Contrary to SVEBs, VEBs reveal a much broader and more deformed QRS morphology. When a VEB occurs, the original wavefront from the SA node is blocked by the refractory period of the excited ventricular cells leading to a compensatory pause [294].

As a matter of fact, automatic SVEB/VEB detection plays an important role and is still considered a hot topic in current research. Applications like PWV evaluation particularly

rely on ectopic-beat-cleaned signals, which can be challenging, especially in episodes of decreased signal quality.

### 2.1.2 Measurement of Blood Pressure

The electro-mechanical pumping mechanism of the heart depicted in the previous section results in a quasi periodic pressure wave traveling through the arterial tree. Its major task is a stable blood supply covering the circulatory system to account for different physical demands. Interestingly, the pulsatile wavefront itself conveys valuable information on the hemodynamic state and can be used to extract associated parameters from both continuous and intermittent blood pressure measurements.

**Non-Invasive Methods** As a matter of fact, the arterial blood pressure wave is one of the oldest vital parameters that attracted physiological interpretation and was used to assess the underlying state of health and disease [12]. Hale's experiments on the crural artery of a horse in 1733, are often cited as the pioneering work on blood pressure measurement, whereas the first serious mechanical measurement devices emerged in the 19th century [26]. These sphygmographs were based on a simple palpation technique to plot the contractions of the radial artery caused by the traveling pressure wave. However, it was not possible to relate these amplitudes to specific pressure values such as systole or diastole. In 1896, the Italian internist Riva-Rocci proposed an inflating cuff attached to the arm in order to entirely obstruct the blood transport in the radial artery. The cuff pressure was then gradually decreased and equaled the systolic pressure when the radial pulse was perceivable again. This significant advance was complemented by observing the Korotkoff sounds (e.g. using a stethoscope) that emerge when the cuff reaches systolic and diastolic blood pressure levels. These acoustic effects are caused by not completely understood mechanisms inside the vessels that affect the blood flow but are assumed to be the result of blood turbulences, sudden stretching of vessel walls or formation of bubbles within the blood [323]. This auscultatory method is still considered the golden non-invasive standard for blood pressure monitoring [235].

Exploiting the advances of electronic systems, the first automated blood pressure instruments were introduced in the early 1970s, based on the oscillometric method. Although this method is quite similar to the auscultatory approach, as the arteries are completely occluded, systolic blood pressure (SBP) and diastolic blood pressure (DBP) values are extracted by evaluating oscillations that occur on the cuff transducer during deflation [253]. The steepest increase of the oscillation frequency is taken as an indicator for systolic blood pressure, the maximum oscillation corresponds to the mean arterial pressure (MAP) and diastolic pressure is often extracted by evaluating the point of maximum decrease in the oscillation rate [176, 253, 323]. Moreover, these pressure values are often related to approximation formulas as in eq. (2.1), which assume a triangular shape of the pulse wave and are referred to in many implementations to extract the diastolic component, being

more robust than direct extraction [323]. A specific MAP value is commonly targeted to ensure proper blood perfusion pressure in the critically ill and is a valuable parameter to monitor hemodynamic failure [11].

$$MAP = \frac{SBP + (2 \cdot DBP)}{3} \quad (2.1)$$

It should be noted that none of these depicted methods is capable of continuous blood pressure monitoring. One intuitive approach that has been suggested for continuous BP extraction aims to determine the force applied to the inner arterial wall when the pressure wave travels along a specific point. This is done by placing a tonometer probe on the skin directly above an artery, to convert the pressures exerted in the arterial wall into a measurable voltage signal. Such applanation tonometry (AT) techniques are based on the principle that in a flattened vessel (forced by applanation), the circumferential wall stress is balanced so that the pressure measured by a sensor equals the intra-arterial blood pressure [12, 59]. Thus, it is possible to gain continuous curves that are related to the arterial blood pressure wave without completely occluding the blood flow. However, calibration as well as exact positioning of the sensor probe is essential in AT, which complicates unsupervised applications and generally requires an expert for sensor set-up and the succeeding measurement procedure. Finally, as the evaluation of AT curves is seriously hampered by sensor displacements or patient motion [179], it remains a rather inconvenient approach in clinical or ambulatory applications.

Another semi-occlusive method, which is implemented in various systems such as the FINAPRES (FINgerArterialPRESsure, Finapres Medical Systems, The Netherlands) or CNAP (CNSystems Medizintechnik AG, Graz, Austria) devices, is based on adjusting the applied pressure of an external finger cuff to regulate the blood volume flowing through its arteries. This idea was first described by Peñáz in the early 1970s [220] and has the great advantage of providing a continuous BP estimate. The mechanism exploited here is based on the observation that the maximum wall dilation during pulse wave systole develops when the luminal pressure of the artery equals the external pressure so that there is no load on the artery wall. The pulse wave itself is analyzed by a photoplethysmographic measurement principle to regulate the applied pressure which yields a continuous representation of the arterial pressure curve. The method's feasibility in realistic settings was proved in longtime measurements where intra-arterial pressure references have been available [113, 217]. As a matter of fact, this method allows for unsupervised operation, but it still remains occlusive, which poses a significant disadvantage for long-term monitoring. Moreover, there is evidence that the accuracy depends on correct positioning of the finger cuff [125] and the BP estimation might be erroneous in patients showing signs of hypotension or vascular insufficiency [323].

**Invasive Methods** The most direct way of BP recordings involves invasive catheter insertion in easy accessible cannulation sites such as the radial, ulnar or femoral arteries.

The intra-arterial cannula is wide and short and is connected to a fluid filled tubing for hydraulic coupling between arterial blood and pressure transducer. The diaphragm of the transducer is typically connected to a strain gauge whose resistance is then measured using a Wheatstone bridge circuit. Once properly inserted, it is possible to immediately derive a continuous pressure curve, allowing accurate waveform analysis and beat to beat evaluation.

Contour analysis of the continuous pressure pulse contributes invaluable information concerning the hemodynamical processes of the cardiorespiratory system. When the blood is ejected from the left ventricle into the systemic cycle, the pulse begins to propagate through the arterial tree with its morphology mainly determined by the pattern of ventricular contraction as well as the geometric and elastic characteristics of the arterial vessels [12]. Due to the elastic properties of the proximal arteries like the aorta, a significant part of the pulse pressure is initially compensated by the expanding vessel walls, which is comparable to the windkessel effect acting like a pressure filter [329]. The stored volume is immediately released during diastole. Assuming a tube of infinite length, this pulse would move ahead with a sinusoidal morphology. At arterial junctions, however, parts of the pulse wave are reflected, which in turn counter-propagate in opposite direction. It is generally accepted that the junctions from aortic to renal and iliac arteries are the two major reflection sites of the arterial tree and contribute a significant part to the morphological changes of the pressure wave [18]. It should be noted that re-reflections occur but are less relevant due to the significantly decreasing amplitude. Figure 2.3 adopted from [18] illustrates the components and propagation of the pressure pulse. Examining the pulse wave during its travel from the aortic root to the peripheral vessels, one generally observes an amplification of the pressure signal. Moreover, different models and transfer functions have been proposed and analyzed in order to estimate the central aortic pressure based on peripheral measurement values. A short introduction and overview of relating works is given in [12].

Nonetheless, there are some significant challenges coming along with invasive BP methods. Although the sensor is located at the physiological source, invasive arterial blood pressure monitoring is generally susceptible to artifacts often caused by systematic measurement errors, such as transducer flushing or external incidents including catheter clotting and motion [182]. Finally, catheterizations are strictly restricted to clinical measurements underlying significant risks and are therefore not considered in ambulatory settings.

### 2.1.3 Photoplethysmography

As briefly depicted in the previous subsection, the cardiac cycle guarantees a quasi periodic supply of oxygenated blood to the arterial vessel system. Due to the pumping mechanism of the heart, the blood is transported in a pulsatile manner through the arteries of the human body. The blood fluid mainly consists of red blood cells (45%), white blood cells (0.3%), platelets (0.15%) and plasma [105]. Approximately 90% of plasma is composed of

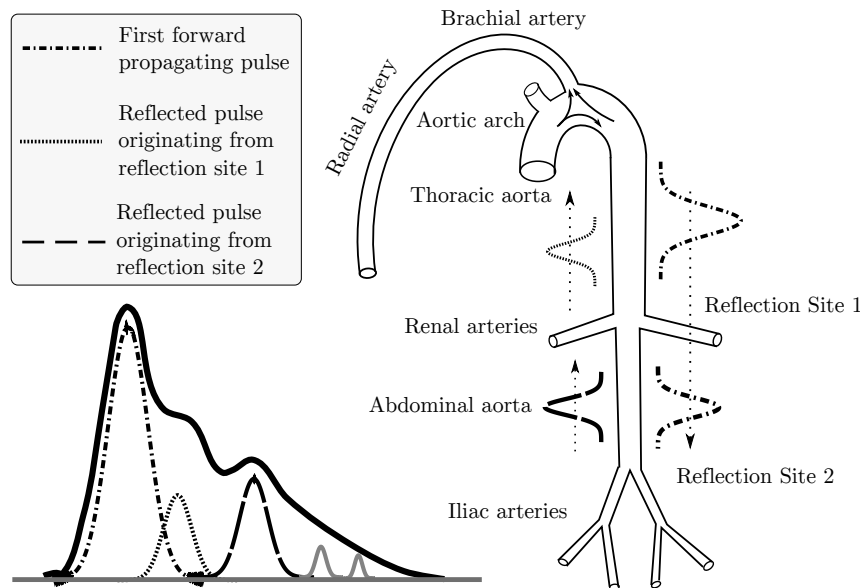


**Figure 2.3:** Pressure pulse morphology commonly observed at the radial artery which is thought to be the result of superimposed pulse waves originating from different reflection sites in the arterial tree. Drawing adopted from [18].

water, which is the reason blood does not completely absorb light in the region of 600 nm to 1000 nm.

Photoplethysmography provides an optical measure to non-invasively track blood volume changes in the vascular bed exploiting the transparent properties of water inside the above mentioned optical window. The haemoglobin fractions, on the other hand, do absorb wavelengths in the red to infrared region, as is shown in the absorption spectra plotted in figure 2.4, where the corresponding absorption coefficients describe the probability of photon absorption per unit path length. Considering light travelling through a blood filled tube, the total absorption of light would thus directly depend on the optical path length. Therefore, the optical measurement approach seems a proper way to track pulsatile changes of blood volume in an elastic arterial vessel. One of the pioneering photoplethysmographic measurements was reported in the late 1930s, where the first optical recordings of blood volume changes and its relation to pressure waves were described in more detail [106].

Pathbreaking applications emerged many years later though. Based on the law of Beer-Lambert and exploiting the different absorption spectra of oxygenated and deoxygenated hemoglobin, it is possible to non-invasively determine arterial oxygen saturation, which was a revolutionary contribution to cardiorespiratory monitoring in the late 1970s [324]. Technically, one chooses two wavelengths with a notable difference in the corresponding extinction coefficients of oxyhemoglobin and hemoglobin fractions, which is true for red light (660 nm) and infrared light (900 nm), as is illustrated in figure 2.4. Evaluating the resulting intensity signals of the transmitted light for both wavelengths, it is easy to

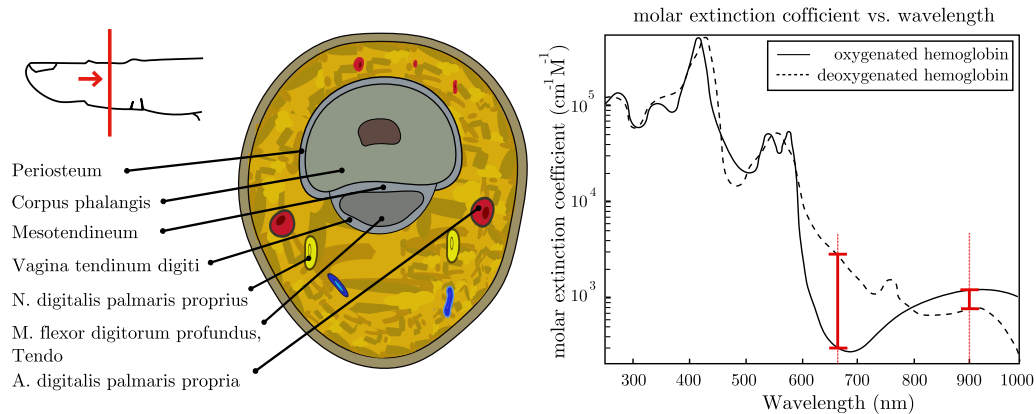


**Figure 2.4: left)** Cross-sectional cut depicting the main anatomical components of the finger (drawing adopted from [284]). Due to its rather small diameters, the fingers can be illuminated by off-the-shelf components, such as standard light-emitting diodes, and are therefore preferred measurement locations in photoplethysmographic applications. **right)** Molar extinction coefficient for oxygenated hemoglobin and deoxygenated hemoglobin at different wavelengths. Choosing wavelengths around 660 nm (red) and 900 nm (infrared) yields perceivable differences, allowing for arterial oxygen saturation calculation [324].

show that the equation of Beer-Lambert allows for the calculation of the arterial oxygen saturation [324].

Multiple terminologies are found when the photoplethysmographic waveform is described, where PPG and digital volume pulse (DVP) are the most frequent ones. The different standards were once summarized in one of Elgendi's works [63], which also serves as a compact overview of PPG contour analysis.

Transmitting light through an artery is especially easy in extremities like the finger, toes or earlobe, where the arterial vessels, its arterioles and connected capillary bed, can be illuminated without major obstacles. Due to its easy applicability, finger plethysmography is one of the most widespread methods for PPG acquisition. Figure 2.4 shows the transverse section through the shaft of the middle phalanx of the middle finger [284]. The red dots represent the small finger arteries known as digitalis palmaris propria, originating from the two main arm arteries ulnaris and radialis. The blue dots are small vessels belonging to the venous return system which are summarized as veins intercapitulares [284], whereas the yellow ones depict the proper digital nerves. The phalanx bone with tendons that are attached to the forearm muscles is centrally positioned and covered by the bone skin (periosteum) with the rest of the finger being mainly filled by fat.

Thus, the finger is a convenient location where a light source and a photodetector can be easily placed opposite or next to each other. The former setting is also known as transmission type PPG, whereas the later is referred to as reflectance type PPG. A deeper insight into the technical details of PPG systems will be given in section 3.2.

Promoted by the rising availability of photoplethysmographic sensor systems, clinical PPG practices have increasingly gained interest in the past decades. Allen et al. published a

repeatedly cited milestone paper in 2007, which gives a neat overview concerning the basics of pulse oximetry, important applications, and their clinical relevance [4].

Methods based on PPG analysis range from simple heart rate extraction [84, 274], to more sophisticated analysis including arterial oxygen saturation [184, 324], respiratory activity [122, 120], cardiac rhythms and arrhythmias [278], vascular assessments [7, 315] and with rising interest, pulse wave velocity considerations [30].

As a matter of fact, the PPG waveform contains very similar morphological properties when compared to the arterial pressure curve discussed in the previous section. Millasseau et al. [2] analyzed the PPG with regard to radial and digital artery pressure waves recorded by tonometry and volume clamp respectively. It is accepted that the PPG resembles the carotid pressure wave and is also susceptible to changes in vasodilation and vasoconstriction. Millasseau pointed out that there are some minor differences regarding the morphology of PPG and pressure waves, such as a slight height difference of the diastolic component and the preceding inflection point. They derived a generalized transfer function to transform PPG to pressure pulses and conclude that the volume pulses underlie the same mechanism governing the shape of pressure pulses and might therefore be used as a surrogate for morphological analysis.

**Conclusion** A neat overview of PPG relating parameters and signal components is given in [62], which also lists further potential diagnostic applications. To sum up, the PPG is an easily acquirable signal that contains complex physiological information helping to assess the cardiovascular state. Unfortunately though, automatic processing approaches are rather challenging because the PPG is prone to disturbances from artifacts. This inevitably limits subsequent methods which build upon PPG derived parameters, requiring careful interpretation and emphasizing the need for reliable preprocessing techniques.

## 2.2 Non-Invasive Blood Pressure Estimation

### 2.2.1 Pulse Wave Velocity Considerations

#### 2.2.1.1 Pulse Wave Velocity Backgrounds

Numerous of recent BPE approaches are based on pulse wave velocity considerations, taking into account the elastic properties of the arterial vessels. In general, elasticity describes the relation of stress to strain in elastic materials. With respect to an elastic tube, stress can be caused by a force  $F$  applied to the cross-sectional area  $A$  specified by the tube's diameter  $D$ , which will result in a longitudinal strain measurable in a change of length  $dl$ . According to the Poisson effect, the transversal strain becomes obvious in a change of diameter  $D$ . Linear elastic materials, which follow Hooke's law, will show a linear relationship as depicted in figure 2.5 where the slope is known as Young's modulus  $E$  and can be interpreted as a measure of stiffness having the units  $\frac{N}{m^2}$ . However, biological materials possess a rather convex stress to strain relation, so that in practice one calculates Young's modulus using the tangent at a specific point, which is then referred to as incremental modulus  $E_{inc}$ . Note that the slope increases with strain, which means that the arteries will become stiffer on higher stress and strain values [331].

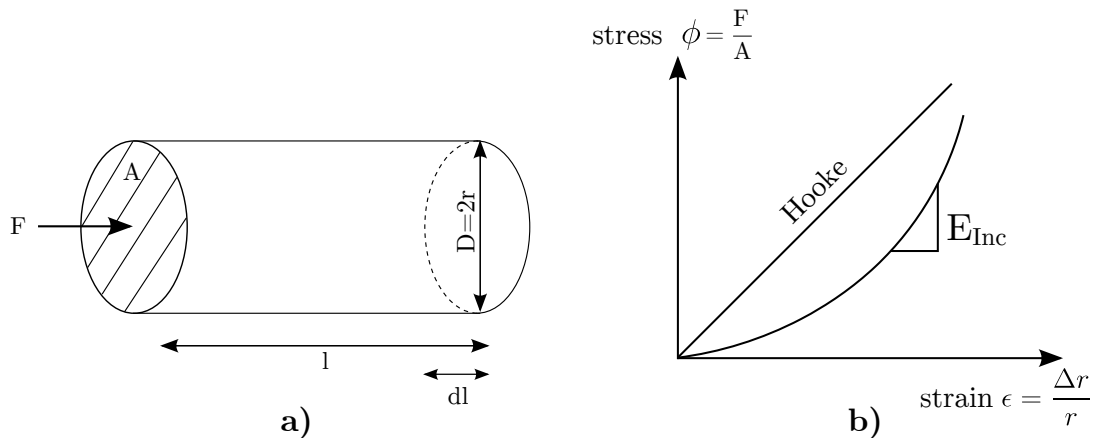


**Figure 2.5:** a) Change of length  $dl$  in an elastic tube due to the force  $F$  applied to the cross-sectional area  $A$ . b) Linear relation of stress to strain following Hooke's law and convex curve found in biological materials [331].

A well appreciated characterization of the structure of an organ is described by the pressure-volume relation  $\frac{\Delta V}{\Delta P}$ , commonly referred to as compliance  $C$ .

$$C = \frac{\Delta V}{\Delta P} \quad (2.2)$$

When considering the cross-sectional area  $C_A$  instead of the volume  $V$  one obtains the so called area compliance  $C_A$ .

$$C_A = \frac{\Delta A}{\Delta P} \quad (2.3)$$

The diameter compliance  $C_D$  is defined as the ratio of the diameter change  $\Delta D$  to the pressure change  $\Delta P$ .

$$C_D = \frac{\Delta D}{\Delta P} \quad (2.4)$$

This leads to the relation expressed by eq. (2.5), assuming a vessel length  $l$  and diameter  $D$ .

$$C = l \cdot C_A = \frac{l \cdot \pi \cdot D^2 \cdot C_D}{4} \quad (2.5)$$

The compliance  $C$  is often illustrated with respect to the total volume  $V$  (or cross-sectional area  $A$ ) of the organ considered, and in this case other terminologies like distensibility or compressibility are found in literature [92] where the volume distensibility  $C_{Dist}$  is given by eq. (2.6).

$$C_{Dist} = \frac{\Delta V}{V} \cdot \frac{1}{\Delta P} \quad (2.6)$$

The inverse of the compliance from eq. (2.2) describes the change of volume  $\Delta V$  of isotropic material in response to an applied pressure change  $\Delta P$  and is known as elasticity EL.

$$EL = \frac{\Delta P}{\Delta V} \quad (2.7)$$

In the same way, the reciprocal of the distensibility from eq. (2.6) is also known as bulk modulus  $K$  or volume elasticity.

$$K = EL \cdot V = \frac{\Delta P \cdot V}{\Delta V} \quad (2.8)$$

Assuming  $V = \pi r^2 l$  and considering the corresponding volume change with respect to luminal radius change  $\frac{dV}{dr} = 2\pi r$  it follows that for small changes of  $\Delta V$

$$\frac{dV}{V} = \frac{\Delta V}{V} = \frac{2\pi r \Delta r}{\pi r^2} = \frac{2\Delta r}{r} = \frac{2\Delta D}{D} \quad (2.9)$$

one can derive the bulk modulus  $K$  expressed in terms of diameter  $D$ .

$$K = \frac{\Delta P \cdot D}{2 \cdot \Delta D} \quad (2.10)$$

Compliance/distensibility and elasticity/bulk modulus provide quantitative measures of mechanical vessel properties that significantly change with age or disease [330]. Arterial compliance, especially in the proximal arteries as the ascending and descending aorta,

plays an important role in buffering the pulsatile ejected pressure waves of the left ventricle.

If one considers the arterial vessel as an elastic tube of isotropic material, then the relation of the transmural pressure within a lumen of an arterial vessel (which provokes the transversal strain in the tube as mentioned earlier) and the wall stress of that vessel can be described by the law of LaPlace [331]. The transmural force corresponds to the stress  $\phi$  which keeps the wall of thickness  $h$  of the cylindrical vessel together leading to

$$\phi = \frac{P \cdot r}{h}. \quad (2.11)$$

As equation (2.11) shows, pressure and resulting wall stress are related by radius and wall thickness. Assuming a thin wall, the incremental elastic modulus can be described by a small change of stress and the corresponding increment of strain

$$E_{inc} = \frac{stress}{strain} = \frac{\Delta\phi}{\frac{\Delta r}{r}} = \frac{\frac{\Delta P \cdot r}{h}}{\frac{\Delta r}{r}} = \frac{r^2}{h} \cdot \frac{\Delta P}{\Delta r} = \frac{D^2}{h} \cdot \frac{\Delta P}{2 \cdot \Delta D} \quad (2.12)$$

with  $r$  being the inner radius (or  $D$  the inner diameter),  $h$  the wall thickness and  $\Delta P$  the transmural pressure change.

Simplified models regarding pulse propagation of incompressible fluid in elastic vessels were proposed in the early 20th century by Otto Frank [75] in form of the characteristic pulse wave velocity  $c$  with  $\rho$  the density of blood and  $K$  the bulk modulus:

$$c = \sqrt{K/\rho}. \quad (2.13)$$

Inserting the definition of the bulk modulus as introduced in eq. (2.8) leads to

$$c = \sqrt{\frac{V \cdot \Delta P}{\Delta V \cdot \rho}} \quad (2.14)$$

and resorting to the area compliance yields

$$c = \sqrt{\frac{A}{C_A \cdot \rho}} \quad (2.15)$$

which provides the wave speed-compliance expression also known as Bramwell-Hill equation [28].

The Moens-Korteweg equation is another frequently applied formula which expresses the

pulse wave velocity  $c$  with respect to the elastic modulus  $E_{inc}$  as introduced earlier in eq. (2.12):

$$c = \sqrt{\frac{h \cdot E_{inc}}{2 \cdot r \cdot \rho}}. \quad (2.16)$$

In order to determine practical in-vivo configurations, Hughes et al. investigated pressure-volume curves at different measurement sites in 12 dogs where the best fitting equation was given by an exponential function [109]:

$$E_{inc} = E_0 \cdot e^{\zeta P}. \quad (2.17)$$

$E_0$  and  $\zeta$  depend on the measurement site and on the subject in general where  $\zeta$  is typically around  $0.017 \text{ mmHg}^{-1}$  [109].

### 2.2.1.2 PWV Measurements

As depicted in the previous section, PWV is directly related to the elastic vessel properties via the Bramwell-Hill (eq. (2.15)) and Moens-Korteweg (eq. (2.16)) equations. Using the former, one can derive the pulse speed based on the lumen cross-sectional area  $A$  and the arterial compliance  $C_A$  which can be determined by ultrasound and tonometry respectively [29, 241, 330]. Similar measurements can be conducted by using magnet resonance imaging (MRI) approaches [316] calculating the wave speed from volume flow and area variations in the ascending aorta. However, these methods are not suited for unsupervised measurements, requiring large and expensive sensor systems that can be operated by experts only.

Alternative methods are based on point to point measurements of the pulse wave acquired at two different locations in the arterial tree. These methods then derive the PVW by evaluating the pulse transit time and the distance of the recording sites [27]. Basically, all measurement principles that output a continuous pulse wave could be suitable for the given task. Buxi et al. presented a detailed overview of the different techniques involving optical, mechanical, bio-impedance, temperature, magnetic and other measurement principles [30]. As pointed out in section 2.1.3, the PPG morphology is closely related to the arterial pressure wave and is therefore often applied for PWV relating measurements. All PWV concerns in this work, will be based upon pulse waves derived by photoplethysmography, if not otherwise stated. Although being not technically correct, the term PWV is also alternatively used in this work when the underlying methods are truly based on transit time calculations only.

The speed of the pulse wave itself could be obtained by measuring the duration of pulse wave propagation  $t$  through a given arterial segment of length  $l$  according to  $c = \frac{l}{t}$ . Using a pulse wave acquisition device such as a two site PPG sensor, the duration  $t$  is determined by

a single pulse transit time measurement. Note that the PTT can be measured at different parts of the body, for example at the brachial artery (using a reflectance pulse oximeter) and the digital artery (using a transmission pulse oximeter). Typical aortic wave speeds lie in the range of 5 to 20 m s<sup>-1</sup> [333]. Thus, it might take less than 10 ms for a fast pulse wave to travel through a short segment of 0.2 m, which approximately covers the distance from the wrist to the finger. This in turn means that the corresponding measurement devices have to provide a high temporal resolution, especially when distributed wireless sensors are involved. Based on these findings, a maximum synchronization error of 100 μs is demanded with reference to the wireless PWV hardware developed in this work, which will be discussed in more depth in chapter 3.

Another widely used PWV parameter is known as pulse arrival time, which is defined as the interval triggered by the electrical activation of the left ventricle (producing the R-Peak visible in the surface ECG, cf. chapter 2.1.1) and the following pulse arrival in the periphery (e.g. digital artery). With PPG signals, PAT measurements are more robust than PTT extraction as one does not necessarily need a reflectance pulse oximeter. On the other hand, when resorting to PAT measurements, one cannot determine the pulse speed  $c$  directly, as the PAT also contains parts of the isovolumetric contraction time (ICT)<sup>1</sup>. Thus, PAT can be seen as the sum of the pre-ejection period (PEP) and PTT of the pulse wave, where the latter describes the traveling time from the aortic valve to the periphery [351].

$$PAT = PEP + PTT \quad (2.18)$$

A robust and automatic detection of PAT and PTT values is a challenging task, especially when derived from PPG signals which are prone to movement artifacts and rather difficult to analyze. This issue will be thoroughly discussed in section 4.1.

### 2.2.1.3 PWV Parameters and Influencing Factors

Whereas the previous section depicted the basic backgrounds regarding PWV, the following part will illuminate some major influencing factors, including physiological as well as external aspects.

#### *Stiffness*

As introduced earlier, arterial stiffness is a major property affecting the speed of wave propagation in the blood vessels. Arterial stiffness itself is a well-appreciated cardiovascular parameter, which is known to increase with age due to the structural change of the wall properties where elastin is replaced by collagen [333]. Various works including Nitzan et al. [201], Allen et al. [6] or Tomiyama et al. [305] evaluated datasets from dedicated studies concentrating on PTT. It was concluded that PTT decreases at different measurement

---

<sup>1</sup>Time from closure of the mitral wave to onset of left ventricular ejection [238].

sites due to age related arterial stiffness, which is indeed a dominant factor contributing to PWV. It is noted, that the impact of changing stiffness from central arteries (aorta) to peripheral vessels (e.g. radial artery) also plays an important role in blood pressure measurements as magnitude and phase of the pressure curve are significantly affected. This issue is well studied with proposed transfer functions to relate peripheral and central pressure values [77, 131].

Further, there are numerous works aiming at the extraction of stiffness related parameters exploiting pulse wave morphology. Millasseau et al., for example, calculated a stiffness index  $SI_{DVP} = \frac{\text{subjectHeight}}{\Delta T_{DVP}}$  derived from the digital volume pulse by determining the time delay  $\Delta T_{DVP}$  between systolic and diastolic peak [187]. It is argued, that  $\Delta T_{DVP}$  corresponds to the transit time of pulse wave from the root of the subclavian artery to the apparent site of reflection and back, with a path length that is assumed to be proportional to the subject's height. A correlation of  $SI_{DVP}$  with the carotid-femoral PWV was manifested in a clinical field study of 87 subjects, advertising  $SI_{DVP}$  as an interesting parameter for arterial stiffness. Comparable results were shown by [7].

Another frequently used parameter is given by the augmentation index (AI) which was used in arterial stiffness estimation [207, 269]. AI is defined as the difference of the primary and secondary peak as a percentage to the absolute pulse pressure (difference of SBP and DBP). Westerhof et al. mentioned a reflection index (RI) which can be calculated even when the inflection point is not clearly distinguishable [328].

Jang et al. presented a low-complexity PPG parameter called P2Ocd which was shown to be suited for arterial stiffness assessment as well [114].

### ***External influences***

Externally applied pressure resulting from sensor placement for example also introduces morphological as well as PWV relating variations. Teng et al. reported significant changes in PTT with varying contact forces [296] and conclude that sensor contact force should be carefully controlled during PTT measurements. Motion artifacts pose a hard challenge on PWV extraction as well. Foo quantified a PTT error of  $20.14 \pm 12.43\%$  even when comparatively small grades of PPG signal distortion are present [71], underlining the importance of signal quality when such parameters are extracted automatically. Next, temperature is also known to alter the perfusion in the extremities which has a direct impact on the pulse wave morphology and on PTT calculation, as discussed in [353].

Posture changes have been associated with subject-specific effects on PAT measurements during constant blood pressure values, although Muehlsteff et al. pointed out that this mainly results from the influence of the underlying pre-ejection period. Therefore, one should take care when analyzing PWV by means of PAT measurements [195].

In fact, PTT is influenced by far more physiological parameters, like heart rate and respiration [58, 70, 121, 237], gender [305], stress [214] and blood pressure, as well as subject characteristic factors including physical condition, smoking or prandial state, which emphasizes the complexity of the structures governing PWV.

### 2.2.2 Blood Pressure Estimation Models

As the previous section depicted several elementary facts on arterial pressure relations, concrete BPE models based on PAT/PTT measures will be discussed next. The first works experimentally evaluating the relationship between PWV and arterial blood pressure in humans emerged in the 1970s [94], already showing great promise of this continuous approach.

Resorting to Hughe's empirical results formulated in eq. (2.17), one gets a direct link between PWV and pressure by substituting the elastic modulus of the Moens-Korteweg equation as given by eq. (2.16):

$$c = \sqrt{\frac{h \cdot (E_0 \cdot e^{\zeta P})}{2 \cdot r \cdot \rho}}. \quad (2.19)$$

The pulse wave velocity is represented by  $c$  and solving eq. (2.19) to  $P$  one obtains

$$P = \frac{1}{\zeta} \ln\left(\frac{2r\rho}{h \cdot E_0} \cdot c^2\right) = \frac{1}{\zeta} \left(\ln\left(\frac{2r\rho}{h \cdot E_0}\right) + 2 \cdot \ln(c)\right). \quad (2.20)$$

The unknown parameters  $\zeta$ ,  $E_0$ ,  $D$ ,  $\rho$  and  $h$  are difficult to determine as they are subject dependent and influenced by multiple factors. Fixing these values by means of calibration measures is a very common way conducted in most BPE methods that are based on PWV measures. Parameterizing the unknowns of eq. (2.20) one arrives at

$$P = \frac{1}{\zeta} \ln\left(\frac{2r\rho}{h \cdot E_0}\right) + \frac{2}{\zeta} \ln(c) = A + B \cdot \ln(c), \quad (2.21)$$

which serves as a common starting point in many BPE models.

Having outlined the most fundamental BPE issues, the following part will provide a compact overview of recently published BPE approaches.

#### Recently Published BPE Approaches

The logarithmic BP-PWV relation was adopted by Poon et al. [240] who investigated the above model by resorting to PAT measurements in patients during neurosurgical operations:

$$BP_{est} = A + B \cdot \ln(PAT). \quad (2.22)$$

A high correlation between SBP and corresponding beat to beat PAT values during short intervals was found, suggesting that frequent recalibration procedures are required to adapt the fast changing and subject dependent coefficients  $A$  and  $B$ .<sup>2</sup>

<sup>2</sup>It is noted, that  $A$  and  $B$  are repeatedly used as model parameters in context specific equations and are not necessarily related to each other.

Quite similar to the model expressed by eq. (2.22), there are a lot of works which evaluate the simple linear PTT-BP or PAT-BP relationship [54, 338, 337, 352]:

$$\begin{aligned} BP_{est} &= A \cdot PTT + B, \\ BP_{est} &= A \cdot PAT + B. \end{aligned} \tag{2.23}$$

Deb et al. [54], had access to PAT and PTT measurements using ECG combined with reflectance type PPG measurements at the brachial and finger arteries. The unknown parameters  $A$  and  $B$  in eq. (2.23) were derived by means of linear regression yielding absolute errors ranging from  $-16$  mmHg to  $25$  mmHg. The authors also note that noise and thus reduced signal quality is a major source regarding estimation inaccuracies. Zhang et al. reported a maximum error of  $8.26$  mmHg where  $A$  and  $B$  were calculated based on measurements of 14 subjects [352]. Wong et al. [337] trained  $A$  and  $B$  by means of least squares regression for each subject and tested the linear model on normotensive subjects during exercise. Six months later, they tested the obtained parameters on each subject again. This resulted, however, in a significantly decreased performance, thereby demonstrating the fluctuation and non-stationarity of the model configuration.

In other works, the linear model as described in eq. (2.23) is extended by further parameters such as instantaneous heart rate [34, 192] or stiffness index [14, 137].

Cattivelli et al. [34] proposed a least squares procedure to find the best fit for the unknown parameters  $\{a_1, b_1, c_1, a_2, b_2, c_2\}$  of the following linear model with multiple calibration measurements:

$$SBP = a_1 \cdot PAT + b_1 \cdot HR + c_1, \tag{2.24a}$$

$$DBP = a_2 \cdot PAT + b_2 \cdot HR + c_2. \tag{2.24b}$$

As can be seen in eq. (2.24a), that model was extended by a term containing information of the current heart rate calculated on the ECG signal. The parameters are updated by intermittent recalibration values (e.g. using cuff measurements) based on a recursive least squares (RLS) approach. The performance was evaluated on 56 datasets drawn from MIMIC database (Multiparameter Intelligent Monitoring in Intensive Care) containing ECG, PPG and ABP signals [191]. When applying a cyclic recalibration every 60 minutes, Cattivelli reported a performance of SBP and DBP standard deviations of  $7.77$  mmHg and  $4.96$  mmHg respectively [34].

Gesche et al. [81] proposed an empiric mathematical function consisting of an exponential,

a polynomial and a constant given by a one-time cuff calibration measurement to estimate SBP values based on PAT measurements:<sup>3</sup>

$$SBP_{PAT} = P_1 \cdot PWV \cdot e^{P_3 \cdot PWV} + P_2 \cdot PWV^{P_4} - (SBP_{PAT,cal} - SBP_{cal}), \quad (2.25)$$

where  $PWV = \frac{0.5 \cdot subjectHeight}{PAT}$

In the lower pressure range of BP values up to 160 mmHg, the maximum error was found to be less than 20 mmHg in all subjects with an overall correlation coefficient (CC) of 0.82. The authors also mention the negative influence of disturbances in the photoplethysmographic signal during motion that might be responsible for outliers in the estimation process.

A very well known work was published by Chen et al. [37], who directly used the Moens-Korteweg formula as given by eq. (2.16) to get an BP estimate depending on PWV only. Describing PWV in terms of the pulse transit time denoted by  $T$ , with respect to a specific distance  $l$

$$PWV = \frac{l}{PTT} \quad (2.26)$$

they get

$$P = \frac{1}{\zeta} \ln\left(\frac{\rho d}{h \cdot E_0} \cdot \frac{l^2}{T^2}\right) = \frac{1}{\zeta} \left[ \ln\left(\frac{\rho d l^2}{h \cdot E_0}\right) - 2 \cdot \ln(T) \right]. \quad (2.27)$$

It is then argued that one can assume

$$\frac{dP}{dT} = \frac{-2}{\zeta T} \quad (2.28)$$

when the changes of  $E_0$ ,  $h$  and  $d$  with respect to changes in blood pressure  $dP$  are negligible, leading to a linear relationship of changes in pulse transit time to changes in blood pressure:

$$\Delta P = \frac{-2}{\zeta T} \Delta T \quad (2.29)$$

Thus, the estimated blood pressure  $P_e$  is expressed as the sum of the base blood pressure level and its change  $\Delta P$ :

$$P_e = P_b + \Delta P. \quad (2.30)$$

---

<sup>3</sup>The parameters P1–P4 were estimated by least square fitting of the function to the data of 13 subjects.

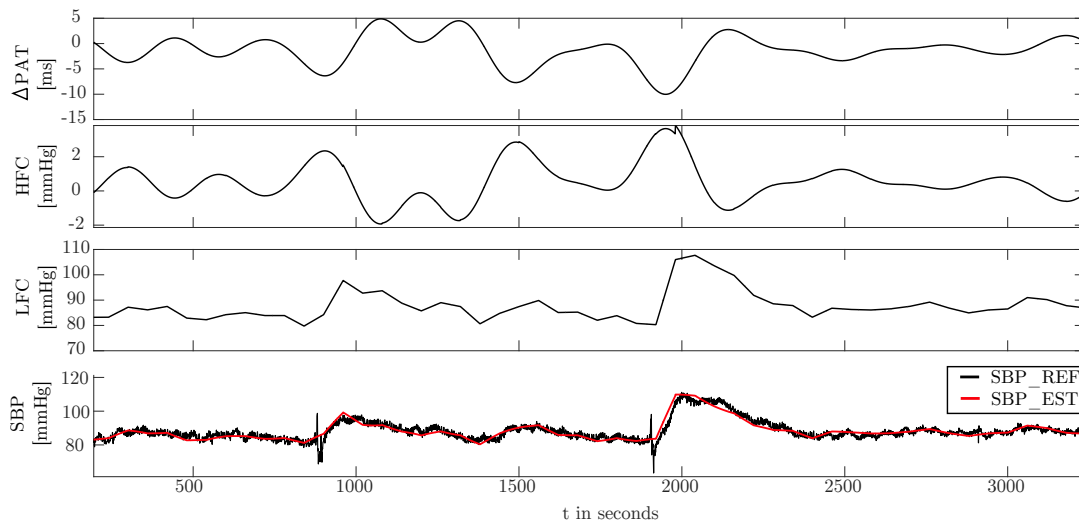


**Figure 2.6:** Blood pressure estimation according to Chen et al. [37]. From top to bottom: *1*) changes of PAT. *2*) estimated blood pressure change according to eq. (2.29) (high frequency component, HFC). *3*) interpolated calibration blood pressure (low frequency component, LFC) *4*) Estimated blood pressure (blue) and invasive reference blood pressure (red).

Using  $\Delta P$  as defined by eq. (2.29), eq. (2.30) becomes

$$P_e = P_b - \frac{2}{\zeta T_b} \Delta T, \quad (2.31)$$

where  $T_b$  represents the pulse transit time corresponding to  $P_b$  which are both obtained by repeated reference calibration measurements. Instead of determining the pulse transit time, Chen et al. resorted to the pulse arrival time which might introduce some inaccuracies due to the PEP component as was discussed earlier (cf. eq. (2.18)). The single sub-signals are depicted in figure 2.6, which also shows the estimated blood pressure curve derived from an ECG-PPG record drawn from the MIMIC database. Their method was tested on 20 subjects undergoing cardiovascular surgery where an invasively measured continuous blood pressure reference was available. The results revealed a correlation between estimated SBP and reference SBP of  $0.97 \pm 0.02$  and a maximum error of  $\pm 10\%$  in 97.8% of the monitoring periods [37].

There are also methods which do not involve any PWV models but resort to simple regression approaches that try to map morphological pulse wave features to corresponding SBP and DBP values. Teng et al. [295] tested several pulse wave properties such as amplitude, width, systolic upstroke time and diastolic period to investigate its correlation to arterial blood pressure. A small study involving 15 patients yielded a mean difference of 0.31 mmHg and standard deviation of 6.64 mmHg between estimated and measured BP. Yan et al. [343] followed a similar approach and extracted a normalized harmonic area feature derived from a frequency transformed PPG curve that was examined for blood pressure estimation on 28 subjects conducting a step-climbing exercise. The first results are promising, with mean error and standard deviation of  $0.37 \pm 4.3$  mmHg.

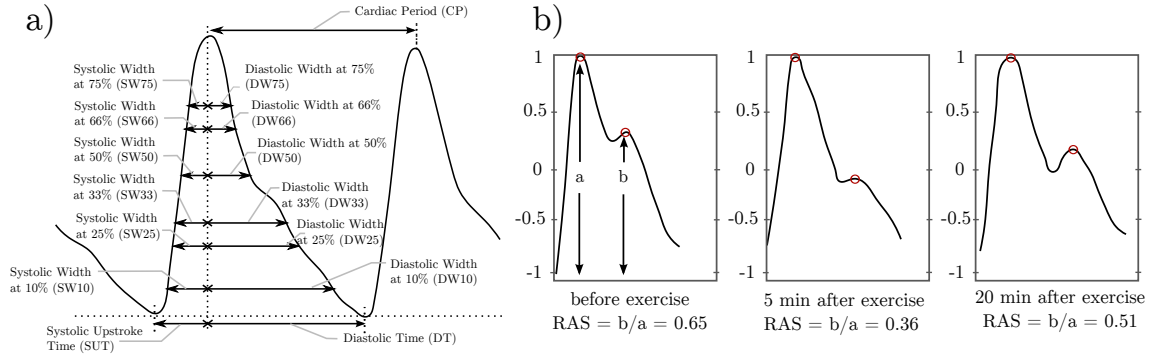


**Figure 2.7:** PPG morphology features based on amplitudes and timing of the pulse signal for continuous blood pressure estimation [96, 143, 295]. *a)* Morphological properties fed to a neural network classifier in [143] *b)* Relative amplitude of secondary peak RAS feature found in [96]. These parameters are likely to contain blood pressure related information but are also sensitive to other influences.

Another interesting way to exploit the pulse wave characteristics was proposed by Kurylak et al. [143] who chose a feed-forward multilayer neural network with two hidden layers to solve the SBP and DBP estimation task. Figure 2.7 a) shows the single PPG features which served as inputs for the neural network and were extracted from each pulse. In total, they analyzed 15000 beats drawn from the MIMIC database where 70 % were used for training resulting in a quite passable performance with mean SBP errors of  $3.8 \pm 3.46$  mmHg and mean DBP errors of  $2.21 \pm 2.09$  mmHg. The neural network was exclusively fed with 21 features describing the morphological shape of the pulse wave such as systolic and diastolic widths at different locations or fractional amplitudes of the pulse peak. These features have been studied in previous pulse wave analysis applications, showing to contain useful physiological information [167, 295].

The reciprocal form as given by eq. (2.32) expresses yet another SBP-PTT relation that is referred to in many BPE approaches.

$$SBP_{est} = \frac{A}{PTT} + B \quad (2.32)$$

With respect to  $A$  and  $B$ , Gu et al. [96] suggest

$$\begin{aligned} A &= (k_1 + p_1(1 - \frac{RAS}{RAS_0})) \cdot SBP_0 \cdot PTT_0, \\ B &= (k_2 + p_2(1 - \frac{RAS}{RAS_0})) \cdot SBP_0, \end{aligned} \quad (2.33)$$

where RAS represents the relative amplitude of the secondary peak which is equal to the ratio of  $a$  and  $b$  as depicted on the right hand side of figure 2.7. With that configuration they achieved an SBP prediction accuracy of  $1.7 \pm 6.8$  mmHg based on 12 subjects who participated in a laboratory experiment involving physical exercises on a treadmill.

It should be emphasized that the authors also mention problems with periods of degraded PPG signal quality, which actually remains a challenge to all kinds of estimation approaches.

Arguing with the kinetic and gravitational energies possessed by the blood pressure wave, Fung et al. [76] resorted to the model defined in eq. (2.34)

$$BP = \frac{A}{PTT^2} + B \quad (2.34)$$

with  $A = (0.6 * subjectHeight)^2 \cdot \frac{\rho}{1.4}$  (with  $\rho$  representing the blood density) and  $B$  obtained by multiple calibrations based on cuff measurements. Noise disturbances, especially in the PPG during subject movements, have been identified as a major limitation of the proposed PTT-BP model due to inaccurate PTT extraction. Evaluating the clinical datasets of 22 patients during anesthesia, the authors reported a preliminary estimation agreement of  $-0.079 \pm 11.32$  mmHg and advocate the method's integration to anesthesia monitors.

Heard et al. [104] investigated a BP estimation model based on the Bramwell-Hill equation (cf. eq. (2.15)). Assuming a constant blood density  $\rho$  one gets the simplified expression

$$\Delta BP \propto c^2 \cdot \frac{\Delta V}{V}, \quad (2.35)$$

where  $c$ , the pulse wave velocity, is given by measurements of the pulse arrival time and  $\frac{\Delta V}{V}$  corresponds to the change in blood volume as was discussed in section 2.2.1.1. In the method used by Heard et al., for each beat a parameter ( $1/c_{dx}$ ) is extracted, which is defined as the time from the peak of the R-Wave to the point in the pulse wave where it reaches 50% of its upslope.

It is argued that this parameter contains information of the pulse arrival time (here the interval enclosing ECG-R and PPG-Onset) as well as information on the blood volume change (interval enclosing PPG-Onset and PPG-50%-slope), therefore being directly related to the right hand side term of eq. (2.35) which leads to the calibration model

$$BP_{systole} = [k_{systole} \cdot (c_{dx}_i)^2] + k_{sys\_cal} \quad (2.36)$$

where,  $c_{dx}$  is calculated for each beat (denoted by index  $i$ ).

Based on 29 intensive care unit patients it was shown that the estimated BP values achieved an accuracy similar to oscillometric pressures when compared to an intra-arterial reference (mean error: 0.5 mmHg, standard deviation of error: 10 mmHg).

A bundled overview of the different BPE methods is provided by table 8.8 in appendix 8.1. Due to the different measurement settings and the respective experiment protocols, it is very hard to compare the performance of the published approaches. Not only do the performance

measures vary among the single publications, but also completely different reference signals are referred to in each work, impeding objective comparisons. In addition, deeper information describing physiological details of the datasets such as a quantitative indicator regarding the variation of the underlying blood pressure is very scarce in many publications. It is clear that a specific BP estimator will perform much better on periods of clean data and constant blood pressure, when compared to another BP estimator which analyzed signals distorted by artifacts and during significantly varying BP values.

In the scope of this work, three BPE models were reimplemented in order to derive a comparative performance evaluation. The chosen models include the works of Chen et al. [37], Cattivelli et al. [34] and Kuryalak et al. [143] which were derived on different ideas and assumptions as discussed earlier. The main focus will be put on the investigation of the methods' vulnerability towards decreased signal quality and ectopic beats which is the central aim of chapter 6.

Driven by the importance of BP as a fundamental vital parameter, there are many applications that would benefit from reliable BPE methods. Some of the presented works already propose specific scenarios such as anesthesia monitoring, BP tracking during exercise or polysomnographic BP tracking. Another very important diagnostic field relying on BP measurements concerns itself with abruptly decreasing systolic pressure values during orthostatic stress, which is known as orthostatic hypotension. Given a robust BPE implementation based on trustworthy PAT or PTT measures, OH diagnosis could be significantly simplified in ambulatory settings. The following last section of this chapter will give a brief introduction to the backgrounds and current findings of OH diagnosis, important definitions, and common diagnostic measurement approaches.

## 2.3 Blood Pressure Measurements for Diagnosing Orthostatic Hypotension

Next to hypertension, orthostatic hypotension is known to be the second most occurring disorder in blood regulation being commonly diagnosed in the elderly [265]. Resolved in a meeting during the Consensus Conference of the American Autonomic Society in 1995, OH has been originally defined as a drop of 20 mmHg in systolic blood pressure or 10 mmHg in diastolic blood pressure within 3 minutes of standing or using a tilt table [134]. When standing up, approximately 750 ml of thoracic blood is immediately translocated downward where 10 %-15 % of the blood pools in the legs. This in turn decreases the venous return which leads to a decreased cardiac output and thus a decreased arterial pressure. The resulting drop in pressure activates the baroreceptors<sup>4</sup> which results in an increased sympathetic outflow and parasympathetic inhibition regulating peripheral vasoconstriction, increased heart rate and contractility [197].

---

<sup>4</sup> Mechanoreceptor sensory neurons located in the blood vessels and getting excited by stretches and sending that information to the central nervous system.

Thus, the blood pressure level is expected to remain at a constant level as the above described mechanism compensates for a change in body position from supine or seated to an upright posture. An impairment of this regulation might lead to different forms of OH, requiring immediate attention and proper treatment.

Generally, one distinguishes between symptomatic and asymptomatic OH [134]. Common symptoms range from weakness, fatigue, visual blurring, vertigo, chest pain, headaches, palpitations, low back pain or dyspnoea [197, 261] to more severe cardiac episodes and finally up to neurocardiogenic syncopes and cardiogenic shocks that are associated with dangerous falls [265].

Numerous studies have been conducted to further investigate the underlying mechanisms and prevalence, as well as influencing factors of OH. In a short manuscript, Judd and Calhoun list some OH related studies with varying conclusions [128]: Concentrating on the +80 years old, Becket et al. stated that a total of 8.3%<sup>5</sup> are OH positive [19]. In [51], 17.3% of the over 60 patient population showed signs of OH<sup>6</sup> [19]. Hiitola et al. [107] found indications for OH being met in 34% of the +75 years old<sup>7</sup> and Valbusa reported an OH prevalence of 18% in home nursing residents of at least 80 years [306]<sup>8</sup>. Hale et al. mentioned a prevalence of 13%-30% when combing literature for different studies [97], Sarasin observed patients presenting with syncope in the emergency department where in 24% OH was considered to be the cause of the fainting [271] and Gorelik reported that OH was present in 64% among elderly patients hospitalised for acute conditions [91].

Thanks to these studies, important conclusions could be drawn leading to proper treatment decisions. A decreased baroreflex activation and loss of large artery compliance are recognized as major cause for OH [128]. However, there are multiple influencing factors, namely autonomic nervous system function, intravascular volume, duration of erect posture, time of day or postprandial state<sup>9</sup> [197, 261].

One also assumes that patients with increased baseline SBP are more likely to suffer from OH, leading to the conclusion that BP control might indeed decrease the risk to develop OH [107]. OH often occurs as a side effect of pressure-lowering and psychiatric medications, and studies have shown that beta blockers are associated with increased likelihood towards orthostatic dysregulation [306]. Next to the well appreciated connection to falls [209], OH serves as an indicator for physical frailness and mortality [178]. Further, it is connected to white matter findings [171] and can serve as a predictor of ischemic stroke [60].

These statistics underline the importance of OH detection which itself requires a reliable and practicable measurement system. In practice, auscultatory/oscillometric cuff measurements

---

<sup>5</sup>Study: “*Hypertension in the Very Elderly Trial (HYVET)*” 3845 patients 80 years and older.

<sup>6</sup> Study: “*Systolic Hypertension in the Elderly Program (SHEP)*” 4736 patients 60 years and older.

<sup>7</sup> Study: “*Home-dwelling elderly in the city of Kuopio, Finland*” 653 patients 75 years and older.

<sup>8</sup> Study: “*French and Italian nursing home residents*” 994 home nursing patients 80 years and older.

<sup>9</sup>(after meal)

or mercury column sphygmomanometers are the most prevalent measurement techniques used for OH diagnosis [197]. However, the major challenge of OH diagnosis is traced back to its poor reproducibility, which demands multiple measurements [197, 218]. Since symptoms may occur in absence of OH (for example caused by panic attacks, occult hyperventilation, cerebrovascular disease or postural tachycardia syndrome [197]) but without showing a drop in blood pressure, continuous SBP measurements would contribute to a significant advantage for clinical routines. More sophisticated systems, such as continuous tonometric or volume-clamp measures, are indeed used in OH diagnosis [87, 88, 265] and have been shown to perform well in defined measurement settings such as head-up tilt tests. Unfortunately, daily diagnosis based on these measurement approaches can be a tedious task, mainly because these methods are susceptible to the difficulties mentioned in section 2.1.2. Thinking one step ahead, they might even become an improper choice when applied to unsupervised longtime recordings, demanding more practical solutions.

The non-continuous cuff measurements mainly suffer from their technically limited low temporal resolution, allowing only one measurement approximately every 60 seconds. Moreover, the occlusive force exerted by the cuff can provoke higher BP values when the patient is startled by the onset of the measurement, masking the true blood pressure situation. Resorting to non-occlusive and continuous alternatives such as BP estimation based on PAT/PTT considerations could therefore significantly improve the current methodologies.



## 3 Acquisition of Vital Parameters

Having dealt with blood pressure estimation applications based on PWV considerations in the previous sections, this chapter now concerns itself with ambulatory biosignal acquisition aiming to provide the corresponding PAT/PTT intervals and underlying raw signals. With regards to BPE monitors, Buxi et al. [30] have written an excellent survey paper covering different measurement principles and system architectures to get an overview of recent developments and unsolved issues. In particular, applicability in ambulatory settings and overall robustness were identified as major shortcomings of current systems and commonly neglected aspects like motion artifact detection and artifact cancellation or ectopic beat extraction were adverted for future implementations.

Driven by the need for continuous and unsupervised PWV recordings, a novel wireless body sensor network was developed in the scope of this work, with special emphasis on synchronized electrocardio- and photoplethysmographic measurements designed for robust PAT extraction. After presenting the basic aspects of ECG and PPG acquisition first, this chapter will give a broad overview of existing BSN systems, highlighting pros and cons of recently published works. Next, the novel rBSN system is presented, accompanied by a thorough discussion of the technical sensor details and evaluation of general performance parameters. Moreover, the implemented wireless synchronization mechanism based on Bluetooth is depicted, achieving clock synchronization accuracies of 30  $\mu$ s.

### 3.1 ECG Acquisition

Research on measuring the electrical activity of the heart started more than a century ago, when Willem Einthoven introduced one of the first commercial ECG devices [61]. Since the 1960s, Holter monitors acquiring the body surface potential variations have been accepted as a well established method for ambulatory longtime measurements, which allows tracking of slowly varying cardiovascular parameters or seldom occurring events.

The surface potentials caused by cardiac activity are typically in the range of several millivolts demanding sophisticated amplification circuits. A common analog ECG frontend architecture is depicted in figure 3.1. This generally begins with a high impedance input buffer that prevents the following circuit from loading the low-voltage electrophysiological signals, which themselves cannot drive high currents.

The second stage consists of a preamplification circuit often realized as an instrumentation

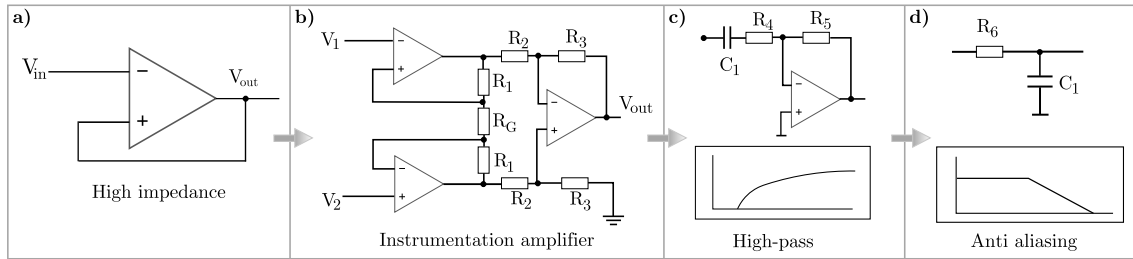


**Figure 3.1:** Key components in typical ECG frontends. **a)** High impedance input buffers are required to prevent significant loading of the cardiophysiological source. **b)** Differential amplification circuits such as the instrumentation amplifier are commonly integrated. This in itself provides a high impedance input, high common-mode-rejection ratios, low drift and low noise, and is primarily applied to elevate the low amplitudes of the ECG signals. **c)** High pass and **d)** low-pass filter structures to remove unwanted frequency components before the analog signals are converted by an ADC unit.

amplifier which elevates the signal's amplitude to several volts. Note that these instrumentation amplifiers already incorporate an high impedance input. Low frequency components (typically below 0.1 Hz) like baseline wander and DC components are suppressed by means of a high-pass filter. This often contains a Bessel characteristic yielding transfer functions that possess almost constant group delays and negligible phase distortion in the pass-band. To further increase the signal-to-noise ratio (SNR), a secondary amplification block is added, followed by an anti aliasing low-pass filter before the signal is finally routed to an analog digital converting (ADC) unit.

Nonetheless, as soon as medical measurements are conducted in everyday situations, new obstacles like motion artifacts and further environmental influences affecting the signal quality have to be properly dealt with, which has been one of the major driving forces in the development of the novel ECG sensor presented in subsection 3.4.2.

## 3.2 PPG Acquisition

Thanks to the popularity of photoplethysmography in oxygen saturation extraction, one finds a lot of material and popular textbooks like Webster's well known work [324] covering the basic principles on the design of PPG hardware systems. In the meantime, the literature continues to provide novel contributions regarding new hardware projects with innovative features or smart algorithms broadening photoplethysmographic applicabilities. As a matter of fact, it is very tedious, if not impossible, to get a clear overview on existing hardware implementations. In general, PPG measurement systems are either applied in transmission or reflectance mode, according to the position of the light sources and the photodetector. In transmission mode, the sensor is placed around an extremity like a finger, toe or earlobe which is typically illuminated by an light-emitting diode (LED) where a photodiode or phototransistor measures the transmitted light on the opposite side. In reflectance mode, the photodetector is mounted on the same side as the light-emitting probe. This increases

the possibilities of measurement sites as theoretically every position on the body surface with arteries beneath are suited for PPG recordings. However, only 2% of the whole light intensity is reflected by the arterial bed [324], resulting in generally lower SNR values.

The majority of PPG sensors have been designed for oxygen saturation extraction rather than pulse wave analysis examining morphologic features. Thus, almost all developed devices provide at least two light sources with different wavelengths in the red and infrared window. As introduced in section 2.1.3, the arterial vessels contribute only a small portion of the full optical path which is the reason why the pulsatile component is much smaller when compared to the signal's DC component. Therefore, DC subtraction filters are sometimes proposed to amplify the AC part of the PPG [157, 272, 279, 348].

To account for different measurement conditions such as ambient light or varying limb properties, light intensity regulation is often found integrated to the analog frontend [272, 279, 320].

Moreover, more and more reference designs employ accelerometers in order to record motion related information during the PPG measurements [158, 185, 239, 313]. PPG sensors are also frequently encountered in wearable body sensor networks, introducing additional issues such as overall power consumption, wireless connectivity, modularization, usability or synchronization issues. As a matter of fact, one does not find PPG hardware architectures which concentrate on all these aspects in a desirable depth. This is why a novel photoplethysmographic sensor was developed in the scope of this work, supporting both transmission as well as reflectance mode. Whereas first revisions have already been published in [224] and [229], a deeper insight will be given in section 3.4.2.

### 3.3 Body Sensor Networks

The previous subsections dealt with general ECG and PPG signal acquisition concepts and illuminated basic hardware issues. As mentioned earlier, exploiting multimodal signal information significantly enhances the possibilities of assessing the cardiovascular state which motivates the development of recording systems comprising multiple sensors. In the following part, such systems will be referred to as body sensor networks, a vast number of which have emerged during the past decades. This section aims to give a dense overview of currently proposed BSNs by carefully evaluating relevant features (as listed in table 3.1) which are inspected in the next paragraphs. During literature research, only works providing sufficient details and introducing a BSN that records at least two physiological signals have been considered.

Reviewing currently published works on wearable monitoring devices has become a difficult and tedious task due to the constant stream of novel contributions appearing in print each year. Nonetheless, there are some survey papers providing a critical examination of relating works covering publications up to 2012 provided by Pantelopoulos and Borbakis [216],

**Table 3.1:** Main features considered during evaluation of the BSN systems.

<p><b>Sensor signals</b></p> <p>The first important feature considered describes the types of signals that can be recorded using the respective BSN (e.g. ECG, PPG, ...).</p>	<p><b>Wireless transmission and maximum data rates</b></p> <p>This point considers eventually employed wireless transmission protocols and particularly its associated maximum data throughput. Moreover, package loss evaluation plays an important role especially with respect to further processing.</p>
<p><b>Wireless sensor architecture</b></p> <p>In literature, the term wireless body area network (WBAN) or wireless body sensor network (WBSN) is commonly used to indicate that the single sensors are battery driven. However, there are a lot of BSNs employing multiple sensors with a wired connection to a base node. In this work, the naming convention true wireless BSN will expect that inter sensor connections do not rely on flexible PCBs or any other sort of wires.</p>	<p><b>Mass data storage and maximum data rates</b></p> <p>Onboard mass storage capability is regarded as the possibility to collect raw data during longtime measurements directly on the BSN hardware allowing independent recordings. In that context, maximum data rates will also be considered as they play a major role especially when designing measurement settings.</p>
<p><b>Synchronization accuracy</b></p> <p>Synchronization mechanisms are an essential part of true wireless BSNs to compensate the two main sources of timing errors, namely drift and offset.</p>	<p><b>Power consumption</b></p> <p>The overall current consumption of a hardware system will determine battery time which might limit multi day longtime measurements.</p>
<p><b>Modularity and implementational details</b></p> <p>Measurements in scientific applications often require adjustments of the hardware systems or additional technical features might need to be added. This demands a modular and open design of the BSN.</p>	<p><b>Unobtrusiveness</b></p> <p>As mentioned earlier, unobtrusiveness is a key aspect in a majority of physiological applications. Smart hardware integration such as woven textile sensors and small device size are thus advantageous for many measurement settings.</p>
<p><b>Special features</b></p> <p>Additional non-standard features like special preprocessing techniques, acceleration signals or any other kind of innovative implementation.</p>	<p><b>Clinical studies</b></p> <p>This column tests whether the device under consideration has proved its usability during a small field study in a clinical environment.</p>

Alemdar and Ersoy, [3] Chen et al. [36] and Patel et al. [219]. Movassaghi [194] has written a great survey on current BSN achievements, but concentrates more on general characteristics such as transmission protocols, channel models, security and data routing instead of comparing existing works with regards to specific applications.

A fair comparison of pros and cons is not always a straight forward task and certainly depends on specific target applications. Pantelopoulos et al. [216] therefore assigned each reviewed measurement system a maturity score, which is based on different evaluation parameters and also incorporates the patient's, physician's and manufacturer's point of

view. The best systems convince with regards to wearability (partly textile integrated sensors), aesthetic issues and their general applicability in real settings, as they have been successfully used in clinical studies. The sensor woven clothes are indeed very suited for unobtrusive and ubiquitous measurements, but they might lack the flexibility for quick adjustments as required in laboratory experiments. It is further noted, that none of the works cited in the above surveys, addresses the issue of wireless inter sensor synchronization, which is a key requirement in multimodal applications as mentioned in section 2.2.1.2.

Regarding the immense amount of works presenting hardware systems designed for wireless biosignal acquisition, a comparatively small portion of contributions really depict body area networks in the sense of wireless inter-sensor connections. BSN systems consisting of a single board, or utilizing wired synchronization mechanisms, are much easier to develop but do not provide the flexibility and unobtrusiveness demanded by a majority of clinical and ambulatory applications. Thus, they will not be further considered in the following review.<sup>1</sup> Furthermore, notably few works really discuss wireless synchronization issues and deal with concrete implementations of respective mechanisms [67, 186, 188, 189, 193, 282, 314].

In the scope of this work, an updated picture of currently published works has been devised to get a complete reference foundation as possible. The resulting overview as provided by tables 8.3 - 8.5 in the appendix does not only highlight strengths and shortcomings, but also reveals the urgent need for novel developments combining important features.

A major limitation can be seen in the absence of crucial implementational details regarding analog frontends, embedded architectures and software structures, which makes it difficult to reimplement the proposed systems.

Another neglected aspect - at least in the scientific publications - seems to be mass storage capabilities, which play an important role, especially when it comes to scientific post processing of the recorded raw data. This is only considered in a minority of systems as in [314] for example. However, no sophisticated evaluations concerning maximum data rates or reliability are given.

These open points have motivated further efforts on a completely new system designed for multimodal signal acquisition in ambulatory and clinical measurement settings. The details which have been partly published in [229] will be thoroughly presented in the following section and are used for a critical comparison with the researched works pointing out the novelties of the proposed rBSN.

---

<sup>1</sup>related publications: [56, 82, 115, 130, 156, 293, 354].

## 3.4 A Novel Robust Body Sensor Network

As initially introduced, a completely new system architecture will be presented in this section that meets the previously discussed demands of a biomedical sensor network and also fulfills the high requirements of scalable pulse wave velocity analysis. Regarding PAT/PTT applications, the proposed system fills the gap of features missed in recently published works including accurate wireless synchronization, elaborate performance analysis, motion detection and sophisticated analog frontends as has been stressed in Buxi's review article [30].

The whole development was driven by two main goals: First, to build a robust and reliable system, where accurate acquisition of raw signals can be guaranteed, and second, to provide as much comfort and functionality as possible with regards to clinical, laboratory as well as personal application environments. Therefore, the project has been termed robust body sensor network.

### 3.4.1 Architectural Overview

Power consumption considerations, usability, reliability and final performance certainly belong the most important key aspects when developing battery driven biosignal devices. The sensors developed in this work are basically composed of low power analog and digital components that are operated by resourceful and energy efficient microcontrollers ( $\mu\text{C}$ ). Technically, there are two critical timing considerations that have to be accounted for to ensure complete and undisturbed data acquisition in wireless sensors. On the one hand, the full data path, comprising analog preprocessing, digitization, buffering in RAM and final depositing on a mass storage device, has to be processed in a given sampling interval in order to permit high sampling frequencies and amplitude resolutions. On the other hand, the time crucial mechanism of timer synchronization requires highest execution priority of the processor. This is the reason a dual controller architecture as depicted in the left hand side of figure 3.2 is proposed, physically separating the communication and data acquisition tasks which also eases firmware development significantly.

To satisfy the demands of reliability, the internal data acquisition process further incorporates elaborate control structures which detect and protocol run-time exceptions like lost data packets or deviations from timing intervals in the synchronization mechanism. Thus, each measurement is assigned a warranty seal confirming completeness and absence of any irregularities.

The aspect of usability also plays a major role, as the system should be designed to permit uncomplicated utilization by non-technicians in clinical or private settings. Therefore, easy applicability and user-friendly interaction pose a significant requirement to the devices. Moreover, the sensor nodes were designed to be as modular as possible, allowing for rapid development of novel sensors by recycling a majority of common modules. This way, the

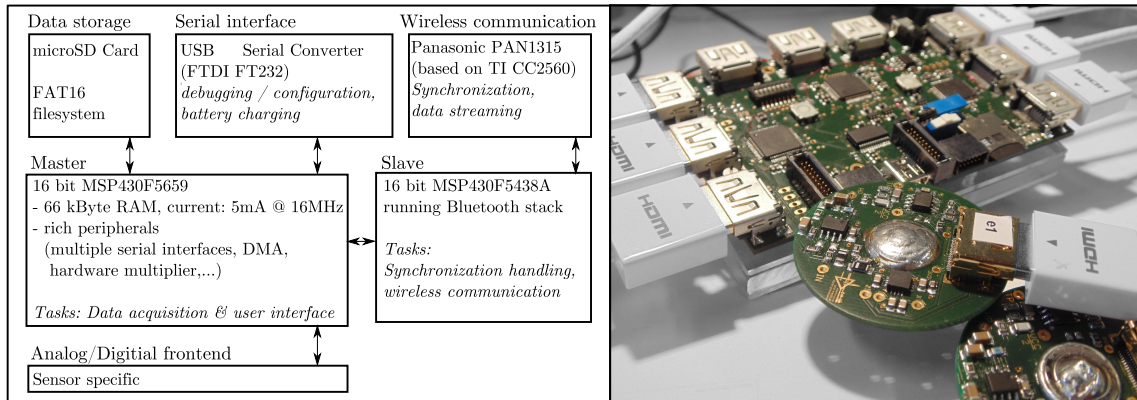


**Figure 3.2:** *left*) Block diagram depicting rBSN sensor node hardware based on dual controller architecture. All modules are powered by low-dropout regulators *TPS72733* (Texas Instruments, Dallas, US) sourced by a 2300 mA h lithium-ion battery. *right*) Assembled rBSN\_HeartCore sensor and its active electrodes. Figure adopted from [229].

system is well suited for scientific applications, allowing uncomplicated extensions and easy changes of the system's behavior.

### Dual Controller Architecture

**Master** The main controller (master) operates the analog frontend and stores the digitized data on a micro SD-card. To enable implementation of potent algorithms and to buffer input datastreams during time consuming FAT filesystem operations, the microcontroller should offer enough SRAM for corresponding data structures defined in the firmware. In particular, sporadic latencies as they typically occur in write processes to the SD-Card should not be underestimated, since the memory demand required by buffering rapidly increases to several kBytes within several milliseconds, risking irreversible data loss.

Additionally, powerful interfaces, high CPU frequencies and configurable low power operation modes should be carefully weighed up, when choosing the right controller that shall satisfy the given specifications.

At the time of decision, the *MSP430F5659* (Texas Instruments, Dallas, US) provided a competitive controller with respect to the rBSN sensors, which is equipped with 66 kB RAM, multiple serial SPI, I2C and UART interfaces, powerful timer, direct memory access, hardware CRC, hardware AES encryption and ADC modules, specifying a power consumption of only 1 mA/MHz at 3.3 V [300]. Due to these economical specifications, this chip was chosen to act as main controller in all rBSN sensors where the master runs an open FAT filesystem provided by Chan [35], handles user inputs and status LEDs, a serial USB interface based on an *FTDI FT232* chip (FTDI, Glasgow, UK) and controls communications with the slave controller. The master's firmware consists of two parts. A high priority interrupt service routine triggers the corresponding ADC devices and writes

the captured samples to an internal ping-pong buffer structure. The timer interrupt itself, which is used to define the sampling interval, is triggered by the slave controller presented in the following paragraph, thereby assuring synchronicity of the recorded data streams. Inside the lower prioritized main loop, full data buffers are safely written to the FAT filesystem when CPU resources become available.

**Slave** As mentioned earlier, the second controller (slave) is intended to spend all its resources operating a wireless radio module to implement timer synchronization and data streaming tasks. Concerning the wireless solution, the Bluetooth specification was chosen for the following reasons. Firstly, BT has become a standard in commercial devices and is found in current smartphones, tablets and laptop computers. Therefore, implementation of sensor network handling, data visualization and configuration can be easily implemented resorting to standard hardware systems. Second, BT offers comparably generous bandwidths up to  $2.1 \text{ Mbit s}^{-1}$  allowing multiple data channels to be streamed at high sampling rates up to several kilohertz. Moreover, BT has been successfully used for timer synchronization [32, 33] and is suited for battery driven devices, as low power modes were introduced in the new low energy specification [95]. To handle these tasks, a *MSP430F5438A* controller (Texas Instruments, Dallas, US) constitutes the slave which runs a StoneStreetOne Bluetopia Bluetooth Stack (StoneStreetOne, Louisville, US). The details of the synchronization mechanism are presented in section 3.4.3.

#### 3.4.2 Sensors

**rBSN\_HeartCore 12-Channel-ECG Sensor Node** After section 3.1 laid out the very basics of ECG hardware, it is now time to present the special features of the novel rBSN ECG node developed in this work, which incorporates active electrodes and further supports motion detection.

The onboard data acquisition is based on the *ADS1298* (Texas Instruments, Dallas, US) single chip solution [298]. This analog ECG frontend provides an eight channel 24 bit delta-sigma converter handling the signal digitization as well as numerous features like Wilson central terminal and right leg driver potential generation. Enabling all eight input ports, a complete 12 channel ECG can be recorded, including the three leads according to Einthoven *I*, *II* and *III*, the six precordial chest electrodes *V1* - *V6* as well as the augmented limb leads *aVR*, *aVL* and *aVF*.

Before being routed to the onboard *ADS1298* device, the signal is preprocessed by an active band-pass circuitry. This is realized by a high impedance input buffer in the first stage, which is followed by a second order high-pass filter removing the DC level at 0.05 Hz in the second stage. To reduce peaks caused by high capacitive loads, an external ‘in-the-loop’ compensation was implemented to enhance noise performance. Next, an active low-pass filter in multiple feedback architecture suppresses frequency components above 250 Hz.

The fourth stage provides a non-inverting amplifier which further intensifies the signal's amplitude. Each active electrode also houses a three axis acceleration *ADXL335* sensor (Analog Devices, Massachusetts, US) [8], providing valuable information concerning the measurement site's movement. This information can be used to significantly enhance automatic signal quality estimation and motion artifact reduction approaches, which still pose an unsolved problem in many signal processing methods. The mainboard provides an additional passive second order low-pass filter with a cutoff frequency at 250 Hz that eliminates aliasing effects for sampling frequencies above 500 Hz.

**rBSN\_DualPulseOximeter** Designed to support optical pulse wave recordings as was briefly introduced in section 2.1.3, the following PPG sensor is also based on the modular rBSN layout depicted earlier in figure 3.2 where the sensor specific frontend is exchanged to meet the requirements of photoplethysmographic measurements.

An early stage of the development has already been published in [224] which since then has been further improved in multiple iterations. As the nickname already suggests, the photoplethysmographic sensor node supports both, transmission as well as reflectance mode whose implementational details are discussed next.

#### **Transmission mode**

For measurements in transmission mode, a standard finger clip housing shelters the PCB with its analog and digital frontends. A comprehensive overview on the respective system is given in figure 3.3, which depicts the electronic subsystems and their corresponding interfaces. Note that the analog and digital frontends are accompanied by a separate microcontroller which is not involved in the actual data acquisition tasks running on the main PCB. Controlled by this integrated  $\mu C$ , the system allows for programmable configuration of the amplification and filter stages, as well as dynamic DC removal based on an OpAmp subtraction circuit, and also light intensity regulation through a voltage controlled LED driver. Subtracting the PPG's DC component followed by amplification of its respective AC part, is a well known approach commonly found in the design of reflectance pulse oximeters where SNR values are particularly low. Nonetheless, this OpAmp subtraction was also employed in the transmission mode PPG as the measurements will focus on pulse wave morphology analysis that requires superb quality signals in order to robustly identify fiducial points such as pulse peaks or onsets.

The finger clip module integrates three low-dropout linear regulators (LDO) which provide a separate 3.3 V power supply of the analog circuits and microcontroller modules respectively. An *LM3678* DC-DC converter (Texas Instruments, Dallas, TX, US) [297] with integrated LDO was used to generate a negative output voltage needed by the OpAmp circuits.

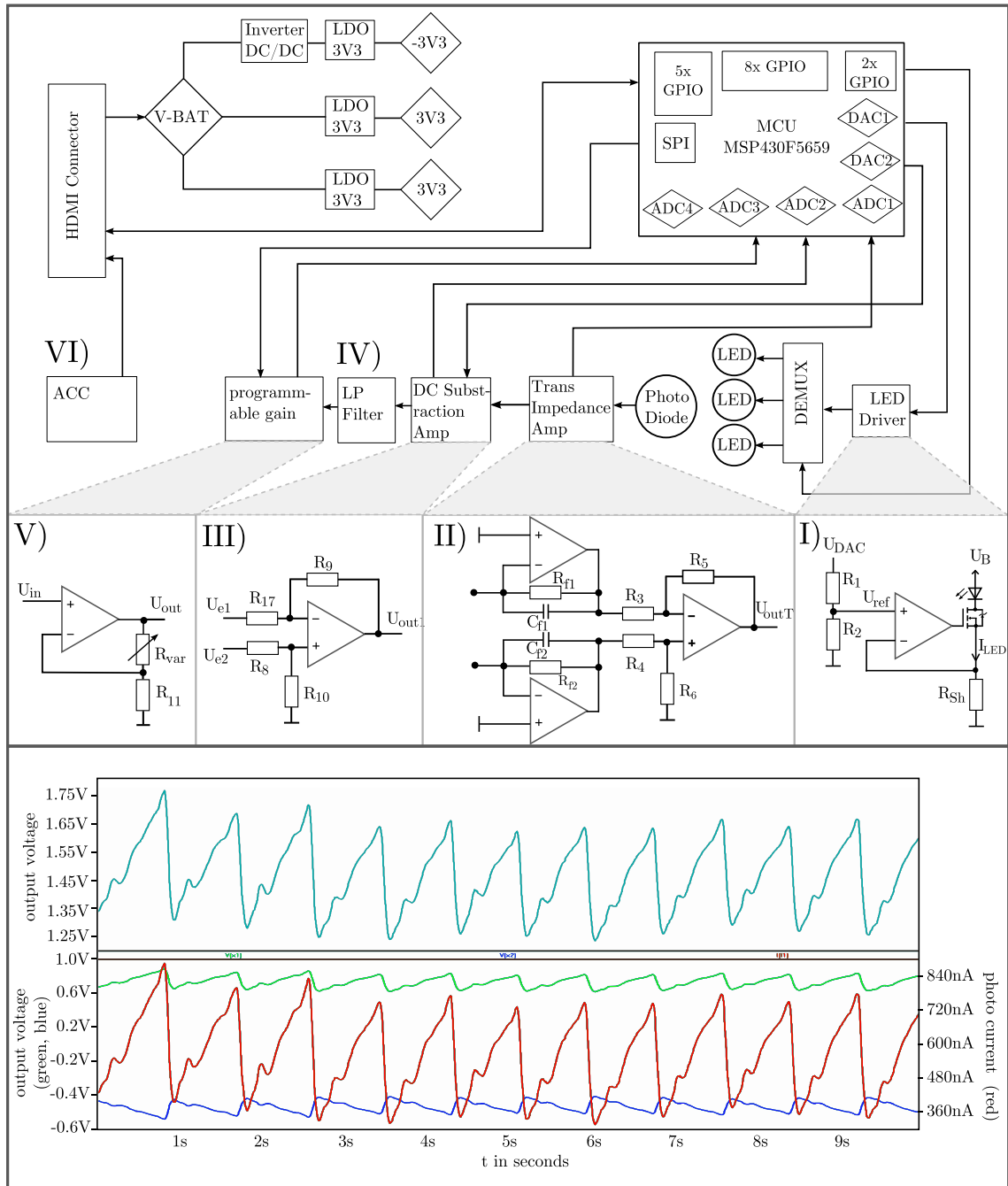


**Figure 3.3:** *rBSN\_DualPulseOxy* transmission mode submodule: **Top)** The upper part depicts the general structure of the whole fingerclip sensor. The board houses three linear voltage regulators which provide the corresponding output voltages required by the analog and digital subsystems including **I)** LED driver, **II)** transimpedance amplifier which transforms the photo current into a measurable and amplified voltage signal which is gathered by ADC1, **III)** DC subtraction circuit, subtracting the  $\mu\text{C}$  calculated DC component from the raw signal, **IV)** a dedicated low-pass filter removing unwanted higher frequency components, **V)** a programmable gain amplifier, configurable by  $\mu\text{C}$  via SPI interface allows to further increase the signals' amplitudes as necessary and **VI)**, an *ADXL335* accelerometer module [8], providing three analog channels containing information on the module's acceleration in x-, y- and z-direction. **Bottom)** Simulation traces. Bottom plot: current produced by photodiode (red), outputs of differential transimpedance amplifier (green, blue). Top plot: Output voltage  $U_{outT}$ .

The finger clip controller was required to fulfill the following specifications:

- Low power consumption
- At least three ADC channels, 12 bit resolution
- Two separate Digital-to-Analog (DAC) converters
- Integrated hardware modules for serial communication (SPI, UART)
- More than six available interrupt pins
- One 16 bit counter, hardware multiplication support
- Memory: > 10 kB RAM, CPU: 16 bit, CPU-clock > 16 MHz to have room for signal processing methods

The choice again fell on an *MSP430F5659* [300] which satisfies the above listed specifications and is available in an *LQFP-100* package that does not exceed the given size limits of the finger clip housing.

### Light intensity regulation in transmission mode finger clip

The light intensity is regulated by a simple OpAmp circuit where the current  $I_{LED}$  can be adjusted by an analog voltage level which itself is digitally provided by the  $\mu C$ 's DAC. The circuit is given in figure 3.3 I) where the current which shall be controlled flows through the LED, a comparatively small resistor  $R_{Sh}$  and eventually towards ground. The voltage at the inverting input of the OpAmp will just equal  $U_{Sh}$  and the voltage difference appearing between the inverting and non-inverting OpAmp inputs is expected to become zero due to the closed feedback loop. Therefore, the output drives the gate of an N-FET transistor where the differential resistor is configured in such a way, that the current running through  $R_{Sh}$  becomes  $I_{LED} = \frac{U_{ref}}{R_{Sh}}$ . One such LED current driver is shared by the different finger clip LEDs via a  $\mu C$  controlled demultiplexer as only one LED will be active in pulse oximetry. The maximum desired current is defined as  $I_{max} = 100 \text{ mA}$  which shall be set when the input voltages reaches its maximum value at  $U_{DAC_{max}} = 3.3 \text{ V}$ . The demultiplexer which is based on the analog switch *TS5A3359* has a maximum on-state resistance  $R_{AS}$  of  $1.5 \Omega$  [302] whereas the maximum drain-source on-state resistance  $R_{DS}$  of the MOSFET is given at  $0.085 \Omega$  [311]. Given a maximal LED forward voltage of  $U_{LED} = 2.7 \text{ V}$  at  $I = 100 \text{ mA}$  [168] one derives a maximum value for the shunt resistance of

$$R_{Sh} = \frac{U_B - U_{Sh}}{I_{max}} - R_{AS} - R_{DS} = 4.415 \Omega. \quad (3.1)$$

Choosing  $R_{Sh} = 1 \Omega$  one obtains the relation  $I_{LED} = \frac{U_{ref}}{R_{Sh}} = \frac{U_{ref}}{1 \Omega}$  which means that a reference voltage of  $100 \text{ mV}$  would yield a LED current of  $100 \text{ mA}$ . By resorting to a simple voltage divider with  $R_1 = 1 \text{ k}5 \Omega$  and  $R_2 = 47 \Omega$  (transforming  $3.3 \text{ V}$  to  $100 \text{ mV}$ ),  $I_{LED}$  can be assigned a current in the range of  $[0 \text{ mA}..102 \text{ mA}]$  in steps of  $25 \mu\text{A}$  which is configured by the firmware using the resulting relation

$$I_{LED} = 25 \mu\text{A} \cdot DAC_{register}. \quad (3.2)$$

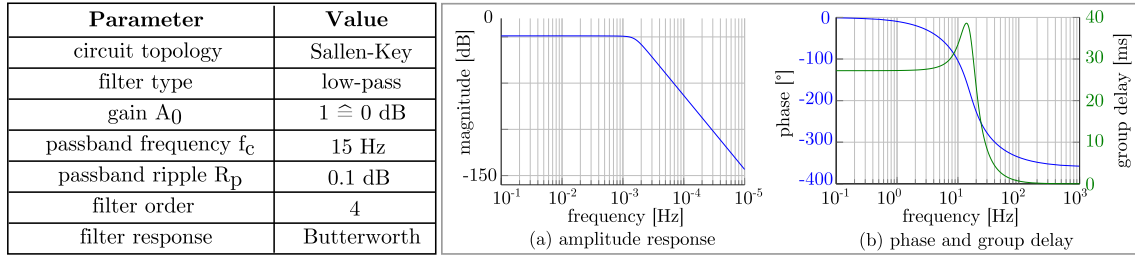


**Figure 3.4:** Architectural details of the employed 15 Hz low-pass filter which is found in both the transmission as well as reflectance mode PPG sensors. To avoid signal distortions caused by misalignment of the single frequency components, a constant group delay is required, covering the range of the fundamental PPG frequencies.

### Photodiode signal acquisition

The current generated by the photodiode is translated into a voltage signal using a differential transimpedance amplifier followed by a subtraction circuit as shown in figure 3.3 II) which has the benefit of common mode rejection of coupled noise [324]. The expected photo current lies in the range of  $1 \mu\text{A}$  [310] demanding for a feedback resistance  $R_f$  that does not exceed  $1.65 \text{ M}\Omega$  to avoid saturation of the OpAmp. In the current implementation,  $R_f$  was assigned  $470 \text{ k}\Omega$  allowing photodiode currents up to  $3.5 \mu\text{A}$  without the output being saturated. Webster mentions a feedback capacitor choice according to

$$C_f = \frac{1}{4\pi R_f f_c} \cdot \left(1 + \sqrt{1 + 8\pi R_f C_I f_c}\right) = 3.06 \text{ pF}$$

where  $R_f = 470 \text{ k}\Omega$ ;  $f_c = 3 \text{ MHz}$ ;  $C_I = 80 \text{ pF}$  (3.3)

$R_f$  feedback resistance;  $f_c$  unity gain frequency of the OpAmp;

$C_I$  sum of photodiode junction capacitance and OpAmp input capacitance

where larger values of capacitance are possible but decrease signal bandwidth [324].  $C_f$  was set to  $10 \text{ pF}$  with the simulated results provided by the bottom plots of figure 3.3.

The subsequent filter stage depends on the mode of operation. When a single channel is sampled continuously, as would be required in pure pulse wave analysis applications, the filter stage can be directly applied on the voltage signal. In the current setup, a fourth order low-pass filter with a cutoff frequency of  $20 \text{ Hz}$  was implemented, fulfilling the function of an anti-aliasing filter. In pulsed mode however, as operated in oxygen saturation calculation, one would need an additional sample and hold block for each channel in order to apply the filters.

To cancel out the signal's DC offset, a simple subtraction circuit is applied which expects the calculated DC from the microcontroller's DAC output as depicted in figure 3.3 III). Moreover, a non-inverting amplifier complements the signal path in the last stage, where the gain can be adjusted by the digital potentiometer *TPL0501* (Texas Instruments,

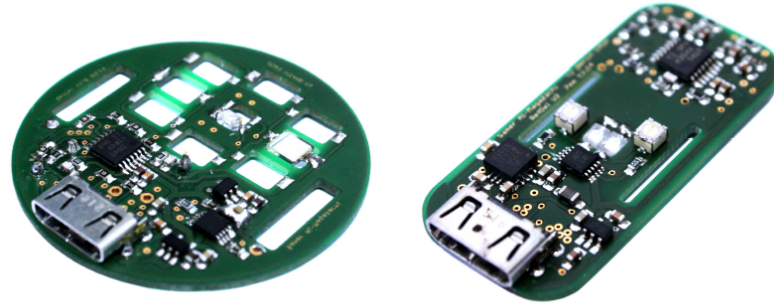


**Figure 3.5:** Assembled reflectance PPG sensor. Each PCB provides different drill hole positions for LED and photodiode placements. The sensors can be conveniently attached anywhere on the skin using small leather wristbands or tapes.

Dallas, US). The resistance between 0 and 100 k $\Omega$  is configured via an SPI interface with a resolution of 256 steps and a fast adjustment time of 3  $\mu$ s [299].

The fingerclip also houses the three axis accelerometer *ADXL335* [8], which is found in all rBSN sensors. Exploiting features derived from the acceleration channels only, it was shown that one can reliably determine typical hand movements that are known to cause serious motion artifacts, which is further discussed in section 5.1.3.

### Reflectance mode

The reflectance mode PPG sensor was designed in a very similar way, incorporating a differential transimpedance amplifier, a Butterworth low-pass filter with Sallen-Key circuit topology as well as an analog/digital AC extraction part.

Figure 3.4 summarizes the low-pass filter specifications and presents the corresponding transfer function. A nearly constant group delay in the range of 0.01 Hz and 15 Hz was a major design criterion to avoid signal distortions due to differently delayed PPG frequency components. A completely assembled reflectance sensor prototype is depicted in figure 3.5, which can be easily placed on different body surface measurement locations.

The current rBSN is complemented by further sensor types including a respirational activity monitor, a skin conductance module and small size actimeters which do not play a significant role in this thesis but have been published elsewhere [227, 229, 231].

**Performance evaluation** The presented sensors were further analyzed during active operation to determine average power consumption and further performance parameters. All sensor nodes are supplied by lithium-ion batteries, typically used in smartphones, which provide capacities up to 3000 mAh. The average power consumed by the rBSN\_HeartCore sensor is approximately 110 mW ( $f_s = 500$  Hz), guaranteeing for more than 48 hours operating time. In comparison, the *rBSN\_DualpulseOximeter* draws considerably more current (due to the LED drivers) as is provided in table 8.10 which shows the total power consumption during different modes of operation. Physical storage capability of the incoming datastreams is another important performance parameter, where the total capacity and supported bandwidth determine the system's potency. Whereas a filesystem

**Table 3.2:** rBSN packet structure. A 16 bit CRC checksum and a 16 bit packet counter are used to verify data correctness. The number of data bytes are specified by *packet length* and the one byte *channel id* allows up to 256 channels in the whole rBSN.

CRC checksum	packet length	packet count	channel id	reserved	data
2 byte	2 byte	2 byte	1 byte	1 byte	[n] byte

significantly eases post-data processing, it also limits the maximum amount of data that can be written to the micro SD-card. Based on the open source FAT filesystem provided by ElmChan [35] and large ping-pong buffer structures, a throughput of 23.77 kB/s without occurring data loss of the written channels has been achieved. All samples belonging to a specific channel are stored in a packet structure which is identified by an 8 byte packet header as shown in table 3.2. The CRC checksum and packet count fields are used to verify recorded datasets for a specific channel. The packet length can be varied according to available space in RAM where 504 bytes have proved to be a proper trade-off. This size is long enough to buffer data for more than one second ( $f_s = 500$  Hz) and results in a reasonable header to data ratio of a single packet (1.5 to 98.5 in that case). Regarding the given write speed, a single channel could be sampled at 11.7 kHz or 24 channels at 500 Hz respectively (assuming 16 bit per sample). It must be mentioned though, that the buffers require 40 kB RAM to guarantee undisturbed datastreams during sporadically occurring SD-card latencies, which can last up to several hundred milliseconds.

### 3.4.3 Clock Synchronization

The introductory chapters stressed the importance of wireless timer synchronization in biomedical sensor networks, especially when accurate sensor data fusion is required for subsequent multimodal signal processing. With respect to simultaneous measurements involving multiple wireless sensors, one has to face two serious problems due to the independent clock sources of the single devices. First, one needs to derive a proper strategy to start all sensors at the same time where deviations are commonly referred to as offset errors. Second, elaborated mechanisms are required to account for the inaccuracies of the CPU clocks which lead to so called drift errors that are depicted in figure 3.7. The following part addresses those important aspects and also presents a reliable implementation of a synchronization mechanism based on Bluetooth used to synchronize the clocks of active sensors in the rBSN system.

With respect to WBSNs, Zigbee [48, 314, 319], ANT (Dynastream Innovations Inc., Cochrane, Canada) [280] and Bluetooth [33, 263] belong to the most common choices of wireless technologies. Further solutions based on the IEEE 802.11 standard have also been examined for synchronization tasks with reported accuracies up to  $\pm 50 \mu\text{s}$  [22]. Whereas ANT and Zigbee offer relatively low maximum data rates (20 kbit/s and 250 kbit/s respectively), the BT specification allows up to 2.1 Mbit/s. Thus, resorting to BT solutions provides considerably more bandwidth for on-line data streaming applications. Furthermore, BT radio modules are broadly available and most commercial end devices like smartphones,

tablets or laptops are equipped with a corresponding BT interface. Specifying a maximum current of 39.2 mA at full throughput and less than 1 mA in sleep and sniff modes, the *CC256x* Bluetooth (Texas Instruments, Dallas, US) module is likewise suited for battery driven applications. However, the Bluetooth Special Interest Group [95] never proposed a profile optimized for synchronization issues. Thus individual solutions are required when corresponding applications are implemented based on BT.

The Bluetooth standard itself has been applied for synchronization issues in different works which advertise promising results. Casas et al. exploit the BT park state mechanism and report a worst case synchronization error of 17.4  $\mu$ s [33]. In a park state, the slave devices remain in an energy-saving sleep mode and synchronize on incoming broadcast messages at predefined beacon intervals.

Unfortunately, the park state is not supported by all BT devices so that the presented synchronization approach of this work will switch to the BT sniff mode instead. Regarding wireless timer synchronization, the BT sniff mode has been successfully applied by Casamassima et al. who presented an accuracy of 313  $\mu$ s [32]. As initially motivated in section 2.2.1.2, a synchronization accuracy of 100  $\mu$ s is postulated, to support high precision PAT/PTT measurements. As a matter of fact, 100  $\mu$ s would also serve well for typical biosignal applications involving PPG and ECG recordings.

Bluetooth supports so called piconets, which can be joined by one master and a maximum of seven slave devices. Once connected to the piconet, the ticks of the slaves' BT clocks are synchronized with the ticks of the master's BT clock. One such BT clock tick is fixed and corresponds to a resolution of 0.3125 ms which is already a good starting point for timer synchronization. Unfortunately, BT does not provide a physical broadcast channel which complicates a more precise synchronization. BT communication in general is based on slots having a fixed length of 625  $\mu$ s providing transmission intervals that are alternately assigned to master and slave devices. Figure 3.6 a) shows a possible communication setup involving one master and two slave devices. When the high temporal resolution of 625  $\mu$ s is not required, the BT sniff mode feature can be activated to drastically reduce power consumption. In sniff mode, each slave is sent to an inactive sleep state for a configurable period of time denoted as sniff interval, whose length is supposed to be a multiple of 625  $\mu$ s. Having waited for the end of the sniff interval, the corresponding slave device wakes up and expects a message from the master. This specific time instance is also known as anchor point as is indicated in figure 3.6 b). When the master sends a broadcast message, each slave receives that message sequentially. More precisely speaking, when there are seven slave devices, the master physically sends seven broadcast messages dislodged by a small temporal offset. Nonetheless, this offset information is encoded inside the BT connection handles allowing a proper offset correction to be easily implemented.

In the presented timer synchronization mechanism, the sniff interval is set to 250 ms meaning that each slave expects a message from the master every 250 ms. Thus, when the slave receives the message, 250 ms have passed with respect to the BT piconet clock (plus

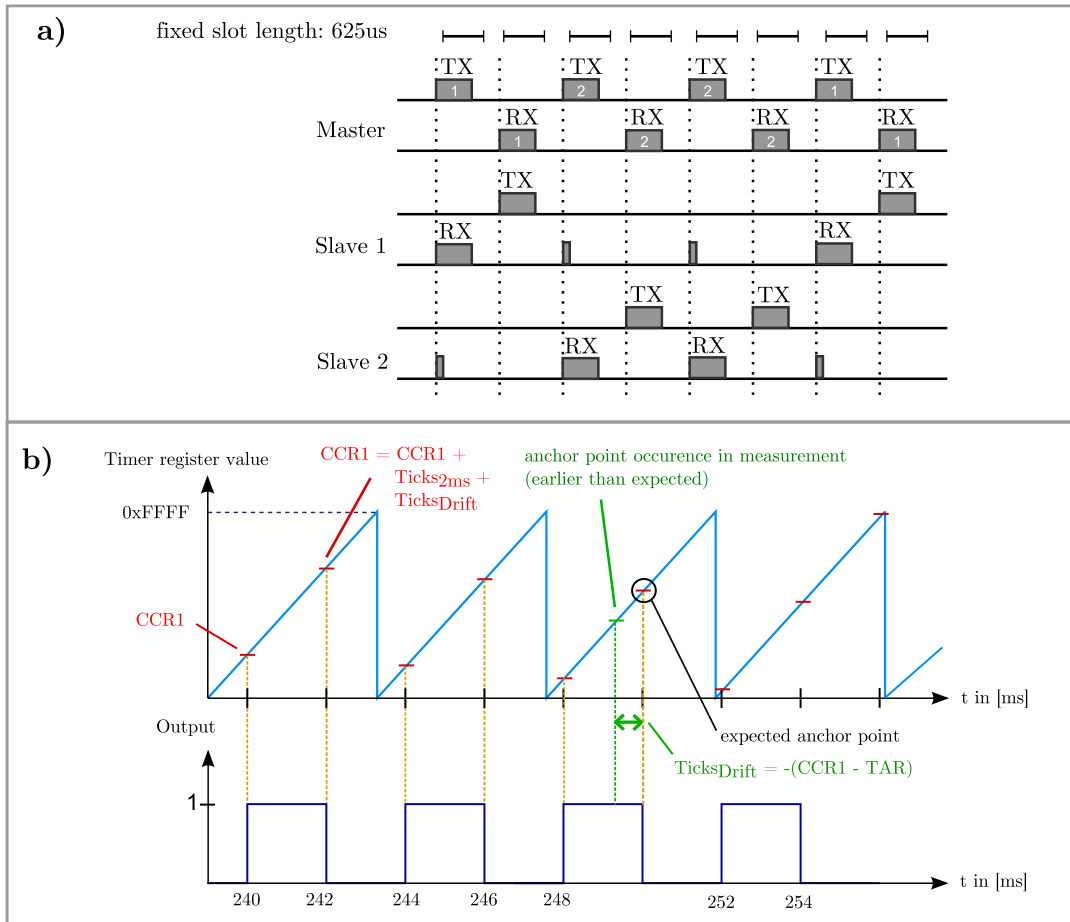


**Figure 3.6:** CPU clock synchronization mechanism based on BT

**a)** Underlying time division duplex mode on which Bluetooth communication is based. Master and slaves can alternately send and receive messages [95]. **b)** Timer drift correction implemented on the sensor device. After each sniff interval, the slave expects a message from the master. When this message is received, 250 ms have passed and the slave’s timer capture compare register (CCR) value can be adjusted accordingly to compensate the time delay denoted by  $Ticks_{Drift}$  with the next periodic CCR update (which happens every 2 ms in the depicted case where  $Ticks_{2ms}$  represents the number of CPU clock cycles needed to delay 2 ms). Drawing adopted from [229].

the known offset as mentioned before). This way each slave device is able to synchronize its timer to the master clock in order to counteract present drift errors caused by its own crystal. As mentioned, the corresponding offset error is corrected by evaluating the devices relative anchor point position, which is known in the BT protocol. The synchronized timers are then used to trigger the sensor’s ADC modules, ideally resulting in time synchronized samples belonging to a multimodal sensor application. Since the drift error accumulating in a short time window is negligible (less than 1 ms in 10 s), the proposed synchronisation mechanism is also robust towards lost BT packets.

The Blutopia Bluetooth stack that is integrated in the firmware of the slave  $\mu C$  provides a host controller interface to access lower level functions that directly communicate with the radio chip. The Blutopia stack further offers a scheduler, which can be used to periodically

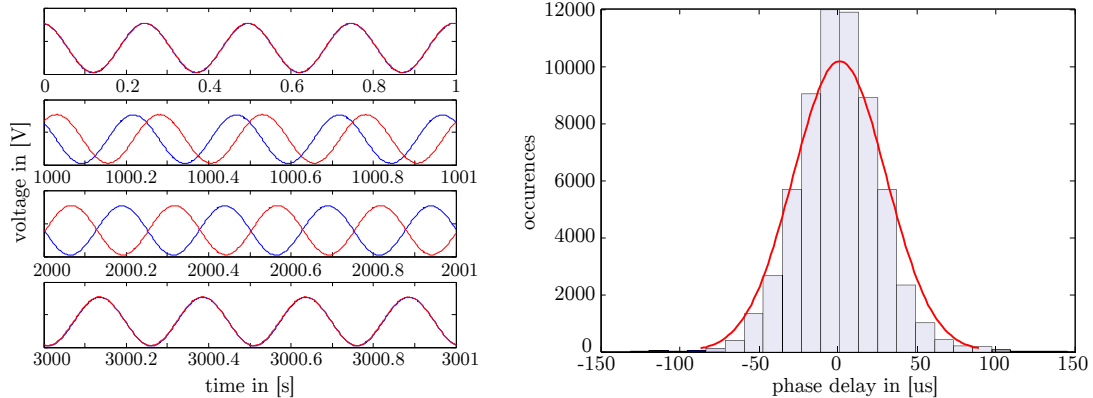


**Figure 3.7:** Clock synchronization performance evaluation *left*) The oscillator drift error is demonstrated in an elaborated experiment: Two sensor devices are sampling a sine wave provided by a frequency generator, with deactivated synchronization mechanisms. As can be seen in the fourth subplot at the bottom of the left figure, the phase delay accumulated to 250 ms within approximately one hour, which is unacceptable for multimodal biosignal applications. *right*) When the proposed synchronization mechanism is turned on, a timer accuracy of 30  $\mu\text{s}$  is achieved. The histogram shows the calculated phase delays between blockwise extracted windows of the recorded sine waves, yielding a standard deviation of 29.38  $\mu\text{s}$ . Drawing adopted from [229].

call functions like sending radio messages. The duration of the complete initialization process depends on the respective Bluetopia functions which are responsible for building up the connection. Repeated measurements in noisy environments revealed a mean pairing duration of 25.30 seconds which should be acceptable in standard applications.

In order to quantitatively examine the synchronization accuracy, an elaborate experiment, as depicted in figure 3.7, was conducted. Two sensors were attached to a frequency generator and configured to continuously record a sinusoid ( $f = 4 \text{ Hz}$ ,  $phase = 0$ ,  $offset = 0$ ,  $amplitude = 3 \text{ V}$ ) at 500 Hz. With deactivated synchronization, the sine waves showed a phase mismatch of approximately 200 ms after 60 minutes, which is unacceptable for almost all biosignal applications (see figure 3.7, left plot). This drift error is found to be in accordance with the possible worst case of 360 ms assuming a crystal accuracy of  $\pm 50$  ppm.

When the synchronization mechanism is turned on, it is supposed to completely eliminate drift and offset errors. As before, the recorded sine waves are analyzed with respect to their phase shifts. First, zero crossings are detected and then blocks of one second, which contain four sine wave periods, are extracted. An unconstrained, nonlinear estimation technique is then applied to estimate the sine wave parameters of the extracted blocks [144]. The difference between the corresponding phase delays serves as a quantitative indicator describing the synchronization accuracy. The right hand side of figure 3.7 shows the phase delays for several long-term measurements. According to the standard deviation, a synchronization accuracy of 30  $\mu\text{s}$  has been achieved, which can be considered an excellent value especially with regards to PWV analyzing applications.

The antenna directivity characteristics of the radio module was investigated in several

**Table 3.3:** Experiment investigating lost packet occurrences during Bluetooth transmission with respect to different sensor orientations (one master and one slave device). The sensors were placed 2 m apart from each other where the radio path was additionally obstructed by a 10 l water bucket positioned between the two sensors.

angle x	angle z	sent packets	received packets	packet lost
0	0	1206	1077	10,69%
45	0	1204	1085	9,88%
90	0	1206	1105	8,37%
135	0	1204	1083	10,04%
180	0	1255	1148	8,52%
225	0	1206	1090	9,61%
270	0	1222	1095	10,39%
315	0	1205	1079	10,45%
0	45	1249	1140	8,72%
0	90	1202	1090	9,31%
0	135	1204	1086	9,8%
0	180	1203	1087	9,64%
0	225	1202	1068	11,14%
0	270	1205	1076	10,70%
0	315	1208	1100	8,94%

communication experiments where the radio transmission path was obstructed by a water filled 10 l bucket, and lost packets were analyzed with respect to varying sensor rotations (see table 3.3). These measurements were conducted in a laboratory environment with active WLAN routers and other BT devices operating in the same 2.4 GHz ISM frequency band. A mean lost packet rate of 9 percent was determined, which did not affect the synchronization accuracy.

The firmware implementation and the conducted experiments to obtain the presented figures of figure 3.7 are the concrete contributions of this work.

### 3.5 Database

This last subsection finally gives an overview on the datasets involved in the presented studies. The chosen records were drawn from either elaborated clinical and laboratory measurements conducted in the scope of this work, or from openly available databases such as PhysioNet [86]. Thus, it is ensured that varying measurement settings and hardware systems are considered, which increases the generality of the presented results.

Two major requirements were posed for choosing proper datasets. In the first place, records containing different grades of signal distortions are needed, in order to serve the purpose of evaluating signal quality detection methods, as will be discussed in the next chapter. Secondly, the analysis of PWV relating applications based on PAT and PTT extraction asks for synchronized datasets containing at least one ECG and one pulse wave channel.

**Table 3.4:** Records selected from rBSN student database\_I.

records used for signal quality estimation			
Record	# Beats	# Beats annotated good	# Beats annotated bad
d_sch2	2328	1163	1165
d_sch3	2160	771	1389
d_sch5	1983	850	1133
d_sch10	1772	863	909
d_sch11	2331	1353	978
d_sch12	2551	1008	1543
d_sch13	2492	1590	902
d_sch18	1847	630	1217
TOTAL	17464	8228	9236

The studies conducted in this work include two measurement series utilizing the rBSN hardware as is depicted next.

#### *rBSN\_studentDatabaseI*

Regarding the first database, 18 healthy subjects (mean age: 24.2 years, 17 male, 1 female) have volunteered to participate in a 20 minutes experiment. Next to resting periods, the protocol consists of different hand movements such as twitch/bump/shake/rotation patterns, and also contains a walking exercise on a treadmill followed by a short period on an ergometer. The full protocol is given in table 8.1, which is found in appendix 8.1. Each subject was equipped with a *rBSN\_HeartCore* sensor (leads: Einthoven I, II and III, V2 and V5) and two *rBSN\_DualPulseOxy* fingerclips that were attached to the right and left index finger each. The settings have been designed to produce datasets containing intervals of clean and undisturbed PPG waveforms as well as periods including coarse artifacts and significant signal degradations. During all experiments, the subjects were advised to leave the left hand as steady as possible in order to provide a clean reference PPG signal.

Due to the variety of conducted movements, different kinds of motion artifacts are expected, leading to varying grades of signal distortions in the PPG channels. Thus, this dataset will provide a profound basis with respect to the evaluation of signal quality estimators.

#### *rBSN\_clinicalDatabaseI*

This database covers clinical measurements in the elderly, which were conducted at the geriatric medicine unit of HELIOS Kliniken Aue and the geriatric medicine unit of Städtisches Klinikum Dresden-Neustadt. In summary, 25 patients (aged  $78y \pm 9y$ , 20 female, 5 male) participated in the cardiovascular measurement performing a Schellong-Test. Schellong's method (named after the German cardiologist Fritz Schellong, 1891 - 1953) is a common practice to examine orthostatic dysregulation in a simple procedure, where the heart rate and blood pressure response are monitored when the subject is asked to stand up from lying position [336]. All patients provided a written consent in accord with the ethics board at Technical University of Berlin, from whom prior approval has been granted (request

**Table 3.5:** Records selected from clinical rBSN database.

records used for signal quality estimation			
Record	# Beats	# Beats annotated good	# Beats annotated bad
d01_001d	577	501	76
d01_002d	1000	861	139
d01_003d	825	728	97
d01_006d	877	826	51
d01_003a	1658	1588	70
d01_004a	1114	1079	35
d01_006a	1353	1344	9
d01_008a	961	831	130
d02_009a	1233	1225	8
d02_007a	927	860	67
d02_008a	692	431	261
d02_009a	834	786	48
d02_010a	1209	857	352
TOTAL	13260	11917	1343

PF\_01\_20140513). Each measurement lasted 15 minutes, where the patients were asked to lie on a bed, stand up and lie on the bed again for periods of 5 minutes each. During the whole procedure, the *rBSN\_HeartCore* and *rBSN\_DualPulseOxy* hardware systems have been deployed. Moreover, systolic and diastolic blood pressure, were recorded at predefined time instances using a cuff based HE-907XL Omron Healthcare blood pressure monitor.

As discussed in chapter 2, PPG datasets comprising elderly patients will contribute pulse waveforms of different morphology, due to the decreased arterial elasticity. Moreover, these datasets are expected to contain further eminent cardiovascular events such as blood pressure variations, an increased number of ectopic beats as well as motion artifacts during the procedure of getting up.

### ***Vasoscreen Database***

The clinical recordings in the geriatric units have been complemented by measurements applying the commercial VasoScreen 3000 system (medis, Medizinische Messtechnik GmbH, Ilmenau, Germany), which is designed for arterial vascular diagnosis. Next to a standard three lead ECG, the VasoScreen offers an ear-clip PPG, a four electrode impedance plethysmograph and simultaneous four channel blood pressure measurements on arms and ankles based on the oscillometric measurement principle (cf. chapter 2.1.2). The device also delivers multiple parameters such as the ankle-brachial-index (ABI), pre-ejection period, stroke volume and others, which are however, not further considered in this work. In total, 60 patients have been measured, undergoing the same procedure as defined in *rBSN\_clinicalDatabaseI* where informed consent was collected according to the ethical guidelines again.

**Table 3.6:** Records selected from Vasoscreen database.

records used for signal quality estimation			
Record	# Beats	# Beats annotated good	# Beats annotated bad
brir26	895	791	104
dran31	1154	1126	28
frel18	680	656	24
gaha39	864	752	112
heev37	822	763	59
huer30	815	739	76
kain24	615	534	81
klge32	829	433	396
kuur39	806	720	86
lehe48	829	824	5
TOTAL	8309	7338	971

### *PhysioNet Database*

For the sake of reproducibility, it was ensured that records from on-line available databases were considered as well. The PhysioNet database is a very prominent platform, which offers access to data of numerous clinical studies with different backgrounds and distinct focuses [86]. With respect to PPG signal quality analysis, the PhysioNet challenge 2015 titled 'Reducing False Arrhythmia Alarms In The ICU: The PhysionNet/Computing In Cardiology Challenge 2015' provides interesting datasets as they contain ECG and PPG signals recorded in the intensive care unit [45]. Eight arbitrary datasets have been selected, where at least one third of each PPG channel is significantly degraded due to motion artifacts or bad probe position (corresponding IDs: *v100s*, *v101l*, *v102s*, *v282s*, *v825l*, *v828s*, *v846s*, *v848s*). Datasets with apparent arrhythmias or frequent extrasystoles were avoided.

In order to allow the evaluation of blood pressure estimation methods, records containing a continuous arterial blood pressure reference are required as well. The MIMIC database is a collection of clinical patient monitor data acquired in a variety of ICUs [268]. Multiple subsets of records containing an ECG, PPG and intra-arterial blood pressure signal have been extracted for the evaluations conducted in the following sections.

Further details regarding the signals properties including number of beats and other basic statistics, preprocessing histories, ratios of clean/corrupted segments and reference annotations are supplied in the given tables (3.4 - 3.7) and in the respective evaluation sections of chapter 4 and chapter 6.

**Table 3.7:** Records selected from PhysioNet database *challenge2015* [45].

records used for signal quality estimation			
Record	# Beats	# Beats annotated good	# Beats annotated bad
v100s	525	427	98
v101l	576	483	93
v102s	518	477	41
v282s	350	229	121
v825l	362	319	43
v828s	405	296	109
v846s	309	173	136
v848s	601	471	130
TOTAL	3646	2875	771
records used for ectopic beat detection			
Record	# Beats	# VEBs	# SVEBs
a624s	302	1	2
a746s	406	5	0
b340s	254	0	22
b341l	260	0	23
b515l	211	2	4
b517l	227	0	6
b560s	139	10	17
b562s	123	29	11
b838s	242	20	28
f642s	457	0	8
t416s	240	1	40
t662s	567	6	0
t680s	348	15	3
t752s	383	0	5
t762s	313	5	38
v132s	227	15	0
v158s	77	6	1
v205l	87	10	9
v253l	535	77	0
v254s	441	35	3
v255l	445	47	0
v368s	329	6	0
v427l	175	0	17
v557l	264	4	0
v559l	354	23	9
v573l	335	0	2
v648s	340	2	1
v696s	237	0	46
v769l	357	25	1
v831l	319	15	0
v833l	217	13	3
TOTAL	9211	372	299

## 4 Enhanced Pulse Wave Discrimination with OPRA

Having discussed the physiological backgrounds and technical measurement insights of pulse travel times in chapter 2 and 3, it is now time to address the challenges of pulse wave processing in difficult environments. In this work, difficult environments are primarily defined as measurement settings accompanied by unpredictable incidents, which are likely to provoke considerable signal artifacts. With reference to PPG recordings, motion is certainly a main factor responsible for signal quality degradations. As a matter of fact, artifacts due to motion are inevitable during unsupervised situations, demanding a very careful treatment of this topic.

A major problem, which is unfortunately still far from being satisfactorily solved, is the fact that the physiological features of noisy pulse wave signals are typically masked by major shape distortions prohibiting accurate analysis procedures. Pulse wave velocity applications based on PAT/PTT detection are especially affected because a reliable extraction of fiducial points cannot be guaranteed anymore. Therefore, this issue has aroused a lot of scientific interest in the past years, including publications on ECG and pulse wave signal quality, numerous works on sophisticated artifact reduction approaches, as well as methods for reliable PAT/PTT extraction.

Although certain PAT/PTT extraction approaches seem to be more robust than others, there is a point where the pulse wave signal does not contain any physiological information at all with fiducial points, like onsets or peaks becoming unidentifiable. This poses a serious limitation to unsupervised settings, as these periods need to be reliably detected in order to stop automatic signal evaluation procedures on these segments. Next to these external influences, pathophysiological incidents such as ectopic beats are also known to affect the pulse wave properties and participating processing methods. To date, there are no published works concerning themselves with the impact of extrasystoles on PAT/PTT extraction, which motivated initial efforts in this work, resulting in a novel multimodal ectopic beat detection method.

The following subsections will address these aspects in more detail to analyze the difficulties of robust pulse wave processing. The focus is then set to PPG signal quality estimation since this stage can be seen as the most crucial part in the given processing chains.

The structure of this chapter is as follows. The most prominent PAT extraction schemes involving different fiducial points are analyzed in section 4.1. This discussion is followed by an overview of current ECG and pulse wave signal quality detection approaches, as these

two signals are most frequently involved in PAT/PTT analysis. Especially with reference to PPG signal quality, none of the methods published so far completely satisfies the tight requirements demanded by unsupervised PWV applications. Therefore, a novel PPG signal quality estimator is presented in section 4.3.2, which outperforms existing methods and incorporates competitive features such as self-calibration, on-line applicability and low computational complexity.

The last section 4.4 concerns itself with ectopic beat detection during PWV applications and presents the results of the proposed multimodal heartbeat classification algorithm.

## 4.1 Determination of PAT and PTT

### PPG fiducial points

In either PAT or PTT calculation (cf. section 2.2.1.2), one needs temporal reference locations within the pulse wave signal, which are referred to as fiducial points. In practice, certain characteristic points are preferred, with the most common ones being illustrated in figure 4.1. The foot of the pulse wave is a very prominent location, which is also known as onset, and describes the beginning of the systolic slope. It is chosen as reference point for PAT/PTT calculation in many publications [181, 195, 255, 338, 352] and is generally assumed to be unaffected by superimposing reflection waves [38]. A frequently used extraction method is the automatic onset detection proposed by Zong [355], which is based on adaptive thresholding of the signal's slope sum function. PAT values determined with the help of this onset will be labeled  $PAT_{Onset}$ .

Nonetheless, there are further proposals on how to define the onset's exact location, taking into account either the absolute minimum sample, or evaluating the intersection of the tangents derived at the pulse minimum and the steepest ascent ( $PAT_{Tangent}$ ) [135, 248]. Further fiducial point suggestions involve predetermined thresholds on the rising slope of the pulse wave [118, 240] (according PAT points will be labeled  $PAT_{Threshold}$ ) or consider the absolute maximum sample value, which typically represents the beat systole. The peak's interpretation remains somewhat challenging as the pulse is additively composed by forward and reflection waves but is used for PAT/PTT calculations in some works [159, 318, 338]. The label  $PAT_{Peak}$  is assigned for relating PAT values derived from this peak characteristic point.

In young subjects with rather elastic vessel properties, one clearly recognizes a secondary peak, which is also referred to as late systolic peak or diastolic peak [62]. The systolic and diastolic peak encompass the dicrotic notch, which might disappear on decreasing vessel elasticity. Secondary peak detection has been thoroughly discussed in [103] but was not contemplated for PAT/PTT detections directly. It is noted that in dependence of the pulse wave propagation speed, the reflection waves overlap with the primary forward wave smearing primary and secondary peaks, which has been recognized as a source of inaccuracy in PWV applications [332].

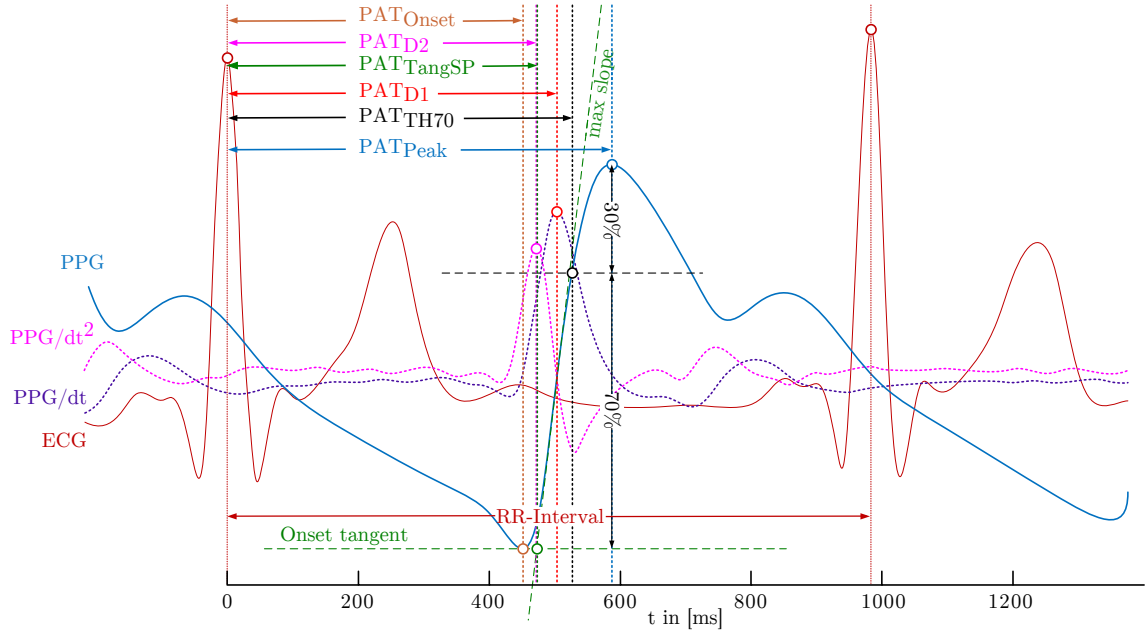


**Figure 4.1:** Common characteristic pulse wave locations which are also referred to as fiducial points. In this work, PAT values are defined as the time distance between the ECG R-Peak and the respective PPG fiducial point.

Although being rarely used in practice, the first and second derivative signals contain specific points known as a, b, c, d and e waves [62, 64, 66], which might contain valuable information for PWV applications as well. The maximum of the first derivative (D1) and the second derivative peak (D2) are commonly used as PAT/PTT fiducial points [81, 129, 163, 183, 296] and are often found as reference points in commercial products such as the Complior<sup>®</sup> system (Alam Medical, France).

Next to the above presented single point methods, multipoint advances are an interesting alternative to derive PAT relating information. Corresponding methods range from simple cross-correlation procedures [289] to more sophisticated approaches as presented by Sola et al. who proposed a parametric PAT estimation method by fitting simple models that reflect the upstroke of the PPG waveform [285]. Once a specific model of the PPG wavefront is determined, the corresponding PAT is derived by properly transforming the parametric description back into time domain. Sola et al. then analyzed the PAT extraction step by comparing two models where the first was designed with the help of a Morlet wavelet and the second is based on a tangent hyperbolic function ( $PAT_{MOR}, PAT_{TANH}$ ), which focuses on the anacrotic phase of the pulse wave.

PAT values determined by the first derivative fiducial point D1 have proved their clinical usefulness in various studies and were compared against the multipoint PAT values  $PAT_{MOR}$  and  $PAT_{TANH}$ . The results have shown high correlation values between  $PAT_{MOR}/PAT_{TANH}$  and  $PAT_{D1}$  along with an increasing noise robustness, advocating this model based PAT extraction scheme [285].

Sola et al. verified the reported results with the help of elaborated agreement and repeatability analysis methods. Due to the significant impact of the fiducial point choice, those

tests have been carried out again in this work, run on datasets recorded with the rBSN system.

### **PAT extraction comparison**

Agreement matrices based on the ideas of Bland and Altman [24] provide a neat option to compare the outputs of  $M$  different PAT approaches [200, 285]. In essence, one considers two PAT outputs (for example  $PAT_{\text{TANH}}$  and  $PAT_{\text{Peak}}$ ) and determines the standard deviation of their differences where small values indicate a good agreement accordingly:

$$AM_{ij} = 2 \cdot STD(PAT_i - PAT_j). \quad i, j \in [1, M] \quad (4.1)$$

The agreement values of the PAT data analyzed on records considered in this work are summarized in table 4.1. In total, 3400 beats have been drawn from 41 subjects of the MIMIC database as well as 27 subjects from the rBSN database (*rBSN\_clinicalDatabaseI* and *rBSN\_studentDatabaseI*). This subset includes patients of different ages (22 - 90 years) and also covers diverse conditions such as rest and exercise.

The absolute values  $AM_{ij}$  of the agreement matrix are higher than those reported by Sola et al., which is most likely due to the fact that in the current evaluation, all PATs were evaluated on single beats and not on ensemble averaged templates as was done in Sola's work [285]. However, the relative differences remain similar. Having a closer look at table 4.1, an increased disagreement becomes obvious in points that are not situated next to each other (compare for example onset and peak), which supports the notion that these points are more liable towards artifacts and cardiovascular influences. Chiu et al. first observed that the characteristic point D1 yielded the smallest standard deviation in PTT extraction, compared to onset and D2, which can be interpreted as a sign of increased robustness when D1 is chosen as reference fiducial point [38].

By resorting to Monte Carlo simulations, as was done in Sola's work, one can further investigate the robustness of different PAT fiducial points in terms of repeatability [285]. The underlying idea of Monte Carlo simulations to test the robustness of different PAT extraction techniques is rather simple and straightforward. First, a clean PPG beat is extracted and repeatedly replicated giving an undistorted sequence composed of exact copies of this single beat, which will result in a constant PAT with reference to the original ECG R-Peak. Next, a band-pass filtered multicolored Gaussian noise signal is generated containing frequency components between 1 Hz and 7 Hz (similar to those caused by motion), which is added to the pulse waveform [285]. As illustrated in figure 4.2, one gets a synthesized PPG incorporating noisy perturbations where the PAT ground truth is known. The decreasing SNR values thereby emulate different ambulatory situations ranging from completely clean beats, as one would expect during periods of rest, to completely distorted pulse shapes, as they typically occur during intense motion [285].

**Table 4.1:** Agreement matrix based on the approach of Bland and Altman [24] where each element yields the difference of two PAT measures in terms of standard deviation (STD). With reference to state of the art PAT technique using the D1 point, the passable performance of the multipoint model reported by Sola et al. [285] could be confirmed, yielding a rather low STD value. Further, points located on the rising slope (inc30, inc50) also appear to be more robust during PAT extraction.

<b>AM</b>	tanh	mor	corr	inc70	inc50	inc30	D2	D1	peak	tang
onset	29,7	40,5	52,6	37,2	30,8	25,9	33,6	33,2	59,9	21,0
tang	21,9	38,6	47,4	28,5	20,8	15,3	23,0	18,8	53,7	
peak	39,3	42,3	33,1	30,2	37,3	43,7	55,8	50,7		
D1	25,2	40,4	46,9	28,0	23,2	22,7	32,9			
D2	27,5	45,1	50,7	32,6	26,0	21,4				
inc30	11,7	32,8	39,1	16,5	7,8					
inc50	9,7	31,0	35,1	9,1						
inc70	13,7	30,6	31,2							
corr	33,9	41,0								
mor	30,3									

In accordance with the results of Sola’s work, it could be shown that for decreasing SNR values, some classes of fiducial points lead to more severe PAT errors than others. This finding is supported by the bottom plot of figure 4.2, which demonstrates the erroneous PAT values at decreasing SNR values of the PPG signal. Further, figure 4.3 sums up the mean PAT error and its standard deviation with respect to the considered fiducial points, deploying a feeling of the difficulties of PAT extraction in noisy signals.

The parametric models proposed by Sola et al. indeed perform comparatively well, especially at low SNR values. In general, it can be confirmed again that reference points, which are located on the rising slope of the pulse wave, are more immune towards small signal distortions when compared to onset- or peak points. However, once the signal quality falls below a reasonable level, a reliable PAT extraction is not feasible anymore, regardless of the underlying extraction scheme. Practical applications will therefore still depend on an automatic signal classification process, which can discriminate between physiologically meaningful content and artifacts or noise.

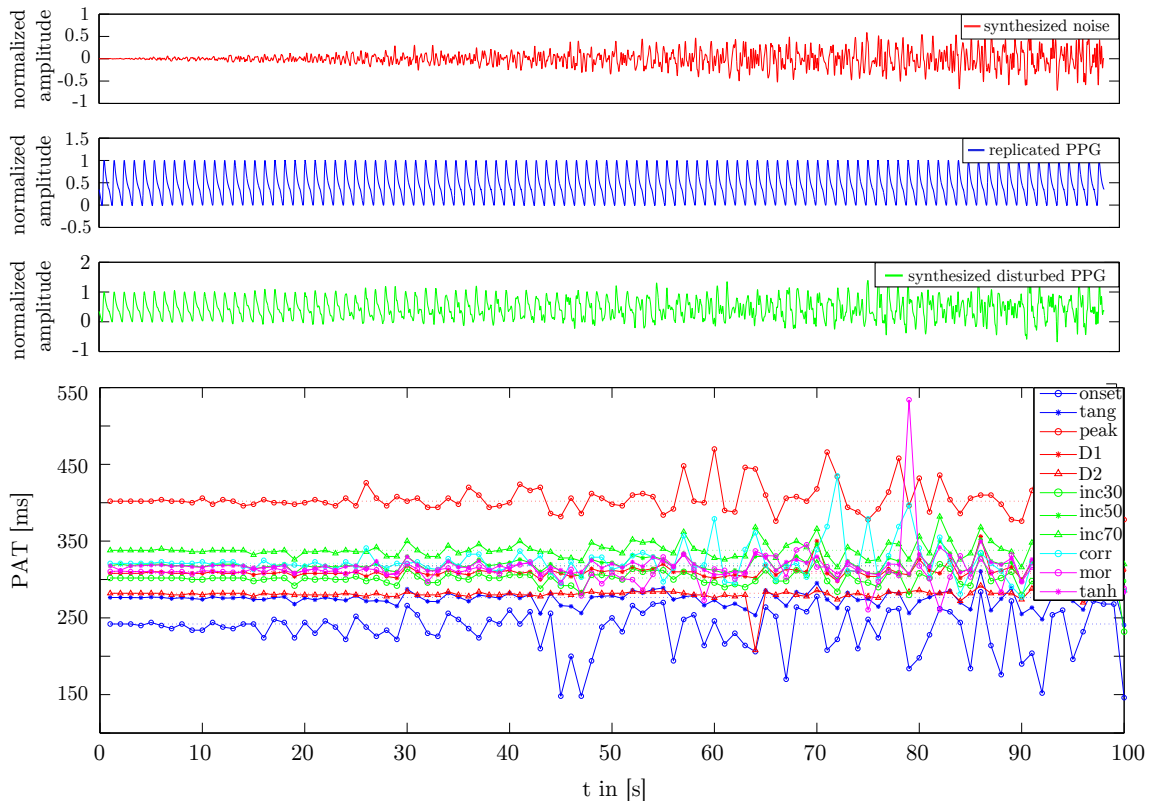


**Figure 4.2:** Monte Carlo simulation providing an insight into the variations of different PAT values extracted at decreasing SNR values of the pulse wave signal. The pulse wave itself was artificially created by multiple copies of a single beat so that the PAT ground truth is always known. The signal’s SNR is lowered in a step by step manner by adding a Gaussian noise signal, thereby allowing the investigation of PAT extraction performance at decreasing signal quality levels. Apparently, fiducial points located on the rising slope of the pulse wave are more robust when compared to others like the onset or peak. The competitive performance of the multipoint  $PAT_{TANH}$  model proposed by Sola et al. [285] was confirmed again.

## 4.2 ECG Signal Quality Detection

Pulse arrival time extraction does not only depend on the ability to detect underlying fiducial points of the pulse wave as was dealt with in the previous section, but also requires a reliable timing reference of the cardiac systole in the heart. For this purpose, the surface ECG is often referred to, in order to approximate the starting time of the pulse wave travel occurring during left ventricular ejection.

The R-Peak - being the most prominent and distinctive point in the ECG - is rather easy to identify, even when the ECG signal is slightly distorted by minor noise levels or inferior motion artifacts.

On the other hand, a complete ECG signal delineation, including more subtle components like T- or P-Waves can be quite challenging, which is why ECG signal quality detection has been subject to intensive research in the past decades. Allan and Murray [5] cite different works dating back to the eighties, discussing ECG signal quality issues

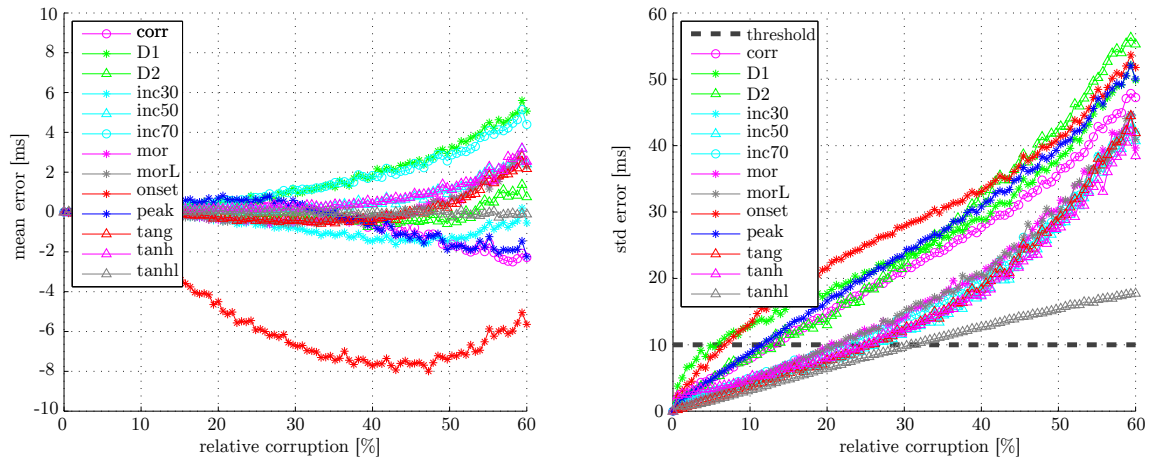


**Figure 4.3:** Mean (left plot) and standard deviation (right plot) of PAT detection error derived by Monte Carlo simulation. Different fiducial points were employed for the PAT extraction process. The multipoint advances as proposed by Sola et. al [285] indeed perform better than PAT values extracted by simple fiducial references. However, once the signal quality falls below a reasonable level, a physiological interpretation becomes unfeasible regardless of the extraction schemes applied.

and common approaches. A majority of the published proposals start to analyze the signal strength in different bandwidths and detect out-of-range events in order to discriminate the connected ECG signal quality. This very basic scheme covering signal feature extraction and comparison to predefined thresholds is still encountered in many later works.

In 2011, the annual challenge of the *Computing in Cardiology* conference put the focus on ECG quality detection titled ‘Improving the Quality of ECGs Collected using Mobile Phones’, which resulted in interesting contributions that are applicable on wearable and battery driven devices [283].

There are several works providing a detailed overview on the different approaches published in the scope of that contest [44, 116]. As these methods are designed for implementation on mobile hardware, one finds rather simple features such as amplitude criteria, zero line detection, spike analysis or statistical properties, which are processed by standard classification methods including neural networks, support vector machines or simple classification trees.

To assure a reliable R-Peak extraction performance with standard QRS complex detection procedures as [213], these methods perform well in discriminating the underlying signal quality and therefore fulfill the requirements of robust PAT calculation. This was also confirmed by the measurements conducted in the present studies, forbearing the need from further addressing the topic of ECG signal quality in this work. The interested reader will find more in depth background information covering recent publications relating to that topic in [78].

### 4.3 Pulse Wave Signal Quality

The preceding study on fiducial point extraction in PAT/PTT applications attested the importance of pulse wave signal quality, which will be thoroughly dealt with in the following section.

Due to the underlying optical measurement principle based on light absorption in the blood filled arteries, the PPG is known to be exceptionally liable towards different kinds of artifacts [4]. Most of the time, present motion at the measurement site is the major contributor for degraded PPG signal quality. Shifting sensor positions, externally applied pressures and acceleration forces lead to changes in the optical path and corrupt the morphological shape of the pulse contour form. Moreover, minderperfusion poses a serious limitation to PPG recordings, especially on distal measurement sites like the fingers, toes or earlobes. Additional impacts on signal properties might be provoked by electromagnetic interference, ambient light conditions, impeding light path obstacles like nail polish, or improper signal conditioning [100]. Figure 4.4 depicts several PPG snippets of six seconds length recorded with the rBSN sensors in different situations. The small head plots show the normalized raw signals of the PPG fingerclip acceleration sensor, yielding an idea of the present motion, whereas the PPG is plotted with a synchronized ECG channel, which helps to discriminate single beats in the noisy periods. It strikes out that different patterns of motions lead to different types of artifacts, demonstrating the difficulty of PPG interpretation in realistic situations.

Automatic evaluation of PPG signal quality is therefore a very important prerequisite for any post processing method. The following subsection 4.3.1 will give a deeper insight into currently proposed algorithms developed for signal quality detection of pulsatile signals such as the PPG or ABP. In the following, no distinction between PPG or ABP signals is made as the main ideas apply for both kinds of signals. Subsection 4.3.2 concerns itself with a very detailed presentation of the novel PPG quality estimation approach, developed in the scope of this work. A thorough performance evaluation of all considered methods is given in subsection 4.3.3.2 proving the potency of the advocated signal quality estimator.

#### 4.3.1 Overview of Currently Published Methods

This subsection briefly depicts the most relevant publications on PPG signal quality estimation. It is noted that up to now, no works concern themselves with a comprehensive comparison of the published advances, which is supplemented by the following evaluations.

To weigh up the respective pros and cons of the single approaches, several descriptive attributes are scrutinized, which are listed in table 4.2. In the first place, the choice of segmentation is a fundamental property of a signal quality estimator, which limits the applicability for specific situations.

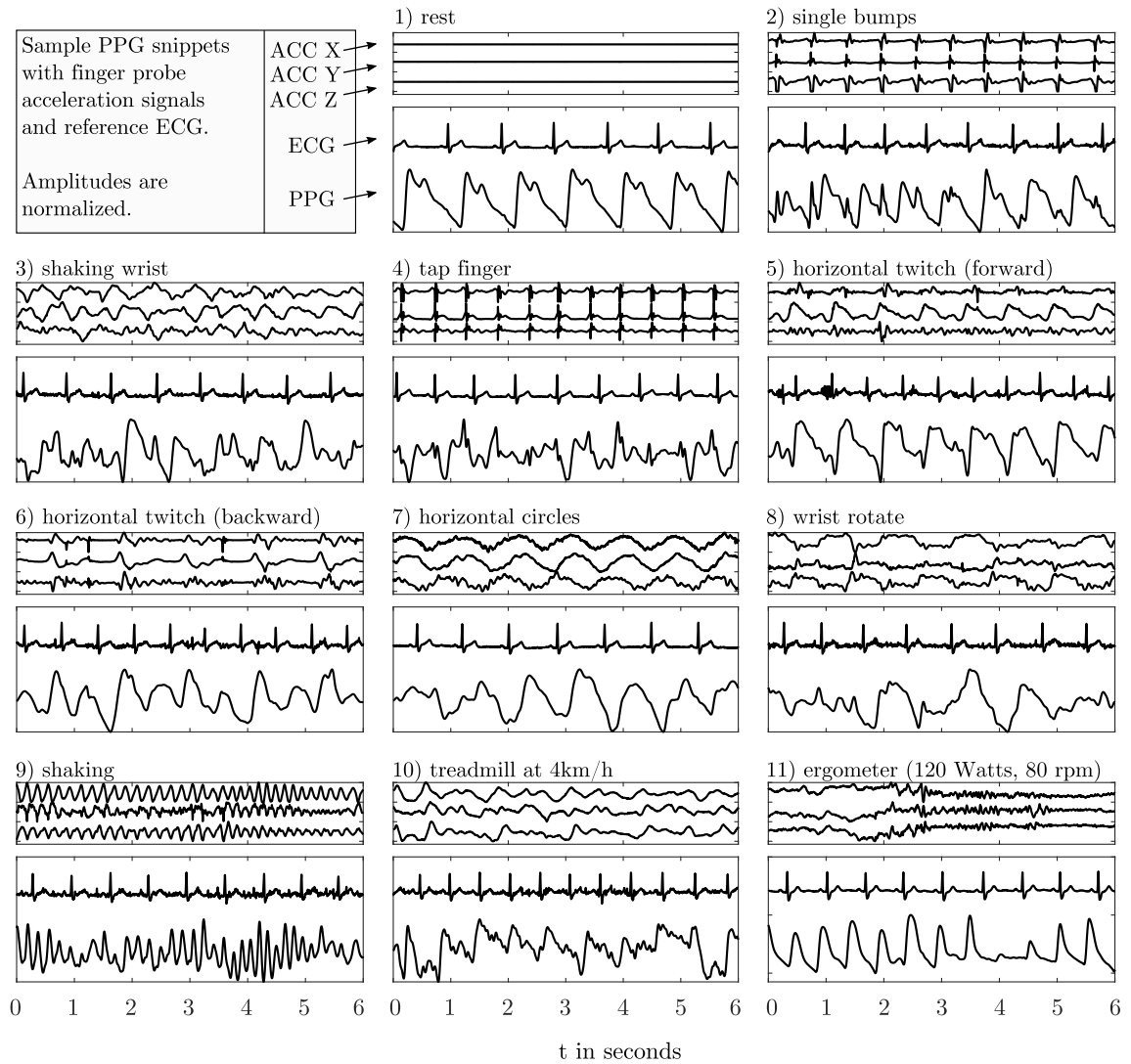


**Figure 4.4:** PPG snippets recorded during different movement experiments and treadmill/ergometer measurements. Top plots: Normalized acceleration signals acquired by rBSN PPG accelerometer (x-, y-, z-components from top to bottom).

Main plots: Normalized ECG and PPG signals. **1)** sitting at rest, no movements **2)** single bumps **3)** shaking whole wrist **4)** tap finger **5)** horizontal twitches forward **6)** horizontal twitches backward **7)** horizontal circles **8)** wrist rotate **9)** shaking **10)** treadmill at  $4 \text{ km h}^{-1}$  **11)** cycling on an ergometer (120 Watts, 80 rpm)

Assigning every single sample a signal quality class (continuous segmentation) yields the maximum possible temporal resolution in contrast to mechanisms that classify longer segments containing multiple beats (windowing). Next, the actual decision output format is another crucial component, which varies among different approaches. The classifier might output either binary classes like *'quality\_good/quality\_bad'* or  $N$  multiclass labels such as *'quality\_excellent'*, *'quality\_very\_good'*, *'quality\_good'* or even continuous numerals ranging inside a given interval.

The final architecture is assessed by further attributes including computational complexity, on-line applicability, dependence on prior calibration routines, adaptivity towards changing

conditions during runtime and of course by its overall classification performance in a given setting.

Regarding the implementational fashion, one generally encounters two principle ways to solve the PPG quality discrimination problem as illustrated in figure 4.5 A). A simple evaluation of signal features derived from time, frequency or statistical domains with adjacent comparison to predetermined thresholds is the first and maybe most intuitive way of classification (upper part, figure 4.5 A)). In this case, the choice of proper features and the subsequent determination of corresponding thresholds is a crucial part, which is typically achieved by either heuristic procedures or supervised classification techniques. A completely different practice focuses on measures of similarity, which is motivated by the fact that in undisturbed recordings, neighbouring beats are expected to retain close morphological shapes (lower part, figure 4.5 A)). This often depends on the formation of a clean reference template, which is compared to each beat under test in order to determine its signal quality class. As a matter of fact, the general ideas proposed in the majority of published methods are based on either of these two options. Table 4.2 lists recently cited works along with their key attributes, which will be discussed now.

Following the first principle mentioned above, Sukor et al. proposed a straight forward two stage classification procedure applying a simple classification tree [292] as depicted by the flow chart in figure 4.5 B). The first step involves the extraction of the three morphological features *pulse amplitude*, *through depth difference* and *pulse width*, which are calculated for each beat. If at least one of these three features exceeds a heuristically determined threshold, the corresponding beat is classified as corrupt. If not, two more features (*Euclidean distance* and *amplitude ratio*) are derived in a second step. These two features are calculated with respect to a mean template beat and are compared to a prior determined threshold again to allow a more granular pulse discrimination into the two classes *bad* and *poor*.

The overall simplicity can be seen as a significant strength of this method, which is therefore a suitable candidate for implementation on battery driven devices with limited processing power. However, the derived features and static thresholds are extremely subject and hardware dependent leading to decreased generalisation and questionable applicability in unsupervised measurement settings. Sukor et al. conducted a small experimental study comprising 13 subjects and reported classification performance values with mean sensitivity, specificity and accuracy of  $89\% \pm 10\%$ ,  $77\% \pm 19\%$  and  $83\% \pm 11\%$  respectively.

A very prominent work based on the second principle was recently published by Li and Clifford [165], which takes advantage of measures describing the similarity of adjacent beats. In their approach, Li and Clifford suggest to form a mean template using undistorted reference pulses only. Once the template is successfully built, it is used to evaluate different correlation coefficients, which serve as the actual measure of similarity between the template and each incoming beat under test. The authors further apply a dynamic time warping technique to account for short-term nonstationarities and nonlinear changes of the morphological features. In the final step, a multilayer perceptron is trained to classify each

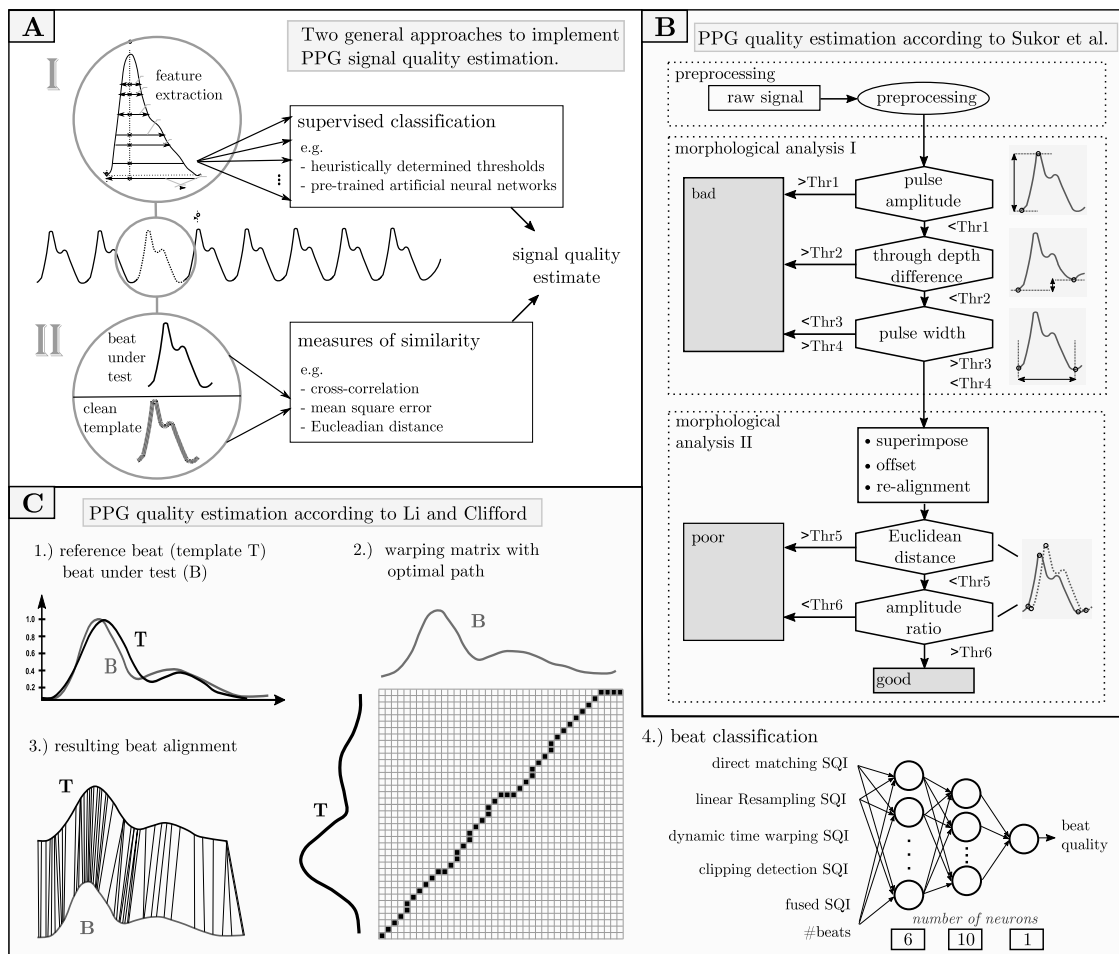


**Figure 4.5:** A) General procedures to approach pulse wave signal quality estimation: A I) Extraction of features from time, frequency or statistical domain, which are typically analyzed by supervised classification structures. Common implementations involve tests with heuristically determined thresholds or apply feature analysis on pre-trained classification architectures. Temporal resolution of the signal quality output can range from single beats to longer segments. A II) Comparison of the beat under test with a clean reference template based on measures of similarity such as correlation coefficient or mean squared error. B) PPG quality detection following principle I as published by Sukor et al. [292], where simple features are compared to heuristically determined thresholds. C) PPG quality detection following principle II as published by Li and Clifford [165], which is based on measures of similarity. Different correlation coefficients are calculated, resorting to dynamic time warping to align single beats. Drawings were partly adopted from the original publications [165, 292].

beat according to its quality class. To provide a visual impression on the overall approach, figure 4.5 C) additionally outlines the main components. Although the authors present a very interesting and powerful method, it requires computational complex computations and also depends on the pre-trained neural network structure, which has to be thoroughly considered before practical utilisation. The algorithm has been tested on a clinical dataset including 104 records from a critical care admission and reportedly achieved sensitivity, specificity and accuracy values of 99 %, 80 % and 95 %.

Karlen et al. [132] introduce an interesting approach, which resorts to repeated Gaussian filters. In essence, these Gaussian bell curves are distributed at likely peak positions based on possible heart rate frequencies, which are derived in parallel using discrete cosine transformations. The authors claim that the highest correlation between the Gaussian filters and the first derivative of the PPG signal will yield a likely estimation of the underlying heart rate and pulse onsets. During the classification procedure, a subset containing clean beats is collected to calculate a superimposed reference beat. A signal quality index (SQI) is derived by a nonlinear scaling function of the cross-correlation value calculated between each incoming pulse and the superimposed reference beat. Thus, this method also fits the second category. The results promise a sensitivity of 96.2% in combination with a positive predictive value of 99.22%.

Selvaraj et al. [275] suggest statistical measures including kurtosis and Shannon entropy to determine an estimate of the underlying PPG quality, where the raw signal is preprocessed by a polynomial detrending technique. Both measures are finally fused to derive a binary decision rule for clean or corrupted segments containing 60 seconds of PPG data. Based on experiments conducted on 24 subjects, specificity, sensitivity and accuracy values of 98.3%, 86.9% and 88.8% have been achieved respectively. However, an exact localization of the artifact is not possible as the proposed algorithm is only able to identify the presence of corresponding distortions inside a given 60 second window in a binary manner. This significantly limits the possibilities of this approach as intervals of clean PPG data which are shorter than 60s duration might never be recognized.

Robles-Robio et al. [264] argue that artifact contaminated PPG signals will embody much larger amplitudes, which is the reason why they propose a filter structure that removes all pulse related information. A root mean square estimate is then used as decision threshold, which quantifies the remaining residual parts that are mainly provoked by artifacts. The detection has been evaluated on data recorded from 23 infants during postoperative care where the probability of detection and probability of false alarm were determined to be 0.89 and 0.13 respectively.

Li et al. [164] propose a Bayesian hypothesis testing approach based on minimalistic features drawn from a reflectance pulse oximeter. The computational complexity of this method is extremely low, allowing on-line implementations on low-resource systems, which were demonstrated on laboratory experiments. The final decision rule is based on the simple Bayesian hypothesis testing method with performance values that state a probability of detection and probability of false alarm of 81% and 20.5% respectively. However, this method involves particular features such as the PPG raw DC component requiring a separate input channel, which is not supported by commercial off-the-shelf pulse oximeters.

Krishnan et al. [139] resort to statistical measures including skew, kurtosis and a bispectral analysis of the PPG in order to distinguish between clean and motion corrupted segments. The different statistical measures are evaluated by means of statistical hypothesis testing,

including a Neyman-Pearson detection rule. The performance has been tested on a small group of 10 subjects, yielding promising detection probabilities, although these are accompanied by rather high false alarm values. The frame length of the single data blocks is not clear, which makes it difficult to further interpret these results.

Yu et. al [350] employ a multimodal approach to derive a signal quality index based on ECG and PPG heart rate consistency and additional evaluation of ECG and PPG features using a support vector machine. The raw signals are processed in frames of 7 seconds. The authors report a sensitivity of 93 % when evaluated on 153 records of data collected from trauma patients during helicopter transports. However, this method is not applicable when a synchronized ECG is not available.

Unfortunately, no efforts have been made so far to objectively compare the performance of different signal quality estimators. Therefore, three of the most promising methods introduced above were reimplemented within the scope of this work to assess the underlying signal quality estimation performance. The corresponding findings are discussed in more detail in the following subsections. Moreover, it will be shown that none of the presented methods ultimately satisfies the demands of an omnipotent beat discriminator supporting reliable PAT/PTT applications. This has indeed motivated the development of a completely novel approach, which can be seen as the key contribution of this thesis.

The first achievements were published in [230], introducing the algorithmic backgrounds along with a preliminary performance evaluation. The specific method is termed OPRA, standing for '*On-line Pulse Reliability Analysis*' and is based on a statistical examination of incoming arterial pulses. It is argued that clean and corrupted beats convey different second order statistics, which are approximated by a single layer perceptron using on-line learning algorithms based on steepest gradient ascent procedures. A more detailed analysis of the presented approach is covered by subsection 4.3.2, which will also review the computational details, performance measures and its applicability in real life settings.

### 4.3.2 A Novel On-line Applicable Approach: OPRA

Having introduced recently published works on PPG signal quality estimation in the previous part, this section now depicts the technical details of the novel signal quality detection approach. Next to the mathematical backgrounds, the major key aspects are presented, carefully weighing up the method's advantages and disadvantages in order to underline its suitability for robust pulse quality analysis.

Concluding from the previous investigation on existing methods, there are two major difficulties when designing automatic signal quality estimators aiming at pulsatile signals like the PPG or ABP. In the first place, one should favour solutions that do not depend on prior configuration of multiple threshold parameters to allow for a broad applicability in changing measurement environments and different hardware systems. Sukor's approach

**Table 4.2:** Literature overview on recent signal quality detection proposals aiming to assess pulsatile signals like the PPG and ABP along with their major descriptive attributes.

reference	algorithmic approach	segmentation	classification output
Sukor [292]	simple signal features with empirically determined thresholds	beat2beat	three classes (good, poor, bad)
Li [165]	correlation based approach employing dynamic time warping	beat2beat	three classes (excellent, acceptable, unacceptable)
Karlen [132]	estimation approach based on Gaussian filters	continuous	SQI
Selvaraj [275]	evaluation of statistical features	60 seconds window	two classes (clean, corrupted)
Robles-Robio [264]	multiple moving average filters with root mean square statistics	continuous	SQI
Li [164]	Bayesian hypothesis testing	3 seconds window	two classes (valid, invalid)
Krishnan [139]	statistical features with Nearman-Pearson Hypothesis testing	beat2beat	two classes (valid, invalid)
Pflugradt [230]	neural network based principal component analysis	beat2beat	two classes (good, bad)

[292] serves as a negative example as it suffers from the dependence of properly configured thresholds, which in turn determine the classification performance of the underlying decision tree.

For example, a good configuration that was fitted on subject A - who has, let's say rather thin fingers leading to higher signal amplitudes - might be improper for subject B - with thicker fingers and thus smaller PPG amplitudes - and vice versa. This demands for a situation dependant adjustment of the corresponding thresholds, posing a tremendous burden on its practical utilization. Adaptivity is therefore an invaluable must have property when seeking a potent implementation of a signal quality estimator.

In the second place, the computational complexity plays an important role when the algorithm is designed for real-time applications on battery driven hardware systems with restricted processing power as they are typically found in off-the-shelf pulse oximeters. This is indeed a serious limitation seen in the majority of the presented methods and in particular an exclusion criterion for the method proposed by Li and Clifford [165], which appeared to be one of the highest performing approaches in the conducted evaluations of this work.

Tackling these two issues was the primary motivation for the development of the method

advertised in this thesis. With respect to robust extraction of PAT and PTT timings as presented in section 4.1, a classifier that is able to discriminate the signal quality on a beat to beat basis would be advantageous, especially when it works reliably in arbitrary measurement settings and is not susceptible to different hardware systems.

The novel OPRA discrimination technique claims to satisfy these needs, thereby offering an indispensable tool accompanying unsupervised PWV applications.

#### 4.3.2.1 Mathematical Preliminaries

##### *Principal component analysis*

Principal component analysis (PCA) is a well established method with respect to analyzing multivariate datasets. Given a vector  $\mathbf{x}$  of  $p$  random variables  $x_1, \dots, x_p$ , PCA basically performs a linear transformation to a new set of variables, which are uncorrelated and ordered according to the variance of the single projections. Two random variables  $x_i$  and  $x_j$  are said to be uncorrelated if their respective covariance as defined by eq. (4.2) is zero, with  $E$  representing the expectation operator and  $m_{x_i/j}$  the corresponding mean values.

$$c_{ij} = E \left\{ (x_i - m_{x_i})(x_j - m_{x_j}) \right\} = 0 \quad (4.2)$$

These second moment values can be positive or negative, forming a symmetric  $p \times p$  covariance matrix  $\mathbf{C}_x$  when calculated for all elements of  $\mathbf{x}$  as shown by eq. (4.3). Note that this matrix is always positive semi-definite and has real and non-negative eigenvalues.

$$\mathbf{C}_x = E \left\{ (\mathbf{x} - \mathbf{m}_x)(\mathbf{x} - \mathbf{m}_x)^T \right\} \quad (4.3)$$

The expectation operator is defined by the probability density  $p_x(\mathbf{x})$  of the corresponding random variable as denoted by eq. (4.4). In practice,  $p_x(\mathbf{x})$  is seldom known but can be estimated from a set of available samples. More details on moments and expectations are found in [303].

$$E \{ \mathbf{x} \} = \int_{-\infty}^{\infty} \mathbf{x} p_x(\mathbf{x}) d\mathbf{x} \quad (4.4)$$

Thus,  $\mathbf{C}_x$  is expected to become a diagonal matrix when applying PCA, due to the uncorrelatedness of the transformed variables. In general, the PCA procedure can be described as follows. First, look for a linear combination  $\alpha_1^T \mathbf{x}$ , which maximizes the variance of the dot product  $z_1$  given by eq. (4.5).

$$z_1 = \alpha_1^T \mathbf{x} = \alpha_{11}x_1 + \alpha_{12}x_2 + \dots + \alpha_{1p}x_p = \sum_{i=1}^p \alpha_{1i}x_i \quad (4.5)$$

Next, one searches for a  $\alpha_2^T \mathbf{x}$ , which is uncorrelated with  $\alpha_1^T \mathbf{x}$  and has maximum variance again, moving on until finding  $\alpha_k^T \mathbf{x}$ , which is uncorrelated with the previous  $\alpha_1^T \mathbf{x} \cdots \alpha_{k-1}^T \mathbf{x}$  and has maximum variance as well. The transformed variables themselves are referred to as principal components (PCs) where  $z_k = \alpha_k^T \mathbf{x}$  is the k-th PC of  $\mathbf{x}$  and  $\alpha_k$  is known as the weight or the vector of coefficients of the k-th PC [124].

Considering  $\mathbf{C}_x$  again, one can easily show that  $\alpha_k$  of the k-th PC  $\alpha_k^T \mathbf{x}$  equals the eigenvector (EV) of the corresponding k-th largest eigenvalue  $\lambda_k$  of  $\mathbf{C}_x$ . If  $\alpha_k^T \alpha_k = 0$  holds and  $\alpha_k^T$  has unit length, the eigenvalue  $\lambda_k$  will represent the variance of the respective variable  $z_k$ . Therefore, the PCA problem can also be solved by eigenvector decomposition of  $\mathbf{C}_x$ . Figure 4.6 provides an illustrating example of the PCA process applied on samples of a two dimensional random vector  $\mathbf{x} = [x_1 x_2]^T$ .

For a complete derivation of the above mentioned results, the reader is referred to [124], which also covers a variety of PCA related applications and provides more sophisticated backgrounds on that topic.

#### *On-line learning algorithms solving the PCA problem*

As introduced in the previous part, one way to solve the PCA problem is found by eigenvector decomposition of the covariance matrix  $\mathbf{C}_x$ , whose elements can be calculated if there are sufficient number of samples available as indicated by equations (4.3) and (4.4). This, however, is a serious limitation in real-time applications, when statistics are needed immediately and have to be estimated even from a small set of data. Moreover, standard numerical methods of eigenvector calculation as carefully analyzed in [89] might not be feasible for high dimensional data sampled at high frequencies, especially when processed on battery driven systems with limited processing power only. Another important aspect are changing statistics of the random variables resulting in non-stationary covariance matrices requiring constant updates on the estimates of  $\mathbf{C}_x$  [111].

A neat way to overcome these problems resorts to adaptive optimization methods based on gradient ascent procedures that try to approximate the corresponding statistics. One of the pioneering works was provided by Oja [204], who proposed a stochastic gradient ascent (SGA) method using a single layer neural network structure (cf. figure 4.7) to estimate the PCs of a given dataset. This basic structure actually implements a linear associator as denoted by eq. (4.6).

$$y_n(k) = \mathbf{w}_n^T(k) \mathbf{x}(k) \quad (4.6)$$

Here,  $\mathbf{w}_n$  represents the n-th weight vector,  $\mathbf{x}$  the input vector and  $y_n$  the corresponding output of the single layer perceptron at time instant  $k$  which is also depicted on the left hand side of figure 4.7. The question to be solved involves a proper selection of  $\mathbf{w}$ , which accounts for the principal component problem by means of a linear transformation as

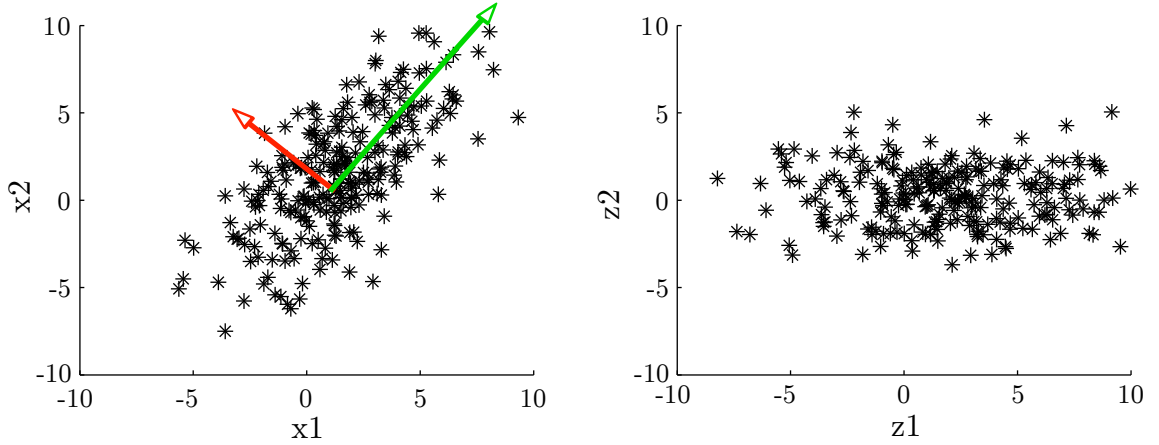


**Figure 4.6: left)** 250 samples of a two dimensional random vector  $\mathbf{x} = [x_1 x_2]^T$  with  $m_{x_1} = 1.5, m_{x_2} = 1.7, \sigma_{x_1} = 7.8, \sigma_{x_2} = 13.5$  and covariance  $c_{12} = 7.3$ . The principal components (weight of PC1 drawn in green, weight of PC2 drawn in red) were obtained by eigenvector decomposition of the covariance matrix  $\mathbf{C}_x$ . **right)** Transformed variables expressed by the first principal component  $z_1$  (variance:  $\sigma_{z_1} = 18.5$ ) and the second principal component  $z_2$  (variance  $\sigma_{z_2} = 2.8$ ). Note that the covariance of the transformed dataset now equals zero ( $c_{12} = 0$ ) as the data has become uncorrelated.

examined by eq. (4.5). With regard to the first output component  $y_1$ , Oja's rule specifies a weight update according to

$$\mathbf{w}_1(k+1) = \mathbf{w}_1(k) + \gamma y_1(k)[\mathbf{x}(k) - y_1(k)\mathbf{w}_1(k)], \quad (4.7)$$

with  $\gamma$  implementing a learning rate which typically adopts small values.

This approach is in fact related with the well known Hebbian learning scheme as given by eq. (4.8), where the weights are increased when input and output values correlate, following the principle 'cells that wire together fire together' [277].

$$\mathbf{w}_1(k+1) = \mathbf{w}_1(k) + \gamma y_1(k)\mathbf{x}(k) \quad (4.8)$$

Applying this classic Hebbian learning rule, practical implementations are faced with the problem of continuously growing weight vector lengths, which is the reason why a proper normalization step is required. Equation (4.9) shows a direct normalization procedure for a single weight component of eq. (4.8), performed after each weight update as was firstly introduced in [204].

$$w_{1_i}(k+1) = \frac{w_{1_i}(k) + \gamma x_i(k)y_1(k)}{\sqrt{\left(\sum_{i=1}^n (w_{1_i}(k) + \gamma x_i(k)y_1(k))^2\right)}} \quad (4.9)$$

This representation is analyzed not only in the original publications [204, 205] but also in

various text books as [102]. Expanding the denominator as a Taylor series of first degree in  $\gamma$  and assuming small values for this learning rate the denominator of eq. (4.9) can be rewritten in the form

$$\begin{aligned}
 \sqrt{\sum_{i=1}^n (w_{1_i}(k) + \gamma x_i(k) y_1(k))^2} &= \sqrt{\sum_{i=1}^n (w_{1_i}^2(k) + 2\gamma w_{1_i}(k) x_i(k) y_1(k) + \gamma^2 x_i^2(k) y_1^2(k))} \\
 &= \sqrt{\sum_{i=1}^n (w_{1_i}^2(k) + 2\gamma w_{1_i}(k) x_i(k) y_1(k))} + O(\gamma^2) \\
 &= \sqrt{\sum_{i=1}^n w_{1_i}^2(k) + 2\gamma y_1(k) \sum_{i=1}^n w_{1_i}(k) x_i(k)} + O(\gamma^2).
 \end{aligned} \tag{4.10}$$

Using the constraint

$$\sum_{i=1}^n w_{1_i}^2(k) = \|\mathbf{w}_1(k)\|^2 = 1 \tag{4.11}$$

and

$$y_1 = \sum_{i=1}^n w_{1_i}(k) x_i(k) \tag{4.12}$$

one can approximate

$$\sqrt{1 + 2\gamma y_1^2(k) + O(\gamma^2)} \approx 1 + \gamma y_1^2(k) + O(\gamma^2) \tag{4.13}$$

for small values of  $\gamma$  [102].

With eq. (4.13), the normalized Hebb variant in the form of eq. (4.9) is found to be

$$\begin{aligned}
 w_{1_i}(k+1) &= \frac{w_{1_i}(k) + \gamma x_i(k) y_1(k)}{1 + \gamma y_1^2(k) + O(\gamma^2)} \\
 &= (w_{1_i}(k) + \gamma y_1(k) x_i(k)) (1 + \gamma y_1^2(k) + O(\gamma^2))^{-1} \\
 &= (w_{1_i}(k) + \gamma y_1(k) x_i(k)) (1 - \gamma y_1^2(k)) + O(\gamma^2) \\
 &= w_{1_i}(k) + \gamma y_1(k) x_i(k) - \gamma y_1^2(k) w_{1_i}(k) + O(\gamma^2),
 \end{aligned} \tag{4.14}$$

which results in Oja's rule (cf. eq. (4.7)) when neglecting second order terms of  $\gamma$  [102].

This rule is also known as principal component analyzer, because the weight vectors tend to represent the eigenvectors of  $\mathbf{C}_x$  as is shown next. Taking into account the weight update of Oja's rule (in vector notation again)

$$\Delta \mathbf{w}_1(k) = \gamma y_1(k)(\mathbf{x}(k) - y_1(k)\mathbf{w}_1(k)), \quad (4.15)$$

assuming convergence ( $E\{\Delta \mathbf{w}_1(k)\} = 0$ ),

and also knowing that  $y_1(k) = \mathbf{x}^T(k)\mathbf{w}_1(k) = \mathbf{w}_1^T(k)\mathbf{x}(k)$ , one derives

$$\begin{aligned} E\{\Delta \mathbf{w}_1(k)\} &= E\{\gamma \mathbf{x}(k)y_1(k)\} - E\{\gamma y_1(k)^2 \mathbf{w}_1(k)\} \\ 0 &= \gamma E\{\mathbf{x}(k)\mathbf{x}^T(k)\mathbf{w}_1(k)\} - \gamma E\{\mathbf{w}_1^T(k)\mathbf{x}(k)\mathbf{x}^T(k)\mathbf{w}_1(k)\mathbf{w}_1(k)\} \\ 0 &= E\{\mathbf{x}(k)\mathbf{x}^T(k)\}\mathbf{w}_1(k) - \mathbf{w}_1^T(k)E\{\mathbf{x}(k)\mathbf{x}^T(k)\}\mathbf{w}_1(k)\mathbf{w}_1(k) \quad (4.16) \\ 0 &= \mathbf{C}_x \mathbf{w}_1(k) - \mathbf{w}_1^T(k)\mathbf{C}_x \mathbf{w}_1(k)\mathbf{w}_1(k) \\ 0 &= \mathbf{C}_x \mathbf{w}_1(k) - \lambda \mathbf{w}_1(k). \end{aligned}$$

As a matter of fact, this condition represents the well known eigenvector equation which yields the direction of maximum variance  $\lambda_1$  (given by  $\mathbf{w}_1^T \mathbf{C}_x \mathbf{w}_1$ ) when  $\mathbf{x}$  is projected on  $\mathbf{w}_1$ .

One can also show that eq. (4.7) is derived by maximizing  $y_1(k)^2 = (\mathbf{w}_1(k)^T \mathbf{x}(k))^2$  under the constraint  $\|\mathbf{w}_1\|^2 = 1$ , which is equal to a stochastic optimization of  $E\{y_1^2\}$  and thereby solves the PCA problem. As in Oja's rule the gradient of  $y_1^2$  is taken into account (instead of  $E\{y_1^2\}$ ) this approach is called stochastic gradient ascent [111]. The right hand side of figure 4.7 gives an idea of the cost function, which corresponds to the two dimensional dataset, that was depicted earlier in figure 4.6. In this case, the cost function represents the variance of the first principal component samples, which approximately has a maximum along the vector  $[1, 1]$ , coinciding with the first eigenvector plotted in green in figure 4.6. Thus, when the Single Layer Perceptron (SLP) converges towards that maximum with the help of this SGA procedure, the first eigenvector can be simply extracted by the weights of the SLP. Derivations, convergence proofs and additional mathematical backgrounds regarding the discussed SGA approach can be further studied in [204] and [206].

Following Oja's publication, numerous alternative methods have emerged in literature, trying to improve the approximation accuracy especially with respect to the number of PCs that can be estimated and their corresponding convergence speeds. A slight modification of Oja's learning rule resulted in the generalized Hebbian algorithm (GHA) by Sanger [270], who revised the deflationary approach to calculate the minor components. An attempt to calculate all the components in parallel by using lateral connections within the neural network was proposed by Kung et al. in their APEX algorithm [142]. Yang et al. suggested the PASTd algorithm [345], which is based on a recursive least squares principle (RLS)

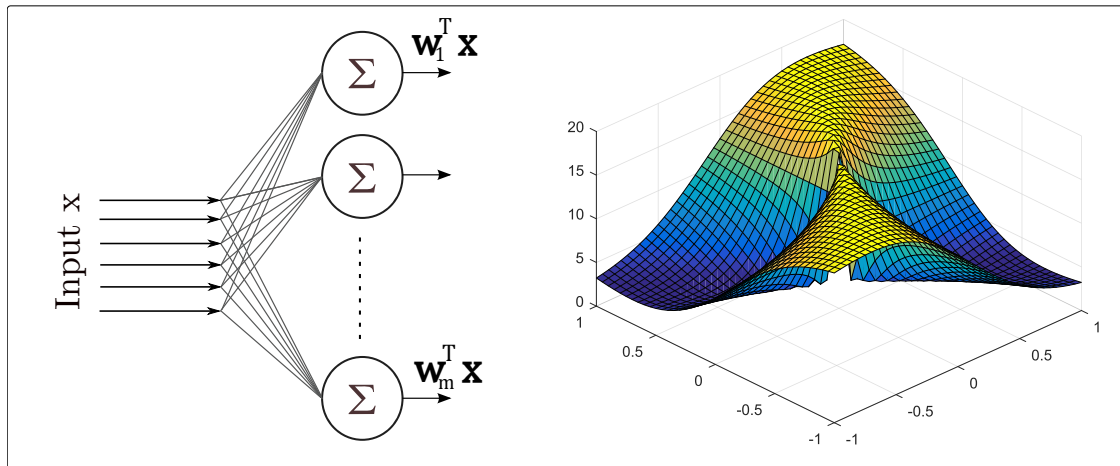


**Figure 4.7:** *left*) Single layer perceptron architecture to estimate the principal components. The neural network outputs  $\mathbf{w}_k^T \mathbf{x}$  represent the PCs as defined by eq. (4.5). *right*) Plot of a two dimensional cost function derived from the sample dataset, presented in figure 4.6, which is optimized in the stochastic evaluation of  $E\{y_1^2\}$ .

depending on the learning rate to enhance the convergence behavior. More recently, a novel learning algorithm, which promises fast convergence speed and robust stability has been proposed by Rao et al. [254] and is called rtPCA.

Compared to the standard eigenvector decomposition approach, these learning rules have significant advantages. As can be easily seen when inspecting Oja's rule in eq. (4.7), single updates require only a few addition and multiplication operations, which makes the depicted on-line approaches feasible for implementation on low-resource systems like the rBSN sensors. A further benefit is the ability to update the PCs on a sample to sample basis, which thereby accounts for non-stationarities without leading to additional costs on the computational complexity.

#### 4.3.2.2 OPRA - On-line Pulse Reliability Analysis

##### *Why data variance is an indicative feature*

The previous introduction on PPG signal quality estimation in section 4.3 revealed that the morphological similarity of clean pulses is a key property which is exploited by various automatic assessment procedures. This notion appears reasonable when inspecting different PPG signals as are shown in figure 4.8. The single plots contain multiple PPG beats drawn from four subjects of the rBSN database where each subject is represented in a single column. The first row contains 50 superimposed clean beats, which received the annotation label *PPG\_Quality\_Good*, whereas the second row presents 50 superimposed corrupted beats of class *PPG\_Quality\_Bad*. Note that the beat intervals are confined by two succeeding onsets, where each beat was processed by a normalization and a fast resampling procedure ( $N = 100$  points) preserving the signals' morphology as described in

[325]. For the sake of clarity, it should be stressed that one such extracted and preprocessed beat is now considered as a single sample of  $\mathbf{x}$ , which has a dimensionality of  $N$  and can be processed as given by eq. (4.5). Therefore, all analysis procedures in the following parts are to be understood on a beat to beat basis. The green line in the third row of figure 4.8 shows the eigenvector derived from the covariance matrix of the clean beats, whereas the red line represents the corresponding EV of the corrupted beats (both EVs have been calculated by off-line eigenvector decomposition). Inspecting the shapes of the two eigenvector pairs for each subject, it strikes out that their directions in the  $N$ -th dimensional space significantly differ. Further, it is revealed that for both, clean and corrupted beats, approximately 30 – 40 percent of the overall dataset variance is retained by the first PC, as can be seen when referring to the variance distribution list given at the bottom of figure 4.8. Regarding the corrupted beats, the distribution of the variance in the minor PCs also has a longer tail in comparison to that of the clean beats.

Following the above depicted variance considerations, it seems legitimate to resort to a principal component based approach, when analyzing the PPG beats' signal quality. As discussed in the previous section, the computation of the principal components - or more precisely, the corresponding eigenvectors - using standard numerical techniques does not seem feasible for the earlier mentioned reasons. Moreover, it would be hard, if not impossible, to identify a single corrupted beat surrounded by otherwise clean pulses using ordinary methods of singular value decomposition. The presented on-line approximation procedures on the other hand, provide a powerful beat to beat analysis framework, which is employed in the proposed OPRA approach.

### ***OPRA - Algorithmic details***

Motivated by the previous considerations, OPRA tries to exploit the signals' second order statistics in order to estimate the underlying beat quality. In essence, the algorithm aims to track changes of the first eigenvector derived from the incoming beats, arguing that two datasets containing morphological different beats will yield significantly different EV estimations of the corresponding  $\mathbf{C}_x$  as motivated by the findings of the previous paragraph. The first EV approximation is calculated using Oja's update rule as defined by eq. (4.7), where  $\mathbf{w}_1$  is expected to converge towards the true first EV as discussed in section 4.3.2.1. The implementation of Oja's rule using the SLP architecture as shown in figure 4.7 thereby constitutes the core unit of the proposed OPRA classifier. The whole framework is shown in figure 4.9, which depicts the two stage approach of the beat classification procedure. The first stage contains the single beat processing method, whereas the second stage implements the actual classification procedure.

#### *Stage I)*

A fast beat segmentation is the first step of the algorithm, where an on-line version of Zong's well established onset detector [355] is implemented to extract adjacent beats of the incoming pulse wave stream. This onset detection approach includes a 150 ms forward-backward search at potential onset points, which is acceptable for real-time applications.

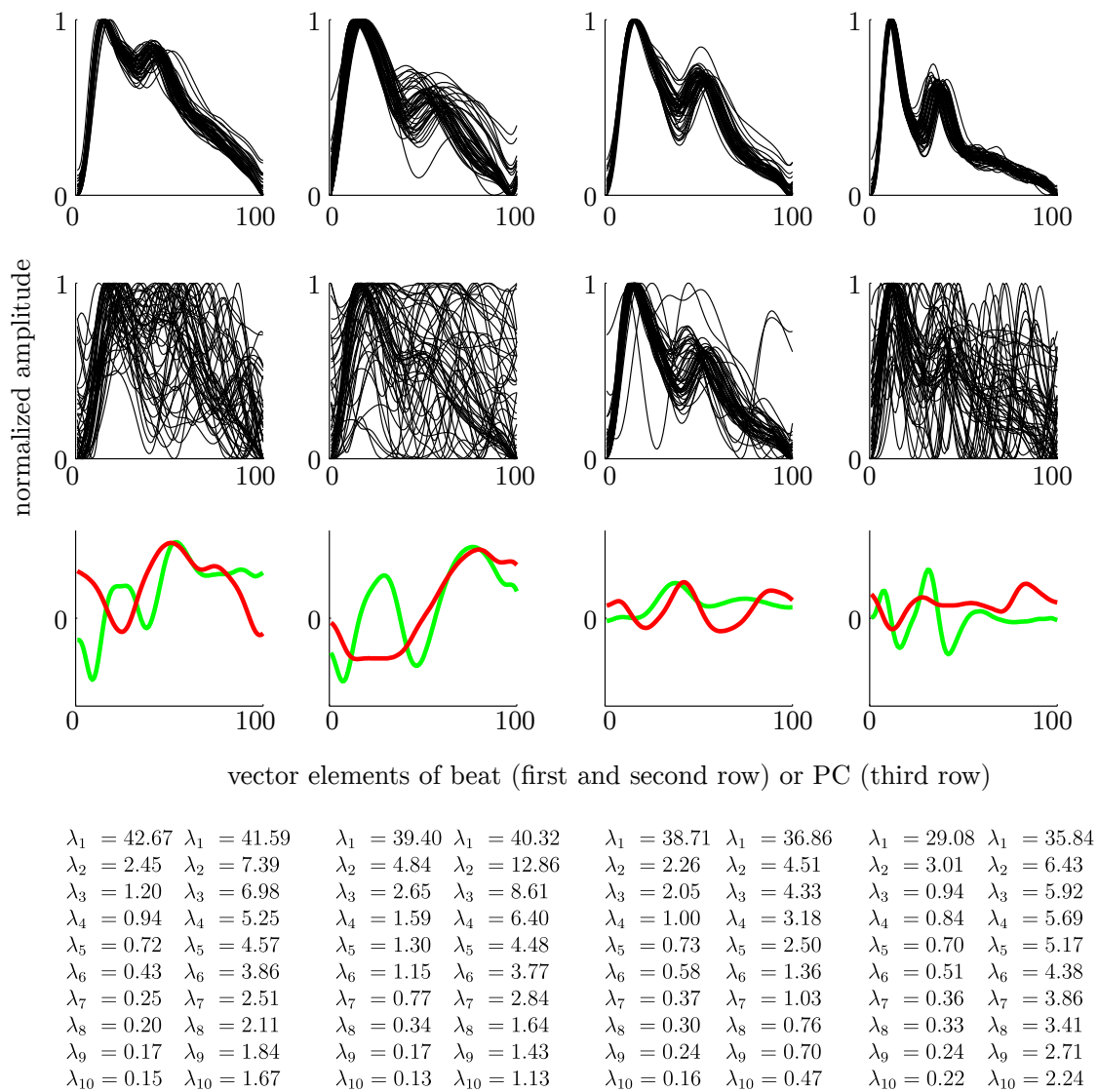


**Figure 4.8:** PPG beats of four subjects drawn from rBSN database. Each column shows 100 sample PPG beats of one subject. **First row:** 50 beats of class *PPG\_Quality\_Good*, which were normalized and resized. **Second row:** 50 beats of class *PPG\_Quality\_Bad*, which were normalized and resized. **Third row:** first PC calculated from clean pulses (green) and first PC calculated from noisy pulses (red), both calculated by singular value decomposition (SVD). **Fourth row:** corresponding variance values  $\lambda_k$  of the first 10 PCs ( $\lambda$  on the left corresponds to clean,  $\lambda$  on the right to corrupted beats).

To compensate different beat lengths at varying heart rates, OPRA resizes each beat to a fixed length of  $N = 100$  samples using the fast resizing approach published by Wei et al. [325] in step II. Next, all signal amplitudes are normalized in step III, before the beats are propagated through the SLP in step IV. After each epoch, the weight components of the SLP are updated according to eq. (4.7) in step V.

#### Stage II)

Once the current beat under test was extracted and processed in stage I, OPRA enters stage II in order to classify its corresponding signal quality. This part basically involves a

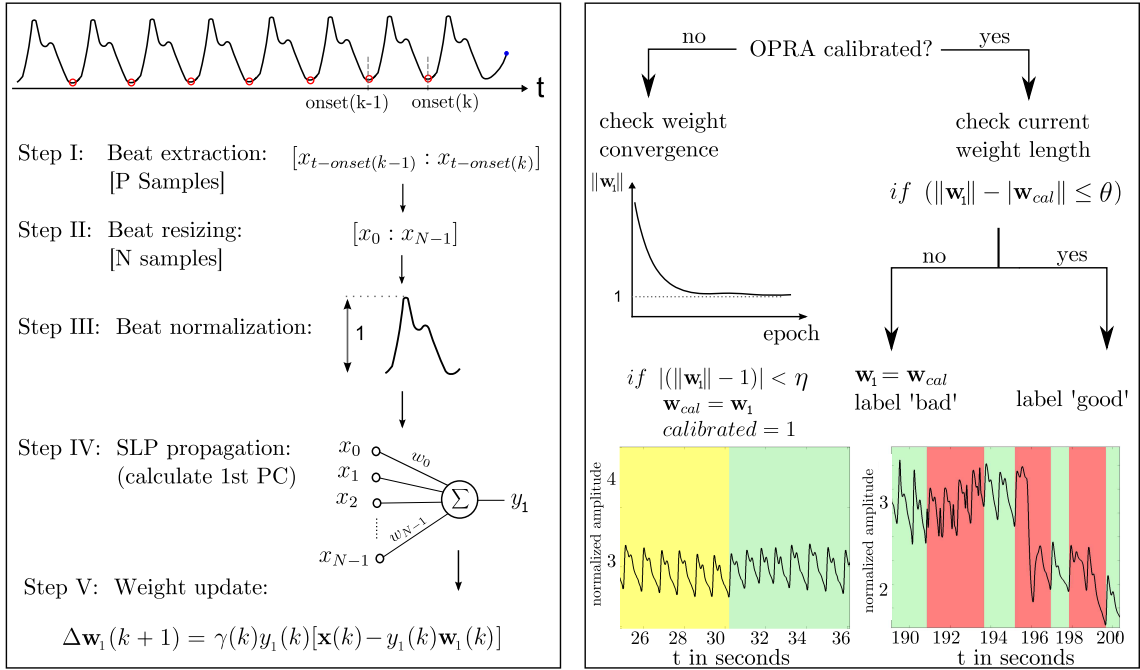


**Figure 4.9: left)** OPRA algorithm stage I (beat processing) - PPG onsets are detected using a simple beat detector according to [355]. Beats are extracted between two adjacent onsets, then resized, normalized and processed by an SLP performing the SGA approach to update the weights after each epoch. **right)** OPRA algorithm stage II (beat classification) - Initially, the SLP weights adapt a representation of the first EV. Successful convergence is indicated by unit length of the weight vector. In this case, the weight is stored as  $\mathbf{w}_{cal}$  and serves as reference for future beat analysis. When the following updated weights deviate from  $\mathbf{w}_{cal}$ , it is argued that the signal morphology has changed and the beat will be classified as corrupt.

fast examination of the current weight vector  $\mathbf{w}_1$ , which is stored in the SLP structure. The idea is as follows: Find a stable weight vector  $\mathbf{w}_1$ , which points into the direction of maximum variance with respect to the last incoming beats. As discussed in the previous section, this direction will not change for beats containing a similar morphology. Once a proper  $\mathbf{w}_1$  is found, OPRA has finished its initial calibration phase and the underlying weight will be stored as the 'calibrated' weight  $\mathbf{w}_{cal}$ . All following weight updates of  $\mathbf{w}_1$  will then be tested against  $\mathbf{w}_{cal}$  to derive a signal quality estimate.

With the first beat, OPRA enters this calibration phase in which the first EV is estimated on the next incoming beat samples by  $\mathbf{w}_1$ . A successful approximation is usually indicated by the weight vector's length, when it converged towards unity [205]. Based on heuristic examinations, a proper stop criterion is defined by the following condition:

$$\|\mathbf{w}_1(k)\| - 1 < \eta, \quad (4.17)$$

were 0.1% was found to be a reasonable value of  $\eta$ .

As pointed out, it is expected that  $\mathbf{w}_1$  will only converge if the incoming beats are undisturbed and provide a similar shape. The converged eigenvector of approximate

**Table 4.3:** *first row*) OPRA execution time on onset detection stage, which is applied on every sample of the PPG signal. *second row*) OPRA execution time on classification function, which is only called when a beat has been extracted. Two implementations have been considered: Java running on a desktop computer and a C program running on the rBSN\_PPG hardware presented in section 3.4.2.

	Java (Intel i7)	C (MSP430 @ 16 MHz)
Onset detection	< 100 ns	487.5 $\mu$ s (7800 clock cycles)
OPRA classification	12 $\mu$ s	181.25 ms (2 900 000 clock cycles)

unit length will be stored as  $\mathbf{w}_{cal}$ , finishing the calibration phase. In case the weight vector length increases to big values during calibration, the learning rate  $\gamma$  is halved by multiplying with 0.5. If the weight vector still does not converge, the weights are reset and the calibrating process is restarted. This assures that the SLP weights are kept in reasonable boundaries and the whole structure remains responsive to the next possible strobe of clean beats.

When the calibration is finished, the learning rate  $\gamma$  is set to four times its initial value, which significantly increases the sensitivity of the neural network. It should be stressed, that this reflects one of the key mechanisms of the presented approach. As deformed beats will now have a very strong impact on the weight update, the weight length difference

$$\| \|\mathbf{w}_1(k)\| - \|\mathbf{w}_{cal}\| \| > \theta \quad (4.18)$$

serves as a proper measure of the estimated signal quality. The smaller  $\theta$  is chosen, the more conservative OPRA will classify as even subtle changes of the weight update (caused by subtle deviations of the beats' morphology) will exceed the given threshold  $\theta$ .

### ***Computational complexity***

For debugging and testing purposes, the depicted algorithm was implemented in MATLAB (MathWorks, Natick Massachusetts, MA, US) as well as in object oriented Java using 64-bit floating-point operations. Further, a 16-bit fixed-point C language implementation of OPRA was developed for the battery driven sensor hardware introduced in section 3.4.2 in order to support real-time applications during active measurements. Table 4.3 gives an overview of the corresponding execution times. Note that each sample is checked as a possible onset candidate, which is the reason why the onset detection function is called every 2 ms, when the sampling frequency is configured to 500 Hz. Only when a new beat was successfully extracted, the OPRA classification function containing the two stages as depicted in figure 4.9 will be called, which is expected once a second depending on the underlying heart rate.

The execution times of the Java implementation were measured using built in timing modules provided by the native java class *System*. The measurements were conducted on a

desktop computer equipped with 8 GB RAM and a Intel(R) Core(TM) i7-3770 CPU clocked at 3.4 GHz. Concerning the  $\mu\text{C}$  firmware implementation, clock cycles of the assembled program were counted allowing an exact determination of the execution time. In its final implementation, the  $\mu\text{C}$  program requires 512 bytes of RAM and fits to a 1 kB text segment in ROM when built with the TI MSP430 compiler v.4.1.9 [301].

#### *Initial convergence during OPRA calibration phase*

During the calibration phase, the underlying neural network structure adjusts its weights to find a local optimum as explained in section 4.3.2.1. This crucial process usually lasts several epochs and determines the length of the calibration phase, which is measured in number of beats  $n_{cal}$ . To determine the duration of an average calibration period, several test measurements were analyzed. Therefore, the true EVs were computed by means of singular value decomposition using hand selected datasets where no artifacts were present. These eigenvectors will be used as reference vectors and are compared to the weight vector yielded by the SLP structure, which is applied on the same dataset.

Convergence is again assumed to be achieved, when the Euclidean distance of the first weight vector and first SVD computed EV is less than 0.1 %. Table 4.4 provides an overview of the convergence times of 20 records drawn from the rBSN database. As the weights are randomly initialized each time OPRA is started, the values  $n_{cal}$  slightly vary when the procedure is applied on the same dataset twice. Therefore, ten test runs were started on each dataset to provide a (mean  $\pm$  STD) value. The results from table 4.4 show that a calibration routine is expected to be finished within 60 seconds, if there are enough clean beats.

#### *Dynamic SLP creation to track varying pulse wave morphologies*

Given the previous algorithmic description, OPRA is able to sort out beats with deviating second order statistics by evaluating the estimated first eigenvector. However, changes in the EV approximations are not only provoked by artifacts but also by physiologically clean beats with different underlying morphological features. This aspect is also illustrated in figure 4.8 where the first eigenvectors of the corresponding clean beats from the four subjects (green lines in third row plots) show clearly different patterns. This naturally leads

**Table 4.4:** Analysis of number of beats needed for successful OPRA calibration on clean datasets. Values are averaged over 10 calculations on the same dataset. This is done because the neural network is initialized with random weights, resulting in slightly varying calibration lengths. The mean calibration period lasts 41 beats.

#	$n_{cal}(\text{beats})$	#	$n_{cal}(\text{beats})$	#	$n_{cal}(\text{beats})$
1	$37.3 \pm 15.03$	8	$28.4 \pm 26.13$	15	$34.9 \pm 19.89$
2	$31.1 \pm 5.48$	9	$25.1 \pm 19.23$	16	$33.6 \pm 11.29$
3	$24.5 \pm 9.28$	10	$47.2 \pm 16.55$	17	$20.2 \pm 8.56$
4	$40.8 \pm 13.3$	11	$15.0 \pm 25.03$	18	$18.0 \pm 4.99$
5	$35.4 \pm 13.72$	12	$26.7 \pm 11.04$	19	$33.7 \pm 10.05$
6	$41.9 \pm 19.89$	13	$38.2 \pm 17.43$	20	$37.8 \pm 13.13$
7	$31.6 \pm 10.84$	14	$28.1 \pm 7.21$	-	-

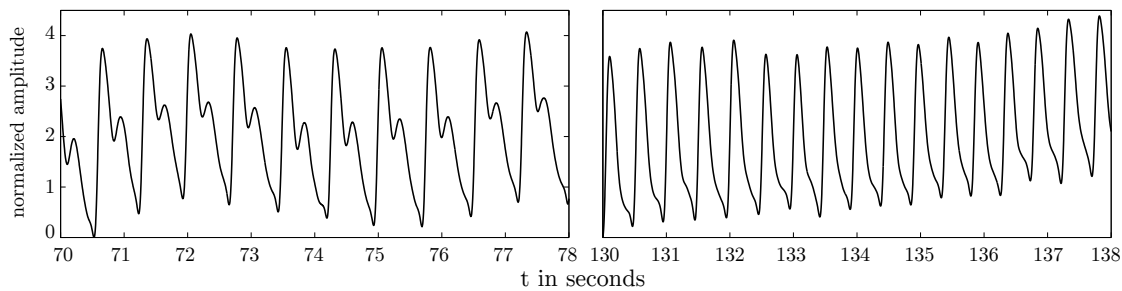


**Figure 4.10:** Good quality PPG signals. *left*) Recording from subject at rest before physical exercise *right*) Recording from same subject at rest immediately after physical exercise. Note that the diastolic notch of the later beats is not as distinct as in the previous ones. However, if no other morphological changes are present these beats are still labeled *PPG\_Quality\_Good*

to problems with changing pulse curve morphologies in a single measurement. Figure 4.10 provides two PPG waveforms recorded from a single subject during one and the same experiment. The left hand side plot shows the PPG where the subject was sitting at rest with normal blood pressure and a steady and slow heart rate. In contrast to that extract, the right hand side shows a PPG trace, which was recorded from the same subject at rest as well, but directly after exercise on a treadmill. Next to a clearly increased heart rate, the PPG morphology has significantly changed with the diastolic notch being almost completely concealed by the systolic peak. This eventually leads to the following behaviour: The initial OPRA SLP will converge after processing the first clean beats as shown on the left of figure 4.10. In the second period as is depicted on the right however, OPRA encounters clean but morphologically different beats where it is likely to assign the label *PPG\_Quality\_Bad* due to the altered shape.

This issue is solved by a dynamic SLP reinitialization strategy every time a beat is classified as corrupt. Only if this additionally created SLP does not converge towards a different EV, the beats under test are indeed likely to be corrupt, confirming the previous classification choice.

The whole idea is demonstrated by another example given by figure 4.11. In this situation, OPRA has successfully trained an initial SLP1, which has been added to a special 'primary' SLP list. Next, at  $t=9$ s, the signal is heavily disturbed, leading to a significant EV update and negative classification output in accordance to the mechanisms discussed earlier. This in turn triggers the above mentioned initialization of a 'secondary' SLP2. In case of enduring artifacts, this SLP2 would not converge and can be dismissed, confirming the presence of a noisy period. In case of a short signal distortion as is the case in the given example, the secondary SLP2 converges on the following clean part (probably between  $t=12$ s and  $t=20$ s). In this case, it is very likely that the SGA procedure will approximate the same stationary point as SLP1 since the PPG morphology has not changed. Thus, the new weight of SLP2 equals the weight of SLP1, so that it will be dismissed too as it only bears redundant information.

primary SLP List:

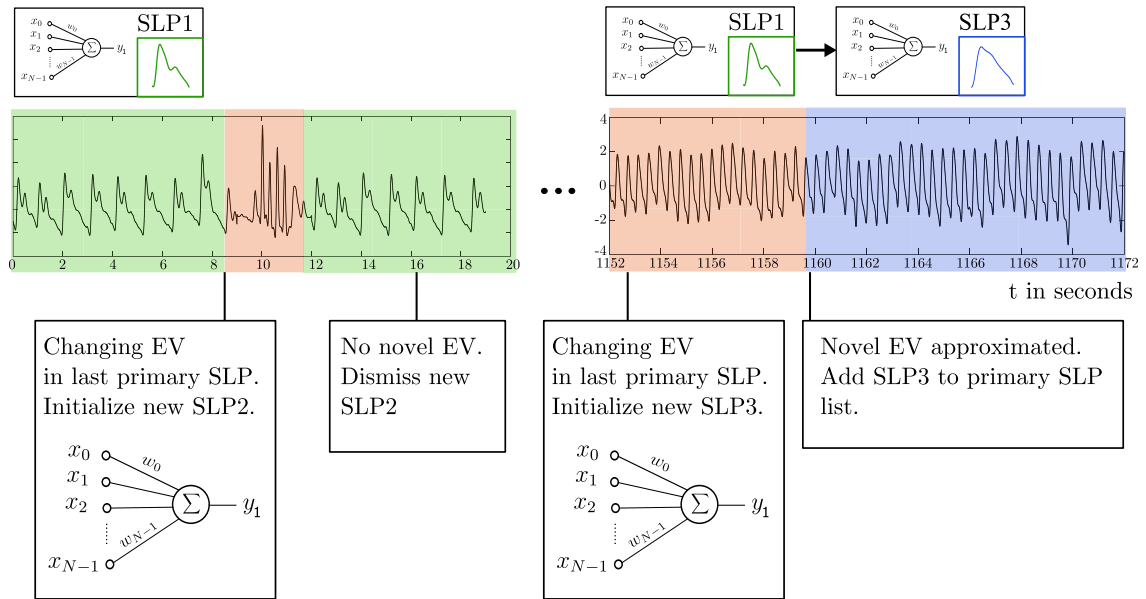


**Figure 4.11:** Multi SLP approach to learn different PPG morphologies. *left*) OPRA has trained an SLP which represents the first EV of clean beats as shown in the green shaded areas. At  $t=9\text{s}$ , the signal is distorted leading to significant changes in the weight update. The underlying beats are going to be classified as *PPG\_Quality\_Bad*. Moreover, a secondary SLP2 is initialized to start a new learning process. However, the corresponding weights do not converge on the short noisy signal extract, but they approximate the same stationary point on the following clean part with unchanged PPG beat morphology so that the secondary SLP2 is dismissed. *right*) The PPG morphology has changed, leading to negative classifications by the first primary SLP1. Again, a new secondary SLP3 is initialized but this time it converges to a novel different EV. In this case, OPRA has learned a novel beat type and the secondary SLP3 is added to the primary SLP list.

Suppose now that the PPG morphology changed during the measurement, as happened in the current case on the right hand side of figure 4.11. Again, this will lead to a change of the first EV approximation, resulting in a secondary SLP initialization (SLP3). This time, the secondary SLP3 converges to a different EV that is currently represented by the weights of the primary SLP1 and it is argued that the corresponding beats (although embodying a different shape) are of good quality as well. In this very situation, OPRA has learned a new beat type, and the secondary SLP3 is added to the primary SLP list. It is stressed again that the primary SLPs represent eigenvectors of valid and clean PPG beats. Therefore, the final classification performs a simple disjunction of the primary SLP outputs: As soon as a single primary SLP provides a positive output, the label *PPG\_Quality\_Good* will be assigned.

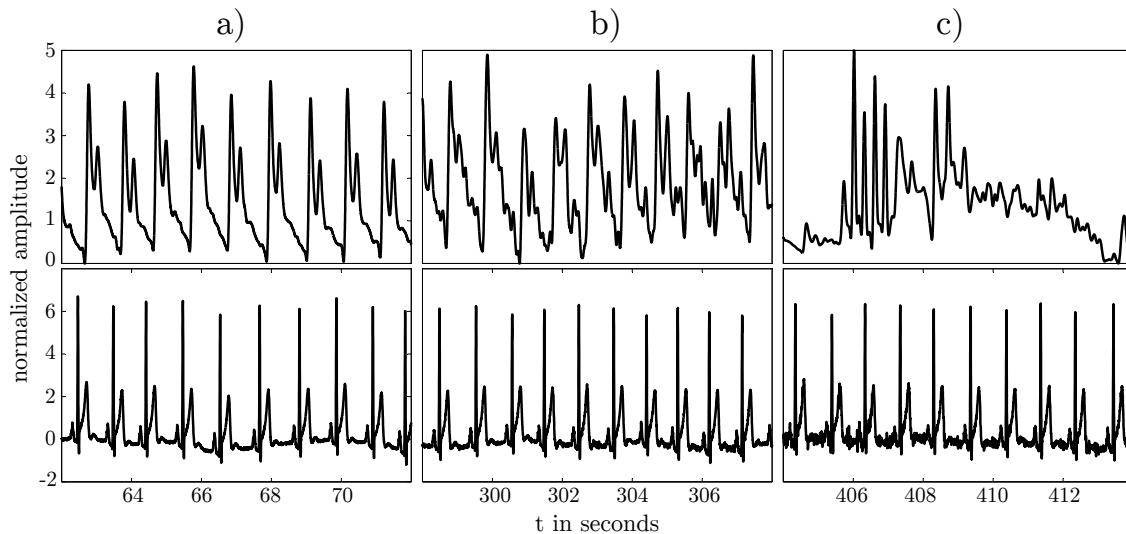


**Figure 4.12:** PPG signals with varying signal quality (*top*) and corresponding ECG Einthoven II reference signal (*bottom*). *a)* Subject at rest with no present artifacts, PPG embodies well distinguishable morphological features. *b)* Subject was walking on a treadmill. Signal quality is already degraded, but applications like pulse rate detection or oxygen saturation might still be possible. *c)* Completely distorted PPG signal during hand shaking experiment. PPG is likely to have lost any cardiovascular information.

### 4.3.3 Performance Evaluation

Testing an algorithm’s signal quality classification performance on a beat to beat basis is not a straightforward task, as the majority of performance measures evaluate the deviation of the algorithm’s output with respect to a given annotation. Especially with reference to the PPG, the annotating process enormously depends on the application as is indicated in figure 4.12. Clearly, the PPG shown in the left plot provides an impeccable waveform in contrast to the PPG on the right, which should be undoubtedly discarded for any further processing or evaluation. Unfortunately, such obvious decisions cannot not be made in many situations. Plot b) in figure 4.12 serves as a typical example, where a proper binary classification into good or bad would depend on the specific application. A pulse rate variability analysis might be difficult but still possible, whereas the signal no longer seems suitable for a detailed morphological analysis to derive stringent cardiovascular features. For that reason, inter-rater disagreements are expected when blindly annotating given PPG datasets.

The performance of the OPRA approach is carefully evaluated on the datasets that were presented in section 3.5. With respect to the underlying signal quality, the following definitions were used to guide the PPG annotation procedures of this work.

**PPG\_Quality\_Good** A good beat is regarded as a pulse segment separated by two consecutive onsets without notable morphological distortions. That is, each beat should be similar to adjacent ones and the peak must be clearly distinguishable inside the given interval. Good beats also require a doubtless identification of dicrotic notches, whenever

they are expected. Note that during physical exercise or specific postures the reflected wave might be hidden by the systolic upstroke, as was the case in the example given in the right plot of figure 4.10. In that case the PPG is also considered to have a good signal quality.

***PPG\_Quality\_Bad*** Motion artifacts constitute the most prominent indicator for insufficient beat quality. In the first place, bad quality beats are identified by abnormal changes of the pulse wave contour where the cardiac cycle containing the systolic and diastolic phase is not clearly visible anymore. Abrupt changes of signal amplitudes are also treated as artifacts as well as segments containing ambiguous peak or onset positions. Beats with disproportional dicrotic notches, which are commonly provoked by external forces, are also sorted out.

A common way to assess the quality of a binary classifier given an annotated ground truth involves the analysis of popular statistical metrics such as sensitivity and specificity. Basically, the most relevant measures are derived by a so-called coincidence matrix, which relates the predicted outcome of a classifier to the true underlying class by counting single output events [208]. In the case of a binary classification decision, one has to define which event marks a positive and which constitutes a negative test decision. With respect to the OPRA labels *PPG\_Quality\_Good* and *PPG\_Quality\_Bad*, either combination will make sense and the latter will be chosen as a positive event in the following evaluations. Literally speaking, the test output *PPG\_Quality\_Bad* will be understood as a positive event when the reference annotation also declares class *PPG\_Quality\_Bad*. With that definition, figure 4.13 depicts a coincidence matrix matching the present beat quality scenario along with some of its most frequently derived metrics.

The true positive rate (TPR), which is also referred to as the sensitivity, is a very crucial measure, as it represents the percentage of all truly corrupted beats that were correctly identified by the classifier under test. The majority of PPG processing applications relies on a robust detection of corrupted beats, which is the reason why providing high TPR values is the major requirement that needs to be fulfilled by the applied discriminator. Whereas high TPR values could be easily achieved by assigning the label *PPG\_Quality\_Bad* in a very lavish manner, this would directly counteract the false positive rate (FPR), which corresponds to the percentage of clean beats that were erroneously declared as corrupted. This metric is also known as probability of false alarm (or fall-out) and is directly related to the specificity of the classifier, which is defined as  $1 - \text{FPR}$ . Accordingly, low FPR values (and consequently a high specificity) are desirable because the lower the specificity, the higher the rate of unnecessary signal discards will become. More backgrounds on further evaluation metrics can be found in [180, 208].

Next to the evaluation of these theoretical metrics, one would like to monitor the performance of a specific method operating in a real life situation. The idea is to assess the classification by its capability to provide segments, which are suitable for physiological parameter extraction. With reference to PPG signal quality estimation, a simple pulse

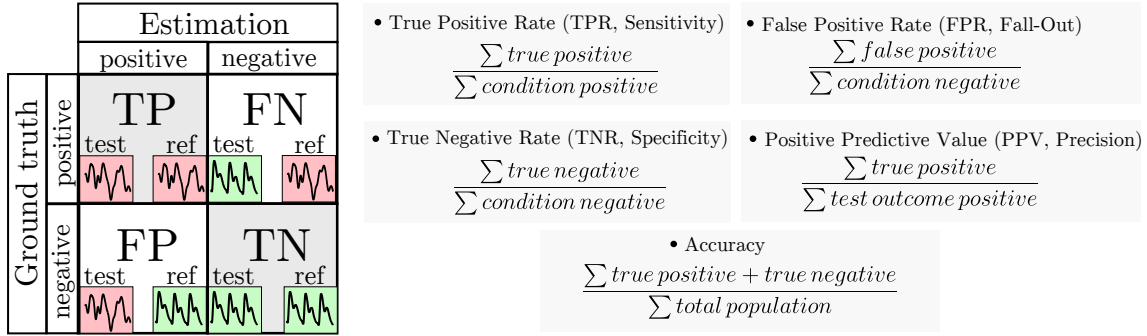


**Figure 4.13:** Interpretation of the PPG quality related coincidence matrix along with some of its derived performance metrics. A correctly classified corrupt beat will be counted as *true positive* whereas a correctly classified clean beat is considered as *true negative* throughout the entire evaluations.

rate extraction already poses an attractive option to reveal the potency of the method under test. As all considered datasets provide at least one reference ECG channel, the true heart rates can be derived by the corresponding RR intervals, which are then compared with the calculated pulse rates from the respective PPG extracts. It is argued that a well performing signal quality detector will only approve clean PPG segments, leading to an undistorted delineation process with accurate pulse rate values. Thus, low pulse rate/heart rate errors are expected, which should be as low as  $\pm 1.1$  beats per minute (bpm) [25, 84, 172, 274].

As mentioned earlier, OPRA classifies a beat by spanning an interval from onset to onset whereas the reference annotations can cover arbitrary lengths. Thus, the respective classification output is tested by evaluating the peak position of every single beat in all evaluations. The next two subsections present further details of the conducted performance evaluation, which incorporates an assessment of the OPRA implementation itself as well as a quantitative comparison to other works.

#### 4.3.3.1 OPRA Parameter Trimming

A major advantage of the OPRA approach is promoted by its simple mechanism to adjust the underlying classification behaviour controlled by the single parameter  $\theta$  (cf. eq. (4.18)), which allows for configurations ranging from a very conservative to a more liberal orientation. The following analysis gives an idea of the impact of changing values of  $\theta$ , demonstrated in repeated classification runs.

The upper left plot in figure 4.14 (1) shows multiple TPR (*sensitivity*) and FPR ( $1 - \text{specificity}$ ) measures, resulting from a stepwise increase of  $\theta$ . This kind of graphical plot is a well established illustration known as receiver operating characteristic (ROC). It serves as a valuable tool to contemplate costs and benefits in dependence of a specific discrimination parameter. A perfect classifier would yield points in the upper left corner representing maximum TPR and minimum FPR values whereas outcomes near the diagonal area are

tantamount to pure chance. Each point in the present ROC curve was calculated on a single record drawn from the PhysioNet database *challenge2015* and is color encoded according to a particular value of  $\theta$  as given in the legend. It can be seen that for values of  $\theta = 0.001$  (orange dots), promising results with true positive rates in the mid 90s and false positive rates centered around 15% are achieved. It is further noted that sporadic outliers are only found at increased FPR rates, but still retain high TPR measures, which is favorable as one would rather skip a beat in ambiguous cases. Table 4.5 lists the most important performance statistics for the varying  $\theta$ , advocating a choice for  $\theta = 0.001$ , with a mean sensitivity of 92% that does not fall below 87% for the entire dataset. The other two canvases of figure 4.14 depict the performance in practical situations. The upper right part demonstrates the impact of signal quality estimation during automatic pulse rate extraction. The records of the PhysioNet database are represented in figure 4.14 plot 2a, which depicts pulse rate / heart rate pairs extracted from the entire signal (left hand side) and PR/HR pairs of the same dataset but where corrupted beats have been automatically discarded by the OPRA approach (right hand side). The same was conducted for datasets of the *rBSN\_studentDatabaseI* in figure 4.14 plot 2b. One clearly recognizes the positive effect of the prior beat discrimination on the pulse rate estimation process, as the majority of outliers is sorted out, yielding reasonable physiological outputs again. To get an impression of the discrimination procedure itself, the third canvas at the bottom of figure 4.14 shows two processed signal extracts classified by OPRA.

#### 4.3.3.2 Performance Comparison

Having discussed the properties of the novel OPRA signal quality estimator and its general classifying performance, it is now time to deal with a scrutinizing analysis, challenging the earlier introduced methods from literature. In the scope of this study, the three most promising works were considered in the following evaluation, including the journal publications from Li and Clifford [165], Sukor et al. [292] and Karlen et al. [132]. The remaining proposals have been ignored in the current analysis, due to their shortcomings discussed in section 4.3.1. Objectively comparing different signal quality implementations is not an easy task, especially as one requires the same datasets and reference annotations to conduct a fair evaluation. Secondly, the sources of published methods are generally not available, which further impedes fast and accurate discrimination tests. Moreover, pulse wave signal quality annotations are not as widespread as ECG relating annotations for example, which might explain the lack of studies concerning themselves with comparative evaluations. The two approaches published by Li and Clifford [165] and Sukor et al. [292] were reimplemented to the best knowledge and belief whereas the authors of the working group around Karlen et al. [132] were nice enough to provide the classification outputs for the records considered in this work (except for the *Vasoscreen* database).

It should be noted, that the configuration of the both reimplemented methods was carefully optimized for each database prior to their application. The first method by Sukor et al. [292] demanded a proper adjustment of the six threshold values (cf. figure 4.5 B)), which directly

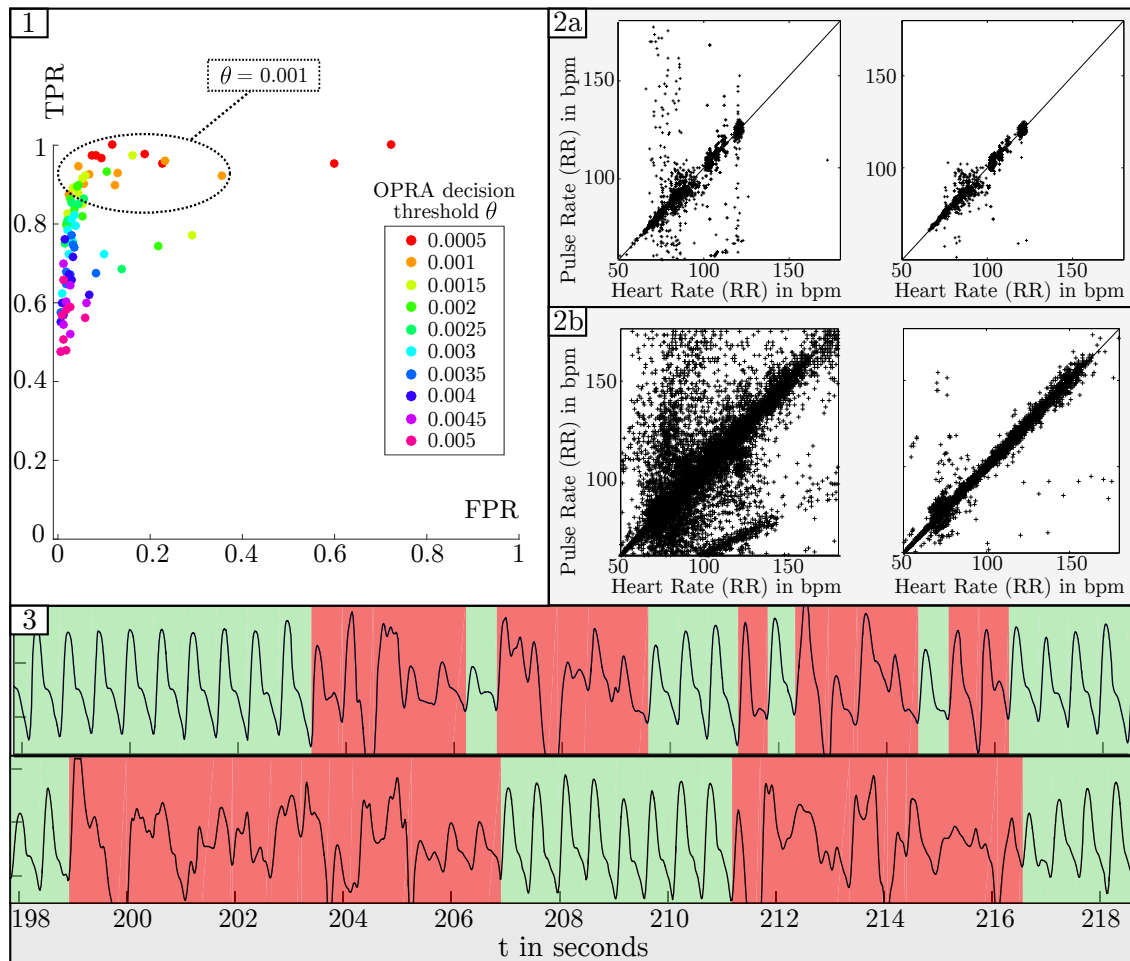


**Figure 4.14:** *1)* ROC curve plot for different values of  $\theta$ . A good trade-off between very high TPR values and rather low FPR values is found for values around  $\theta = 0.001$ . *2a)* Heart rate / pulse rate errors before (*left*) and after automatic signal quality detection (*right*) evaluated on records drawn from the PhysioNet database *challenge2015* and on records drawn from the *rBSN\_studentDatabaseI* (*2b)* *bottom*) Example classifications on extracts taken from the PhysioNet database.

determine the decision output in the classification tree. This turned out to be a tedious task, due to the changing nature of the signals (numerous patients, different hardware settings and diverse environmental conditions), but was necessary to achieve reasonable operation. The multilayer perceptron applied in the method of Li and Clifford [165] was also pre-trained on each database, using 40% of the annotated beats.

Table 4.6 summarizes the performance metrics for the considered methods derived from their outputs on the four different databases. First, one recognizes perceptible performance fluctuations among the single datasets. One reason for this phenomenon can be explained by the individual compositions of the signals, where heavily corrupted extracts with sporadic clean parts (as is the case in the *rBSN\_studentDatabaseI*) are much harder to discriminate than clean records with occasional disturbances. As discussed before, the TPR measure constitutes the most crucial performance measure, that is required to maintain high percentages values without exception. A classifier yielding low TPR values would

**Table 4.5:** OPRA classification performance on annotated PhysioNet data records with respect to increasing values of  $\theta$ . A value of 0.001 seems a good choice, with TPR values around 92 % along with an expected fall-out rate of 11 %. The column  $\min(\text{TPR})$  represents the minimum TPR value among all records of the considered database.

$\theta$	TPR $mean \pm STD$	FPR $mean \pm STD$	$\min(\text{TPR})$	$\max(\text{FPR})$
0.00025	$0.978 \pm 0.027$	$0.382 \pm 0.323$	0.925	1.000
0.00050	$0.971 \pm 0.035$	$0.289 \pm 0.290$	0.900	0.772
0.00075	$0.952 \pm 0.030$	$0.167 \pm 0.152$	0.900	0.473
0.00100	$0.922 \pm 0.039$	$0.120 \pm 0.098$	0.874	0.313
0.00125	$0.898 \pm 0.042$	$0.110 \pm 0.104$	0.848	0.327
0.00150	$0.871 \pm 0.069$	$0.089 \pm 0.097$	0.775	0.301
0.00175	$0.867 \pm 0.061$	$0.080 \pm 0.080$	0.771	0.257
0.00200	$0.853 \pm 0.053$	$0.067 \pm 0.065$	0.762	0.213
0.00225	$0.814 \pm 0.059$	$0.055 \pm 0.054$	0.743	0.180
0.00250	$0.804 \pm 0.046$	$0.047 \pm 0.047$	0.748	0.159

miss many corrupt beats and is not applicable in any practical situations. It is noticed that apart from a few single cases, all four methods provide reasonable TPR values around 90 % on the four databases, with the OPRA method being the most stable approach that closely wins on each set of records. However, there are major differences when it comes to the evaluation of the respective FPR values. Sukor’s reimplemented classifier dismisses the biggest portion of actually clean beats (sometimes around 50 %), whereas the Li-Clifford and OPRA discriminators provide convincingly small percentages of inadequately discarded beats. The different nature of the respective databases becomes clear when inspecting the resulting heart rate / pulse rate errors, which vary from low deviations of  $\pm 2$  bpm in the clinical datasets to rather high discrepancies of up to  $\pm 50$  bpm in the laboratory student database. Be aware that the low precision values encountered in the assessment of the *Vasoscreen* database can result from the rather small proportion of corrupted beats, where already a few false positives lead to a significant decrease of the positive predictive value.

## 4.4 Ectopic Beat Detection

As was thoroughly discussed in the previous sections, pulse wave analysis relies on the detection of fiducial points to track even minor timing variations. This is the reason why signal quality analysis, artifact handling, and movement detection play such an important role, and are mandatory prior to the application of sophisticated processing methods. Next to these external influences, pathophysiological factors also need to be considered, especially in an unsupervised processing chain. With reference to pulse arrival time and pulse transit time calculations, one would like to assure that the underlying cardiovascular mechanisms were caused by a regular physiological process, which itself

**Table 4.6:** Performance overview resulting from the introduced comparative study. The discrimination output of the most promising signal quality proposals from literature were considered, including the work of Sukor et al. [292], Li and Clifford [165] and Karlen et al. [132]. The former two were reimplemented, whereas the authors of [132] provided the corresponding output sequences for the considered records (except for the *Vasoscreen* database). The following assesment is based on the performance metrics true positive rate (TPR), false positive rate (FPR), precision (PRC), accuracy (ACY) and heart rate / pulse rate errors (HPE).

	PhysioNet Database					rBSN_studentDatabaseI				
	TPR	FPR	PRC	ACY	HPE	TPR	FPR	PRC	ACY	HPE
OPRA	0.92	0.13	0.71	0.89	8.82	0.87	0.23	0.80	0.82	29.14
Sukor [292]	0.92	0.25	0.52	0.79	10.92	0.78	0.55	0.64	0.64	47.40
Li [165]	0.90	0.07	0.82	0.93	8.94	0.86	0.39	0.70	0.76	33.31
Karlen [132]	0.90	0.27	0.51	0.78	7.40	0.87	0.35	0.74	0.77	31.85
	rBSN_clinicalDatabaseI					Vasoscreen Database				
	TPR	FPR	PRC	ACY	HPE	TPR	FPR	PRC	ACY	HPE
OPRA	0.87	0.14	0.39	0.87	1.63	0.93	0.25	0.28	0.78	2.38
Sukor [292]	0.81	0.45	0.21	0.57	2.8	0.94	0.53	0.18	0.48	0.51
Li [165]	0.85	0.19	0.31	0.82	1.62	0.90	0.37	0.26	0.77	2.21
Karlen [132]	0.91	0.29	0.29	0.73	1.62	-	-	-	-	-

resulted from an undisturbed propagation of the electrical wavefront in the myocardium (cf. section 2.1.1).

Ectopic beats (also known as extrasystoles) are a primary source for causing irregularities in the electrical activity of the cardiac cycle, which are known to hamper cardiovascular investigations and should therefore be excluded from further processing in methods such as heart rate variability (HRV) analysis or PWV applications.

One very prominent field of application, which is, in turn, directly affected, involves various approaches aiming to solve the problem of continuous blood pressure estimation as introduced in section 2.2.

A very interesting survey on that topic was recently published by Buxi et al. [30], who depict the basic underlying mechanisms, list current approaches and achievements and also critically highlight open aspects and unsolved issues. The issue of ectopic beats is underlined as an unaddressed problem in PAT/PTT detection, which has motivated the efforts of this work and will be the focus of the present subsection. The majority of the following results were recently published in [225] and are complemented by additional background information presented next.

This section starts with a short introduction on the backgrounds of extrasystoles and discusses currently published ectopic beat detectors. Finally, a novel multimodal detection approach is presented, which was developed to support PAT/PTT applications considered in this work and shows significant advantages when exploiting features derived from both, PPG and ECG signals.

Ectopic means *out of place* and originates from the word *ektopios* in ancient Greek language. Ectopic beats are heartbeats, which are not caused by normal sinus node paces,

**Table 4.7:** Different types of heartbeats according to AAMI [74]. This standard discriminates the most common heartbeat types in cardiology into five superclasses.

AAMI class	description	heartbeat types
N	not in AAMI class S, V, F or Q	normal beat, left bundle branch block beat, right bundle branch block beat, atrial escape beats, nodal (junctional) escape beat
S	SVEB	atrial premature beat, aberrated atrial premature beat, nodal (junctional) premature beat, supraventricular premature beat
V	VEB	premature ventricular contraction, ventricular escape beat
F	Fusion beat	fusion of ventricular and normal beat
Q	Unknown beat	paced beat, fusion of paced and normal beat, unclassified beat

but by an electrical potential located somewhere else, referred to as the *ectopic focus*. The physiological backgrounds of ectopic beats have been subject to decades of research with accepted understandings and detailed definitions that can be found in basic ECG literature [173].

As was briefly discussed in section 2.1.1, one generally distinguishes between supraventricular ectopic beats and ventricular ectopic beats according to the origin of the ectopic focus. SVEBs have their origin above the atrioventricular node, occasionally leading to a distorted P-Wave but otherwise morphologically normal QRS complex, as the electromechanical propagation occurs regularly through the AV node. VEBs on the other hand may arise from any spot within the cardiac muscle and spread through the myocardium in an abnormal manner. The most obvious observations associated with VEBs are a missing P-Wave, an early, malformed QRS complex and a compensatory pause as a result of the refractory state of the chambers after the ectopic beat [173]. The modified QRS complex is often broader and yields a higher amplitude and energy.

The Association for the Advancement of Medical Instrumentation (AAMI) committee released a standard to classify the most common heartbeats into one of the five categories listed in table 4.7 [74].

Whereas strobos of SVEBs and especially VEBs have a perceptible impact on the cardiac output and can develop to life threatening tachycardias, sporadic occurring extrasystoles usually do not play a significant role and can be considered as a harmless myocardial event that is also experienced in the healthy subject [148]. With respect to automatic signal processing methods on the other hand, even single ectopic beats can indeed have a crucial influence that needs to be accounted for, especially when tight heart rate timings are involved. This is not only a serious issue in heart rate variability analysis, but also in further applications depending on reliable fiducial point detection, including pulse transit time and pulse arrival time investigations. Figure 4.15 depicts the effects of premature ventricular beats on synchronized ECG-PPG recordings. Due to the early contraction, the

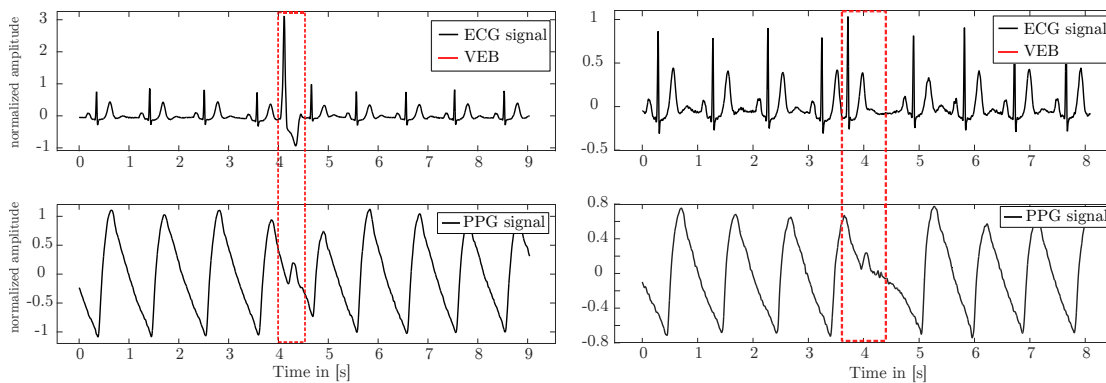


**Figure 4.15:** Synchronized ECG (Einthoven II) and PPG waveforms. *left*) Single premature ventricular ectopic beat at  $t=4s$ , *right*) Single premature supraventricular ectopic beat at  $t=3.8s$ . Both types of extrasystoles have a significant impact on the morphology of the arterial pulse wave, which degrades to a notch-like peak that is hard to distinguish from normal PPG dirotic notches or slight motion artifacts. As a consequence, accurate timing considerations including pulse arrival time extraction are seriously hampered.

left ventricular output volume is significantly decreased, resulting in a comparatively small premature pulse wave peak. Unfortunately, automatic delineation approaches, like the commonly applied peak detector according to Zong et al. [355], fail in reliably locating those ectopic pulse wave notches, which becomes even harder - if not impossible - in slightly noisy periods. These visual impressions confirm the concerns mentioned before and underline the need for ectopic beat detection, especially in unsupervised PAT/PTT applications.

#### 4.4.1 Established Ectopic Beat Detection Approaches

Automatic ectopic beat detection - or more generalized, heartbeat classification - has been subject to research for several decades with literature providing an astonishing variety of ECG beat discrimination proposals. This section provides an overview of the most influential approaches and identifies common elements.

Early approaches based on ECG morphology applied the underlying pattern recognition techniques directly on the sampled datapoints around the delineated QRS complexes. This strategy yields good results in distinguishing beats of different morphology, as is the case in normal heartbeats and VEBs. In 1992 Chow et al. proposed a method for detecting VEB in two-lead ECG recordings, which is based on this direct sampling method in combination with a backpropagation artificial neural network (ANN) for the classification task [39]. When trained on data of the same patient, a sensitivity of 97.39% was reported, along with a positive predictivity of 93.58%.

Clifford et al. further elaborated upon this idea in around 2000 and published related approaches, where the focus was set on learning patient-specific ECG morphology with auto-associative neural networks [42, 43].

A very comprehensive work was proposed by Martis et al. [177] in 2013. The authors, just like their predecessors, cut a window of fixed size around every R-Peak. The single extracts are then filtered using wavelet analysis. To reduce the dimensionality of the feature space, different methods, including principal component analysis, independent component analysis (ICA) and linear discrimination analysis (LDA), have been considered. Thereafter, the reduced feature vectors were classified by support vector machines (SVM), ANN and probabilistic neural networks (PNN). The best performance was achieved with the combination of ICA and PNN. The results for specificity, sensitivity, accuracy and precision are all above 99 %, tested on the MIT-BIH database (Massachusetts Institute of Technology - Beth Israel Hospital), but the underlying random 10-fold evaluation scheme does not consider generalisation across patients.

More recent methods usually rely on a combination of features including signal amplitudes and time intervals, statistical measures and more abstract features. The work from Chazal et al. [53] introduces a set of morphological features, which were later used and extended by many other researchers. The noise reduced ECG signal is first delineated to determine relevant fiducial points including on- and offsets of QRS-, T-, and P-Waves of each heartbeat. Next, the feature extraction stage calculates intervals and amplitudes at different points of the heartbeats. These features are then processed by two LDA classifiers, whose outputs are combined to get the resulting membership function. The reported accuracy of 84.5 % on the MIT-BIH database is competitive, as they used data of different patients for training and testing the algorithm.

Some of these features were taken up by Sadiq and Khan in 2011 [267]. Resorting to only 9 morphology and interval features, they calculate membership functions and classify the heartbeats with a neuro-fuzzy ANN. The reported results of 95 % specificity and an average sensitivity of 91.17 % for SVEB and VEB beats on the MIT-BIH database are quite impressive, as they did not evaluate their classifier on data of known patients.

Whereas the majority of ectopic beat detection is based on ECG processing as the methods listed above, one also finds proposals that incorporate different signals such as the PPG. One example is the work of Solosenko et al., who dealt with the detection of ectopic beats by evaluating features derived from PPG recordings only. Two of their works target VEBs with an approach based on temporal features and variance [287] or power ratios [288] of the PPG signal after automatic artifact removal. Using an ANN for the classification, a final sensitivity and specificity above 92.4 % and 99.9 % are achieved respectively. Another approach by Solosenko et al. proposes a set of simple, temporal and amplitude based features in combination with a naive Bayes (NB) classifier to detect both, VEBs and SVEBs [286]. The resulting performance of 96.4 % sensitivity and 99.92 % specificity is astonishing and should be interpreted with care. The algorithms are evaluated on data drawn from the MIMIC and MIMIC II databases (Multiparameter Intelligent Monitoring in Intensive Care) as well as data obtained from clinical studies and with respect to unknown patients.

Drijkonigen et al. dealt with the transferability of ECG heartbeat interval features to PPG signals, recorded with a smartphone camera for ectopic beat discrimination [57]. By evaluating the peak to peak intervals within a single window, they successfully detected artificially induced supraventricular ectopic beats.

While it was demonstrated that ectopic beats can be detected from different signals, there has been little effort on multimodal approaches to the problem.

One work was proposed by Palaniappan et al. in 2004, who utilised a set of derivative based features from ECG and arterial blood pressure signals, which were then presented to a backpropagation multilayer perceptron (MLP) for classification [211, 212]. The not further specified classification performance of 96.47% on the MGH/MF database (Massachusetts General Hospital/Marquette Foundation) seems promising, although the evaluation scheme is not described in depth.

To sum up this short excursion into ectopic beat detection, table 4.8 summarizes the key attributes of related works researched in the scope of this thesis.

The novel beat detection algorithm proposed in the next subsection adopts the general structure of the above presented approaches, including the steps of delineation, feature extraction and classification, with the help of a properly trained architecture. In the first place, it was developed to support BPE applications, ideally yielding reasonable performance on different patients without prior per-patient training. Since PWV analysis applications have access to synchronized ECG and pulse wave signals anyway, the presented ectopic beat discrimination method derives features from both signals, similarly to the multimodal ABP-ECG method published by Palaniappan [211]. As ABP signals are typically measured invasively and require trained medical staff as well as sterile conditions, the proposed PPG-ECG approach provides an interesting, non-invasive and non-occlusive alternative to extract pulse wave related parameters and corresponding timings in ambulatory settings.

Table 4.8: Literature overview of automatic ectopic beat detection methods.

Main Author	Output Classes	Classification inputs	Classifier	Sensitivity	Specificity	eval
Chazal [53]	AAMI types	RR interval, ECG morphology	LDA	76.8	97.0	cross
Chazal [52]	SVEB, VEB, N	RR interval, ECG morphology	LDA	80.55	96.85	cross
Chow [39]	VEB, N	samples around R-Peak	ANN	97.39		same
Clifford [42, 43]	VEB, N	samples around R-Peak	ANN			same
Gomez-Herrero [90]	VEB, N	PCA derived	LDA	98.88	97.73	
Hamilton [98]		RR interval, template match, dominant type	LD	93.2		cross
Jokic [123]	VEB,SVEB, N	T,P, QRS model based	ANN	93.39	96.04	same
Karraz [133]	5 beat types	RR interval, ECG morph	ANN	96.26	95.86	
Leutheuser [162]	Path I, Path II, N	ECG stat, ECG morph	LR,NB,SVM,PART, C4.5		81.22	same
Lin [166]	SVEB, VEB, N	RR interval, ECG morph	LDA	85.6		
Llamedo [170]	VEB,SVEB,N	RR interval, ECG morph	LD	68		cross
		WT subband morph				
Palaniappan [211, 212]	VEB, SVEB, N	RR int, ECG morph, ABP stat, ABP morph	ANN			
Rabee [242]	14 beat types	Wavelet (WT) coefficients	SVM	95.95	100	same
Sadiq [267]	SVEB, VEB, F, N	RR interval, ECG morph	ANN	91.17	95	same
Wiens [335]	VEB, N	RR int, WT coeff, template match	SVM	96.2	99.9	same
Martis [177]	AAMI types	ICA, PCA	SVM, ANN, PNN			same
Drijckoningen [57]	SVEB, N	PPG int	LD			cross
Solosenko [286]	VEB,SVEB, N	PPG int, PPG power	NB	96.4	99.92	cross
Solosenko [287]	VEB, N	PPG int, PPG power	ANN	95.71	99.83	cross

#### 4.4.2 A Novel Multimodal Ectopic Beat Detection Method

In the scope of this work, a novel ectopic beat detection approach based on multimodal PPG and ECG features is proposed to clean ambulatory data records from extrasystoles for subsequent PAT/PTT analysis. Due to the well established understandings of extrasystoles, that to some extent also provide exact definitions regarding the properties of a single ectopic beat, supervised classification approaches seem a very convenient method to tackle the final discrimination procedure.

Three well known architectures including naive Bayes, artificial neural networks and support vector machines were applied and compared to each other with respect to the respective multimodal EB classification performance. A wide range of features were contemplated as is discussed next.

##### *Feature extraction*

The proposed ectopic beat detection method weighs a number of manifold features from preprocessed single-lead ECG and PPG signals. In order to calculate the features for one heartbeat, the preceding as well as the following ECG R-Peak and PPG pulse wave onset are considered.

The implemented features are partly adopted from other works and are extended by novel proposals, as is discussed next. A complete list of all features contemplated for the presented ectopic beat discriminator is given in table 8.6 of appendix 8.1, from which a final subset will be evolved. For better readability table 4.9 lists the subordinated feature groups. All features are designed to be independent of the absolute amplitude of the input signals and do not need to be normalized with respect to other heartbeats. These properties aim to support a simple and robust on-line implementation that only needs to buffer the signal encompassing three ECG R-Peaks in order to calculate the features for one heartbeat.

First, all R-Peaks are detected using the well known method proposed by Pan and Tompkins [213] whereas the pulse wave peaks are determined by a trivial maximum search between two adjacent R-Peak locations. In the next step, further ECG fiducial points such as QRS on-/offset, P-Wave and T-Wave as well as additional PPG specific locations are determined. QRS onset and QRS offset are detected resorting to the method of Manriquez and Zhang [112]. They calculated an envelope function with the help of the Hilbert transform in order to maximize a corresponding surface indicator  $A(t)$  as given by

$$A(t) = \int_{t-W}^t [env(\tau) - env(t)] d\tau. \quad (4.19)$$

Eq. (4.19) includes an envelope function  $env(t)$  which is defined as

$$env(t) = \sqrt{ECG^2(t) + HT(ECG(t))^2}, \quad (4.20)$$

**Table 4.9:** The various features can be divided into seven groups, based on their target properties. To account for the different markers required for the calculation, subgroups are introduced. A detailed list of all features can be found in table 8.6.

feature #	group #	feature group	required markers
1..5	1a	ECG interval I	R-Peak
6..8	1b	ECG interval II	R,P,T-Peak QRS on/off
9..28	2a	ECG amplitude I	R-Peak
29..30	2b	ECG amplitude II	P,T-Peak
31..42	3	ECG ICA	R-Peak
43..46	4a	ECG sig/stat I	QRS on/off
47..50	4b	ECG sig/stat II	R-Peak
51..56	5	PPG morph	PPG peak, onset
57..79	6	PPG amplitude	PPG peak, onset
80..82	7	PPG sig/stat	PPG peak, onset

where HT represents the Hilbert transform. Manriquez and Zhang reported detection errors (mean  $\pm$  STD) of  $-2.6ms \pm 7.1ms$  for QRS onsets and  $0.7ms \pm 8.0ms$  for QRS offsets respectively, tested on annotated datasets from the PhysioNet QT database [146].

Next, features derived from ECG P- and T-Waves play an important role in most ectopic beat detection approaches. A promising method for T-Wave detection was presented by Elgendi et al. [65] with a performance of 97.14% sensitivity and 99.29% positive predictivity on the QT and MIT-BIH Arrhythmia databases. This method was chosen for P- and T-Wave delineation in this work where the parameters were slightly changed and configured in a way to always output a T- and P-Wave index, regardless of physiological meaningfulness.

It appears obvious that ECG interval based features, such as the RR interval, provide simple but significant information for ectopic beat classification. SVEBs appear earlier than expected (non-compensatory pause) with a longer subsequent RR interval and VEBs introduce a full compensatory pause, which are both well represented by the RR length. Thus, RR related features as combined in group 1a in table 4.9 can be seen as an essential basis. Requiring an accurate R-Peak detection only, they can be reliably extracted and merely involve simple integer arithmetics. A more sophisticated group of features is bundled in group 1b, which demands the more sophisticated delineation procedures to locate P- and T-Waves as well as QRS onsets and QRS offsets. This allows the inclusion of further standard clinical ECG parameters as QT and PQ intervals.

As was repeatedly indicated already, extrasystoles have a significant influence on the ECG morphology. Especially VEBs, with missing P-Wave due to omitted atrial depolarization, additionally show a significantly distorted QRS complex. Thus, amplitude based features are likely to serve as a valuable indicator. The morphology of SVEBs remains almost unchanged, however. The P-Wave often overlaps with the preceding T-Wave, which is accounted for by the features of groups 2a and 2b as well.

Attempting to describe the signals by statistical features like mean, standard deviation or higher order statistics such as skew and kurtosis is also quite common practice in ectopic beat detection [41]. These features are complemented by a measure of power, which is defined by mean squared signal values represented by group 4a and group 4b.

Frequency domain features might also contribute valuable information for VEB/SVEB detection. Resorting to wavelet coefficients from the last 5 levels of a 6 level wavelet decomposition using a Daubechies 2 wavelet was proposed in [335]. In [177], a wavelet transformation is used to investigate signal properties in different parts of the spectrum, where a window of fixed size is cut around the R-Peak and decomposed using a fourth order wavelet transformation choosing a Mayer's wavelet. It is argued, that the 4th level detail (11.25 Hz – 22.5 Hz) and approximation (0 Hz – 11.25 Hz) of the output contain discriminatory information on the heartbeat type. To reduce the dimensionality, independent component analysis is applied which yields six features for both subbands. Corresponding features are found in group 3.

Groups 5 to 7 contain different morphological features derived from the PPG signal only, which were partly inspired by pulse wave analysis procedures including [295].

All derived features are centered (subtract mean) and scaled (unit variance) in order to minimise inter feature and inter subject variability.

### *Classification methods*

As introduced, the given heartbeat discrimination problem is tackled by three well established classification architectures, which were implemented and compared to each other with reference to their EB detection performance. The chosen structures include a simple naive Bayes classifier, a support vector machine and an artificial neural network. The conceptual details are well examined in standard references on pattern recognition or machine learning (e.g. [23]) and therefore will not be discussed completely again.

#### *Naive Bayes*

The naive Bayes classifier belongs to a family of very simple probabilistic classification approaches. Bayes' theorem describes the conditional probability  $P(C_k|\mathbf{x})$  of the class instance  $C_k$  given the feature vector  $\mathbf{x}$ , in terms of the conditional probability of the feature vector  $\mathbf{x}$  belonging to class instance  $C_k$  (i.e.  $p(\mathbf{x}|C_k)$ ), the probability of  $C_k$  (i.e.  $P(C_k)$ ) and the probability of  $\mathbf{x}$  (i.e.  $p(\mathbf{x})$ ) also called likelihood, prior and evidence respectively:

$$P(C_k|\mathbf{x}) = \frac{p(\mathbf{x}|C_k)P(C_k)}{p(\mathbf{x})}. \quad (4.21)$$

In practice, the denominator does not play an important role as it does not depend on the class  $C_k$  whereas the likelihood  $p(\mathbf{x}|C_k)$  is calculated from labeled training data.

#### *Support vector machines*

Support vector machines are widely spread among supervised binary classifiers. In short, one tries to find a linear hyperplane separating the samples of the feature space. This is achieved by spotting so called support vectors, which consist of points having the largest possible margin towards the hyperplane that separates the training data. Also, SVMs often further transform the features into a higher dimensional space to solve nonlinear structures. For the sake of computational complexity, kernel methods are used to calculate the support vectors in the original feature space. The choice of a proper kernel function remains a sensitive topic and also determines the performance of the SVM. Nonetheless, there are some popular kernels such as radial basis functions (RBF) which are often implemented and perform reasonably for a wide range of standard problems [273].

#### *Artificial neural networks*

Artificial neural networks play a very important role in classification techniques and can be applied as unsupervised (cf. OPRA method) or supervised classifiers. Multilayer ANNs in general have been appreciated as universal function approximators [108] making them especially interesting due to their close link to regression and classification. In the supervised context, the backpropagation of error algorithm has gained significant popularity to optimize the weights of the ANN, which then transforms the input space to the output space optimized by means of smallest mean squared error. The basic design considerations involve a proper choice of hidden layers, number of neurons and their specific transfer functions. More in-depth information can be found in [266].

#### ***Performance evaluation***

The preliminary classification results presented in the left plot of figure 4.16 already provide a general idea on the performance of the three classification architectures using the complete multimodal feature set of table 4.9. For the first tests, the ANN was configured as a two layer network with 10 neurons in the first hidden layer, 20 neurons in the second hidden layer, and three output neurons for the classes N, VEB and SVEB. The SVM resorts to an RBF kernel and the naive Bayes classifier was trained to classify into the three types N, VEB and SVEB respectively.

In that configuration and without any prior and further optimization considerations, the ANN turned out to provide the highest sensitivity and specificity values. Although the performance of the latter two approaches could certainly be improved by proper parameter adjustments they were discarded from further analysis in this work, leaving the whole concentration on the promotion of the ANN method.

#### ***ANN optimization***

Having chosen the ANN as preferred classification architecture, a number of parameters are optimized next to achieve the best performance for the EB discrimination task. The ANN is trained using the earlier mentioned backpropagation of error method, which evaluates the gradient of a loss function depending on the network's weights [266]. The learning process itself involves labeled training data demanding adequate features.

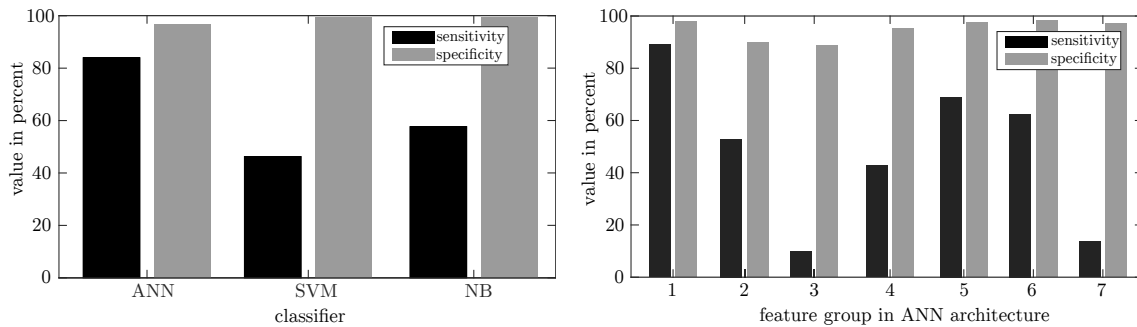


**Figure 4.16:** Preliminary ectopic beat discrimination performance. Using all 82 features as listed in table 8.6, three popular classification algorithms were tested yielding the performance given in the left plot. To get a feeling for the usefulness of the feature groups as summarized in table 4.9, they are exclusively applied in the ANN classification procedure. The resulting values for sensitivity and specificity given in the right hand side plot have to be treated with caution, as the groups contain different numbers of features and the classifier is not further optimised across the groups.

Proper feature selection is a tedious task and has a significant impact on the overall performance of the classifier. The right hand side plot in figure 4.16 gives an idea of the influence of the different feature groups in terms of sensitivity and specificity after being fed to the ANN again. This represents under no circumstances a feature selection procedure, but it might indicate the ability of the respective features to discriminate ectopic beats. As a matter of fact, feature group 1 already provides very good results. Further, the novel group 5 and group 6 features derived from the PPG also seem to contain useful information from which the classifier might further profit. It is stressed again that the different characteristics and number of features per group make an objective comparison very difficult. Additionally the parameters were not optimised across the groups.

When searching for a simple and convenient way to extract a suitable subset of the given features, blunt brute-force methods can be applied as long as the computational complexity and number of permutations do not exceed reasonable boundaries. Testing all  $2^{82} - 1$  possible feature combinations would go far beyond manageable efforts. Trying out all  $2^8 - 1$  permutations of the feature groups on the other hand is calculated rapidly. Table 4.10 lists the ten feature combinations that yielded the best classification performance with respect to highest mean of sensitivity and specificity each.

After the final feature candidates were derived, the ANN structure underwent further fine tunings in order to maximize the classification performance for the given EB detection task.

First, the overall ANN size and underlying neuron organization is a crucial factor regarding the network’s discrimination potency. Analyzing the impact of the number of hidden layers and especially the number of neurons in each layer itself is therefore a good starting point of the whole optimization process.

To avoid possible overfitting, the final network size should not become too complex. Moreover, multilayer networks including more than three hidden layers are known to

**Table 4.10:** Top ten combinations of feature sets applied in the proposed ectopic beat detector measured by sensitivity (se) and specificity (sp). Features include timings (interval), signal statistics (sig/stat) or amplitude and morphology (morph) properties.

se	sp	feature sets
92.39	97.85	ECG interval, ECG sig/stat, PPG sig/stat
91.70	97.87	ECG interval, ECG sig/stat, PPG morph, PPG sig/stat
91.46	98.03	ECG interval, ECG amplitude, PPG morph, PPG sig/stat
90.31	99.09	ECG interval
91.70	97.65	ECG interval, ECG amplitude, ECG sig/stat, PPG sig/stat
90.89	98.46	ECG interval, ECG ICA, ECG sig/stat, PPG amplitude
91.35	97.59	ECG interval, ECG sig/stat
91.23	97.59	ECG interval, ECG amplitude, ECG ICA, PPG sig/stat
90.43	98.33	ECG interval, ECG ICA, ECG sig/stat, PPG morph, PPG amplitude
92.04	96.69	ECG interval, ECG amplitude, ECG sig/stat

yield poor results during the learning phase, especially when standard gradient descent procedures such as the backpropagation of error approach are applied [150]. Therefore, the current ANN is restricted to three hidden layers where the maximum number of neurons in each layer is limited to 50. Figure 8.1 in appendix 8.2 provides two heat plots, which depict the classification performance for different ANN sizes. A three dimensional grid search on the number of neurons in layer one, layer two and layer three was applied in order to analyze the performance of the respective network. It is important to note that the input in all configurations is the whole set of 82 features as given in table 8.6. The results are not transferable to a different set of features, however they can be used as an example of how to derive a suitable network architecture at this point. While the diagrams in figure 8.1 do not provide a clear recommendation for a network size, they exhibit interesting areas indicating advantageous configurations. The observation on the numbers of hidden layers confirmed that a bigger network does not necessarily provide better results. Looking at the right corners of the diagrams, there seems to be a decreased performance for a bottleneck setting that contains a comparably small middle layer. Apparently a two layer configuration with relatively small last hidden layer would be a good choice, as the areas in the left part of the first diagrams in both settings are comparably bright.

Eventually, a multilayer perceptron with 20 input neurons (features), two hidden layers with 10 and 8 neurons, respectively, and three output neurons (representing the heartbeat classes N, SVEB and VEB) was chosen and is randomly initialized during the training process.

#### *Computational complexity and final feature set*

Regarding the implementation on small embedded devices, which are bound to limited hardware resources, the computational complexity plays a superordinate role. The presented EB detection method was therefore designed to demand system requirements, which can be satisfied by typical battery driven hardware systems as the rBSN sensor nodes depicted in section 3.4.

**Table 4.11:** ECG and PPG derived features, which are extracted from each heartbeat and processed by the presented multimodal ectopic beat detector. All features can be calculated with information drawn from the preceding and following heartbeat only, which allows for a small memory footprint and low detection delay. Furthermore, they are designed to adequately reflect both major classes of ectopic beats.

Number	Description
1	leading/trailing RR interval
2	ECG heartbeat power
3	ECG heartbeat mean
4	ECG heartbeat max/min
5..14	samples around R-Peak
15..17	PPG fractional amplitude
18	PPG pulse wave power
19	PPG pulse wave mean
20	current/next PPG pulse peak amplitude

For the given problem, there are basically two components affecting the computational complexity of the resulting algorithm. The actual classification itself is realized by the calculations of the ANN structure for each epoch where a single epoch involves the complete processing of one incoming beat. A single artificial neuron calculation step generally consists of three operations including  $n$  multiplications and additions per input (multiply and accumulate operations) and the evaluation of the activation function to determine the actual output which is always a scalar function. Consequently, the complexity rises approximately linearly with the number of neurons and addition of further hidden layers.

Table 4.9 presented the dependence of the single feature groups on their required wave delineation processes. As discussed earlier, features which are based on prominent fiducial points such as the ECG R-Peak or PPG onset require rather simple delineation techniques, whereas features relying on the location of more undistinctive points (e.g. ECG P-Wave) incorporate more complicated delineation procedures.

This actual feature calculation step is the second critical point to consider when it comes to the optimization of execution time. While some of the features can be derived with the help of single integer operations others employ more sophisticated methods such as wavelet transforms or ICA, which may impose severe performance restrictions. The execution times of the single feature groups were superficially inspected in a MATLAB environment. Although parts of the implementations are based on library functions with a very high level of abstraction and the underlying Java-VM impedes exact measurements on a clock-cycle level, one still gets a coarse impression of the computational costs. Table 8.9 in appendix 8.2 summarizes the corresponding insights.

Based on these findings, a final feature set containing 20 features was derived, which is listed in table 4.11 and is discussed in detail next.

The first feature is inspired by the work of Chazal et al. [53], but, instead of calculating the

**Table 4.12:** The EB detection algorithm is implemented on TI’s MSP432 MCU. Clock cycles and RAM usage are measured for every step of the algorithm. The results are given for a sample rate of 500 Hz and a heart rate of 72 bpm.

Step	per	Clock Cycles		RAM usage [B]	
		ECG	PPG	ECG	PPG
Filter	64 samples	2414	2414	68	68
Delineation	sample	418	75	388	44
Feature Extraction	heartbeat	8822	8445	4000	4000
Classification	heartbeat	980		1200	
Total	heartbeat	283239		4456	

preceding and following intervals of two consecutive R-Peaks (RR intervals) as separate features, the ratio of both is determined, which makes the feature independent of the current heart rate and sampling frequency. This feature has shown to reliably indicate SVEBs. The next three ECG features 2-4, which represent signal power, mean and max/min of the ECG signal amplitude aim at the distorted morphology resulting from VEBs. They are calculated for a window spanned by the starting and ending point of  $ECG_R - 0.35 \cdot RR_{preceding}$  and  $ECG_R + 0.65 \cdot RR_{following}$  respectively. Within the same window, the amplitude of the ECG signal is sampled at equally spaced points around the R-Peaks (features 5-14). These features, also inspired by Chazal’s work [53], indicate abnormalities in beat morphology and have proved beneficial to the detection of both classes of ectopic beats. The PPG fractional amplitude features 15-17, proposed by Teng et al. [295], capture the pulse wave morphology and are repurposed in this context. Features 18 and 19 are calculated in the same way as their ECG counterparts and represent the generally lower blood volume as a result of a premature contraction. They are calculated for an interval between two PPG onsets. Feature 20 relates the amplitude of the current pulse wave to the next one, which is often higher than a regular pulse wave following a normal heartbeat.

The complete algorithm was implemented on the rBSN hardware system. The main controller was upgraded to an TI MSP432 MCU (Texas Instruments, Texas, TX, US), which is based on an 32-bit ARM Cortex-M4 (ARM Holdings, Cambridge, UK) and has access to an integrated floating point unit. The filter and delineation routines work on blocks of 64 samples. A complete heartbeat processing step is then executed in less than 300,000 CPU clock cycles and requires approximately 4.5 kB RAM. More details are found in table 4.12.

### ***Evaluation dataset***

To investigate the applicability in clinical and ambulatory environments, the ectopic beat algorithm is exercised on data recorded with the rBSN hardware system. Therefore, a small clinical study was prepared, including patients of the geriatric units from ‘Staedtisches Klinikum Dresden, Germany’ and ‘HELIOS Klinikum Aue, Germany’ hospitals, who were selected by a cardiologist with respect to the occurrence of ectopic beats (cf. section 3.5). The study was confirmed by the ethical board at Technical University of

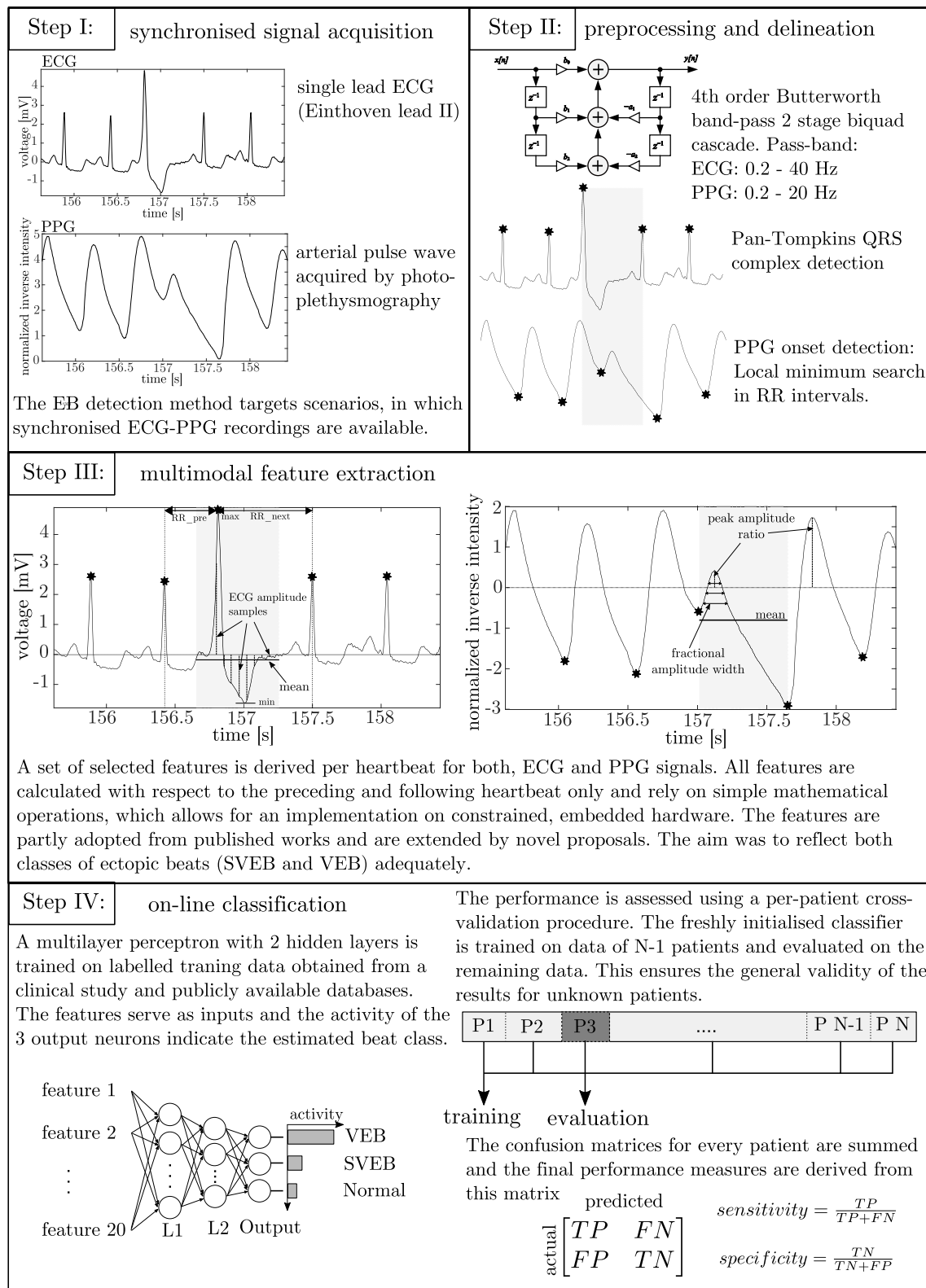


**Figure 4.17:** Overview of the single stages of the proposed ectopic beat detection approach.

Berlin (request PF\_01\_20140513), and all participants declared their voluntariness and consent.

As an addition to the records gained from these measurements, another source of data was required for a larger amount of training data and better significance of the evaluation results. The PhysioNet Challenge 2015 (PhyCh15) training database contains 750 datasets recorded from different patients in clinical environments [45], which are publicly available on the Physiobank database [86]. An important inclusion criterion was the existence of an ECG lead II and a PPG channel, which are required to derive the features of the presented algorithm. Moreover, a sufficient presence of ectopic beats was demanded, whereas records and segments with heavy artifacts in any of the channels were excluded, resulting in a total of 31 datasets (cf. table 3.7). The signals in the PhyCh15 records occasionally appeared to be out of synchronization, which became obvious when comparing the ECG R-Peak to the corresponding PPG pulse wave. In some cases, a large offset between the ECG and PPG recordings was recognized, which was probably introduced by the original measurement setup. In the current processing, this offset is compensated by shifting the signals to fulfill the aforementioned assumption that the resulting pulse wave in the PPG signal follows the R-Peak of the corresponding heartbeat in the ECG signal. With regards to PWV applications, the affected records are unusable, but they can still be applied to evaluate the proposed EB detection algorithm.

Finally, all records were first annotated by two non-experts, followed by a thorough review by an expert cardiologist. Segments around ambiguous heartbeats were excluded.

#### ***Ectopic beat detection performance***

A per-patient cross-validation procedure is adopted to evaluate how well the detection algorithm performs. A new instance of the ANN is trained on the data from all but one patient. The trained network is then presented with the features of the remaining data of the left out patient and the resulting output is compared to the ground truth to calculate a confusion matrix. This procedure is repeated for all N datasets, where the confusion matrices are summed up in each step. The final performance measures - sensitivity and specificity - are derived from that matrix, describing the whole database. Sensitivity is defined as the ratio of the number of correctly classified ectopic beats to the total number of beats labeled as ectopic. Specificity is the ratio of the number of correctly classified normal beats to the total number of beats labeled as normal. A high sensitivity lowers the influence of ectopic beats on the given application, whereas the specificity is not inherently crucial regarding the performance. However, a low specificity limits the number of sampling points, which, in turn, affects the achievable accuracy. The applied evaluation scheme guarantees that the resulting performance is generally valid for unknown patients, since the classifier is never trained on data obtained from the same patient as it is evaluated for. To examine the usefulness of the multimodal approach, the evaluation is repeated for features from both signals separately (features 1 to 14 and features 15 to 20 of table 4.11). The input layer of the MLP is changed accordingly to reflect the reduced number of features.

**Table 4.13:** The evaluation of the ectopic beat discrimination is conducted on the complete set of features and also on ECG and PPG features separately. The sensitivity is calculated for all ectopic beats and for both classes, respectively.

Set of Features	Sensitivity	Sensitivity SVEB	Sensitivity VEB	Specificity
PPG	77.7	68.2	87.6	95.5
ECG	91.12	87.2	95.3	98.9
All	95.7	96.1	95.3	99.0

Additionally, the per class sensitivity is calculated in order to verify whether the proposed solution is able to detect both VEBs and SVEBs.

The results in table 4.13 demonstrate the effectiveness of the proposed EB detector. Unfortunately, a comparative analysis with respect to the published methods introduced earlier is hard to realize, due to the lack of a common, annotated reference database and consistent performance measures. Moreover, an impeccable comparison would require accurate reimplementations of the original works, which could not be provided in this thesis. Nonetheless, the achieved performance values of the proposed EB detector in terms of sensitivity and specificity are favourable, especially under the constraint that training and testing was performed on records of different patients. The presented method is able to reliably detect and distinguish both classes of ectopic beats and could therefore be extended to a heartbeat classifier for other application scenarios. As shown in the second row of table 4.13, the classification based on the implemented ECG features performs well already. This finding is consistent with the popular focus on ECG signals for detection of ectopic beats. In contrast, the PPG only detection (table 4.13, first row) seems to underperform, especially for SVEBs. The high performance achieved by other published PPG based methods remains questionable and might call for a revision of the implemented PPG features. The improved sensitivity of the multimodal approach, however, underlines the benefit of combining features from both signals. Moreover, it was successfully demonstrated that all stages of the algorithm can be executed on state of the art low power microcontrollers, which is a significant advantage of the proposed EB detector.

## 5 Artifact Suppression for Pulse Wave Signals

Being able to reliably identify corrupted segments of pulse wave recordings, one can either discard affected periods or move one step ahead in an attempt to suppress unwanted noise components. In the last decades, manifold publications have piled up in literature, providing manifold ideas and concrete procedures on PPG artifact cancellation. By exploiting the acceleration signals of the rBSN sensor hardware, preliminary findings of an enhanced PPG artifact reduction method based on blind source separation are presented in section 5.1, along with a short overview of published works on PPG denoising. Furthermore, the onboard ACC signals of the rBSN PPG sensors were successfully used to implement an automatic hand movement detection in order to recognize typical motion patterns that are known to provoke burdensome artifacts.

### 5.1 PPG Artifact Reduction

Although PPG signals offer captivating possibilities for cardiovascular assessments as was introduced in section 2.1.3, their artifact prone nature seriously hampers practical applications. The most important prerequisite in PPG signal processing is therefore a reliable detection of inferior signal quality, which was carefully dealt with in the previous chapter. Simply discarding artifact contaminated periods is undoubtedly the most secure choice in practical situations. Nonetheless, in many such cases the abandoned signals still bear a reasonable amount of physiological information, which could be retrieved when the noise components were canceled out in a reliable fashion.

Possible sources provoking signal artifacts in PPG recordings are manifold. Among all external influences, motion is considered the primary cause for degraded signal quality as it often leads to a mechanical displacement of the sensor probe and accelerates blood in the otherwise non-pulsatile venous bed [15, 100]. This notion was already confirmed by the motion experiments depicted in figure 4.4, which emphasize the devastating effect of acceleration forces on the pulse waveform itself. Further impeding influences are constituted by varying ambient light, optical obstacles including nail polish or dark pigmented skin, electromagnetic interference and low perfusion [223].

Due to the potential benefits in practical applications, artifact cancellation in PPG recordings is an exceptionally researched topic in current literature. The following section will give a brief overview on recent publications and aims to point out the general difficulties of PPG noise suppression. As pointed out above, pulse wave artifacts are closely related to the underlying movements, which is the reason why a lot of works propose incorporating additional movement information acquired near the measurement site. This strategy was followed in this work as well by equipping all sensor nodes with a 3-axis accelerometer as introduced in the respective hardware sections of chapter 3.3. This extra piece of movement information allows implementation of more sophisticated methods found in recent literature, as will be discussed next.

### 5.1.1 Methods Currently in Use

Applying simple low- and high-pass filtering techniques with static cutoff frequencies is not a well performing option in many practical situations, especially when the frequency components of the physiological signal and present artifacts overlap. This brought forth numerous advanced ideas to increase the performance of artifact reduction in PPG processing. Trying to overcome the limitations of fixed pass-bands and stop-bands, Lee et al. proposed a parallel filter bank structure to remove PPG artifact components [154]. First, a clean reference signal is obtained (thus requiring some sort of supervised calibration scheme), which then serves as a template to choose the best filter bank channel. The filter bank output yielding the maximum correlation coefficient with respect to the reference signal is finally chosen as the artifact cancelled PPG signal. The authors conducted a small measurement incorporating different experiments (shivering, respiration, external taps on the finger probe, walking) on a not further specified population. To evaluate the performance, they provide a measure of ratio variation (typically derived for arterial oxygen saturation ( $SpO_2$ ) calculation) only, which makes it hard to interpret the output of the proposed method.

Adaptive filters are another common approach to tackle artifact contaminated signal extracts. The early works of Widrow, which introduce techniques of adaptive noise cancellation (ANC) [334], define the underlying architecture commonly applied by artifact reduction methods. Figure 5.2 A) presents the basic principle of the ANC approach, designed to estimate the distorted components of the PPG signal given proper reference information. Following the ANC theory, one assumption requires the artifact component to be uncorrelated with the physiological signal. The reference channel typically comprises some sort of independent motion measure (e.g. provided by an additional acceleration or piezo signal) or is derived by a model describing either the physiological or the noise components. In most cases, the adaptive filter itself is realized as a finite impulse response filter type (FIR) whose coefficients are adopted by real-time algorithms such as the recursive least squares approach [101]. Slightly varying ANC implementations designed for PPG artifact reduction were evaluated by different groups leading to a couple of publications

with similar approaches. The Massachusetts working group around Asada, Wood and Gibbs [10, 83, 339, 340, 341] analyzed their ANC methods on not further specified datasets, with rather casual performance measures based on visual inspection, mean squared error or heart rate extraction deviation.

Foo et al. [73, 72] dealt with the performance of ANC artifact suppression in pulse transit time and pulse rate extraction applications. Although the considered records were drawn from a single subject only, different settings were considered including poor perfusion, breathing and varying kinds of hand motions.

Yousefi et al. [349] performed different hand motion experiments (up-down and left-right motions, bending finger, standing, walking and running) and tested their proposed ANC method on six subjects. The artifact cancellation procedure was evaluated by assessing the performance of calculating arterial oxygen saturation and heart rate out of the cleaned signals. Comtois et al. [47] followed a similar approach, proposing an ANC architecture for artifact reduction in PPG measurements recorded during jogging. Their database include seven subjects running on a treadmill with PPG sensors attached to both hands. One hand was kept as still as possible, which then served as reference channel to compare calculated  $SpO_2$ , pulse rates and signal deviation (in terms of root mean squared error (RMSE)) between processed and reference outputs.

For the sake of completeness, one encounters further minor works dealing with the ANC approach although it is not always clear how to interpret the results as additional information on the performance evaluation and the datasets under tests are sometimes missing or poorly motivated [17, 99, 138, 141, 259, 281, 326].

Coetzee et al. [46] resorted to a synthetic reference signal in order to reconstruct the physiological PPG with the help of an ANC structure, which was tested on 8 volunteers performing specific exercises (finger tapping, arm waving) and on signals acquired from 11 subjects of a neonatal clinic with  $SpO_2$  extraction accuracy serving as a performance measure. This idea resembles the approach of Ram et al. who generated a noise reference by means of an inverse fast Fourier transform (FFT) (with prior zeroing of physiological frequency components) [252]. In a sequel publication Ram et al. pursued a strategy where they proposed to dynamically choose from three different statistically derived references (calculated by means of FFT, SVD and ICA techniques) that are fed to the adaptive filter [249]. The performance is discussed on several statistical measures including peak to peak sample variations of the reconstructed beats, signal to noise ratios, root mean squared error measures and multiple physiological timings such as the length of the rising slope. Unfortunately, it is not clear how many datasets and subjects were considered in the final analysis but the authors reported increased SNR values, minor peak to peak variations and more stable  $SpO_2$  measures (although lacking a trustworthy reference). A major advantage is the fact that their ANC method does not require an additional motion input channel and could therefore be applied on off-the-shelf pulse oximetry hardware. Pengfei et al. [221] applied a constrained ICA technique to extract an artifact correlated signal which is fed as reference input to the ANC. The efficacy was evaluated on artificial signals as well as on real life datasets recorded in a small experimental study provoking various artifacts again

(vertical and horizontal finger movements, bending the finger, pressurizing the probe clip and hand waving). With reference to the synthesized signals, the root mean squared error was calculated for increasing SNR values to compare the performance of the respective outputs. The rather small real life dataset was inspected visually accompanied by statistical peak amplitudes considerations. Additionally, they reimplemented the ANC approach after Ram et al. [252] (introduced above) where they could demonstrate a slight superiority of their ICA-ANC approach on the considered datasets.

Lee et al. discussed an adaptive comb filter, which also works without the need for an additional reference channel, but the evaluation is based on artificial noise components only [152].

It is stressed that many authors repeatedly emphasized the dependence of the specific artifact reduction performance on the chosen reference signal, and especially on the type of movement that provoked the signal distortion. Further assessment of the available movement information could therefore contribute to the decisions made in the presented approaches, which will be picked up later.

Next to the ANC ideas, wavelet based PPG reconstruction is another frequently encountered method to tackle artifacts in PPG recordings. Lee et al. [153] prepared a small experiment on 15 volunteers performing various finger movements. The PPG signal was decomposed by the wavelet transform, where the coefficients above a certain level were set to zero in order to remove noise in the low frequency bands. Two PPG modules (one attached to the moving hand, the other to the resting) and an additional ECG sensor were applied to analyze heart rate errors in the performance evaluation [153]. Further works incorporating different wavelet types were proposed by [126, 243, 245, 246], although the evaluation schemes remain somewhat superficial, which are sometimes limited to loosely comparisons of heart rate variability and  $SpO_2$  outcomes only. It is noted that those wavelet based methods are typically accompanied by the need of a proper coefficient threshold selection, which might hinder effortless applications in different settings.

Having a critical glance on the artifact suppression procedure, Foo et al. directly compared ANC and wavelet techniques in another interesting work [69], which builds upon the findings of three conducted measurements including tidal breathing, scratching finger movements and arm waving. As reference PPG and ECG were available, heart rate errors and pulse transit time deviations could be tracked. It was concluded that both methods might introduce phase shifts, which affect temporal properties that are crucial for timing applications such as pulse transit time measures.

Kalman filters are also found among the manifold proposals of PPG artifact reduction. Lee et al. give an in depth introduction to Kalman filtering in PPG denoising [151] and compare the performance with conventional ANC procedures. As in other works, they run simulations on artificially contaminated PPG extracts to compare the artifact suppression performance quantified by a cross-correlation coefficient of the denoised signal and its clean reference version. In the second part, the methods are applied upon datasets conducted in a small experiment with 20 trials, where the Kalman filter approach outperformed the implemented

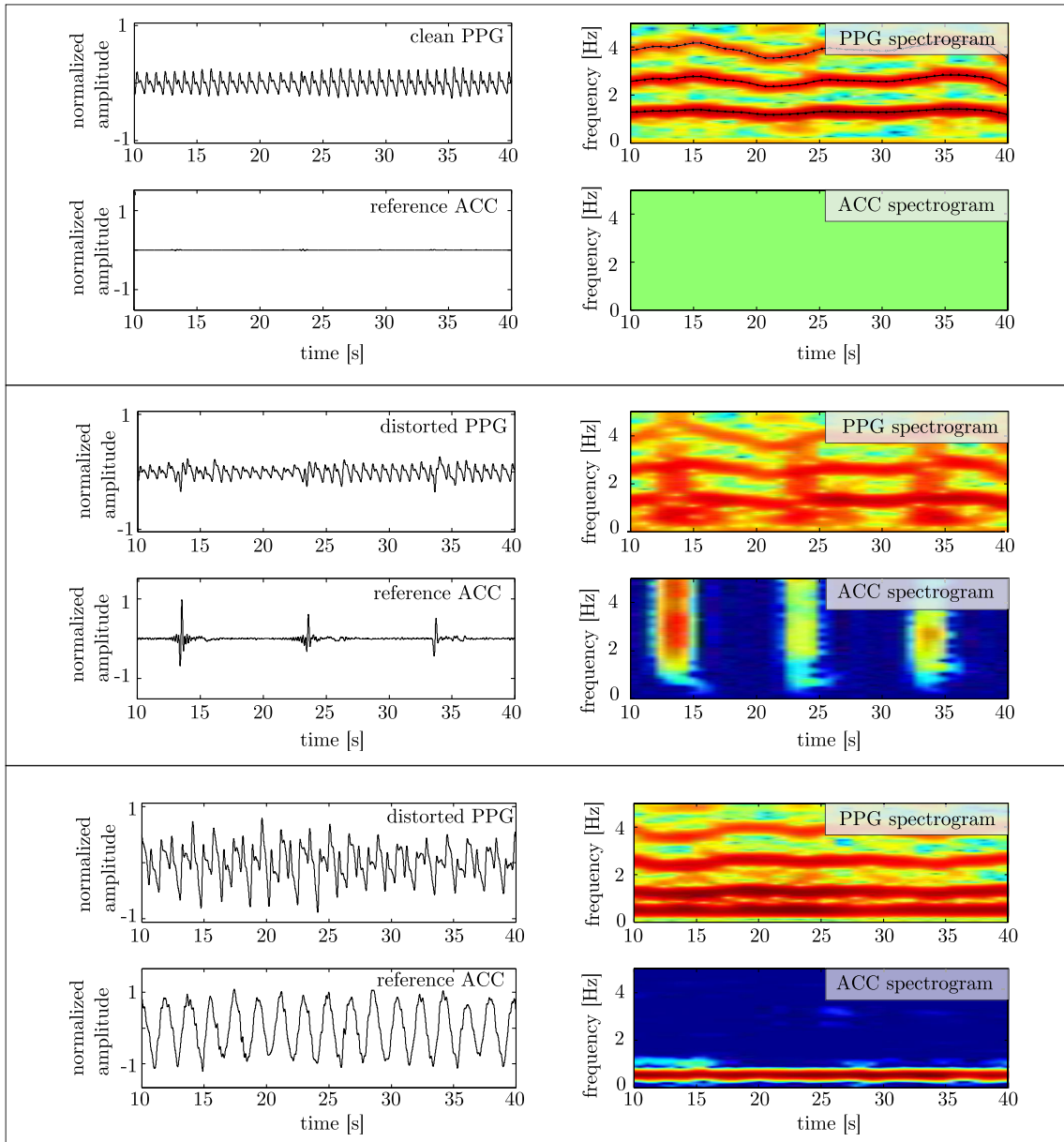


**Figure 5.1:** Time signals and spectrograms of the PPG and a single acceleration channel. *Top)* PPG recorded at rest without any artifacts. One clearly recognizes the typical PPG frequencies between 1 Hz and 4 Hz on the right hand side. *Middle)* PPG recording with sudden hand movements. As is nicely depicted in the spectrogram, the frequencies of the acceleration references overlap with the physiological components, hampering classic artifact reduction approaches. *Bottom)* PPG signal during periodic movements introducing a non-physiological spectral line.

ANC methods in terms of cross-correlation between the reference PPG and the reconstructed signal. Further Kalman filter oriented works were published in various proceedings, but provide rather unsatisfying evaluation schemes [155, 169, 276].

Yan et al. concentrated on reliable  $SpO_2$  extraction and favoured a smoothed Wigner-Ville distribution over classic FFT approaches to estimate the AC component in the PPG

spectrogram, which was substantiated by six dedicated measurements of volunteers during motion and at rest [342].

Moving on combing literature, there are numerous suggestions from Indian work groups based on cycle by cycle Fourier analysis [256, 257], Hilbert-Huang transform [244], singular value decomposition [258], advanced PCA methods [251] and ICA techniques [250]. The evaluation schemes are similar to the previous works, with performance measures derived from small sample records only. Therefore, one might want to stay reluctant to draw premature conclusions by a direct comparison of the reported results.

Further works presenting results on PPG artifact reduction include techniques of particle filters [160], empirical mode decomposition [244, 321], PCA [260], saturation transforms [93, 344], nonlinear artifact reduction using an additional wavelength channel [100] and especially in the last years an increased influx of ICA based procedures.

Kim et al. applied the fastICA algorithm [110] on interleaved PPG blocks (signal period was detected with the help of an autocorrelation measure) and tested the noise suppression efficacy on synthesized signals by evaluating SNR and mean squared error (MSE) values. Moreover they provided visually inspected real life data to suggest some potential of the applied procedure. Stetson artificially mixed clean PPG data and noise to analyze the efficacy of an instantaneous ICA model in the separation process [290, 291]. Foo analyzed an ICA reconstructed PPG signal in pulse transit time applications and reported a promising performance of this approach [71] whereas Krishnan et al. propose a frequency domain ICA technique considering only magnitude information [140]. Krishnan's method is tested upon experimental data gathered from ten subjects performing different hand movements. Visual inspections and quantitative assessments including a correlation coefficient between reconstructed and clean reference signals showed a promising performance, although the approach depends on its performance to reliably detect clean segments that are needed for period estimation in a preprocessing step [140]. Ram et al. combined their wavelet denoising approach with an additional ICA processing block, which aims to separate respirational activity from artifact related components [250]. The performance was evaluated on a small experimental database conducted on 15 volunteers and was reported superior to standard wavelet approaches. Jensen et al. [117] reported an increased accuracy in  $SpO_2$  estimation after comparing different ICA algorithms in a prior PPG denoising step and Volmer advocated the use of a convoluted ICA approach to increase the robustness of oxygen saturation calculation during periods of decreased signal quality [312].

Volmer's promising results on  $SpO_2$  extraction and the fact that he did not further evaluate the ICA denoising scheme on pulse wave relating error measures has motivated further efforts in this work. The main idea was to increase the artifact suppression efficacy by combining Volmer's ICA approach and additional acceleration input channels. More detailed backgrounds on the implementation and initial tests with elaborated experiments will be presented in the next subsection.

### 5.1.2 Enhanced PPG Artifact Reduction by Blind Source Separation

Having outlined current publications on PPG artifact reduction, this section presents an extension to Volmer's ICA approach as described in [312]. The initial results were already published in [234] and will be summarized next.

Volmer argued that the measured pulse wave can be understood as a convolutive mixture of the pressure wave ejected during systole with components resulting from reflections at arterial junctions, damping processes in the elastic vessels and external motion influences. The convolutive ICA model as depicted in figure 5.2 B) therefore seems a proper structure to separate the acquired signals into its noise and physiological components. Whereas Volmer only fed a red and infrared PPG channel into the demixing process, this work evaluates the benefits of separating a single disturbed PPG channel given a proper ACC reference. Figure 5.1 already depicted three sample spectrograms of a rBSN PPG fingerclip signal and its acceleration reference during rest and motion. One clearly recognizes the spectral overlap of the physiological and motion components complicating the artifact reduction process. Assuming that the artifact components in the PPG signal are caused by the corresponding motions, it seems legitimate to use the acceleration information as input source in the ICA demixing model.

The underlying theoretical aspects of blind source separation techniques will not be discussed here again. Instead the interested reader is referred Volmer's introduction on his method [312] or advanced literature like [111], which cover relating topics in thorough detail.

The well studied ANC as illustrated in figure 5.2 A) was implemented to provide a reference output of the artifact reduction task. This allows a first comparative evaluation of the novel approach applied on records of the same database.

#### 5.1.2.1 Motion Reference Data

As examined in the previous literature review, acceleration signals acquired by onboard MEMS sensors contain valuable information, which can be directly exploited to suppress motion induced artifacts in PPG recordings. For both approaches (ANC and ICA), different ACC reference configurations were analyzed to optimize the artifact reduction performance.

Given the signals of the three axis accelerometer built into the rBSN sensors (providing information corresponding to the acceleration in mediolateral (x-), anteroposterior (y-) and vertical (z-) direction, cf. figure 5.2 A)), multiple arrangements to establish a single channel reference were tested. Ideally, the chosen reference should reasonably represent the artifact component, which was repeatedly discussed in the previous ANC papers with different configurations reported. The following five patterns to extract a single reference from the three axis ACC sensors were contemplated in the studies of this work:

- 1) single channel ACC-x
- 2) single channel ACC-y
- 3) single channel ACC-z
- 4) mean value of ACC-x, y- and z-component
- 5) 1st PC of three dimensional ACC vector (max. variance projection)

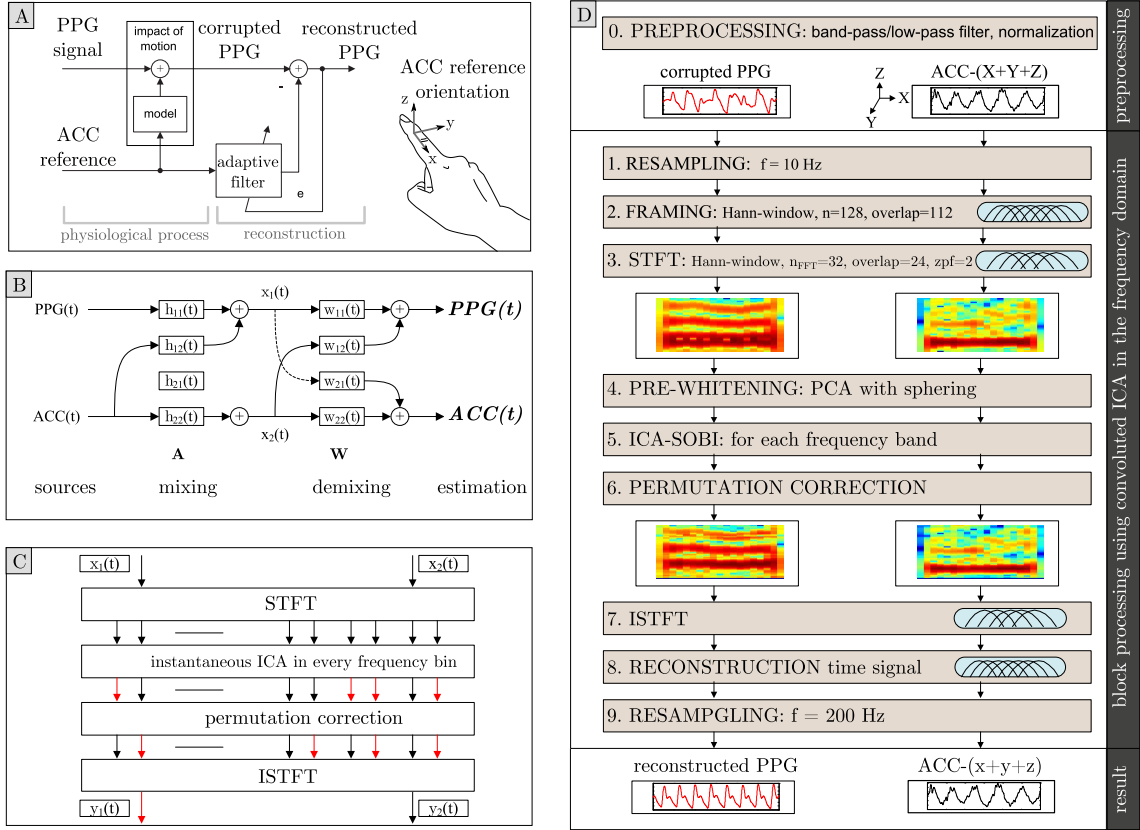
### 5.1.2.2 ICA Artifact Elimination Framework

Figure 5.2 D) depicts the complete ICA artifact reduction framework. The first stage includes a low-pass/band-pass filter to remove high frequency components above 5 Hz. Next, the signal is downsampled to 10 Hz, primarily to decrease the computational burden of the following steps. PPG and ACC signals are then segmented into single blocks of  $n = 128$  samples, weighted by an Hann-window. The window is shifted by 16 samples after each iteration, which results in an overlap of 112 samples. The short time Fourier transform (STFT) is realized with blocks of  $n_{stft} = 32$  points overlapping in 24 samples. Zero-padding is applied to increase the frequency resolution to 0.16 Hz. To reduce leakage effects, the blocks are also weighted with the help of a Hann-window.

Every frequency band is pre-whitened (decorrelation with unit variance normalization) before all bands are processed by the SOBI (second order blind identification) algorithm [21] performing the blind source separation. In prior tests, further algorithms including fastICA [110], InfoMax [20] and JADE [31] were tested as well, but did not reach the efficacy of the SOBI method, which is shown in the following subsection again. Each STFT block is processed by an instantaneous ICA procedure working on complex signals resulting in 32 ICA calculations for each step. The SOBI algorithm creates  $n_{cov} = 5$  time-lagged covariance matrices, which are diagonalized using the Jacobi procedure yielding a demixing matrix for each frequency band. To account for the permutations and scaling errors in every frequency band, the permutation correction according to [247] was applied.

### 5.1.2.3 Performance Evaluation

The proposed method is analyzed with respect to different hand movements that were encountered in previous works and are known to provoke motion artifacts of different degrees. A total of 18 hand motion patterns were conducted in various laboratory measurements including sharp jerks as well as smooth periodic hand movements at different speeds. This experimental dataset was used to examine the influence of the adjustable parameters, particularly the ACC reference channel and the underlying ICA algorithm. To run a quantitative evaluation, the most common performance measures as employed in the relating publications (cf. subsection 5.1.1) were adopted for the following considerations.



**Figure 5.2:** Block diagram depicting the proposed ICA artifact reduction scheme. **A)** ANC structure, which was applied for a comparative evaluation. **B)** BSS principle adjusted for the current needs. The acceleration reference does not bear any physiological pulse wave information making  $h_{21}$  superfluous. **C)** Convolutive ICA is solved in the frequency domain by applying an instantaneous ICA procedure on each frequency bin. **D)** Flow diagram depicting steps of the proposed artifact reduction method.

Since a clean reference PPG was available (measured on the resting hand), the SNR of the raw and reconstructed signals could be calculated according to

$$\text{SNR}|_{dB} = 10 \cdot \log_{10} \frac{P_{\text{signal}}}{P_{\text{noise}}} \quad (5.1)$$

where  $P_{\text{signal}}$  is the average power of the physiological signal and  $P_{\text{noise}}$  is the average power of the unwanted background noise respectively. The noise component of the recorded PPG<sup>1</sup> is estimated by subtracting the clean reference signal  $s_{\text{ref}}$  from the motion corrupted signal  $s_{\text{mot}}$  allowing for the following SNR calculation:

$$\text{SNR}|_{dB} = 10 \cdot \log_{10} \frac{\sum_{n=1}^N (s_{\text{ref}}(n))^2}{\sum_{n=1}^N (s_{\text{ref}}(n) - s_{\text{mot}}(n))^2}. \quad (5.2)$$

<sup>1</sup>For better readability the PPG is denoted by  $s$  in the following equations.

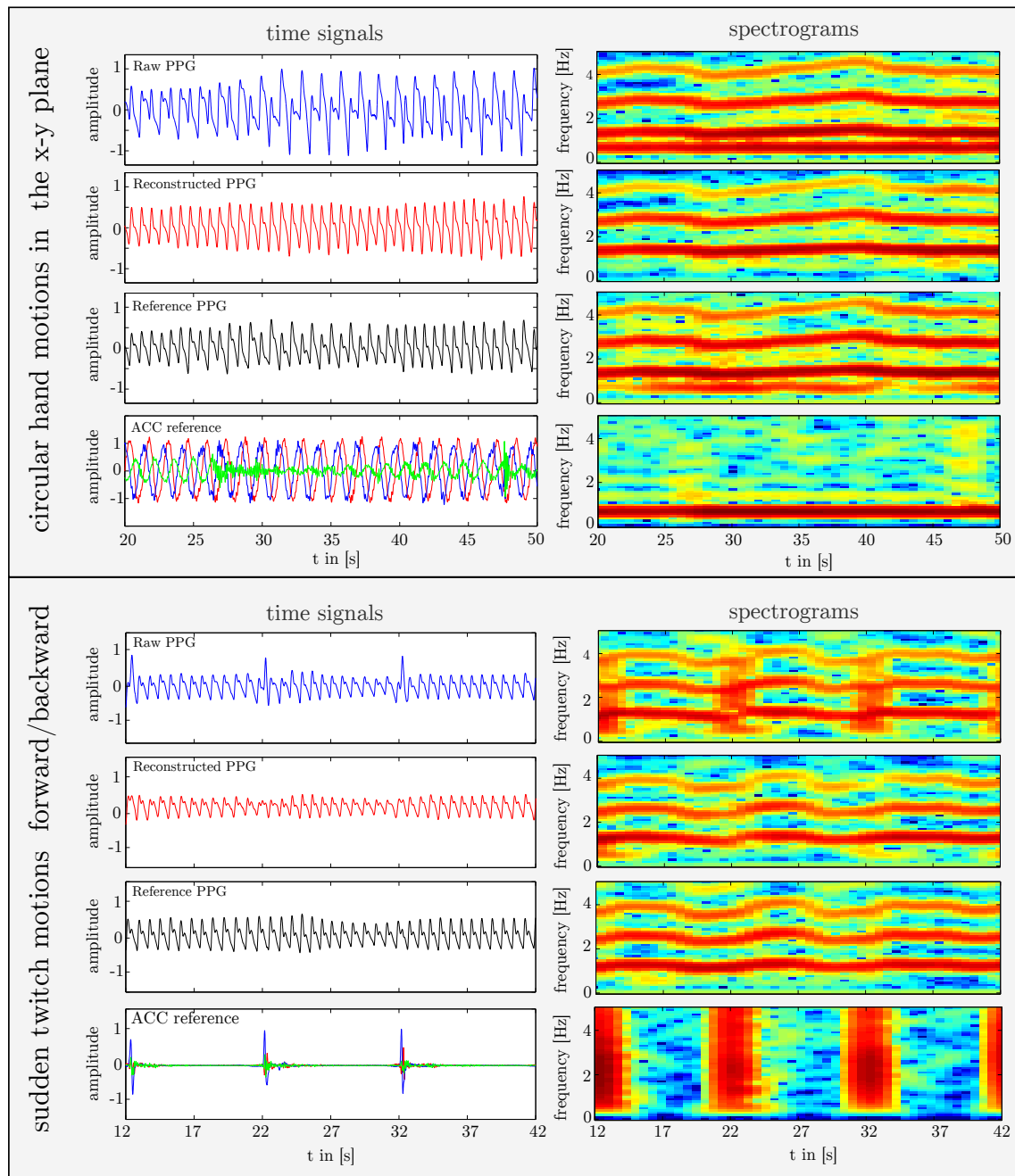


**Figure 5.3:** Time signals and spectrograms of two records before and after reconstruction. **Top)** extract depicting circular hand motions in the horizontal plane. Raw signal, denoised signal, clean reference PPG acquired from resting hand and the acceleration reference from the rBSN sensor attached to the performing hand. The spectrogram on the right demonstrates the effectiveness of removing the artifact component. STFT parameters:  $n_{stft} = 32$ , overlap: 24, window: Hann **Bottom)** extract acquired at rest with sudden hand movements. The artifact components completely overlap all physiological frequency components but are still satisfactorily separated after reconstruction.

The SNR change determined by SNR calculation before and after reconstruction serves as a quantitative measure characterizing the denoising procedure.

$$\Delta\text{SNR}|_{dB} = \text{SNR}_{\text{before}} - \text{SNR}_{\text{after}} \quad (5.3)$$

Note that the PPG signal is normalized before SNR calculation

$$s_{norm} = \frac{s - \mu_s}{s_{std}} \quad \text{with} \quad \mu_s = \frac{1}{n} \cdot \sum_{i=1}^n (s(i)), \quad s_{std} = \sqrt{\frac{1}{n-1} \cdot \sum_{i=1}^n (s(i) - \mu_s)^2}, \quad (5.4)$$

and that the SNR values are determined on small blocks with the final SNR being derived by their mean value:

$$SNR_{total} = \frac{1}{m} \cdot \sum_{i=1}^m SNR(k) \quad \text{with} \quad k = 1 \cdots m. \quad (5.5)$$

Moreover, a correlation coefficient  $r_{s_{ref}s}$  and the mean squared error were determined from the reconstructed and reference signal pair as well:

$$r_{s_{ref}s} = \frac{\frac{1}{n} \sum_{i=1}^n (s(i) - \mu_s)(s_{ref}(i) - \mu_{s_{ref}})}{\sqrt{\frac{1}{n} \sum_{i=1}^n (s(i) - \mu_s)^2} \cdot \sqrt{\frac{1}{n} \sum_{i=1}^n (s_{ref}(i) - \mu_{s_{ref}})^2}}. \quad (5.6)$$

Last but not least the mean absolute pulse rate error (MAPRE) is additionally considered, which is defined as the mean of the absolute differences of pulse rates extracted from the clean reference ( $PR_{ref}$ ) and motion corrupted signal ( $PR_{sig}$ ).

$$MAPRE = \frac{1}{n} \cdot \sum_{i=1}^n |PR_{ref}(i) - PR_{sig}(i)| \quad (5.7)$$

Figure 5.4 a) provides the derived SNR values of the raw signal (grey bar in the background) compared to the reconstructed signals when the proposed method was run with the five different ACC references as defined earlier (cf. subsection 5.1.2.1). The resulting differences are plotted beneath in figure 5.4 b). The first aspect to be aware of is the fact that the SNR improvement significantly varies for the different movements. This is reasonable because the SNR of the unprocessed raw signal itself also alters and is much higher during slow movements for example. The second point concerns the impact of the reference channel. Note that the SNR even slightly decreases after reconstruction of periods during smooth movements, revealing a minor shortcoming of the proposed method. Thus, one might want to deactivate the artifact suppression in such situations, which requires a reliable detection of the corresponding movements though.

Interestingly, the acceleration in y-direction yields comparatively good results in the conducted experiments indicating a strong correlation with artifacts provoked by movements in the direction of the arterial flow.

The correlation coefficient and the mean squared error measure convey a similar message regarding the artifact suppression performance and are plotted in figure 8.2 found in appendix 8.2.

As mentioned earlier, different ICA approaches were tested to solve the blind source separation problem. The subplot in figure 5.4 c) shows the reconstruction results of the applied algorithms in terms of SNR improvement again. It turns out that the SOBI algorithm outperforms the other methods in the given disciplines, which were not further evaluated in the scope of this work.

Finally, figure 5.4 d) directly compares the outputs of the ICA approach (using the single reference channel ACC-y) to the classic ANC reconstruction applied with each of the five ACC reference combinations again. As a matter of fact, the ICA approach is superior in the majority of the conducted experiments, whereas the performance of the ANC implementation more seriously depends on the selected ACC reference during the different movements.

### 5.1.3 Hand Movement Detection

The previous investigations made clear that the majority of signal distortions in the PPG are caused by different kinds of motions of the subject's extremities. It was also shown, that corresponding artifact suppression algorithms might succeed in specific motion patterns, but fail in others, which complicates their application in practical situations.

Next to the considered movements of the previous part, which are predicated on a rather laboratory nature, Tobin et al. published an interesting study [304] where they analyzed typical movements known to provoke PPG artifacts in clinical environments.

Referring to the previous findings, an automatic detection of the different types of motions would contribute valuable information that is exploitable by the respective artifact suppression methods. A reliable discrimination of slow periodic movements for example, might serve as proper indicator to turn off the proposed ICA approach, which revealed slight erroneous results when faced with those kinds of artifacts.

It is also imaginable that a robust classification of distinct motions could be used to combine different artifact suppression approaches in order to benefit from their respective strengths and to avoid known weaknesses.

Moreover, an automatic detection of slight movements and still periods might also enhance certain properties of the previously introduced OPRA approach. Given this additional piece of information, one would only start a new calibration phase when the movement detector excludes underlying activity to name just one possible option.

Therefore, this topic has attracted the attention of this work and was considered in additional experiments that focus on the automatic classification of different finger, wrist and general hand motions.

Classifying full body activities like walking, running, jumping or determining changing postures was subject to intense research in the last years [149]. However, there are no works that concentrate on dedicated hand movement detections, which would enrich PPG preprocessing as just discussed. Therefore, another small experimental study was prepared to get an idea on the feasibility of hand movement detection based on reference

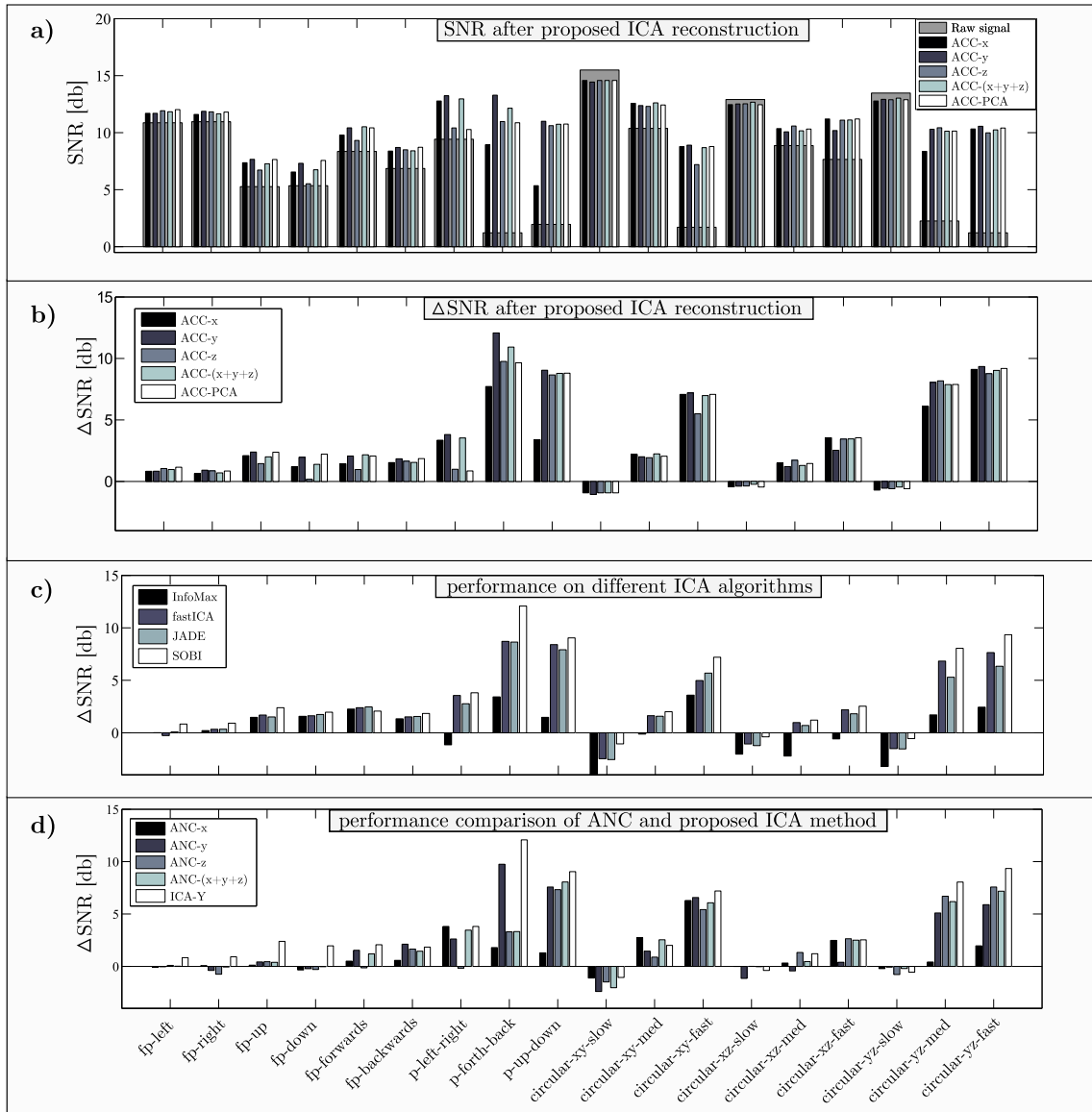


**Figure 5.4:** Reconstruction performance of the proposed method. **a)** SNR before and after reconstruction using different ACC combinations. In the given experiments, the ACC reference in anteroposterior direction (y-direction, compare figure 5.2 1)) yielded the most promising results along with the PCA derived option. The SNR improvement varies for the different exercises with impressive artifact suppression performance on the one hand but also declines in periods of slow motions with minor artifact presence. **b)** Corresponding differences  $\Delta$ SNR for better readability **c)**  $\Delta$ SNR values resulting after running different ICA algorithms solving the blind source separation task (using ACC-y as reference). It turns out that the SOBI approach outperformed the other methods in the majority of the considered cases. **d)** Comparison of the proposed ICA method with a traditional ANC approach. The performance of the ANC implementation strongly depends on the chosen reference during the respective types of motion. The ICA implementation has proved superior in the conducted experiments.

acceleration data only. This task is approached by evaluating features extracted from the three channel acceleration sensor attached on the rBSN PPG fingerprobe, where the first preliminary results of an automatic hand movement detector were already published in

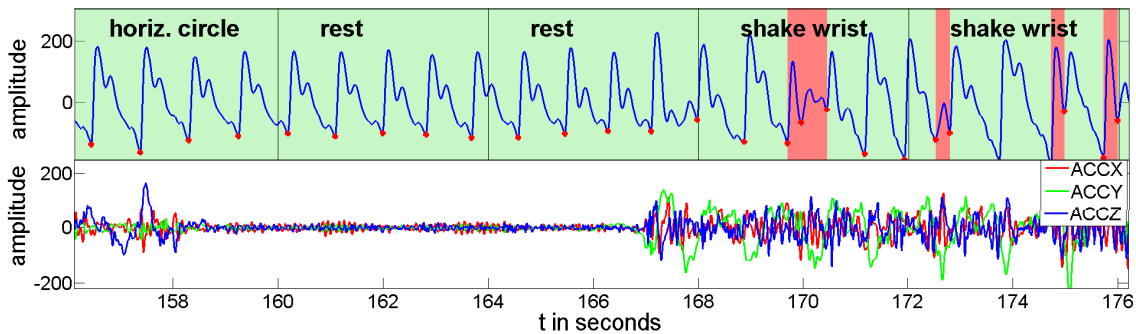


**Figure 5.5:** Hand movement detection on three axis acceleration signal during hand movement experiments. Drawing adopted from [232].

[232]. The experiments involved two PPG modules, one attached to the forefinger of the hand performing different motion patterns and the other fastened to the forefinger of the resting hand providing the clean reference signal.

The following types of motions were performed:

Bump, disturb finger probe, rest, shake wrist, tap finger, horizontal twitch left, horizontal twitch right, horizontal twitch forward, horizontal twitch backward, vertical twitch up, vertical twitch down, horizontal periodic right/left, horizontal periodic forward/backward, horizontal circle, vertical periodic up/down, wrist rotate, trembling.

With regard to the motion detection, only the three acceleration channels in x-, y- and z-direction are taken into account. The succeeding feature extraction is performed on the raw signals without any specific preprocessing being involved. In total, 52 features in the time and frequency domain as well as statistical properties are calculated from each sample block. The derived features are then enclosed in a large data matrix, which also contains the labeled classes listed above. Thus, supervised machine learning methods can be applied to classify the different types of motions.

Two classification methods were scrutinized in the initial tests including a naive Bayes network as well as a multilayer perceptron. Both approaches are well suited for later on-line prediction, as the computational complexity is relatively low. The classification of the acceleration data with respect to different hand motions yielded very promising results. Applying a stratified 10 fold cross-validation, the naive Bayes approach classified 83.1 % instances properly. The multilayer perceptron was trained using the backpropagation of error method. In a 10 fold cross-validation 95.6 % of the classes have been predicted correctly. With the help of a subset size forward selection method, the number of significant features was reduced to 22 elements. Figure 5.5 depicts a classified signal extract along with the raw acceleration signals. This preliminary evaluation has shown that it seems principally possible to detect and distinguish various 'PPG artifact provoking' hand movements. Further aspects as the relation of the single types of movements with the underlying signal quality were also evaluated but are skipped here and can be examined in [232].

## 6 Unsupervised Blood Pressure Estimation Based on PAT Measurements

Chapter 4 concerned itself with the detection of degrading pulse wave signal quality and also provided first evaluations regarding the effects on practical applications such as heart rate extraction. The following part will now concentrate on the robustness of blood pressure estimation routines in different situations where the pulse wave is expected to contain significant morphological distortions. In total, three different kinds of BPE models are considered, the details of which were introduced in section 2.2. To provide a compressed overview, figure 6.1 depicts the most important details of the three BPE methods again, which were reimplemented to undergo a thorough performance analysis in the presence of artifacts and ectopic beats. It is noted that the methods were primarily selected according to their methodological approaches rather than their possible clinical significance, as the main goal was to demonstrate the invariable vulnerability of the single BPE solutions towards external impacts. Moreover, specific decisions pertaining to the implementation of the respective BPE methods (i.e. fiducial point choice in the PAT determination phase, recalibration intervals, etc.) were not questioned here, with the original specifications being straightly adopted as published by the corresponding authors.

First, the BP estimation outcome in well defined measurement scenarios with signals free of artifacts is presented in section 6.1, giving an impression of the general efficacy of the corresponding methods and verifying their correct reimplementation. In the next step, the performance will be reassessed on datasets contaminated by signal artifacts (section 6.2) and during increased ectopic beats presence (section 6.3). In that context, it will be investigated as to how far the BPE output can be improved when the proposed OPRA method (cf. section 4.3.2) and the multimodal ectopic beat detector (cf. section 4.4.2) are applied prior to the BPE process.

### 6.1 BPE Performance on Clean Signals

To test the implementation of the three considered BP estimation methods, clean subsets from various data records were chosen with the concrete aim to reproduce the originally reported performance values. Only datasets containing continuous blood pressure references are included to allow an exact evaluation of the estimation results. Moreover, datasets with varying blood pressure levels were preferred to challenge the algorithms to prove that

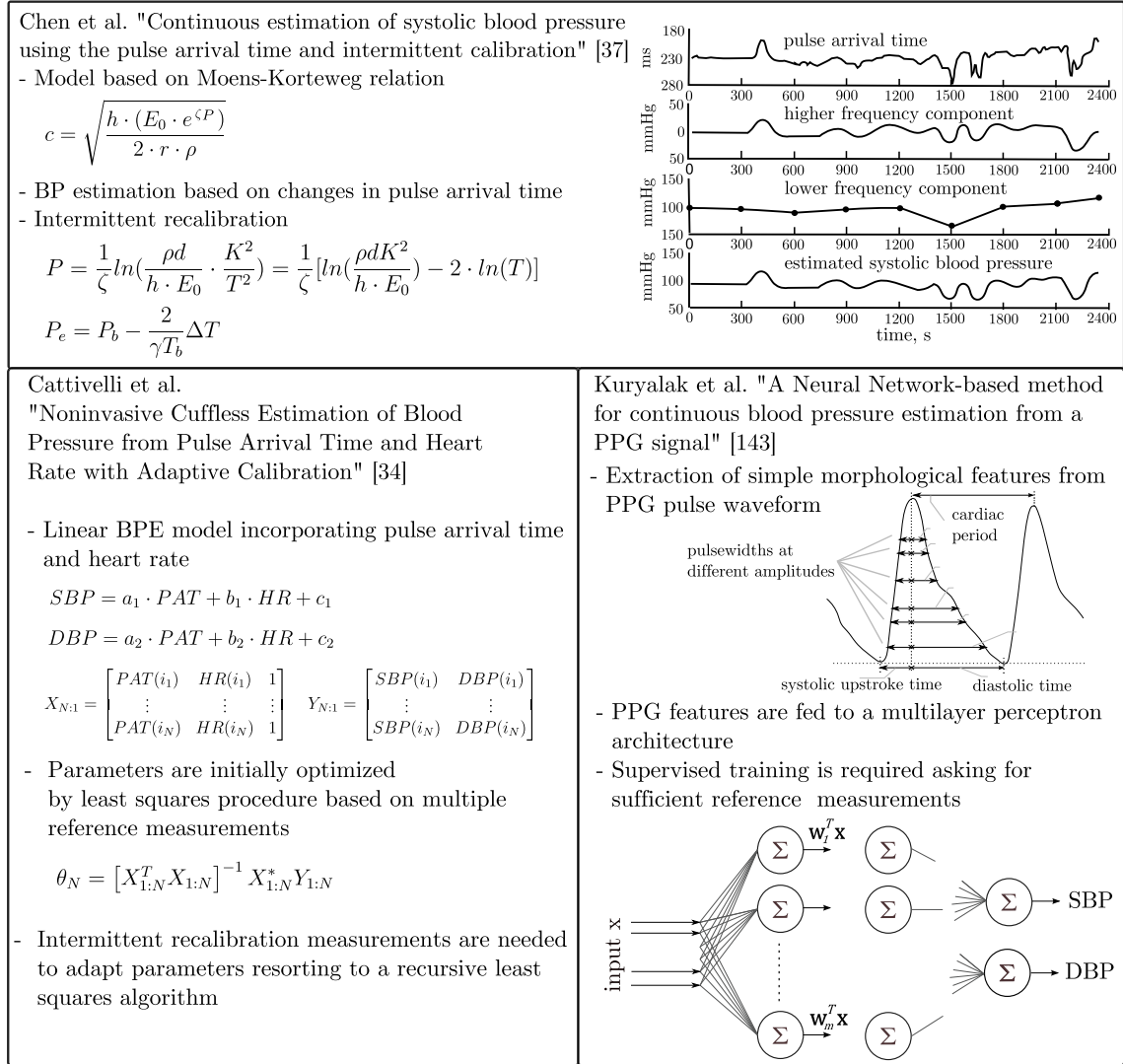


**Figure 6.1:** Overview of reimplemented BPE methods from literature. Figures were partly adopted from the original publications as was done in [225].

they can cope with changes of the cardiovascular state. This is indeed a neglected issue in current publications, as there are a lot of databases containing long periods of constant blood pressure.

The first method according to Chen et al. [37] (cf. section 2.2, eq. (2.31)) was tested with the same specifications as proposed in the original paper. Therefore, recalibration was conducted every five minutes using manually chosen SBP points to ensure correct reference values. The algorithm's outcome was originally analyzed on a beat to beat basis from which different error measurements were determined, including correlation coefficient, mean error and root mean squared error derived from estimated and reference SBP values, which is adopted for the present evaluation as well (cf. table 6.1).

Cattivelli's implementation [34] (cf. section 2.2, eq. (2.24a)) is tested in the same manner. The original paper proposes 40 initial calibration samples followed by recalibration periods

**Table 6.1:** Blood pressure estimation approach after Chen et al. [37]. Performance measures applied in the original publication including mean error, correlation coefficient, root mean square error and a probability of error distribution (Prob. 10% = range of normalized error within 10%).

Mean Error	RMSE	CC	Prob. 0%	Prob. 10%	Prob. 16%
0.06 mmHg	3.70 mmHg	0.97	38.8 %	97.8 %	99.4 %

**Table 6.2:** BPE approach after Cattivelli et al. [34]. Performance measures applied in the original publication evaluating the SBP estimation routine. DBP estimation is not considered in this work.

Mean Error	STD Error	MSE
-0.41 mmHg	7.77 mmHg	70.05 mmHg <sup>2</sup>

at intervals of 60 minutes [34]. The specific initial calibration and succeeding recalibration points were hand selected in order to provide optimal conditions for the BPE approach. Cattivelli et al. resorted to mean error and standard deviation values as well as the mean squared error averaged on all datasets to measure the BPE performance, which is adopted in the following evaluation again (cf. table 6.2).

Kuryalak’s neural network method was chosen because it follows a completely different way to solve the BPE problem [143] (cf. section 2.2). Instead of evaluating some kind of PWV model, the neural network is applied to exploit possible relations between SBP values and morphological changes of the pulse wave. The evaluation scheme in Kuryalak’s work [143] considered a subset of 15000 beats drawn from the MIMIC database were 70 % have been used for training, 15 % for validation and 15 % for testing. The chosen architecture is a two layer perceptron with 35 and 20 neurons as was proposed to be an optimum configuration in [143]. Unfortunately, the original work does not mention the number of different records used, which makes a comparable assessment somewhat difficult. However, it is assumed that Kuryalak et al. trained the neural network once, including beats of every subject. Kuryalak et al. presented two performance measures including the absolute and relative error of SBP and DBP estimations as defined by eq. (6.1).

$$e_a = |BP_{est} - BP|, \quad e_r = \frac{e_a}{BP} \quad (6.1)$$

Only the SBP estimation is considered, however.

**Table 6.3:** BPE approach according to Kuryalak et al. [143]. Performance measures applied in the original publication. Absolute error  $e_a$ : absolute magnitude between estimated SBP and reference SBP. Relative error  $e_r$ : Absolute error  $e_a$  divided by corresponding reference SBP.

absolute error $e_a$	relative error $e_r$
$3.80 \pm 3.46\text{mmHg}$	$3.48 \pm 3.19\%$

Table 6.4 presents the single performance measures of each BPE implementation applied on the clean datasets. It was also ensured that only records with an artifact free ABP reference channel were chosen. Comparing the results of the current evaluation with the performance reported by Chen et al., one observes only slightly declined averaged values of RMSE (original: 3.7 mmHg, current: 4.59 mmHg) and CC (original: 0.97, current: 0.76) but still being in accordance with the original results and thereby demonstrating proper reimplementations. The performance of the second BPE method yielded reasonable results with even better values of STD (original: 7.77 mmHg, current: 4.57 mmHg) and MSE (original: 70.05 mmHg<sup>2</sup>, current: 28.52 mmHg<sup>2</sup>) as published by Cativelli et al. The achieved results of Kuryalak’s method have also proved to be in accordance with the original work with similar measures of  $e_a$  (original:  $3.80 \pm 3.45$  mmHg, current:  $3.92 \pm 3.65$  mmHg) and  $e_r$  (original:  $3.48 \pm 3.19\%$ , current:  $3.79 \pm 3.59\%$ ). These results indicate a correct implementation of the BPE methods, which will be used to analyze the results during artifacts and ectopic beats next.

## 6.2 BPE Performance on Artifact Contaminated Signals

Having demonstrated a proper performance of the BPE models in the previous section, it is now time to investigate the robustness during periods of signal quality degradations. This will give a true notion of their applicability in unsupervised settings where motion provoked artifacts are frequently expected. The evaluation scheme will remain the same as applied to the clean datasets before, allowing for a meaningful comparison of the results.

What is striking is that the performance drastically decreases when the blood pressure is estimated on blindly extracted PAT values as is shown by the corresponding results of table 6.5. Distorted signal periods will inevitably lead to non-physiological pulse waveforms and infeasible PAT values. Especially corrupted beats that are used in the recalibration procedures will have a huge impact on the following estimation phase resulting in totally flawed estimated SBP values. The BPE procedure after Chen et al. for example suffers extremely when determining the recalibration parameter  $T_b$  within bad quality segments, as this will affect the entire period until the next recalibration (cf. eq. (2.29)). As Cativelli’s method relies on RLS optimization using few samples only, one occasionally observes convergence problems during recalibration on corrupted beats leading to intolerable outputs.

**Table 6.4:** Performance evaluation of the three different blood pressure estimation methods applied on clean datasets only. The records have been drawn from multiple studies including different hardware systems, measurement conditions, and reference blood pressure signals. The respective performance measures have been drawn from the original works. All methods yield reasonable results similar to the published values.

record	#beats	mean	STD	CC	MSE	RMSE	$e_a$	$e_r$
<i>Chen</i>								
r212_23p0	5573	0.26	2.74	0.90	7.59	2.75	$2.12 \pm 1.76$	$2.09 \pm 1.75$
r212_37p0	6226	-0.13	2.90	0.88	8.45	2.91	$1.99 \pm 2.12$	$2.24 \pm 2.42$
r212_20p8	5956	-0.61	3.56	0.92	13.03	3.61	$2.54 \pm 2.56$	$2.68 \pm 2.67$
rec041_0	5597	0.86	5.67	0.91	32.83	5.73	$3.72 \pm 4.36$	$3.50 \pm 3.87$
rec041_9	4710	0.32	3.89	0.64	15.21	3.90	$3.10 \pm 2.37$	$2.47 \pm 1.88$
rec041_11	4566	-0.13	4.39	0.49	19.27	4.39	$3.25 \pm 2.96$	$2.58 \pm 2.35$
d02_012_sub	211	5.43	5.68	0.58	61.53	7.84	$6.60 \pm 4.25$	$4.07 \pm 2.62$
sum/avg	32839	1.11	4.12	0.76	22.56	4.45	$3.33 \pm 2.91$	$2.81 \pm 2.51$
<i>Cattivelli</i>								
r212_23p0	5573	0.01	2.90	0.89	8.43	2.90	$1.85 \pm 2.24$	$1.84 \pm 1.75$
r212_37p0	6226	0.32	3.93	0.79	15.51	3.94	$2.13 \pm 3.31$	$2.38 \pm 2.42$
r212_20p8	5956	-1.37	4.87	0.90	25.58	5.06	$3.21 \pm 3.91$	$3.32 \pm 2.67$
rec041_0	5597	1.07	6.57	0.89	44.28	6.65	$4.40 \pm 5.00$	$4.16 \pm 3.87$
rec041_9	4710	0.60	4.46	0.55	20.28	4.50	$3.29 \pm 3.07$	$2.61 \pm 1.88$
rec041_11	4566	-0.22	4.57	0.40	20.93	4.58	$3.57 \pm 2.87$	$2.83 \pm 2.35$
d02_012_sub	211	-5.88	3.88	0.59	49.57	7.04	$6.14 \pm 3.45$	$3.83 \pm 2.62$
sum/avg	32839	1.35	4.45	0.71	26.37	4.95	$3.51 \pm 3.41$	$3.00 \pm 3.04$
<i>Kuryalak</i>								
r212_60m_23p0	5573	3.49	5.64	0.43	43.95	6.63	$5.58 \pm 3.59$	$5.50 \pm 1.65$
r212_60m_37p0	6226	-0.44	4.80	0.60	23.20	4.82	$3.53 \pm 3.27$	$3.96 \pm 2.33$
r212_60m_20p8	5956	-3.96	7.10	0.50	66.04	8.13	$6.26 \pm 5.18$	$6.96 \pm 2.58$
rec041_60m_0	5597	0.59	7.54	0.84	57.22	7.56	$5.28 \pm 5.42$	$5.21 \pm 3.85$
rec041_60m_9	4710	-0.11	2.50	0.86	6.25	2.50	$1.97 \pm 1.54$	$1.57 \pm 1.86$
rec041_60m_11	4566	0.10	3.38	0.68	11.45	3.38	$2.10 \pm 2.65$	$1.66 \pm 2.05$
d02_012_sub	211	-0.25	4.75	0.50	22.49	4.74	$2.72 \pm 3.89$	$1.70 \pm 2.69$
sum/avg	32839	1.28	5.10	0.63	32.94	5.39	$3.92 \pm 3.65$	$3.79 \pm 3.59$

The neural network approach proposed by Kuryalak et al. also fails when confronted with morphologically distorted beats, which is expected as the estimation completely depends on the evaluation of pulse curve features.

It becomes obvious that unsupervised BP estimation is in no way feasible without proper signal quality considerations, especially when artifacts and noise are present. A reliable automatic signal quality estimator could reintroduce a reasonable estimation performance, which is investigated next. The results of table 6.6 present the positive impact of applying an automatic signal quality detection routine prior to the BPE process. In that evaluation run (incorporating the same records as used in table 6.5), only beats which have been assigned a good signal quality label using the OPRA algorithm introduced in section 4.3.2 were considered in the respective BPE method, otherwise they are discarded. The overall performance significantly increases again as estimation output outliers caused by deformed

**Table 6.5:** Performance evaluation of the three different blood pressure estimation methods applied on artifact contaminated signals. The respective performance measures significantly decrease, partly falling below reasonable levels which underlines the importance of signal quality considerations during BPE applications.

record	#beats	mean	STD	CC	MSE	RMSE	$e_a$	$e_r$
<i>Chen</i>								
m3_417_1	4669	-1.25	13.42	0.30	181.56	13.47	$6.57 \pm 11.77$	$6.22 \pm 10.13$
m3_417_3	4002	1.76	10.38	0.53	110.86	10.53	$4.76 \pm 9.39$	$4.62 \pm 8.90$
m3_417_6	3406	1.77	11.49	0.30	135.08	11.62	$4.96 \pm 10.51$	$4.61 \pm 9.06$
m3_417_8	5860	0.30	12.57	0.52	158.13	12.57	$5.24 \pm 11.43$	$5.50 \pm 11.73$
m3_781_5	9192	-1.35	10.49	0.34	111.78	10.57	$6.18 \pm 8.58$	$5.80 \pm 8.25$
m3_781_7	10258	4.28	28.25	0.16	816.10	28.57	$11.74 \pm 26.04$	$10.12 \pm 22.33$
m3_860_3	8974	2.27	22.33	0.26	503.77	22.44	$7.27 \pm 21.24$	$5.59 \pm 16.92$
sum/avg	46361	1.86	15.56	0.34	288.18	15.68	$6.67 \pm 14.14$	$6.07 \pm 12.47$
<i>Cattivelli</i>								
m3_417_1	4669	1.11	6.96	0.61	49.66	7.05	$4.87 \pm 5.10$	$4.67 \pm 10.13$
m3_417_3	4002	-0.35	4.13	0.85	17.20	4.15	$3.21 \pm 2.63$	$3.13 \pm 8.90$
m3_417_6	3406	-0.70	4.45	0.82	20.26	4.50	$3.41 \pm 2.93$	$3.25 \pm 9.06$
m3_417_8	5860	-0.53	5.19	0.82	27.24	5.22	$3.30 \pm 4.04$	$3.43 \pm 11.73$
m3_781_5	9192	0.32	5.85	0.66	34.34	5.86	$4.04 \pm 4.24$	$3.77 \pm 8.25$
m3_781_7	10258	-0.85	7.35	0.68	54.79	7.40	$4.43 \pm 5.93$	$3.81 \pm 22.33$
m3_860_3	8974	0.10	6.76	0.38	45.69	6.76	$4.50 \pm 5.04$	$3.41 \pm 16.92$
sum/avg	46361	0.56	5.81	0.69	35.60	5.85	$3.97 \pm 4.27$	$3.64 \pm 3.89$
<i>Kuryalak</i>								
m3_417_1	4669	-4.77	17.89	0.15	362.78	19.04	$7.02 \pm 9.15$	$7.87 \pm 10.13$
m3_417_3	4002	-1.08	14.81	0.38	123.10	11.10	$5.53 \pm 5.27$	$5.44 \pm 8.90$
m3_417_6	3406	-4.07	24.81	0.25	424.32	20.6	$7.70 \pm 8.26$	$8.57 \pm 11.06$
m3_417_8	5860	-1.65	16.11	0.28	137.74	11.74	$5.81 \pm 6.82$	$5.29 \pm 11.73$
m3_781_5	9192	2.29	15.71	0.34	332.68	18.24	$5.19 \pm 6.89$	$4.93 \pm 8.25$
m3_781_7	10258	-3.05	27.30	0.23	754.33	27.47	$14.70 \pm 11.68$	$14.01 \pm 22.33$
m3_860_3	8974	1.17	15.80	0.24	733.64	27.09	$12.51 \pm 9.64$	$13.41 \pm 16.92$
sum/avg	46361	-1.59	18.92	0.27	409.8	19.33	$8.35 \pm 8.24$	$8.5 \pm 9.9$

pulses were reliably removed. This result confirms the need for an automatic signal quality detection stage prior to unsupervised BPE. Especially during crucial periods, such as recalibration procedures, the signal quality detector should classify in a very conservative manner in order suppress major inaccuracies as discussed earlier.

### 6.3 BPE Performance During Ectopic Beats

The second part of the current analysis deals with the effects of ectopic beats on the accuracy of different BPE procedures. As mentioned earlier, this issue has given rise to particular concern in recent publications [30] and requires reliable solutions when BPE methods are to be applied. Therefore, further evaluations similar to those in the previous section were conducted, this time with datasets containing an increased amount of ectopic beats to confront the BPE methods with the burden of a more difficult waveform analysis.

**Table 6.6:** BP estimation on disturbed data on OPRA cleaned signals

record	beats (% bad)	mean	STD	CC	MSE	RMSE	$e_a$	$e_r$
<i>Chen</i>								
m3_417_1	4669 (42)	-0.54	4.48	0.77	20.35	4.51	$3.61 \pm 2.71$	$3.52 \pm 2.69$
m3_417_3	4002 (7)	0.11	3.96	0.87	15.70	3.96	$3.12 \pm 2.44$	$3.05 \pm 2.45$
m3_417_6	3406 (5)	0.54	4.32	0.80	18.93	4.35	$3.47 \pm 2.62$	$3.34 \pm 2.49$
m3_417_8	5860 (11)	-0.23	4.59	0.86	21.09	4.59	$3.67 \pm 2.76$	$3.93 \pm 2.98$
m3_781_5	9192 (36)	0.91	4.74	0.70	23.27	4.82	$3.63 \pm 3.17$	$3.30 \pm 2.87$
m3_781_7	10258 (27)	0.11	5.14	0.58	26.39	5.14	$3.87 \pm 3.37$	$3.39 \pm 3.04$
m3_860_3	8974 (29)	-0.02	5.46	0.63	29.78	5.46	$4.21 \pm 3.47$	$3.17 \pm 2.62$
sum/avg	46361 (25)	0.35	4.67	0.74	22.22	4.69	$3.66 \pm 2.93$	$3.39 \pm 2.74$
<i>Cattivelli</i>								
m3_417_1	4669 (42)	0.24	4.54	0.73	20.62	4.54	$3.59 \pm 2.78$	$3.47 \pm 2.69$
m3_417_3	4002 (7)	-0.47	3.85	0.86	15.04	3.88	$3.05 \pm 2.39$	$2.98 \pm 2.45$
m3_417_6	3406 (5)	-0.65	4.10	0.84	17.26	4.15	$3.21 \pm 2.64$	$3.07 \pm 2.49$
m3_417_8	5860 (11)	-0.41	3.83	0.88	14.85	3.85	$2.84 \pm 2.60$	$3.00 \pm 2.98$
m3_781_5	9192 (36)	0.23	4.49	0.72	20.21	4.50	$3.14 \pm 3.22$	$2.88 \pm 2.87$
m3_781_7	10258 (27)	0.36	5.21	0.59	27.24	5.22	$3.70 \pm 3.68$	$3.23 \pm 3.04$
m3_860_3	8974 (29)	-0.13	6.98	0.40	48.73	6.98	$4.40 \pm 5.42$	$3.29 \pm 2.62$
sum/avg	46361 (25)	0.36	4.71	0.72	23.42	4.73	$3.42 \pm 3.25$	$3.13 \pm 2.94$
<i>Kuryaluk</i>								
m3_417_1	4669 (42)	0.71	7.82	0.09	61.66	7.85	$5.99 \pm 5.08$	$5.68 \pm 2.69$
m3_417_3	4002 (7)	0.08	4.95	0.77	24.55	4.95	$3.77 \pm 3.22$	$3.66 \pm 2.45$
m3_417_6	3406 (5)	-0.43	5.39	0.69	29.27	5.41	$3.58 \pm 4.05$	$3.44 \pm 2.49$
m3_417_8	5860 (11)	-0.42	6.20	0.67	38.65	6.22	$4.90 \pm 3.83$	$5.17 \pm 2.98$
m3_781_5	9192 (36)	0.54	6.02	0.46	36.59	6.05	$4.39 \pm 4.16$	$4.12 \pm 2.87$
m3_781_7	10258 (27)	-0.25	7.67	0.34	58.90	7.67	$4.48 \pm 6.23$	$3.77 \pm 3.04$
m3_860_3	8974 (29)	0.48	6.03	0.36	36.56	6.05	$4.72 \pm 3.77$	$3.55 \pm 2.62$
sum/avg	46361 (25)	0.42	6.30	0.48	40.88	6.31	$4.55 \pm 4.34$	$4.20 \pm 3.87$

First, each BPE implementation is exercised on datasets full of extrasystoles, which are assumed to have a serious impact on the estimation performance. In the second run, the same signals are presented to the algorithms again, but this time preprocessed by the proposed EB discriminator from section 4.4.2, removing VEBs and SVEBs prior to the subsequent BPE procedure.

Figure 6.2 gives a visual impression on the influence of EBs on an example BPE process (based on Chen’s approach [37]). The upper part presents two timelines where the PAT signal is drawn at the top and the estimated systolic blood pressure (bold) along with the continuous SBP reference in the bottom plot. The ectopic beats can be identified by the sharp deflections in the PAT trace, which are due to the difficulties in detecting the pulse wave onsets (cf. discussion in section 4.1). The overall estimation output is clearly hampered, with even more severe deviations occurring when a recalibration routine is based on an inaccurate PAT value caused by an extrasystole. The second plot, on the other hand, presents the same signal extract, where all PAT values that were determined during an underlying ectopic beat have been discarded. As can be seen, this results in a roughly undisturbed PAT curve.

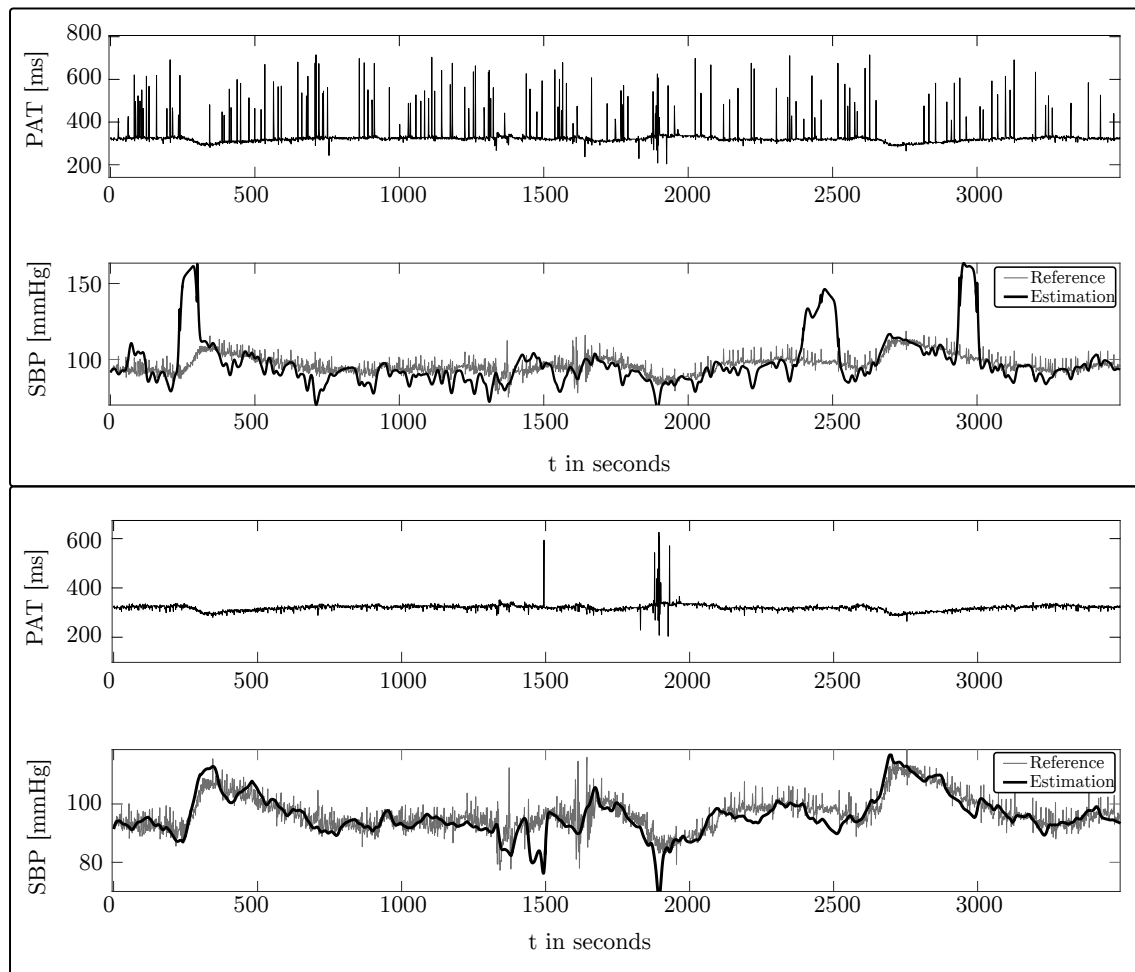


**Figure 6.2:** Example BPE estimation output (Chen’s method [37]) before (*top*) and after automatic ectopic beat clearance (*bottom*). The PAT trace is given in the top plots, whereas the estimated systolic blood pressure (bold) along with the continuous SBP reference are plotted at the bottom. Figure adopted from [225].

The corresponding performance results are summarized in table 6.7 listing the same error measures discussed in the previous section. It is stressed once more that the three methods were chosen due to their different nature of approaching the BPE process in order to check whether all models are affected by ectopic beat presence to the same extent. The absolute values of the performance measures are not further scrutinized here, as this work only concentrates on the relative changes before and after ectopic beat clearance. A thorough interpretation of these values would actually require much more effort and particularly more detailed information on the single datasets. As noted before, datasets containing segments with significantly varying PAT and BP values pose a clearly higher demand on the BPE process when compared to extracts consisting of steady and nearly constant signals. Unfortunately, such considerations are neglected in most of the original publications, calling for future efforts and further comparative investigations.

When analyzing the BPE performance during periods of ectopic beats, as is presented in table 6.7 A), one clearly recognizes the notable drops of the single error measures. The

**Table 6.7:** BPE performance evaluation. A) BPE error measurements on datasets containing ectopic beats. B) BPE error measurements on same datasets used in A) where the ectopic beat cancellation using the multimodal method proposed in this work was applied prior to the BPE process.

method	mean error	STD error	CC	MSE	RMS	$e_a$	$e_r$
<b>A) BPE performance on datasets with ectopic beat presence</b>							
Chen	0.96	9.41	0.2966	89.36	9.45	$6.98 \pm 6.4$	$7.15 \pm 6.6$
Cattiveli	4.25	25.6	0.07	674.5	25.97	$6.32 \pm 25.2$	$6.32 \pm 24.7$
Kuryalak	-83.9	8.01	0.13	7112	84.3	$83.9 \pm 8.1$	$87.4 \pm 12.0$
<b>B) BPE performance with ectopic beat presence, after prior EB clearance</b>							
Chen	-0.81	5.09	0.88	26.7	5.17	$3.81 \pm 3.5$	$4.02 \pm 3.7$
Cattiveli	0.17	4.23	0.91	17.9	4.24	$2.92 \pm 3.1$	$3.06 \pm 3.1$
Kuryalak	0.05	4.41	0.84	19.41	4.41	$3.29 \pm 2.9$	$3.55 \pm 3.3$

estimation outputs partly exceed physiologically meaningful boundaries, underlining the serious difficulties in handling a reliable pulse wave timing extraction during ectopic beats. Table 6.7 B) demonstrates the capability of the proposed multimodal ectopic beat discriminator to remove the previous encountered outliers when it is applied for EB clearance prior to the BPE process, resulting in feasible performance values again. However, it is worth remembering that for each detected ectopic beat, the corresponding pulse wave feature and its connected BPE sample is discarded. Thus, a continuous blood pressure estimation during periods of ventricular tachycardia, for example, would not be possible anymore.



## 7 Conclusion

This last section will finish the work by summarizing its major achievements in the different disciplines. It is further discussed how far the reported results can be transferred to practical applications, recapitulating their capabilities and outlining known limits. Finally, open points are addressed, encouraging future works to build on the groundwork laid by this thesis.

### 7.1 Major Contributions of This Work

The preceding chapters concentrated on automatic pulse wave analysis in practical situations and addressed several important aspects ranging from hardware related questions to sophisticated signal processing issues. The importance of PWA was demonstrated by the example of contemporary applications including blood pressure estimation based on PAT/PTT calculation, which turned out to pose firm requirements on the involved procedures. As PAT intervals are typically derived by ECG and PPG recordings, wireless body sensor networks are applied in practical measurement setups that played a central role in the investigations conducted in this work. To get an up-to-date overview on existing BSN systems, literature was combed to examine the strengths and shortcomings of current implementations. Driven by the desire to further improve PWA methods, a novel low power BSN was developed, incorporating competitive features such as Bluetooth based clock synchronization with errors below  $30\ \mu\text{s}$ , modular sensor design, robust data acquisition mechanisms and onboard motion recognition.

Next, published BPE routines and underlying PWA signal processing steps such as fiducial point extraction were introduced and scrutinized with respect to their application on ambulatory datasets. Whereas it was confirmed that the single delineation techniques depend on external influences to different extents none was able to provide reasonable results once the pulse wave signal quality fell below a certain level. This underlined the urgent need for reliable pulse wave signal quality detection especially in PAT/PTT based scenarios. In consequence literature proposals for signal quality detection were thoroughly researched to find solutions aiding unsupervised PWV measurements on small battery driven BSN devices. Unfortunately, none of the considered methods could comprehensively convince, either lacking satisfying performance and applicability or incorporating excessive computational loads.

This triggered the presented development of a novel pulse wave signal quality estimator, which has shown to outperform existing methods in the different disciplines. The superior performance of the proposed method and its applicability on low power battery driven devices can be seen as the major contribution of this thesis. In a second step, it was evaluated on different BPE procedures, which demand superb signal quality to reliably extract the required pulse wave features. The following insights could be gathered during the conducted evaluations.

First, different BPE implementations were challenged on the same datasets to reassess multiple performance measures as reported in the original publications. Such direct comparisons are rare in literature and are - to the best knowledge of the author - not available for BPE methods yet. It was shown that all methods invariably fail when confronted with artifact contaminated records but perform reasonably again once guarded by the novel signal quality estimator. Next to artifacts provoked by motion present in the measurements, pathophysiological influences such as ectopic beats were additionally examined, which was called for in recent publications. Therefore, proper datasets containing an increased presence of extrasystoles were collected, to prove that they lead to severe distortions of the BPE routines.

After reviewing prominent approaches for EB detection, an effective multimodal ectopic beat discrimination algorithm was presented, accompanied by a demonstration of on-line extrasystole cancellation during BPE procedures. It turned out that the inclusion of multimodal features improves the sensitivity and specificity of the ectopic beat detection process, which is interesting for applications that have access to synchronized ECG and pulse wave signals anyway.

Recovering artifact contaminated signals is a logical consequence, once the signal quality was reliably detected. Thus, this work also included a broad examination of the manifold artifact reduction schemes that appeared in the last years. As methods involving additional observations linked to the source of artifacts (in particular motion related information) were reported to yield more promising results, a novel approach exploiting the onboard acceleration sensors by means of blind source separation was promoted. In preliminary experiments, it could be shown that the presented BSS method outperforms traditional ANC procedures, advertising itself to enhance unsupervised PWA applications. The conducted research and analysis on PPG artifact cancellation gave forth another important byproduct. As different hand movements are known to provoke different kind of artifacts in pulse wave forms, an efficient hand movement detector was additionally proposed, which yields reliable classification results by evaluating features derived from the PPG sensor's ACC modules only.

## 7.2 Limitations and Unsolved Issues

Whereas the presented results provide a significant enrichment for applications involving automatic pulse wave analysis, possible restrictions are discussed next.

As the proposed OPRA method mastered all performance tests with superior results, the basic idea to analyze morphological differences of adjacent beats was confirmed as a proper starting point to tackle PPG signal quality detection problems. Nonetheless, one possible situation could still introduce significant difficulties. Although this issue was not encountered in the datasets of this work, artifacts producing morphologically similar beats, could be mistakenly classified as clean samples. Fortunately, this situation is not expected in realistic settings too often. Periodic motions during the ergometer and treadmill exercises that were part of the conducted stress tests all produced varying waveform distortions. Still, it is conceivable that strong and periodic arm movements might introduce monomorphic artifacts. To handle this rare case, the evaluation of additional motion information as presented in this work would be a reliable way to overcome this limitation, requiring more advanced devices such as the rBSN sensors.

Next, the multimodal ectopic beat discriminator yielded excellent results but is only applicable when synchronous ECG and PPG recordings are available. This is a serious limitation compared to methods requiring sole ECG channels only. One might even argue that the comparatively small performance increase does not justify the operation of an additional pulse wave channel. However, when both signals are needed anyway (as is the case in BPE applications), the proposed method provides a free performance gain.

With respect to PPG artifact suppression, a rather computationally complex solution was presented, which does not only require powerful hardware, but also additional sensors providing acceleration signals. When power consumption does not play a major role, this method should be considered for application, otherwise alternative methods might be preferable. It is noted that low power consumption is one of the key features of the presented rBSN system in order to support longtime measurement while enabling robust acquisition of multichannel biosignals at high sampling rates. As a consequence, processing capabilities in general are limited, restricting the full integration of sophisticated algorithms running on the sensors' microcontrollers.

Although many results were thoroughly analyzed in this work, several aspects remain untouched in the respective investigations. One important point to mention involves the evaluation of the PAT/PTT based BPE methods, which were focused to assess the performance of the presented signal quality and ectopic beat discriminators in a practical scenario. It was shown that different BPE methods are equally hampered by degrading pulse wave signal quality and increased ectopic beat presence. However, only relative changes of prominent error measures were considered, skipping an objective assessment of the absolute BPE performances themselves. In fact, it was demonstrated that the performance significantly decreases on contaminated periods, which can be mitigated with the help of the proposed detection methods. To interpret the absolute performance values, further efforts are necessary. This would include a deeper discussion of the single parameters as recalibration intervals, the training process of the neural network approach or the constitution of the datasets.

With respect to the novel multimodal EB detector, no direct comparison with existing

methods was performed, as this would have required a reimplementation of the published approaches. The same issue holds for the evaluation of the ICA artifact reduction procedure, which was merely challenged against an ANC based noise cancelator. Such undertakings are rather hard to realize as one has to provide the different inputs required by the single methods, which might not be available on every dataset. Furthermore, the feasibility of artifact suppression in BPE applications was not investigated in this work.

### 7.3 Future Works and Outlook

Concluding from the different discussions of the previous chapters, several aspects were identified that call for future works to further improve automatic PWA applications.

It is clear that the development of BSN related hardware will never cease, with integrated circuits becoming smaller, cheaper and more powerful. Thus, more sophisticated implementations can be expected. As the sensors become more integrated and unobtrusive, the possibilities of treatments and applications broaden steadily.

With respect to the presented signal processing advances, several points still remain unsolved. Although this work provided a novel contribution with preliminary results to suppress motion artifacts in PPG signals, its benefits for BPE methods have not yet been scrutinized yet. As a matter of fact, this requires a thorough understanding of the influence of the artifact elimination procedures on the physiological content of the pulse wave. Therefore, further investigations need to be conducted, showing that the physiological information of the processed pulse waves remain unaltered, which is essential for correct PAT/PTT extraction. In that context, the inspection of more artifact reduction and ectopic beat detection reimplementations would portentously contribute to a competitive analysis of the published methods. Furthermore, one should contemplate integrating the proposed hand movement detector in the processing steps, which could guide automated decisions during artifact reduction and related procedures.

The presented improvements of robust PWA were demonstrated by three different BPE approaches, which have revealed a significant vulnerability towards motion artifacts and ectopic beats. This investigation should be extended by including more BPE methods and by fine tuning the single implementations (e.g. choosing more reliable fiducial points as discussed in section 4.1, revising recalibration strategies etc.). Moreover, a quantitative evaluation of the absolute error measurements is required to discuss the applicability of the BPE methods in a specific application such as orthostatic hypotension analysis.

# 8 Appendix

## 8.1 Tables

**Table 8.1:** Exercise protocol for measurements of database *rBSN\_studentDatabaseI*.

section	activity	duration in [s]
control phase	rest	120
	bump	40
hand movements	pause	20
	shake wrist	40
	pause	20
	tap finger	40
	pause	20
	horizontal twitch forwards	40
	pause	20
	horizontal twitch backwards	40
	pause	20
	horizontal circle	40
	pause	20
	wrist rotate	40
	pause	20
	shaking	40
	pause	20
	walking	walking on a treadmill at 4 km/h
pause		20
cycling	ergometer at 120 Watts, 80 rpm	180
control phase	rest	120

Table 8.3: Literature overview on body sensor networks I.

BSN	sensor signals	onboard data storage	technology, true WBSN	sync. accuracy	BSN power consumption	application / special features	clinical studies
Espina [67]	1 ch. ECG, ear PPG ( $f_s = 200Hz$ )	n.a.	IEEE 802.15.4 yes	FTSP $48\mu s$	n.a.	PAT monitoring SBP estimation	n.a.
Ghoshdastider [82]	ECG, EMG, EEG, ACC ( $f_s = 1000Hz$ )	n.a.	IEEE 802.11b yes	no wireless synchronization	n.a.	neurophysiological monitoring	n.a.
Shnayder [282]	1 ch. ECG, PPG, EMG, ACC, Gyro ( $f_s = 1Hz..1kHz$ )	n.a.	IEEE 802.15.4 yes	no wireless synchronization	25mA (ACC sensor)	multicast routing topology	yes
Milenkovic [186], [127] [127]	single ch. ECG ACC ( $f_s = 200Hz$ )	n.a.	IEEE 802.15.4 yes	modified FTSP $48\mu s$ [48]	21mA (ACC sensor)	-	n.a.
Monton [189]	ECG, EMG, EEG, SBP ( $f_s = 100Hz$ )	n.a.	IEEE 802.15.4 yes	Beacon based mean: $59, 5\mu s$ max: $262, 3\mu s$	n.a.	modular design with analog and digital recording interfaces	n.a.
Gay [80] [161]	ECG, ACC	n.a.	IEEE 802.15.1 yes	n.a.	n.a.	commercial sensors attached to a PDA	n.a.
Volmer [314]	1 ch. ECG, PPG, ACC, PCG ( $f_s = 100..500Hz$ )	yes	IEEE 802.15.4 yes	$4\mu s$	16mA	-	n.a.
Jin [119]	2 ch. ECG, ACC $f_s = 300Hz$ (8-bit)	yes	IEEE 802.15.1 no	-	-	signal processing framework on PDA	n.a.

Table 8.4: Literature overview on body sensor networks II.

BSN	sensor signals	onboard data storage	technology, true WBSN	sync. accuracy	BSN power consumption	application / special features	clinical studies
Dias [56]	ECG ( $f_s = 1kHz$ ), ACC ( $f_s = 300Hz$ ), EMG ( $f_s = 4kHz$ )	yes	IEEE 802.15.1, no	-	-	textile worn sensors	n.a.
Varatharajah [309]	ECG, nasal flowrate, temp., ACC	yes	IEEE 802.15.4, yes	-	-	energy expenditure	n.a.
Perez [222]	3 ch. ECG, PPG, temp, respiration)	n.a.	IEEE 802.15.4, yes	n.a	n.a	n.a	n.a
Luprano [174]	ECG	n.a.	IEEE 802.15.4 no	n.a	n.a	unobtrusive textile electrodes	n.a
Noury [203]	ECG, ACC, temp.	n.a.	GSM, no	n.a	n.a	textile electrodes	n.a
Mundt [196]	ECG (II, V5), temp., SpO2, ACC	32 MByte Flash	802.15.1, no	n.a	0.36W streaming, 0.2W logging	extreme env. applications	n.a
Chung [40]	1 ch. ECG (200Hz), PPG (75Hz) ACC	8 MByte Flash	802.15.4, yes	n.a	n.a	-	n.a
Curtis[49]	ECG, SpO2, ACC	PDA	802.15.11, no	n.a	n.a	sensors woven in fabrics	yes
Pandian [215]	ECG (Einthoven), PPG, GSR, temp., GPS	-	not specified, no	n.a	n.a	blood pressure estimation	yes

Table 8.5: Literature overview on body sensor networks III.

BSN	sensor signals	onboard data storage	technology, true WBSN	sync. accuracy	BSN power consumption	application / special features	clinical studies
Wang [322]	EKG (Einthoven), PPG, ACC,	-	not specified, yes	n.a	n.a	activity recognition	no
Aziz, [13]	PPG (Ear), ACC	-	not specified, no	n.a	n.a	monitoring postoperative recovery at home in patients undergoing abdominal surgery	no
Gao [79] (AID-N)	two lead ECG, SpO <sub>2</sub> , Blood pressure (Advantage Mini)	n.a.	IEEE 802.15.4, n.a	n.a	n.a	triage, sensors based on MICAz, TmoteSky	n.a
Di Rienzo [262] (MagIC)	EKG, respiration, ACC	n.a.	not specified, no	n.a	n.a	textile woven sensors	n.a

**Table 8.6:** This table contains a complete list of the EB detection features implemented as a part of this work. They can be divided into seven groups, based on their target properties. The different markers required for the calculation can be found in the right column.

#	feature group	descriptor	required markers	
1	ECG Interval	post RR interval	R-Peak	
2		pre RR interval		
3		pre/post RR interval		
4		local RR interval		
5		average RR interval		
6		PR distance		R-, P-Peak
7		RT distance		R-, T-Peak
8		QRS width		QRS onset, offset
9				
10				
11				
12				
13		10 samples in -50 +100 ms around R-Peak		
14				
15				
16				
17				
18	ECG amplitude	_____	R-Peak	
19				
20				
21				
22			9 samples in +150 +500 ms around R-Peak	
23				
24				
25				
26				
27		_____		
28		R-Peak amplitude		
29		T-Peak amplitude	T-Peak	
30		P-Peak amplitude	P-Peak	
31				
32				
33	ECG ICA	6 IC from 4th level approximation	R-Peak	
34				
35				
36				
37		_____		
38				
39		6 IC from 4th level detail		
40				

41		
42		
43		QRS mean
44		QRS std
45		QRS kurtosis
46	ECG sig/stat	QRS energy
47		beat mean
48		beat std
49		beat kurtosis
50		beat energy
51		pre/post PPG interval
52		Pulse wave width
53	PPG morph	PPG peak amplitude
54		$\frac{\text{peak amp}}{\text{pre peak amp}}$
55		$\frac{\text{peak amp}}{3 \text{ peak local avg peak amp}}$
56		$\frac{\text{post peak amp}}{3 \text{ peak local avg peak amp}}$
57		
58		fractional amplitudes
59		
60		
61		
62		
63		
64		10 samples in -50 +100 ms around PPG peak
65		
66		
67		PPG Peak, onset, offset
68	PPG amplitude	
69		
70		
71		
72		
73		
74		10 samples in -50 +100 ms around next PPG peak
75		peak
76		
77		
78		
79		
80		pulse wave kurtosis
81	PPG sig/stat	pulse wave mean
82		pulse wave energy

**Table 8.8:** Published BP estimation models

author	model	study	signals	results
Poon et. al [240]	$BP_{est} = A \cdot \ln(PAT) + B$ (A and B determined by least square fitting)	nine patients undergoing neurosurgical operation	PAT measured by ECG and PPG. Reference provided by invasive BP using radial artery catheter	STD of absolute error ranging from 4.1 to 17.6 mmHg
Deb et. al [54]	$BP_{est} = A \cdot PAT + B$ (A and B determined by linear regression)	five subjects in laboratory exercise	PAT/PTT measured by ECG and PPG(brachial and finger arteries).	absolute error ranging from -16 to 25 mmHg
Zhang et. al [352]	$BP_{est} = A \cdot PAT + B$ (A and B determined by linear regression)	14 subjects in laboratory measurement	PAT measured by ECG and fingertip PPG.	absolute error ranging from 1.58 to 8.26 mmHg
Wong et. al [337]	$BP_{est} = A \cdot PAT + B$ (A and B determined by least squares regression)	14 subjects in during exercise measurement on a treadmill with repeated measurements after 6 months	PAT measured by ECG and fingertip PPG.	absolute error of $1.4 \pm 10.2$ mmHg
Cattivelli et. al [34]	$SBP_{est} = A \cdot PAT + B \cdot HR + C$ (A, B and C determined by RLS method)	34 records from MIMIC database	PAT measured by ECG and PPG	mean error: -0.41 mmHg s.d.: 7.77 mmHg MSE: 70.05 mmHg <sup>2</sup>
Mottaghi et. al [192]	$SBP_{est} = A \cdot \Delta PAT + B \cdot \Delta HR + C \cdot BP_{est-1} + D$ (A, B, C and D determined by least squares method)	55 healthy subjects during exercise stress test on a treadmill	PAT measured by ECG and PPG	RMS: 5.21 mmHg, correlation: 0.691
Baek, Kim et. al [137] [14]	$SBP_{est} = A \cdot \Delta PAT + B \cdot \Delta HR + C \cdot TDB + D$ (A, B, C and D determined by multiple regression)	several laboratory measurements including 5 to 10 healthy subjects and 10 patients during dental anesthesia.	PAT measured by ECG and PPG. Continuous reference BP provided by invasive catheter in clinical datasets and volume clamp in ambulatory datasets.	correlation: > 0.8
Gesche et. al [81]	$SBP_{PAT} = P_1 \cdot PWV \cdot e^{P_3 \cdot PWV} + P_2 \cdot PWV^{P_4} - (SBP_{PAT,cal} - SBP_{cal})$ , where $PWV = \frac{0.5 \cdot height}{PAT}$ ( $P_1, P_2, P_3$ and $P_4$ determined by least square fitting)	63 volunteers during exercise on bicycle ergometer.	PAT measured by ECG and PPG.	correlation: > 0.83
Chen et. al [37]	$P_e = P_b - \frac{2}{\gamma T_b} \Delta T$	20 patients undergoing cardiovascular surgery.	PAT measured by ECG and PPG, invasive arterial blood pressure reference available.	correlation: $0.97 \pm 0.02$ , average RMS: 3.7 mmHg
Gu et. al [96]	$SBP_{est} = \frac{A}{PTT} + B, A = (k_1 + p_1(1 - \frac{RAS}{RAS_0})) \cdot SBP_0 \cdot PTT_0, B = (k_2 + p_2(1 - \frac{RAS}{RAS_0})) \cdot SBP_0$	12 subjects during laboratory treadmill exercise	PAT measured by ECG and PPG .	mean error: $1.7 \pm 6.8$ mmHg
Kurylyak et. al [143]	multilayer perceptron	15000 beats drawn from MIMIC database	PAT measured by ECG and finger PPG .	mean absolute error $3.8 \pm 3.46$ mmHg
Fung et. al [76]	$BP = \frac{A}{PTT^2} + B, A = (0.6 * height)^2 \cdot \frac{p}{1.4}$ , (B determined by least squares fitting)	22 subjects during anesthesia	PAT measured by ECG and PPG .	mean absolute error $-0.079 \pm 11.32$ mmHg

**Table 8.9:** Estimation of the computational complexity of the corresponding feature groups. The execution times of the single feature groups were superficially inspected in a MATLAB environment. Although abstract high level library functions and the underlying Java-VM running on a desktop computer impede exact timing measurements on a clock-cycle level, one still gets a coarse impression of the computational costs. For better significance, the values were calculated as the average over all heartbeats. In a second step they were divided by the maximum value to project them on a 0 to 1 scale. The time for the delineation was calculated for T- and P-Peaks, QRS on- and offset and PPG peak. Column three contains the sum of the calculated indicators for all required markers.

feature group	required markers	normalized feature time	normalized delineation time
ECG interval I	R-Peak	0.0020	0.0000
ECG interval II	R-, P-, T-Peak QRS on/off	0.0010	1.5858
ECG amplitude I	R-Peak	0.0050	0.0000
ECG amplitude II	P, T-Peak	0.0005	0.5858
ECG ICA	R-Peak	1.0000	0.0000
ECG sig/stat I	QRS on/off	0.0700	0.2680
ECG sig/stat II	R-Peak	0.0800	0.0000
PPG morph	PPG peak, onset	0.0270	0.1670
ECG sig/stat II	R-Peak	0.0610	0.1670
ECG sig/stat II	R-Peak	0.0820	0.1670

## 8.2 Performance Measures

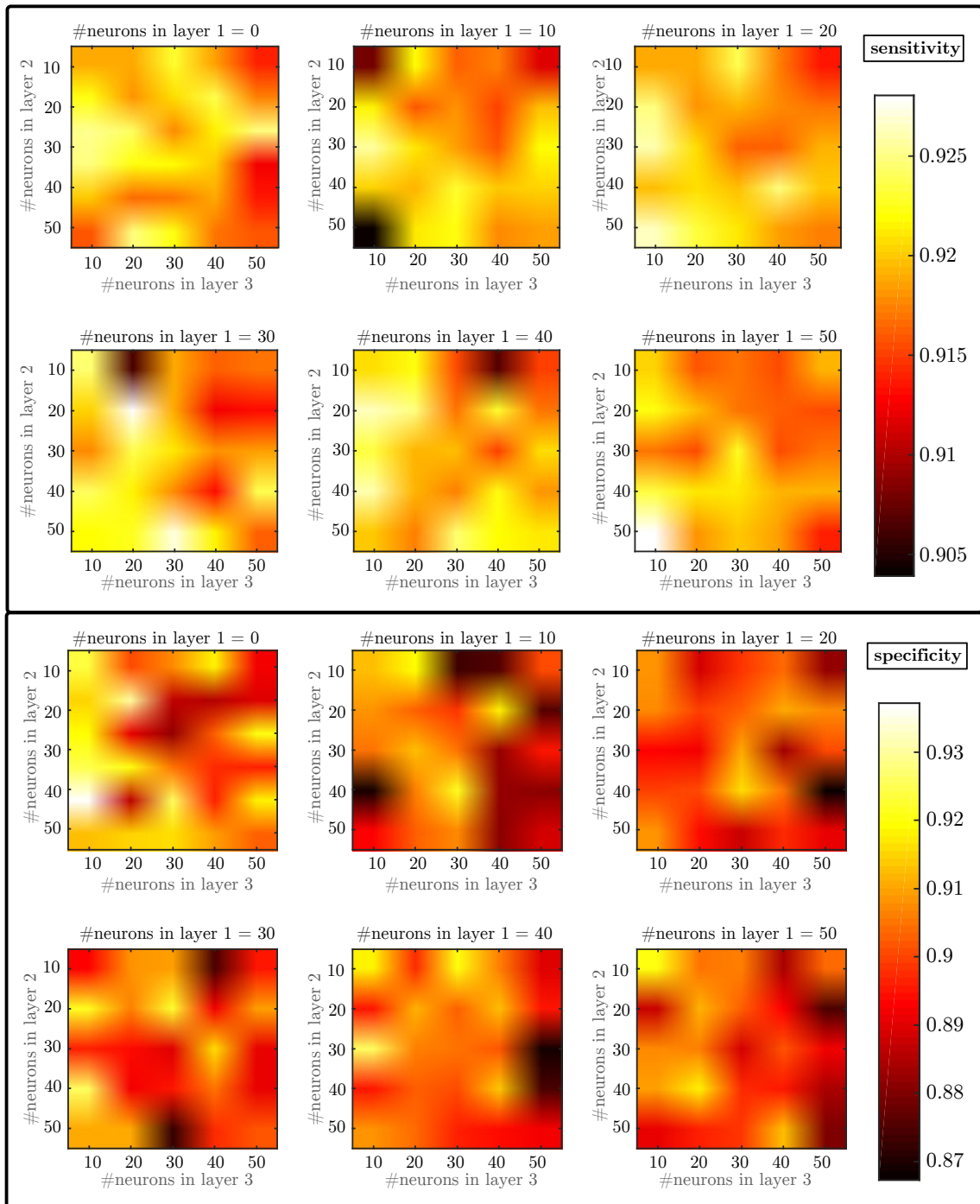


**Figure 8.1:** A three dimensional grid search is applied in order to derive an indication for an appropriate net size of the ectopic beat classifier. All features listed in table 8.6 are engaged in this evaluation. To visualise the resulting performance for different settings, two heatmaps illustrating the sensitivity (*top*) and specificity (*bottom*) are drawn. Each plot contains 6 subplots which correspond to the number of neurons in the first hidden layer (0,10,20,30,40 and 50) whereas the x- and y-axes of the subplots indicate the number of neurons in the second and third hidden layer respectively.

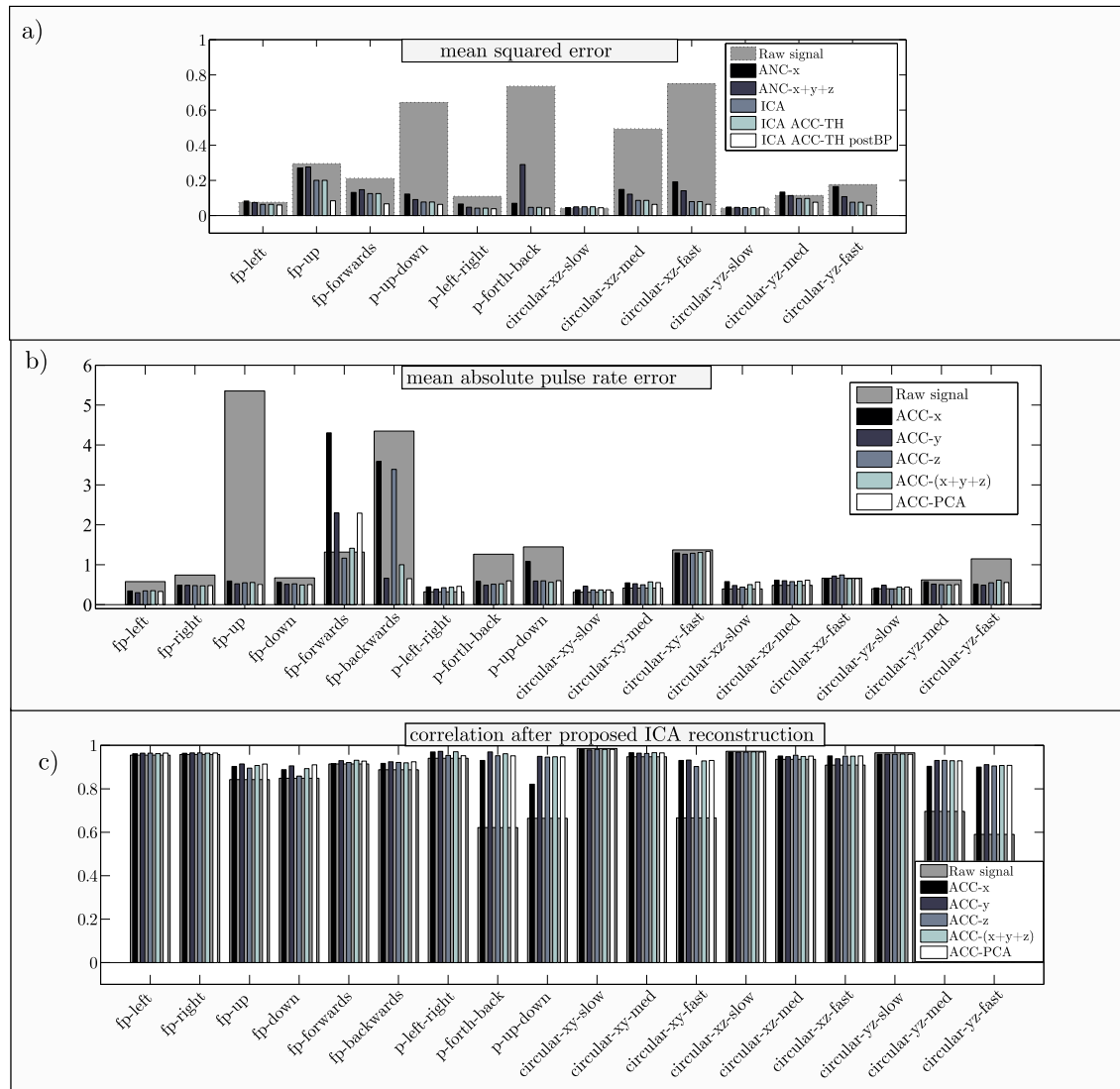


**Figure 8.2:** PPG artifact reduction performance of the proposed ICA approach. Comparison of different reference ACC combinations.

**Table 8.10:** Power consumption of *rBSN\_DualPulseOxi* and operating time on 2100 mA h lithium-ion battery.

mode of operation	current [mA]	operating time [h]
no BT, standby, reflectance+transmission	33.6	62.5
no BT, standby, reflectance	32.5	64.62
no BT, standby, transmission	14.4	145.83
no BT, active, reflectance+transmission	65.0	32.31
no BT, active, reflectance	55.0	38.19
no BT, active, transmission	35.0	60.0
BT activated, standby, reflectance+transmission	30.66	62.5
BT activated, standby, reflectance	67.5	31.11
BT activated, standby, transmission	49.9	42.08
BT activated, active, reflectance+transmission	115.0	18.26
BT activated, active, reflectance	100.0	21.00
BT activated, active, transmission	85.0	24.71

## 8.3 Additional Information

### Works published by the author

#### Journal papers

- [225] M. Pflugradt, K. Geissdoerfer, M. Goernig and, R. Orglmeister. **A fast multimodal ectopic beat detection method applied for blood pressure estimation based on pulse wave velocity measurements in wearable sensors.** *Sensors*, 17(1), 2017.
- [229] M. Pflugradt, S. Mann, T. Tigges, M. Görnig and, R. Orglmeister. **Multi-modal signal acquisition using a synchronized wireless body sensor network in geriatric patients.** *Biomedical Engineering/Biomedizinische Technik*, 61(1):57–68, 2016
- [227] M. Pflugradt, S. Mann, V. Feller, Y. Lu and, R. Orglmeister. **Online learning algorithms for principal component analysis applied on single-lead ecgs.** *Biomedizinische Technik/Biomedical Engineering*, 58(2):121–130, 2013.

#### Conference proceedings (first authorship)

- [230] M. Pflugradt, B. Moeller and, R. Orglmeister. **Opra: A fast on-line signal quality estimator for pulsatile signals.** In *9th IFAC Symposium on Biological and Medical Systems*, pages 408–413, 2015.
- [232] M. Pflugradt and R. Orglmeister. **Improved signal quality indication for photoplethysmographic signals incorporating motion artifact detection.** In *2014 6th Annual International Conference of the IEEE Engineering in Medicine and Biology Society*, pages 1872–1875, Aug 2014.
- [224] M. Pflugradt, I. Fritzsich, S. Mann, T. Tigges and, R. Orglmeister. **A novel pulseoximeter for bluetooth synchronized measurements in a body sensor network.** In *Education and Research Conference (EDERC), 2014 6th European Embedded Design in*, pages 21–25. IEEE, 2014.
- [233] M. Pflugradt and, R. Orglmeister. **Mobile ecg-ppg combined heart rate estimation using a wireless body sensor network.** *Biomedical Engineering/Biomedizinische Technik*, 59(1), 2014.
- [234] M. Pflugradt, M. Rose, and, R. Orglmeister. **A novel method for motion artifact removal in wearable ppg sensors based on blind source separation.** *Biomed Tech*, 58:1, 2013.

- [231] M. Pflugradt and R. Orglmeister. **Flexible small size actimeter for continuous movement acquisition.** In *2013 11th Interdisziplinäres Symposium des Fachausschusses AUTOMED der Deutschen Gesellschaft fuer Biomedizinische Technik (DGBMT) und der Gesellschaft fuer Mess- und Automatisierungstechnik (GMA) im VDE e.V.*, Sep 2013
- [228] M. Pflugradt, S. Mann, V. Feller and, R. Orglmeister. **On-line learning algorithms for extracting respiratory activity from single lead ecgs based on principal component analysis.** *Biomed Tech*, 57:1, 2012.
- [226] M. Pflugradt, N. Hofmeyr and, R. Orglmeister. **Multi-channel biosignal processing on an omap 3530 system.** In *Education and Research Conference (EDERC), 2012 5th European DSP*, pages 124–128. *IEEE*, 2012.

#### Conference proceedings (secondary authorships)

- [236] A.G. Pielmus, M. Pflugradt, T. Tigges, M. Klum, A. Feldheiser, O. Hunsicker, and R. Orglmeister. **Novel computation of pulse transit time from multi-channel ppg signals by wavelet transform.** *Current Directions in Biomedical Engineering*, 2(1):209–213, 2016.
- [68] V. Feller, F. Mielentz, T. Klewe, M. Krause, R. Orglmeister, and M. Pflugradt. **Ultrasonic phased array for investigations of concrete components.** In *International Symposium Non-Destructive Testing in Civil Engineering (NDT-CE)*, 2015.
- [85] M. Goernig, S. Weise, M. Pflugradt, and J. Haueisen. **Registration and evaluation of alternative non-invasive parameters for orthostatic hypotension in geriatric patients** *Annual Meeting of the German Society of Biomedical Engineering and Joint Conference in Medical Physics*, 2017.

## Acknowledgements

The results presented in this dissertation would certainly not have conveyed its achieved diversity and final quality without the help of all the fellow student scientists, who so passionately joined the research and provided invaluable input to help develop the novel solutions of the presented problems.

The outstanding commitment found in each of the involved Bachelor, Master and Diploma theses was remarkable, untiringly pushing forward further efforts and novel ideas. Not only did the written results, but also the uncountable discussions, contribute to the evolution of the final achievements.

Therefore, special thanks go to the many individuals who have offered support and inspiration, with special gratitude to Lukas Mannheimer, Ricky Kettlitz, Viktor Feller, Neels Hofmeyr, Marcus Rose, Felix Bohn, Timo Lausen, Yirong Lu, Igor Fritzs, Thomas Möller, Tim Klewe, Thomas Färber, Daniel Schäufele, Samer Al-Magazachi, Alexander Dethof, Kai Geißdörfer, Stephan Bauroth, Christiane Schiller, Oliver Wallin, Stefan Laufmann, David Martens, Fabian Hömcke, Leonhard Gollnick, Robert Hering, Daniel Weber, Tom Lehmann, Zenit Music, Benjamin Möller and thanks to Megan Hadgraft for her patience in checking my language.

Beyond that, I would like to thank my colleagues Steffen, Viktor, Marcus, Timo, Alex and Micha for pulling the same rope all the time and to Priv.-Doz. Dr. habil. Matthias Görnig, for making the clinical measurements possible and sharing his medical expertise especially during the assessment of the manifold datasets.

I am also indebted to Prof. Dr.-Ing. K. Mylvaganam from University College of Southeast Norway and Priv.-Doz. Dr.med. E. Wellnhofer from Deutsches Herzzentrum Berlin, who agreed to evaluate the written thesis.

Finally, I owe my deepest gratitude to Prof. Dr.-Ing. Reinhold Orglmeister, who succeeded in showing me the appeal of science and paved the way for all my scientific milestones of the last years.



# List of Figures

2.1	Oxyhemoglobin dissociation curve and hemoglobin molecules. . . . .	8
2.2	Physiology of the human heart. . . . .	9
2.3	Pressure pulse morphology in the arterial tree. . . . .	14
2.4	Cross-sectional cut through finger and absorption spectra of oxygenated and deoxygenated hemoglobin. . . . .	15
2.5	Young's modulus in elastic materials. . . . .	17
2.6	Example blood pressure estimation procedure according to Chen et al. . . . .	26
2.7	Morphological pulse wave features . . . . .	27
3.1	ECG frontend block diagram. . . . .	34
3.2	Block diagram rBSN sensor modules. . . . .	39
3.3	Block diagram of rBSN fingerclip pulse oxymeter. . . . .	42
3.4	rBSN PPG analog low-pass filters. . . . .	44
3.5	Assembled reflectance rBSN PPG modules . . . . .	45
3.6	CPU clock synchronization based on Bluetooth . . . . .	48
3.7	Clock synchronization performance evaluation . . . . .	49
4.1	PPG fiducial points in PAT/PTT extraction. . . . .	57
4.2	Monte Carlo simulation principle to assess different PAT measures. . . . .	60
4.3	Results Monte Carlo Simulation on different PAT measures. . . . .	61
4.4	PPG snippets during different movement experiments. . . . .	63
4.5	PPG signal quality estimation approaches from literature. . . . .	65
4.6	PCA demonstration on sample datapoints. . . . .	71
4.7	Single layer perceptron performing PCA method. . . . .	74
4.8	Principal Component feature derived from extracted PPG beats. . . . .	76
4.9	OPRA block diagram. . . . .	77
4.10	Clean PPG signals before and after exercise. . . . .	80
4.11	OPRA multi SLP feature. . . . .	81
4.12	PPG extracts with varying signal quality. . . . .	82
4.13	Coincidence Matrix in PPG signal quality assessment. . . . .	84
4.14	OPRA performance evaluation. . . . .	86
4.15	SVEB and VEB examples. . . . .	90
4.16	Performance of proposed ectopic beat detection method. . . . .	98
4.17	Overview of proposed ectopic beat detector. . . . .	102
5.1	PPG time signals and spectrograms. . . . .	109

5.2	PPG motion artifact reduction with proposed ICA approach. . . . .	113
5.3	PPG time signals and spectrograms before and after ICA reconstruction. . .	114
5.4	PPG motion artifact reduction performance with proposed ICA method. . .	117
5.5	Hand movement detection with rBSN acceleration signals. . . . .	118
6.1	Reimplemented BPE methods from literature. . . . .	120
6.2	BPE snippet before and after EB cancellation. . . . .	126
8.1	ANN finetuning for proposed EB detector. . . . .	141
8.2	PPG artifact reduction performance of the proposed ICA approach. Com- parison of different reference ACC combinations. . . . .	142

# List of Tables

1.1	Overview on common biosignals with related measurements and features. . . . .	2
3.1	BSN features and parameters . . . . .	36
3.2	rBSN packet structure. . . . .	46
3.3	Bluetooth radio transmission tests. . . . .	50
3.4	Datasets rBSN student database_I. . . . .	51
3.5	Datasets rBSN clinical database_I. . . . .	52
3.6	Datasets Vasoscreen database. . . . .	53
3.7	Datasets PhysioNet database. . . . .	54
4.1	Agreement matrix on different PAT measures. . . . .	59
4.2	Overview on PPG signal quality literature. . . . .	68
4.3	OPRA execution times. . . . .	78
4.4	OPRA calibration evaluation. . . . .	79
4.5	OPRA classification performance evaluation. . . . .	87
4.6	PPG signal quality estimators performance comparison. . . . .	88
4.7	Heartbeat types according to AAMI. . . . .	89
4.8	Literature overview of automatic ectopic beat detection methods. . . . .	93
4.9	Feature groups in proposed ectopic beat detector. . . . .	95
4.10	Top ten combinations of feature sets applied in the proposed ectopic beat detector measured by sensitivity (se) and specificity (sp). Features include timings (interval), signal statistics (sig/stat) or amplitude and morphology (morph) properties. . . . .	99
4.11	ECG and PPG features in proposed ectopic beat detector. . . . .	100
4.12	Computational complexity of proposed EB detection method. . . . .	101
4.13	Performance evaluation of proposed ectopic beat detector. . . . .	104
6.1	Performance measures BPE in Chen et al. [37] . . . . .	121
6.2	Performance measures BPE in Cativelli et al. [34] . . . . .	121
6.3	Performance measures BPE in Kuryalak et al. [143] . . . . .	122
6.4	Performance comparison of different BPE methods on clean data. . . . .	123
6.5	Performance comparison of different BPE methods on artifact contaminated data. . . . .	124
6.6	BP estimation on disturbed data on OPRA cleaned signals . . . . .	125
6.7	BPE error measurements before and after EB cancellation . . . . .	127

8.1	Exercise protocol for measurements of database <i>rBSN_studentDatabaseI</i> .	133
8.3	Literature overview on body sensor networks I.	134
8.4	Literature overview on body sensor networks II.	135
8.5	Literature overview on body sensor networks III.	136
8.6	Complete list of features EB detection	137
8.8	Published BP estimation models	139
8.9	Feature groups computational complexity	140
8.10	<i>rBSN_DualPulseOxi</i> power consumption	142

# Bibliography

- [1] AHA database for evaluation of ventricular arrhythmia detectors. available from: ECRI, 5200 butler pike, plymouth meeting, pa 19462 usa.
- [2] S. C. Millasseau and F. G. Guigui, R. P. Kelly, K. Prasad, J. R. Cockcroft, J. M. Ritter, and P. J. Chowienczyk. Noninvasive assessment of the digital volume pulse comparison with the peripheral pressure pulse. *Hypertension*, 36(6):952–956, 2000.
- [3] H. Alemdar and C. Ersoy. Wireless sensor networks for healthcare: a survey. *Computer Networks*, 54(15):2688–2710, 2010.
- [4] J. Allen. Photoplethysmography and its application in clinical physiological measurement. *Physiological measurement*, 28(3):R1–R39, 2007.
- [5] J. Allen and A. Murray. Assessing ecg signal quality on a coronary care unit. *Physiological measurement*, 17(4):249, 1996.
- [6] J. Allen and A. Murray. Age-related changes in peripheral pulse timing characteristics at the ears, fingers and toes. *Journal of human hypertension*, 16(10):711–717, 2002.
- [7] S. R. Alty, N. Angarita-Jaimes, S. C. Millasseau, and P. J. Chowienczyk. Predicting arterial stiffness from the digital volume pulse waveform. *IEEE Transactions on Biomedical Engineering*, 54(12):2268–2275, Dec 2007.
- [8] Analog Devices. *Small Low Power 3-Axis 3g Accelerometer ADXL335 Rev. B [Online Available]*: <http://www.analog.com/media/en/technical-documentation/data-sheets/ADXL335.pdf>, February 2017. last visited: 2016.03.29.
- [9] G. Angius, D. Barcellona, E. Cauli, L. Meloni, and L. Raffo. Myocardial infarction and antiphospholipid syndrome: A first study on finger ppg waveforms effects. In *2012 Computing in Cardiology*, pages 517–520, Sept 2012.
- [10] H. H. Asada, H. H. Jiang, and P. Gibbs. Active noise cancellation using mems accelerometers for motion-tolerant wearable bio-sensors. In *The 26th Annual International Conference of the IEEE Engineering in Medicine and Biology Society*, volume 1, pages 2157–2160, Sept 2004.
- [11] J. F. Augusto, J. L. Teboul, P. Radermacher, and P. Asfar. Interpretation of blood pressure signal: physiological bases, clinical relevance, and objectives during shock states. *Intensive care medicine*, 37(3):411–419, 2011.
- [12] A. P. Avolio, M. Butlin, and A. Walsh. Arterial blood pressure measurement and pulse wave analysis - their role in enhancing cardiovascular assessment. *Physiological measurement*, 31(1):R1, 2009.
- [13] O. Aziz, L. Atallah, B. Lo, M. ElHelw, L. Wang, G. Z. Yang, and A. Darzi. A pervasive body sensor network for measuring postoperative recovery at home. *Surgical Innovation*, 14(2):83–90, 2007.

- [14] H. J. Baek, K. K. Kim, J. S. Kim, B. Lee, and K. S. Park. Enhancing the estimation of blood pressure using pulse arrival time and two confounding factors. *Physiological measurement*, 31(2):145, 2009.
- [15] S. J. Barker and N. K. Shah. The effects of motion on the performance of pulse oximeters in volunteers (revised publication). *Anesthesiology*, 86(1):101–108, 1997.
- [16] A. R. Barnes, H. E. B. Pardee, P. D. White, Frank N F. N. Wilson, and C. C. Wolfarth. Standardization of precordial leads: Supplementary report. *American Heart Journal*, 15(2):235–239, 1938.
- [17] A. B. Barreto, L. M. Vicente, and I. K. Persad. Adaptive cancelation of motion artifact in photoplethysmographic blood volume pulse measurements for exercise evaluation. In *Proceedings of 17th International Conference of the Engineering in Medicine and Biology Society*, volume 2, pages 983–984 vol.2, Sep 1995.
- [18] M. C. Baruch, D. E. R. Warburton, S. S. D. Bredin, A. Cote, , D. W. Gerdt, and C. M. Adkings. Pulse decomposition analysis of the digital arterial pulse during hemorrhage simulation. *Nonlinear biomedical physics*, 5(1):1, 2011.
- [19] N. S. Beckett, R. Peters, A. E. Fletcher, J. A. Staessen, L. Liu, D. Dumitrascu, V. Stoyanovsky, R. L. Antikainen, Y. Nikitin, and C. Anderson. Treatment of hypertension in patients 80 years of age or older. *New England Journal of Medicine*, 358(18):1887–1898, 2008.
- [20] A. J. Bell and T. J. Sejnowski. An information-maximization approach to blind separation and blind deconvolution. *Neural computation*, 7(6):1129–1159, 1995.
- [21] A. Belouchrani, K. Abed-Meraim, J. F. Cardoso, and E. Moulines. A blind source separation technique using second-order statistics. *IEEE Transactions on Signal Processing*, 45(2):434–444, Feb 1997.
- [22] A. Berger, A. Potsch, and A. Springer. Synchronized industrial wireless sensor network with ieee 802.11 ad hoc data transmission. In *Measurements and Networking Proceedings (M N), 2013 IEEE International Workshop on*, pages 7–12, Oct 2013.
- [23] C. M. Bishop. *Pattern recognition and machine learning*. springer, 2006.
- [24] J. M. Bland and D. G. Altman. Measuring agreement in method comparison studies. *Statistical methods in medical research*, 8(2):135–160, 1999.
- [25] M. Bolanos, H. Nazeran, and E. Haltiwanger. Comparison of heart rate variability signal features derived from electrocardiography and photoplethysmography in healthy individuals. In *2006 International Conference of the IEEE Engineering in Medicine and Biology Society*, pages 4289–4294, Aug 2006.
- [26] J. Booth. A short history of blood pressure measurement. *Proceedings of the Royal Society of Medicine*, 70(11):793, 1977.
- [27] P. Boutouyrie, M. Briet, C. Collin, S. Vermeersch, and B. Pannier. Assessment of pulse wave velocity. *Artery Research*, 3(1):3–8, 2009.
- [28] J. C. Bramwell and A. V. Hill. The velocity of the pulse wave in man. *Proceedings of the Royal Society of London. Series B, Containing Papers of a Biological Character*, pages 298–306, 1922.
- [29] P. J. Brands, J. M. Willigers, L. A. F. Ledoux, R. S. Reneman, and A. P. G. Hoeks. A noninvasive method to estimate pulse wave velocity in arteries locally by means of ultrasound. *Ultrasound in medicine & biology*, 24(9):1325–1335, 1998.

- [30] D. Buxi, J. M. Redouté, and M. R. Yuce. A survey on signals and systems in ambulatory blood pressure monitoring using pulse transit time. *Physiological measurement*, 36(3):R1–R26, 2015.
- [31] J. F. Cardoso. High-order contrasts for independent component analysis. *Neural computation*, 11(1):157–192, 1999.
- [32] F. Casamassima, E. Farella, and L. Benini. Synchronization methods for bluetooth based wbans. In *2013 IEEE International Conference on Body Sensor Networks*, pages 1–6, May 2013.
- [33] R. Casas, H. J. Gracia, A. Marco, and J. L. Falco. Synchronization in wireless sensor networks using bluetooth. In *Third International Workshop on Intelligent Solutions in Embedded Systems, 2005.*, pages 79–88, May 2005.
- [34] F. S. Cattivelli and H. Garudadri. Noninvasive cuffless estimation of blood pressure from pulse arrival time and heart rate with adaptive calibration. In *2009 Sixth International Workshop on Wearable and Implantable Body Sensor Networks*, pages 114–119, June 2009.
- [35] ChaN. *FatFs - Generic FAT File System Module (May. 2014) [Online Available]*: [http://elm-chan.org/fsw/ff/00index\\_e.html](http://elm-chan.org/fsw/ff/00index_e.html). last visited: 2016.03.29.
- [36] M. Chen, S. Gonzalez, A. Vasilakos, H Cao, and V. C. Leung. Body area networks: A survey. *Mobile networks and applications*, 16(2):171–193, 2011.
- [37] W. Chen, T. Kobayashi, S. Ichikawa, Y. Takeuchi, and T. Togawa. Continuous estimation of systolic blood pressure using the pulse arrival time and intermittent calibration. *Medical and Biological Engineering and Computing*, 38(5):569–574, 2000.
- [38] Y. C. Chiu, P. W. Arand, S. G. Shroff, T. Feldman, and J. D. Carroll. Determination of pulse wave velocities with computerized algorithms. *American heart journal*, 121(5):1460–1470, 1991.
- [39] H. S. Chow, G. B. Moody, and R. G. Mark. Detection of ventricular ectopic beats using neural networks. In *Computers in Cardiology 1992, Proceedings of*, pages 659–662, Oct 1992.
- [40] W. Y. Chung, Y. D. Lee, and S. J. Jung. A wireless sensor network compatible wearable u-healthcare monitoring system using integrated ecg, accelerometer and spo2. In *2008 30th Annual International Conference of the IEEE Engineering in Medicine and Biology Society*, pages 1529–1532, Aug 2008.
- [41] G. Clifford, F. Azuaje, and P. McSharry. *ECG Data Analysis*. ARTECH HOUSE, INC., 2006.
- [42] G. Clifford, L. Tarassenko, and N. Townsend. Fusing conventional ecg qrs detection algorithms with an auto-associative neural network for the detection of ectopic beats. In *Signal Processing Proceedings, 2000. WCCC-ICSP 2000. 5th International Conference on*, volume 3, pages 1623–1628 vol.3, 2000.
- [43] G. Clifford, L. Tarassenko, and N. Townsend. One-pass training of optimal architecture auto-associative neural network for detecting ectopic beats. *Electronics Letters*, 37(18):1126–1127, Aug 2001.
- [44] G. D. Clifford and G. B. Moody. Signal quality in cardiorespiratory monitoring. *Physiological Measurement*, 33(9), 2012.
- [45] G. D. Clifford, I. Silva, B. Moody, Q. Li, D. Kella, A. Shahin, T. Kooistra, D. Perry, and R. G. Mark. The physionet/computing in cardiology challenge 2015: Reducing false arrhythmia alarms in the icu. In *2015 Computing in Cardiology Conference (CinC)*, pages 273–276, Sept 2015.
- [46] F. M. Coetzee and Z. Elghazzawi. Noise-resistant pulse oximetry using a synthetic reference signal. *IEEE Transactions on Biomedical Engineering*, 47(8):1018–1026, Aug 2000.

- [47] G. Comtois, Y. Mendelson, and P. Ramuka. A comparative evaluation of adaptive noise cancellation algorithms for minimizing motion artifacts in a forehead-mounted wearable pulse oximeter. In *2007 29th Annual International Conference of the IEEE Engineering in Medicine and Biology Society*, pages 1528–1531, Aug 2007.
- [48] D. Cox, E. Jovanov, and A. Milenkovic. Time synchronization for zigbee networks. In *Proceedings of the Thirty-Seventh Southeastern Symposium on System Theory, 2005. SSST '05.*, pages 135–138, March 2005.
- [49] D. Curtis, E. Shih, J. Waterman, J. Guttag, J. Bailey, T. Stair, R. A. Greenes, and L. Ohno-Machado. Physiological signal monitoring in the waiting areas of an emergency room. In *Proceedings of the ICST 3rd international conference on Body area networks*, page 5. ICST (Institute for Computer Sciences, Social-Informatics and Telecommunications Engineering), 2008.
- [50] N. Daimiwal, M. Sundhararajan, and R. Shriram. Respiratory rate, heart rate and continuous measurement of bp using ppg. In *2014 International Conference on Communication and Signal Processing*, pages 999–1002, April 2014.
- [51] W. B. Applegate and B. R. Davis, H. R. Black, W. McFate Smith, S. T. Miller, and A. J. Burlando. Prevalence of postural hypotension at baseline in the systolic hypertension in the elderly program (shep) cohort. *Journal of the American Geriatrics Society*, 39(11):1057–1064, 1991.
- [52] P. de Chazal. Detection of supraventricular and ventricular ectopic beats using a single lead ecg. In *2013 35th Annual International Conference of the IEEE Engineering in Medicine and Biology Society (EMBC)*, pages 45–48, July 2013.
- [53] P. de Chazal, M. O’Dwyer, and R. B. Reilly. Automatic classification of heartbeats using ecg morphology and heartbeat interval features. *IEEE Transactions on Biomedical Engineering*, 51(7):1196–1206, July 2004.
- [54] S. Deb, C. Nanda, D. Goswami, J. Mukhopadhyay, and S. Chakrabarti. Cuff-less estimation of blood pressure using pulse transit time and pre-ejection period. In *2007 International Conference on Convergence Information Technology (ICCIT 2007)*, pages 941–944, Nov 2007.
- [55] K. I. Diamantaras and S. Y. Kung. *Principal component neural networks: theory and applications*. John Wiley & Sons, Inc., 1996.
- [56] R. Dias and J. Machado da Silva. A flexible wearable sensor network for bio-signals and human activity monitoring. In *Wearable and Implantable Body Sensor Networks Workshops (BSN Workshops), 2014 11th International Conference on*, pages 17–22, June 2014.
- [57] L. Drijkoningen, F. Lenaerts, J. Van der Auwera, K. Leysen, D. Nuyens, P. Vandervoort, and L. Grieten. Validation of a smartphone based photoplethysmographic beat detection algorithm for normal and ectopic complexes. In *Computing in Cardiology 2014*, pages 845–848, Sept 2014.
- [58] M. J. Drinnan, J. Allen, and A. Murray. Relation between heart rate and pulse transit time during paced respiration. *Physiological measurement*, 22(3):425, 2001.
- [59] G. M. Drzewiecki, J. Melbin, and A. Noordergraaf. Arterial tonometry: review and analysis. *Journal of biomechanics*, 16(2):141–152, 1983.
- [60] M. L. Eigenbrodt, K. M. Rose, D. J. Couper, D. K. Arnett, R. Smith, and D. Jones. Orthostatic hypotension as a risk factor for stroke the atherosclerosis risk in communities (aric) study, 1987–1996. *Stroke*, 31(10):2307–2313, 2000.
- [61] W. Einthoven. The telecardiogram. *American Heart Journal*, 53(4):602–615, 1957.

- [62] M. Elgendi. On the analysis of fingertip photoplethysmogram signals. *Current cardiology reviews*, 8(1):14, 2012.
- [63] M. Elgendi. Standard terminologies for photoplethysmogram signals. *Current cardiology reviews*, 8(3):215, 2012.
- [64] M. Elgendi. Detection of c, d, and e waves in the acceleration photoplethysmogram. *Computer methods and programs in biomedicine*, 117(2):125–136, 2014.
- [65] M. Elgendi, B. Eskofier, and D. Abbott. Fast t wave detection calibrated by clinical knowledge with annotation of p and t waves. *Sensors*, 15(7):17693–17714, 2015.
- [66] M. Elgendi, I. Norton, M. Brearley, D. Abbott, and D. Schuurmans. Detection of a and b waves in the acceleration photoplethysmogram. *Biomedical engineering online*, 13(1):139, 2014.
- [67] J. Espina, T. Falck, J. Muehlsteff, and X. Aubert. Wireless body sensor network for continuous cuff-less blood pressure monitoring. In *2006 3rd IEEE/EMBS International Summer School on Medical Devices and Biosensors*, pages 11–15, Sept 2006.
- [68] V. Feller, F. Mielentz, T. Klewe, M. Krause, R. Orglmeister, and M. Pflugradt. Ultrasonic phased array for investigations of concrete components. In *International Symposium Non-Destructive Testing in Civil Engineering (NDT-CE)*, 2015.
- [69] J. Y. A. Foo. Comparison of wavelet transformation and adaptive filtering in restoring artefact-induced time-related measurement. *Biomedical signal processing and control*, 1(1):93–98, 2006.
- [70] J. Y. A. Foo. Pulse transit time in paediatric respiratory sleep studies. *Medical engineering & physics*, 29(1):17–25, 2007.
- [71] J. Y. A. Foo. Use of independent component analysis to reduce motion artifact in pulse transit time measurement. *IEEE Signal Processing Letters*, 15:124–126, 2008.
- [72] J. Y. A. Foo and S. J. Wilson. A computational system to optimise noise rejection in photoplethysmography signals during motion or poor perfusion states. *Medical and Biological Engineering and Computing*, 44(1-2):140–145, 2006.
- [73] J. Y. A. Foo, S. J. Wilson, G. R. Williams, M. Harris, and D. M. Cooper. Motion artefact reduction of the photoplethysmographic signal in pulse transit time measurement. *Australasian Physics & Engineering Sciences in Medicine*, 27(4):165–173, 2004.
- [74] Association for the Advancement of Medical Instrumentation et al. *Testing and Reporting Performance Results of Cardiac Rhythm and ST-segment Measurement Algorithms*. AAMI, 1999.
- [75] O. Frank. Die theorie der pulswellen. *Z Biol*, 85:91–130, 1926.
- [76] P. Fung, G. Dumont, C. Ries, C. Mott, and M. Ansermino. Continuous noninvasive blood pressure measurement by pulse transit time. In *The 26th Annual International Conference of the IEEE Engineering in Medicine and Biology Society*, volume 1, pages 738–741, Sept 2004.
- [77] D. Gallagher, A. Adji, and M. F. O’Rourke. Validation of the transfer function technique for generating central from peripheral upper limb pressure waveform, 2004.
- [78] N. Gambarotta, F. Aletti, G. Baselli, and M. Ferrario. A review of methods for the signal quality assessment to improve reliability of heart rate and blood pressures derived parameters. *Medical & biological engineering & computing*, 54(7):1025–1035, 2016.

- [79] T. Gao, T. Massey, L. Selavo, D. Crawford, B. r. Chen, K. Lorincz, V. Shnayder, L. Hauenstein, F. Dabiri, J. Jeng, A. Chanmugam, D. White, M. Sarrafzadeh, and M. Welsh. The advanced health and disaster aid network: A light-weight wireless medical system for triage. *IEEE Transactions on Biomedical Circuits and Systems*, 1(3):203–216, Sept 2007.
- [80] V. Gay and P. Leijdekkers. A health monitoring system using smart phones and wearable sensors'. *International Journal of ARM*, 8(2):29–35, 2007.
- [81] H. Gesche, D. Grosskurth, G. K uchler, and A. Patzak. Continuous blood pressure measurement by using the pulse transit time: comparison to a cuff-based method. *European journal of applied physiology*, 112(1):309–315, 2012.
- [82] U. Ghoshdastider, R. Viga, and M. Kraft. Non-invasive synchronized spatially high-resolution wireless body area network. In *2014 IEEE Ninth International Conference on Intelligent Sensors, Sensor Networks and Information Processing (ISSNIP)*, pages 1–6, April 2014.
- [83] P. Gibbs and H. H. Asada. Reducing motion artifact in wearable bio-sensors using mems accelerometers for active noise cancellation. In *American Control Conference, 2005. Proceedings of the 2005*, pages 1581–1586. IEEE, 2005.
- [84] E. Gil, M. Orini, R. Bail on, J. M. Vergara, L. Mainardi, and P. Laguna. Photoplethysmography pulse rate variability as a surrogate measurement of heart rate variability during non-stationary conditions. *Physiological Measurement*, 31(9):1271, 2010.
- [85] M. Goernig, S. Weise, M. Pflugradt, and J. Hauelsen. Registration and evaluation of alternative non-invasive parameters for orthostatic hypotension in geriatric patients. *Annual Meeting of the German Society of Biomedical Engineering and Joint Conference in Medical Physics*, 62(1), 2017.
- [86] A. L. Goldberger, L. A. N. Amaral, L. Glass, J. M. Hausdorff, P. Ch. Ivanov, R. G. Mark, J. E. Mietus, G. B. Moody, C. K. Peng, and H. E. Stanley. Physiobank, physiotoolkit, and physionet components of a new research resource for complex physiologic signals. *Circulation*, 101(23):e215–e220, 2000.
- [87] D. S. Goldstein, S. Pechnik, C. Holmes, B. Eldadah, and Y. Sharabi. Association between supine hypertension and orthostatic hypotension in autonomic failure. *Hypertension*, 42(2):136–142, 2003.
- [88] D. S. Goldstein and Y. Sharabi. Neurogenic orthostatic hypotension a pathophysiological approach. *Circulation*, 119(1):139–146, 2009.
- [89] G. H. Golub and C. F. Van Loan. *Matrix computations*, volume 3. JHU Press, 2012.
- [90] G. Gomez-Herrero, I. Jekova, V. Krasteva, I. Christov, A. Gotchev, and K. Egiazarian. Relative estimation of the karhunen-loeve transform basis functions for detection of ventricular ectopic beats. In *Computers in Cardiology, 2006*, pages 569–572, Sept 2006.
- [91] O. Gorelik, G. Fishlev, V. Litvinov, D. Almozmino-Sarafian, I. Alon, M. Shteinshnaider, S. Chachashvily, D. Modai, and N. Cohen. First morning standing up may be risky in acutely ill older inpatients. *Blood pressure*, 14(3):139–143, 2005.
- [92] R. G. Gosling and M. M. Budge. Terminology for describing the elastic behavior of arteries. *Hypertension*, 41(6):1180–1182, 2003.
- [93] J. M. Graybeal and M. T. Petterson. Adaptive filtering and alternative calculations revolutionizes pulse oximetry sensitivity and specificity during motion and low perfusion. In *The 26th Annual International Conference of the IEEE Engineering in Medicine and Biology Society*, volume 2, pages 5363–5366, Sept 2004.

- [94] B. Gribbin, A. Steptoe, and P. Sleight. Pulse wave velocity as a measure of blood pressure change. *Psychophysiology*, 13(1):86–90, 1976.
- [95] Bluetooth Special Interest Group. *Bluetooth Core Specification, Core Version 4.1. (Dec. 2013)*. [Online Available]: <https://www.bluetooth.org/en-us/specification/adopted-specifications>. last visited: 2016.03.29.
- [96] W. B. Gu, C. C. Y. Poon, and Y. T. Zhang. A novel parameter from ppg dirotic notch for estimation of systolic blood pressure using pulse transit time. In *2008 5th International Summer School and Symposium on Medical Devices and Biosensors*, pages 86–88, June 2008.
- [97] W. A. Hale and M. L. Chambliss. Should primary care patients be screened for orthostatic hypotension? *The Journal of family practice*, 48(7):547–552, 1999.
- [98] P. Hamilton. Open source ecg analysis. In *Computers in Cardiology, 2002*, pages 101–104, Sept 2002.
- [99] H. Han, M. J. Kim, and J. Kim. Development of real-time motion artifact reduction algorithm for a wearable photoplethysmography. In *2007 29th Annual International Conference of the IEEE Engineering in Medicine and Biology Society*, pages 1538–1541, Aug 2007.
- [100] M. J. Hayes and P. R. Smith. A new method for pulse oximetry possessing inherent insensitivity to artifact. *IEEE Transactions on Biomedical Engineering*, 48(4):452–461, April 2001.
- [101] S. S. Haykin. *Adaptive filter theory*. Pearson Education India, 2008.
- [102] S. S. Haykin. *Neural networks and learning machines*, volume 3. Pearson Upper Saddle River, NJ, USA, 2009.
- [103] X. He, R. A. Goubran, and X. P. Liu. Secondary peak detection of ppg signal for continuous cuffless arterial blood pressure measurement. *IEEE Transactions on Instrumentation and Measurement*, 63(6):1431–1439, June 2014.
- [104] S. O. Heard, A. Lisbon, I. Toth, and R. Ramasubramanian. An evaluation of a new continuous blood pressure monitoring system in critically ill patients. *Journal of clinical anesthesia*, 12(7):509–518, 2000.
- [105] I. P. Herman. *Physics of the human body*. Springer Science & Business Media, 2007.
- [106] A. B. Hertzman. Photoelectric plethysmography of the fingers and toes in man. *Experimental Biology and Medicine*, 37(3):529–534, 1937.
- [107] P. Hiitola, H. Enlund, R. Kettunen, R. Sulkava, and S. Hartikainen. Postural changes in blood pressure and the prevalence of orthostatic hypotension among home-dwelling elderly aged 75 years or older. *Journal of human hypertension*, 23(1):33–39, 2009.
- [108] K. Hornik, M. Stinchcombe, and H. White. Multilayer feedforward networks are universal approximators. *Neural networks*, 2(5):359–366, 1989.
- [109] D. J. Hughes, C. F. Babbs, L. A. Geddes, and J. D. Bourland. Measurements of young’s modulus of elasticity of the canine aorta with ultrasound. *Ultrasonic Imaging*, 1(4):356–367, 1979.
- [110] A. Hyvärinen. Fast and robust fixed-point algorithms for independent component analysis. *IEEE Transactions on Neural Networks*, 10(3):626–634, May 1999.
- [111] A. Hyvärinen, J. Karhunen, and E. Oja. *Independent component analysis*, volume 46. John Wiley & Sons, 2004.

- [112] A. Illanes-Manriquez and Q. Zhang. An algorithm for robust detection of qrs onset and offset in ecg signals. In *2008 Computers in Cardiology*, pages 857–860, Sept 2008.
- [113] B. P. Imholz, G. J. Langewouters, G. A. van Montfrans, G. Parati, J. van Goudoever, K. H. Wesseling, W. Wieling, and G. Mancia. Feasibility of ambulatory, continuous 24-hour finger arterial pressure recording. *Hypertension*, 21(1):65–73, 1993.
- [114] D. G. Jang, S. H. Park, and M. Hahn. Enhancing the pulse contour analysis-based arterial stiffness estimation using a novel photoplethysmographic parameter. *IEEE Journal of Biomedical and Health Informatics*, 19(1):256–262, Jan 2015.
- [115] N. Javaid, S. Faisal, Z. A. Khan, D. Nayab, and M. Zahid. Measuring fatigue of soldiers in wireless body area sensor networks. In *Broadband and Wireless Computing, Communication and Applications (BWCCA), 2013 Eighth International Conference on*, pages 227–231, Oct 2013.
- [116] I. Jekova, V. Krasteva, I. Christov, and R. Abächerli. Threshold-based system for noise detection in multilead ecg recordings. *Physiological measurement*, 33(9):1463, 2012.
- [117] T. Jensen, S. Duun, J. Larsen, R. G. Haahr, M. H. Toft, B. Belhage, and E. V. Thomsen. Independent component analysis applied to pulse oximetry in the estimation of the arterial oxygen saturation (spo2) - a comparative study. In *2009 Annual International Conference of the IEEE Engineering in Medicine and Biology Society*, pages 4039–4044, Sept 2009.
- [118] G. Y. Jeong, K. H. Yu, and N. G. Kim. Continuous blood pressure monitoring using pulse wave transit time. In *2005 ICCAS Int. Conf. Control, Automation and Systems*, Jun 2005.
- [119] A. Jin, B. Yin, G. Morren, H. Duric, and R. M. Aarts. Performance evaluation of a tri-axial accelerometry-based respiration monitoring for ambient assisted living. In *2009 Annual International Conference of the IEEE Engineering in Medicine and Biology Society*, pages 5677–5680, Sept 2009.
- [120] A. Johansson. Neural network for photoplethysmographic respiratory rate monitoring. *Medical and Biological Engineering and Computing*, 41(3):242–248, 2003.
- [121] A. Johansson, C. Ahlstrom, T. Lanne, and P. Ask. Pulse wave transit time for monitoring respiration rate. *Medical and Biological Engineering and Computing*, 44(6):471–478, 2006.
- [122] A. Johansson and P. Å. Öberg. Estimation of respiratory volumes from the photoplethysmographic signal. part i: experimental results. *Medical & biological engineering & computing*, 37(1):42–47, 1999.
- [123] S. Jokić, S. Krčo, V. Delic, D. Sakač D., I. Jokič, and Z. Lukič. An efficient ecg modeling for heartbeat classification. In *Neural Network Applications in Electrical Engineering (NEUREL), 2010 10th Symposium on*, pages 73–76, Sept 2010.
- [124] I. T. Jolliffe. *Principal Component Analysis*. Springer, second edition, Oct 2002.
- [125] R. D. M. Jones, J. P. Kornberg, C. J. Roulson, A. R. Visram, and M. G. Irwin. The finapres 2300e finger cuff. *Anaesthesia*, 48(7):611–615, 1993.
- [126] G. Joseph, A. Joseph, G. Titus, R. M. Thomas, and D. Jose. Photoplethysmogram (ppg) signal analysis and wavelet de-noising. In *2014 Annual International Conference on Emerging Research Areas: Magnetics, Machines and Drives (AICERA/iCMMD)*, pages 1–5, July 2014.
- [127] E. Jovanov, A. Milenkovic, C. Otto, and P. C. De Groen. A wireless body area network of intelligent motion sensors for computer assisted physical rehabilitation. *Journal of NeuroEngineering and rehabilitation*, 2(1):6, 2005.

- [128] E. Judd and D. A. Calhoun. Hypertension and orthostatic hypotension in older patients. *Journal of hypertension*, 30(1):38, 2012.
- [129] D. K. Jung, G. R. Kim, K. N. Kim, B. C. Choi, D. J. Suh, G. R. Jeon, and S. Y. Ye. Changes of pulse wave velocity in arm according to characteristic points of pulse wave. In *2007 International Conference on Convergence Information Technology (ICCIT 2007)*, pages 821–826, Nov 2007.
- [130] E. Kantoch, P. Augustyniak, M. Markiewicz, and D. Prusak. Monitoring activities of daily living based on wearable wireless body sensor network. In *2014 36th Annual International Conference of the IEEE Engineering in Medicine and Biology Society*, pages 586–589, Aug 2014.
- [131] M. M. A. R. Karamanoglu, M. F. O’rourke, A. P. Avolio, and R. P. Kelly. An analysis of the relationship between central aortic and peripheral upper limb pressure waves in man. *European heart journal*, 14(2):160–167, 1993.
- [132] W. Karlen, K. Kobayashi, J. M. Ansermino, and G. A. Dumont. Photoplethysmogram signal quality estimation using repeated gaussian filters and cross-correlation. *Physiological measurement*, 33(10):1617, 2012.
- [133] G. Karraz and G. Magenes. Automatic classification of heartbeats using neural network classifier based on a bayesian framework. In *2006 International Conference of the IEEE Engineering in Medicine and Biology Society*, pages 4016–4019, Aug 2006.
- [134] H. Kaufmann. Consensus statement on the definition of orthostatic hypotension, pure autonomic failure and multiple system atrophy. *Clinical autonomic research: official journal of the Clinical Autonomic Research Society*, 6(2):125–126, 1996.
- [135] E. Kazanavicius, R. Gircys, A. Vrubliauskas, and S. Lugin. Mathematical methods for determining the foot point of the arterial pulse wave and evaluation of proposed methods. *Information Technology and control*, 34(1), 2015.
- [136] B. S. Kim and S. K. Yoo. Motion artifact reduction in photoplethysmography using independent component analysis. *IEEE Transactions on Biomedical Engineering*, 53(3):566–568, March 2006.
- [137] J. S. Kim, K. K. Kim, H. J. Baek, and K. S. Park. Effect of confounding factors on blood pressure estimation using pulse arrival time. *Physiological measurement*, 29(5):615, 2008.
- [138] S. H. Kim, D. W. Ryoo, and C. Bae. Adaptive noise cancellation using accelerometers for the ppg signal from forehead. In *2007 29th Annual International Conference of the IEEE Engineering in Medicine and Biology Society*, pages 2564–2567, Aug 2007.
- [139] R. Krishnan, B. Natarajan, and S. Warren. Analysis and detection of motion artifact in photoplethysmographic data using higher order statistics. In *2008 IEEE International Conference on Acoustics, Speech and Signal Processing*, pages 613–616, March 2008.
- [140] R. Krishnan, B. Natarajan, and S. Warren. Motion artifact reduction in photoplethysmography using magnitude-based frequency domain independent component analysis. In *2008 Proceedings of 17th International Conference on Computer Communications and Networks*, pages 1–5, Aug 2008.
- [141] S. Kunchon, T. Desudchit, and C. Chinrungrueng. Comparative evaluation of adaptive filters in motion artifact cancellation for pulse oximetry. In *2009 5th International Colloquium on Signal Processing Its Applications*, pages 307–311, March 2009.
- [142] S. Y. Kung, K. I. Diamantaras, and J. S. Taur. Adaptive principal component extraction (apex) and applications. *IEEE Transactions on Signal Processing*, 42(5):1202–1217, May 1994.

- [143] Y. Kurylyak, F. Lamonaca, and D. Grimaldi. A neural network-based method for continuous blood pressure estimation from a ppg signal. In *2013 IEEE International Instrumentation and Measurement Technology Conference (I2MTC)*, pages 280–283, May 2013.
- [144] J. C. Lagarias, J. A. Reeds, M. H. Wright, and P. E. Wright. Convergence properties of the nelder–mead simplex method in low dimensions. *SIAM Journal on optimization*, 9(1):112–147, 1998.
- [145] P. Laguna and R. Jané and P. Caminal. Automatic detection of wave boundaries in multilead ecg signals: Validation with the cse database. *Computers and biomedical research*, 27(1):45–60, 1994.
- [146] P. Laguna, R. G. Mark, A. Goldberg, and G. B. Moody. A database for evaluation of algorithms for measurement of qt and other waveform intervals in the ecg. In *Computers in Cardiology 1997*, pages 673–676, Sep 1997.
- [147] P. Langley, E. J. Bowers, and A. Murray. Principal component analysis as a tool for analyzing beat-to-beat changes in ecg features: Application to ecg-derived respiration. *IEEE Transactions on Biomedical Engineering*, 57(4):821–829, April 2010.
- [148] L. Laplante and B. S. Benzaquen. A review of the potential pathogenicity and management of frequent premature ventricular contractions. *Pacing and Clinical Electrophysiology*, 23(7):723–730, 2016.
- [149] O. D. Lara and M. A. Labrador. A survey on human activity recognition using wearable sensors. *IEEE Communications Surveys Tutorials*, 15(3):1192–1209, Third 2013.
- [150] H. Larochelle, Y. Bengio, J. Louradour, and P. Lamblin. Exploring strategies for training deep neural networks. *Journal of Machine Learning Research*, 10(Jan):1–40, 2009.
- [151] B. Lee, J. Han and H. J. Baek, J. H. Shin, K. S. Park, and W. J. Yi. Improved elimination of motion artifacts from a photoplethysmographic signal using a kalman smoother with simultaneous accelerometry. *Physiological measurement*, 31(12):1585, 2010.
- [152] B. Lee, Y. Kee, J. Han, and W. J. Yi. Adaptive comb filtering for motion artifact reduction from ppg with a structure of adaptive lattice iir notch filter. In *2011 Annual International Conference of the IEEE Engineering in Medicine and Biology Society*, pages 7937–7940, Aug 2011.
- [153] C. M. Lee and Y. T. Zhang. Reduction of motion artifacts from photoplethysmographic recordings using a wavelet denoising approach. In *IEEE EMBS Asian-Pacific Conference on Biomedical Engineering, 2003.*, pages 194–195, Oct 2003.
- [154] J. Lee, W. Jung, I. Kang, Y. Kim, and G. Lee. Design of filter to reject motion artifact of pulse oximetry. *Computer Standards & Interfaces*, 26(3):241–249, 2004.
- [155] J. W. Lee. Design of kalman filter to estimate heart rate variability from ppg signal for mobile healthcare. *Journal of information and communication convergence engineering*, 8(2):201–204, 2010.
- [156] S. Y. Lee, J. H. Hong, C. H. Hsieh, M. C. Liang, S. Y. Chang Chien, and K. H. Lin. Low-power wireless ecg acquisition and classification system for body sensor networks. *IEEE Journal of Biomedical and Health Informatics*, 19(1):236–246, Jan 2015.
- [157] Y. Lee, H. Shin, J. Jo, and Y. K. Lee. Development of a wristwatch-type ppg array sensor module. In *2011 IEEE International Conference on Consumer Electronics -Berlin (ICCE-Berlin)*, pages 168–171, Sept 2011.
- [158] Y. D. Lee, S. J. Jung, Y. S. Seo, and W. Y. Chung. Measurement of motion activity during ambulatory using pulse oximeter and triaxial accelerometer. In *2008 Third International Conference on Convergence and Hybrid Information Technology*, volume 1, pages 436–441, Nov 2008.

- [159] Y. J. Lee, C. K. Lee, M. Kang, S. J. Kang, K. N. Kim, K. Kim, K. S. Kim, and J. W. Lee. Magneto-plethysmographic sensor for peripheral blood flow velocity. *IEEE Sensors Journal*, 14(5):1341–1342, May 2014.
- [160] Y. K. Lee, O. W. Kwon, H. S. Shin, J. Jo, and Y. Lee. Noise reduction of ppg signals using a particle filter for robust emotion recognition. In *2011 IEEE International Conference on Consumer Electronics -Berlin (ICCE-Berlin)*, pages 202–205, Sept 2011.
- [161] P. Leijdekkers and V. Gay. A self-test to detect a heart attack using a mobile phone and wearable sensors. In *2008 21st IEEE International Symposium on Computer-Based Medical Systems*, pages 93–98, June 2008.
- [162] H. Leutheuser, T. Gottschalk, L. Anneken, M. Struck, A. Heuberger, M. Arnold, S. Achenbach, and B. M. Eskofier. Automatic ecg arrhythmia detection in real-time on android-based mobile devices. In *Proceedings of International Conference on Mobile and Information Technologies in Medicine and Health 2014*, November 2014.
- [163] K. Li and S. Warren. Initial study on pulse wave velocity acquired from one hand using two synchronized wireless reflectance pulse oximeters. In *2011 Annual International Conference of the IEEE Engineering in Medicine and Biology Society*, pages 6907–6910, Aug 2011.
- [164] K. Li, S. Warren, and B. Natarajan. Onboard tagging for real-time quality assessment of photoplethysmograms acquired by a wireless reflectance pulse oximeter. *IEEE Transactions on Biomedical Circuits and Systems*, 6(1):54–63, Feb 2012.
- [165] Q. Li and G. D. Clifford. Dynamic time warping and machine learning for signal quality assessment of pulsatile signals. *Physiological Measurement*, 33(9):1491, 2012.
- [166] C. C. Lin, W. Hu, and C. M. Yang. Automatic classification of arrhythmic heartbeats using the linear prediction model. In *Computing in Cardiology Conference (CinC), 2013*, pages 971–974, Sept 2013.
- [167] S. P. Linder, S. M. Wendelken, E. Wei, and S. P. McGrath. Using the morphology of photoplethysmogram peaks to detect changes in posture. *Journal of clinical monitoring and computing*, 20(3):151–158, 2006.
- [168] LITE ON ELECTRONICS. *LTST-C930CKT datasheet [Online Available]*: <http://datasheet.octopart.com/LTST-C930CKT-Lite-On-datasheet-159357.pdf>. last visited: 2016.03.29.
- [169] S. H. Liu, K. M. Chang, and S. C. Yang. Using a kalman filter to compensate for photoplethysmogram artifacts when monitoring ct examinations. In *2009 2nd International Conference on Biomedical Engineering and Informatics*, pages 1–5, Oct 2009.
- [170] M. Llamedo and J. P. Martinez. Heartbeat classification using feature selection driven by database generalization criteria. *IEEE Transactions on Biomedical Engineering*, 58(3):616–625, March 2011.
- [171] W. T. Longstreth, T. A. Manolio, A. Arnold, G. L. Burke, N. Bryan, C. A. Jungreis, P. L. Enright, D. O’Leary, and L. Fried. Clinical correlates of white matter findings on cranial magnetic resonance imaging of 3301 elderly people the cardiovascular health study. *Stroke*, 27(8):1274–1282, 1996.
- [172] G. Lu, F. Yang, J. A. Taylor, and J. F. Stein. A comparison of photoplethysmography and ecg recording to analyse heart rate variability in healthy subjects. *Journal of Medical Engineering & Technology*, 33(8):634–641, 2009.
- [173] A. Bayes De Luna. *Clinical electrocardiography: a textbook*. John Wiley & Sons, 2012.

- [174] J. Luprano, J. Sola, S. Dasen, J. M. Koller, and O. Chetelat. Combination of body sensor networks and on-body signal processing algorithms: the practical case of myheart project. In *Wearable and Implantable Body Sensor Networks, 2006. BSN 2006. International Workshop on*, pages 4 pp.–79, April 2006.
- [175] G. Mancina, R. Fagard, K. Narkiewicz, J. Z. Redon, A. Zanchetti, M. Bohm, T. Christiaens, R. Cifkova, G. De Backer, and A. Dominiczak. 2013 esh/esc guidelines for the management of arterial hypertension the task force for the management of arterial hypertension of the european society of hypertension (esh) and of the european society of cardiology (esc). *European heart journal*, 34(28):2159–2219, 2013.
- [176] P. L. Marino and K.M. Sutin. *The ICU book*, volume 2. Williams & Wilkins Baltimore., 1998.
- [177] R. J. Martis, U. R. Acharya, and L. C. Min. Ecg beat classification using pca, lda, ica and discrete wavelet transform. *Biomedical Signal Processing and Control*, 8(5):437–448, 2013.
- [178] K. H. Masaki, I. J. Schatz, C. M. Burchfiel, D. S. Sharp, D. Chiu, D. Foley, and J. D. Curb. Orthostatic hypotension predicts mortality in elderly men: The honolulu heart program. *Circulation*, 98(21):2290–2295, 1998.
- [179] K. Matthys and P. Verdonck. Development and modelling of arterial applanation tonometry: a review. *Technology and health care: official journal of the European Society for Engineering and Medicine*, 10(1):65–76, 2001.
- [180] D. Mayer. *Essential evidence-based medicine*, volume 1. Cambridge University Press, 2004.
- [181] D. B. McCombie, A. T. Reisner, and H. H. Asada. Adaptive blood pressure estimation from wearable ppg sensors using peripheral artery pulse wave velocity measurements and multi-channel blind identification of local arterial dynamics. In *2006 International Conference of the IEEE Engineering in Medicine and Biology Society*, pages 3521–3524, Aug 2006.
- [182] B. H. McGhee and E. J. Bridges. Monitoring arterial blood pressure: what you may not know. *Critical Care Nurse*, 22(2):60–79, 2002.
- [183] K. Meigas, R. Kattai, and J. Lass. Continuous blood pressure monitoring using pulse wave delay. In *2001 Conference Proceedings of the 23rd Annual International Conference of the IEEE Engineering in Medicine and Biology Society*, volume 4, pages 3171–3174 vol.4, 2001.
- [184] Y. Mendelson. Pulse oximetry: theory and applications for noninvasive monitoring. *Clinical chemistry*, 38(9):1601–1607, 1992.
- [185] Y. Mendelson, R. J. Duckworth, and G. Comtois. A wearable reflectance pulse oximeter for remote physiological monitoring. In *2006 International Conference of the IEEE Engineering in Medicine and Biology Society*, pages 912–915, Aug 2006.
- [186] A. Milenković, C. Otto, and E. Jovanov. Wireless sensor networks for personal health monitoring: Issues and an implementation. *Computer communications*, 29(13):2521–2533, 2006.
- [187] S. C. Millasseau, R. P. Kelly, J. M. Ritter, and P. J. Chowienczyk. Determination of age-related increases in large artery stiffness by digital pulse contour analysis. *Clinical science*, 103(4):371–378, 2002.
- [188] L. Mo, S. Liu, R. X. Gao, and P. S. Freedson. Energy-efficient and data synchronized body sensor network for physical activity measurement. In *2013 IEEE International Instrumentation and Measurement Technology Conference (I2MTC)*, pages 1120–1124, May 2013.

- [189] E. Monton, J. F. Hernandez, J. M. Blasco, T. Hervé, J. Micallef, I. Grech, A. Brincat, and V. Traver. Body area network for wireless patient monitoring. *IET communications*, 2(2):215–222, 2008.
- [190] G. B. Moody and R. G. Mark. A database to support development and evaluation of intelligent intensive care monitoring. In *Computers in Cardiology 1996*, pages 657–660, Sept 1996.
- [191] G. B. Moody and R. G. Mark. The impact of the mit-bih arrhythmia database. *IEEE Engineering in Medicine and Biology Magazine*, 20(3):45–50, May 2001.
- [192] S. Mottaghi, M. H., Moradi, and L. Roohisefat. Cuffless blood pressure estimation during exercise stress test. *International Journal of Bioscience, Biochemistry and Bioinformatics*, 2(6):394, 2012.
- [193] Y. Le Moullec, Y. Lecat, P. Annus, R. Land, A. Kuusik, M. Reidla, T. Hollstein, U. Reinsalu, K. Tammema, and P. Ruberg. A modular 6lowpan-based wireless sensor body area network for health-monitoring applications. In *Asia-Pacific Signal and Information Processing Association, 2014 Annual Summit and Conference (APSIPA)*, pages 1–4, Dec 2014.
- [194] S. Movassaghi, M. Abolhasan, J. Lipman, D. Smith, and A. Jamalipour. Wireless body area networks: A survey. *IEEE Communications Surveys Tutorials*, 16(3):1658–1686, Third 2014.
- [195] J. Muehlsteff, X. A. Aubert, and G. Morren. Continuous cuff-less blood pressure monitoring based on the pulse arrival time approach: The impact of posture. In *2008 30th Annual International Conference of the IEEE Engineering in Medicine and Biology Society*, pages 1691–1694, Aug 2008.
- [196] C. W. Mundt, K. N. Montgomery, U. E. Udoh, V. N. Barker, G. C. Thonier, A. M. Tellier, R. D. Ricks, R. B. Darling, Y. D. Cagle, N. A. Cabrol, S. J. Ruoss, J. L. Swain, J. W. Hines, and G. T. A. Kovacs. A multiparameter wearable physiologic monitoring system for space and terrestrial applications. *IEEE Transactions on Information Technology in Biomedicine*, 9(3):382–391, Sept 2005.
- [197] J. E. Naschitz and I. Rosner. Orthostatic hypotension: framework of the syndrome. *Postgraduate medical journal*, 83(983):568–574, 2007.
- [198] L. Nilsson, A. Johansson, and S. Kalman. Monitoring of respiratory rate in postoperative care using a new photoplethysmographic technique. *Journal of clinical monitoring and computing*, 16(4):309–315, 2000.
- [199] L. Nilsson, A. Johansson, and S. Kalman. Respiration can be monitored by photoplethysmography with high sensitivity and specificity regardless of anaesthesia and ventilatory mode. *Acta anaesthesiologica scandinavica*, 49(8):1157–1162, 2005.
- [200] G. Ning, J. Du, Y. Li, J. Lu, and X. Zheng. Comparison of pulse wave velocity computed by different characteristic points. *Proceedings of the 3rd International Association of Science And Technology for Development*, pages 335–340, 2005.
- [201] M. Nitzan, B. Khanokh, and Y. Slovik. The difference in pulse transit time to the toe and finger measured by photoplethysmography. *Physiological measurement*, 23(1):85, 2002.
- [202] B. Noble and J. W. Daniel. *Applied linear algebra*, volume 3. Prentice-Hall New Jersey, 1988.
- [203] N. Noury, A. Dittmar, C. Corroy, R. Baghai, J. L. Weber, D. Blanc, F. Klefstat, A. Blinovska, S. Vaysse, and B. Comet. Vtamn - a smart clothe for ambulatory remote monitoring of physiological parameters and activity. In *The 26th Annual International Conference of the IEEE Engineering in Medicine and Biology Society*, volume 2, pages 3266–3269, Sept 2004.
- [204] E. Oja. Simplified neuron model as a principal component analyzer. *Journal of mathematical biology*, 15(3):267–273, 1982.

- [205] E. Oja. Principal components, minor components, and linear neural networks. *Neural Networks*, 5(6):927–935, 1992.
- [206] E. Oja and J. Karhunen. On stochastic approximation of the eigenvectors and eigenvalues of the expectation of a random matrix. *Journal of mathematical analysis and applications*, 106(1):69–84, 1985.
- [207] J. J. Oliver and D. J. Webb. Noninvasive assessment of arterial stiffness and risk of atherosclerotic events. *Arteriosclerosis, Thrombosis, and Vascular Biology*, 23(4):554–566, 2003.
- [208] D. L. Olson and D. Delen. *Advanced data mining techniques*. Springer Science & Business Media, 2008.
- [209] W. L. Ooi, M. Hossain, and L. A. Lipsitz. The association between orthostatic hypotension and recurrent falls in nursing home residents. *The American journal of medicine*, 108(2):106–111, 2000.
- [210] C. Otto, A. Milenkovic, C. Sanders, and E. Jovanov Emil. System architecture of a wireless body area sensor network for ubiquitous health monitoring. *Journal of Mobile Multimedia*, 1(4):307–326, 2006.
- [211] R. Palaniappan, C. Navin Gupta, Chan Kap Luk, and S. M. Krishnan. Multi-parameter detection of ectopic heart beats. In *IEEE International Workshop on Biomedical Circuits and Systems, 2004.*, pages S2–4–1–4, Dec 2004.
- [212] R. Palaniappan and S. M. Krishnan. Detection of ectopic heart beats using eeg and blood pressure signals. In *Signal Processing and Communications, 2004. SPCOM '04. 2004 International Conference on*, pages 573–576, Dec 2004.
- [213] J. Pan and W. J. Tompkins. A real-time qrs detection algorithm. *IEEE Transactions on Biomedical Engineering*, BME-32(3):230–236, March 1985.
- [214] R. L. C. Pan and J. K. J. Li. A noninvasive parametric evaluation of stress effects on global cardiovascular function. *Cardiovascular Engineering*, 7(2):74–80, 2007.
- [215] P. S. Pandian, K. Mohanavelu, K. P. Safeer, T. M. Kotresh, D. T. Shakunthala, P. Gopal, and V. C. Padaki. Smart vest: Wearable multi-parameter remote physiological monitoring system. *Medical engineering & physics*, 30(4):466–477, 2008.
- [216] A. Pantelopoulos and N. G. Bourbakis. A survey on wearable sensor-based systems for health monitoring and prognosis. *IEEE Transactions on Systems, Man, and Cybernetics, Part C (Applications and Reviews)*, 40(1):1–12, Jan 2010.
- [217] G. Parati, R. Casadei, A. Groppelli, M. Di Rienzo, and G. Mancia. Comparison of finger and intra-arterial blood pressure monitoring at rest and during laboratory testing. *Hypertension*, 13(6 Pt 1):647–655, 1989.
- [218] A. Patel, A. Maloney, and A. N. Damato. On the frequency and reproducibility of orthostatic blood pressure changes in healthy community-dwelling elderly during 60-degree head-up tilt. *American heart journal*, 126(1):184–188, 1993.
- [219] S. Patel, H. Park, P. Bonato, L. Chan, and M. Rodgers. A review of wearable sensors and systems with application in rehabilitation. *Journal of neuroengineering and rehabilitation*, 9(1):21, 2012.
- [220] J. Penaz. Photoelectric measurement of blood pressure, volume and flow in the finger. In *Digest of the 10th international conference on medical and biological engineering*, volume 104. International Federation for Medical and Biological Engineering, Publishers New York, 1973.

- [221] F. Peng, Z. Zhang, X. Gou, H. Liu, and W. Wang. Motion artifact removal from photoplethysmographic signals by combining temporally constrained independent component analysis and adaptive filter. *Biomedical engineering online*, 13(1):1, 2014.
- [222] J. J. Perez, A. J. Saldarriaga, and J. Bustamante. A wireless body sensor network platform to measure vital signs in clinical monitoring. In *Health Care Exchanges (PAHCE), 2013 Pan American*, pages 1–6, April 2013.
- [223] M. T. Petterson, V. L. Begnoche, and J. M. Graybeal. The effect of motion on pulse oximetry and its clinical significance. *Anesthesia & Analgesia*, 105(6):S78–S84, 2007.
- [224] M. Pflugradt, I. Fritzsche, S. Mann, T. Tigges, and R. Orglmeister. A novel pulseoximeter for bluetooth synchronized measurements in a body sensor network. In *2014 6th European Embedded Design in Education and Research Conference (EDERC)*, pages 21–25, Sept 2014.
- [225] M. Pflugradt, K. Geissdoerfer, M. Goernig, and R. Orglmeister. A fast multimodal ectopic beat detection method applied for blood pressure estimation based on pulse wave velocity measurements in wearable sensors. *Sensors*, 17(1), 2017.
- [226] M. Pflugradt, N. Hofmeyr, and R. Orglmeister. Multi-channel biosignal processing on an omap 3530 system. In *2012 5th European DSP Education and Research Conference (EDERC)*, pages 124–128, Sept 2012.
- [227] M. Pflugradt, S. Mann, V. Feller, Y. Lu, and R. Orglmeister. Online learning algorithms for principal component analysis applied on single-lead ecgs. *Biomedizinische Technik/Biomedical Engineering*, 58(2):121–130, 2013.
- [228] M. Pflugradt, S. Mann, V. Feller, and R. Orglmeister. On-line learning algorithms for extracting respiratory activity from single lead ecgs based on principal component analysis. *Biomed Tech*, 57:1, 2012.
- [229] M. Pflugradt, S. Mann, T. Tigges, M. Görnig, and R. Orglmeister. Multi-modal signal acquisition using a synchronized wireless body sensor network in geriatric patients. *Biomedical Engineering/Biomedizinische Technik*, 61(1):57–68, 2016.
- [230] M. Pflugradt, B. Moeller, and R. Orglmeister. Opra: A fast on-line signal quality estimator for pulsatile signals. In *9th IFAC Symposium on Biological and Medical Systems*, pages 408–413, 2015.
- [231] M. Pflugradt and R. Orglmeister. Flexible small size actimeter for continuous movement acquisition. In *2013 11th Interdisziplinäres Symposium des Fachausschusses AUTOMED der Deutschen Gesellschaft fuer Biomedizinische Technik (DGBMT) und der Gesellschaft fuer Mess- und Automatisierungstechnik (GMA) im VDE e. V.*, Sep 2013.
- [232] M. Pflugradt and R. Orglmeister. Improved signal quality indication for photoplethysmographic signals incorporating motion artifact detection. In *2014 36th Annual International Conference of the IEEE Engineering in Medicine and Biology Society*, pages 1872–1875, Aug 2014.
- [233] M. Pflugradt and R. Orglmeister. Mobile ecg-ppg combined heart rate estimation using a wireless body sensor network. *Biomedical Engineering/Biomedizinische Technik*, 59(1), 2014.
- [234] M. Pflugradt, M. Rose, and R. Orglmeister. A novel method for motion artifact removal in wearable ppg sensors based on blind source separation. *Biomed Tech*, 58:1, 2013.

- [235] T. G. Pickering, J. E. Hall, L. J. Appel, B. E. Falkner, J. Graves, M. N. Hill, D. W. Jones, T. Kurtz, S. G. Sheps, and E. J. Roccella. Recommendations for blood pressure measurement in humans and experimental animals part 1: blood pressure measurement in humans: a statement for professionals from the subcommittee of professional and public education of the american heart association council on high blood pressure research. *Hypertension*, 45(1):142–161, 2005.
- [236] A. G. Piemuş, M. Pflugradt, T. Tigges, M. Klum, A. Feldheiser, O. Hunsicker, and R. Orglmeister. Novel computation of pulse transit time from multi-channel ppg signals by wavelet transform. *Current Directions in Biomedical Engineering*, 2(1):209–213, 2016.
- [237] D. J. Pitson, A. Sandell, and R. Van den Hout. Use of pulse transit time as a measure of inspiratory effort in patients with obstructive sleep apnoea. *European Respiratory Journal*, 8(10):1669–1674, 1995.
- [238] G. Pocock, C. D. Richards, and A. D. Richards. *Human physiology*. Oxford university press, 2013.
- [239] M. Z. Poh, N. C. Swenson, and R. W. Picard. Motion-tolerant magnetic earring sensor and wireless earpiece for wearable photoplethysmography. *IEEE Transactions on Information Technology in Biomedicine*, 14(3):786–794, May 2010.
- [240] C. C. Y. Poon, Y. T. Zhang, G. Wong, and W. S. Poon. The beat-to-beat relationship between pulse transit time and systolic blood pressure. In *2008 International Conference on Information Technology and Applications in Biomedicine*, pages 342–343, May 2008.
- [241] S. I. Rabben, N. Stergiopoulos, L. R. Hellevik, O. A. Smiseth, S. Slørdahl, S. Urheim, and B. Angelsen. An ultrasound-based method for determining pulse wave velocity in superficial arteries. *Journal of biomechanics*, 37(10):1615–1622, 2004.
- [242] A. Rabee and I. Barhumi. Ecg signal classification using support vector machine based on wavelet multiresolution analysis. In *2012 11th International Conference on Information Science, Signal Processing and their Applications (ISSPA)*, pages 1319–1323, July 2012.
- [243] M. Raghuram, K. V. Madhav, E. H. Krishna, N. R. Komalla, K. Sivani, and K. A. Reddy. Dual-tree complex wavelet transform for motion artifact reduction of ppg signals. In *2012 IEEE International Symposium on Medical Measurements and Applications Proceedings*, pages 1–4, May 2012.
- [244] M. Raghuram, K. V. Madhav, E. H. Krishna, N. R. Komalla, K. Sivani, and K. A. Reddy. Hht based signal decomposition for reduction of motion artifacts in photoplethysmographic signals. In *2012 IEEE International Instrumentation and Measurement Technology Conference Proceedings*, pages 1730–1734, May 2012.
- [245] M. Raghuram, K. V. Madhav, E. H. Krishna, and K. A. Reddy. Evaluation of wavelets for reduction of motion artifacts in photoplethysmographic signals. In *10th International Conference on Information Science, Signal Processing and their Applications (ISSPA 2010)*, pages 460–463, May 2010.
- [246] M. Raghuram, K. V. Madhav, E. H. Krishna, and K. A. Reddy. On the performance of wavelets in reducing motion artifacts from photoplethysmographic signals. In *Bioinformatics and Biomedical Engineering (iCBBE), 2010 4th International Conference on*, pages 1–4, June 2010.
- [247] K. Rahbar and J. P. Reilly. A frequency domain method for blind source separation of convolutive audio mixtures. *IEEE Transactions on Speech and Audio Processing*, 13(5):832–844, Sept 2005.
- [248] M. W. Rajzer, W. Wojciechowska, M. Klocek, I. Palka, M. Brzozowska-Kiszka, and K. Kawecka-Jaszcz. Comparison of aortic pulse wave velocity measured by three techniques: Complior, sphygmocor and arteriograph. *Journal of hypertension*, 26(10):2001–2007, 2008.

- [249] M. R. Ram, K. V. Madhav, E. H. Krishna, N. R. Komalla, and K. A. Reddy. A novel approach for motion artifact reduction in ppg signals based on as-lms adaptive filter. *IEEE Transactions on Instrumentation and Measurement*, 61(5):1445–1457, May 2012.
- [250] M. R. Ram, K. V. Madhav, E. H. Krishna, N. R. Komalla, K. Sivani, and K. A. Reddy. Ica-based improved dtcwt technique for ma reduction in ppg signals with restored respiratory information. *IEEE Transactions on Instrumentation and Measurement*, 62(10):2639–2651, Oct 2013.
- [251] M. R. Ram, K. V. Madhav, E. H. Krishna, K. N. Reddy, and K. A. Reddy. Use of multi-scale principal component analysis for motion artifact reduction of ppg signals. In *2011 IEEE Recent Advances in Intelligent Computational Systems*, pages 425–430, Sept 2011.
- [252] M. R. Ram, K. V. Madhav, E. H. Krishna, K. Nagarjuna Reddy, and K. A. Reddy. On the performance of time varying step-size least mean squares(tvs-lms) adaptive filter for ma reduction from ppg signals. In *2011 International Conference on Communications and Signal Processing*, pages 431–435, Feb 2011.
- [253] M. Ramsey. Noninvasive automatic determination of mean arterial pressure. *Medical and Biological Engineering and Computing*, 17(1):11–18, 1979.
- [254] Y. N. Rao and J. C. Principe. A fast, on-line algorithm for pca and its convergence characteristics. In *Neural Networks for Signal Processing X. Proceedings of the 2000 IEEE Signal Processing Society Workshop (Cat. No.00TH8501)*, volume 1, pages 299–307 vol.1, 2000.
- [255] T. Rassaf, J. Muehlsteff, O. Such, M. Kelm, and C. Meyer. The pulse arrival time approach for non-invasive hemodynamic monitoring in low-acuity settings. *Medical Science Monitor*, 16(11):MT83–MT87, 2010.
- [256] K. A. Reddy, B. George, and V. J. Kumar. Motion artifact reduction and data compression of photoplethysmo-graphic signals utilizing cycle by cycle fourier series analysis. In *2008 IEEE Instrumentation and Measurement Technology Conference*, pages 176–179, May 2008.
- [257] K. A. Reddy, B. George, and V. J. Kumar. Use of fourier series analysis for motion artifact reduction and data compression of photoplethysmographic signals. *IEEE Transactions on Instrumentation and Measurement*, 58(5):1706–1711, May 2009.
- [258] K. A. Reddy and V. J. Kumar. Motion artifact reduction in photoplethysmographic signals using singular value decomposition. In *2007 IEEE Instrumentation Measurement Technology Conference IMTC 2007*, pages 1–4, May 2007.
- [259] A. R. Relente and L. G. Sison. Characterization and adaptive filtering of motion artifacts in pulse oximetry using accelerometers. In *Proceedings of the Second Joint 24th Annual Conference and the Annual Fall Meeting of the Biomedical Engineering Society [Engineering in Medicine and Biology]*, volume 2, pages 1769–1770 vol.2, 2002.
- [260] P. Renevey, R. Vetter, J. Krauss, P. Celka, and Y. Depeursinge. Wrist-located pulse detection using ir signals, activity and nonlinear artifact cancellation. In *2001 Conference Proceedings of the 23rd Annual International Conference of the IEEE Engineering in Medicine and Biology Society*, volume 3, pages 3030–3033 vol.3, 2001.
- [261] F. Ricci, R. De Caterina, and A. Fedorowski. Orthostatic hypotension: epidemiology, prognosis, and treatment. *Journal of the American College of Cardiology*, 66(7):848–860, 2015.

- [262] M. Di Rienzo, F. Rizzo, G. Parati, G. Brambilla, M. Ferratini, and P. Castiglioni. Magic system: a new textile-based wearable device for biological signal monitoring. applicability in daily life and clinical setting. In *2005 IEEE Engineering in Medicine and Biology 27th Annual Conference*, pages 7167–7169, 2005.
- [263] M. Ringwald and K. Romer. Practical time synchronization for bluetooth scatternets. In *Broadband Communications, Networks and Systems, 2007. BROADNETS 2007. Fourth International Conference on*, pages 337–345, Sept 2007.
- [264] C. A. Robles-Rubio, K. A. Brown, and R. E. Kearney. A new movement artifact detector for photoplethysmographic signals. In *2013 35th Annual International Conference of the IEEE Engineering in Medicine and Biology Society (EMBC)*, pages 2295–2299, July 2013.
- [265] R. Romero-Ortuno, L. Cogan, T. Foran, R. A. Kenny, and C. W. Fan. Continuous noninvasive orthostatic blood pressure measurements and their relationship with orthostatic intolerance, falls, and frailty in older people. *Journal of the American Geriatrics Society*, 59(4):655–665, 2011.
- [266] D. E. Rumelhart, G. E. Hinton, and R. J. Williams. Learning representations by back-propagating errors. *Cognitive modeling*, 5(3):1, 1988.
- [267] I. Sadiq and S. A. Khan. Heart beat classification of ecgs using morphology and beat intervals. In *Bioinformatics and Biomedical Engineering, (iCBBE) 2011 5th International Conference on*, pages 1–5, May 2011.
- [268] M. Saeed, M. Villarroel, A. T. Reisner, G. Clifford, L. W. Lehman, G. Moody, T. Heldt, T. H. Kyaw, B. Moody, and R. G. Mark. Multiparameter intelligent monitoring in intensive care ii (mimic-ii): a public-access intensive care unit database. *Critical care medicine*, 39(5):952, 2011.
- [269] M. E. Safar. Review: Pulse pressure, arterial stiffness and wave reflections (augmentation index) as cardiovascular risk factors in hypertension. *Therapeutic advances in cardiovascular disease*, 2(1):13–24, 2008.
- [270] T. D. Sanger. Optimal unsupervised learning in a single-layer linear feedforward neural network. *Neural networks*, 2(6):459–473, 1989.
- [271] F. P. Sarasin, M. Louis-Simonet, D. Carballo, S. Slama, A. F. Junod, and P. F. Unger. Prevalence of orthostatic hypotension among patients presenting with syncope in the ed. *The American journal of emergency medicine*, 20(6):497–501, 2002.
- [272] R. Sarpeshkar and M. T. Dastjerdi. Ultra-low-power pulse oximeter implemented with an energy-efficient photoreceptor, August 14 2012. US Patent 8,242,429.
- [273] B. Scholkopf, Kah-Kay Sung, C. J. C. Burges, F. Girosi, P. Niyogi, T. Poggio, and V. Vapnik. Comparing support vector machines with gaussian kernels to radial basis function classifiers. *IEEE Transactions on Signal Processing*, 45(11):2758–2765, Nov 1997.
- [274] N. Selvaraj, A. Jaryal, J. Santhosh, K. K. Deepak, and S. Anand. Assessment of heart rate variability derived from finger-tip photoplethysmography as compared to electrocardiography. *Journal of medical engineering & technology*, 32(6):479–484, 2008.
- [275] N. Selvaraj, Y. Mendelson, K. H. Shelley, D. G. Silverman, and K. H. Chon. Statistical approach for the detection of motion/noise artifacts in photoplethysmogram. In *2011 Annual International Conference of the IEEE Engineering in Medicine and Biology Society*, pages 4972–4975, Aug 2011.
- [276] S. Seyedtabaai and L. Seyedtabaai. Kalman filter based adaptive reduction of motion artifact from photoplethysmographic signal. *Proceedings of World Academy of Science: Engineering & Technology*, 39, 2008.

- [277] C. J. Shatz. The developing brain. *Scientific American*, 267(3):60–67, 1992.
- [278] K. H. Shelley. Photoplethysmography: beyond the calculation of arterial oxygen saturation and heart rate. *Anesthesia & Analgesia*, 105(6):S31–S36, 2007.
- [279] H. Shen, Y. H. Yang, C. C. Wu, S. T. Sune, Y. C. Lee, S. S. Lee, W. C. Zhang, Y. S. Shih, S. C. Huang, Y. C. Huang, and L. C. Chou. A novel 500 samples/sec 4 by 4 photoplethysmography (ppg) array based cosmetic chip design. In *2010 International Computer Symposium (ICS2010)*, pages 942–947, Dec 2010.
- [280] N. Sheriff. Time synchronization in ant wireless low power sensor network. 2011.
- [281] T. Shimazaki, S. Hara, H. Okuhata, H. Nakamura, and T. Kawabata. Cancellation of motion artifact induced by exercise for ppg-based heart rate sensing. In *2014 36th Annual International Conference of the IEEE Engineering in Medicine and Biology Society*, pages 3216–3219, Aug 2014.
- [282] V. Shnayder, B. R. Chen, K. Lorincz, T. R. F. F. Jones, and M. Welsh. Sensor networks for medical care. In *SenSys*, volume 5, pages 314–314, 2005.
- [283] I. Silva, G. B. Moody, and L. Celi. Improving the quality of ecgs collected using mobile phones: The physionet/computing in cardiology challenge 2011. In *2011 Computing in Cardiology*, pages 273–276, Sept 2011.
- [284] J. Sobotta. *Sobotta atlas of human anatomy I*. Williams & Wilkins, 1997.
- [285] J. Solà, R. Vetter, P. Renevey, O. Chételat, C. Sartori, and S. F. Rimoldi. Parametric estimation of pulse arrival time: a robust approach to pulse wave velocity. *Physiological measurement*, 30(7):603, 2009.
- [286] A. Sološenko and V. Marozas. Automatic extrasystole detection using photoplethysmographic signals. In Laura M. Roa Romero, editor, *XIII Mediterranean Conference on Medical and Biological Engineering and Computing 2013*, volume 41 of *IFMBE Proceedings*, pages 985–988. Springer International Publishing, 2014.
- [287] A. Sološenko and V. Marozas. Automatic premature ventricular contraction detection in photoplethysmographic signals. In *2014 IEEE Biomedical Circuits and Systems Conference (BioCAS) Proceedings*, pages 49–52, Oct 2014.
- [288] A. Sološenko, A. Petrėnas, and V. Marozas. Photoplethysmography-based method for automatic detection of premature ventricular contractions. *IEEE Transactions on Biomedical Circuits and Systems*, 9(5):662–669, Oct 2015.
- [289] A. Stankus, Z. Lukosius, D. Aponkus, A. Andziulis, V. Stankus, M. Kurmis, and U. Locans. Comparison of point-to-point and multipoint human artery pulse wave transit time measurement algorithms. *Electronics and Electrical Engineering*, 123(7):95–98, 2012.
- [290] P. F. Stetson. Independent component analysis of pulse oximetry signals based on derivative skew. In *International Conference on Independent Component Analysis and Signal Separation*, pages 1072–1078. Springer, 2004.
- [291] P. P. Stetson. Independent component analysis of pulse oximetry signals. In *The 26th Annual International Conference of the IEEE Engineering in Medicine and Biology Society*, volume 1, pages 231–234, Sept 2004.
- [292] J. A. Sukor, S. J. Redmond, and N. H. Lovell. Signal quality measures for pulse oximetry through waveform morphology analysis. *Physiological measurement*, 32(3):369, 2011.

- [293] F. Sun, Z. Zhao, Z. Fang, D. Chen, X. Chen, and Y. Xuan. Design and implementation of an ultra low power health monitoring node for wireless body sensor network. In *Digital Manufacturing and Automation (ICDMA), 2013 Fourth International Conference on*, pages 417–422, June 2013.
- [294] B. Surawicz and T. Knilians. *Chou's electrocardiography in clinical practice: adult and pediatric*. Elsevier Health Sciences, 2008.
- [295] X. F. Teng and Y. T. Zhang. Continuous and noninvasive estimation of arterial blood pressure using a photoplethysmographic approach. In *Proceedings of the 25th Annual International Conference of the IEEE Engineering in Medicine and Biology Society (IEEE Cat. No.03CH37439)*, volume 4, pages 3153–3156 Vol.4, Sept 2003.
- [296] X. F. Teng and Y. T. Zhang. The effect of applied sensor contact force on pulse transit time. *Physiological measurement*, 27(8):675, 2006.
- [297] Texas Instruments. *High-Performance Miniature 1.5-A Step-Down DC-DC Converter for Handheld Applications SNVS464C* [Online Available]: <http://www.ti.com/lit/ds/symlink/lm3678.pdf>, April 2008. last visited: 2017.11.05.
- [298] Texas Instruments. *ADS129x Low-Power, 8-Channel, 24-Bit Analog Front-End for Biopotential Measurements SBAS459K* [Online Available]: <http://www.ti.com/lit/ds/symlink/ads1298.pdf>, January 2010. last visited: 2017.11.05.
- [299] Texas Instruments. *256 Taps Single Channel Digital Potentiometer With SPI Interface* [Online Available]: <http://www.ti.com/lit/ds/sl136a/sl136a.pdf>, September 2011. last visited: 2016.03.29.
- [300] Texas Instruments. *MSP430F665x, MSP430F645x, MSP430F565x, MSP430F535x Mixed Signal Microcontrollers SLAS700C* [Online Available]: <http://www.ti.com/lit/ds/symlink/msp430f5659.pdf>, October 2012. last visited: 2017.11.05.
- [301] Texas Instruments. *MSP430 Optimizing C/C++ Compiler v 4.4 User's Guide SLAU132J* [Online Available]: <http://www.ti.com/lit/ug/slau132j/slau132j.pdf>, November 2014. last visited: 2016.03.29.
- [302] Texas Instruments. *TS5A3359 1- $\bar{I}$  SP3T Bidirectional Analog Switch 5-V/3.3-V Single-Channel 3:1 Multiplexer and Demultiplexer SCDS214E* [Online Available]: <http://www.ti.com.cn/cn/lit/ds/symlink/ts5a3359.pdf>, January 2016. last visited: 2016.03.29.
- [303] C. W. Therrien. *Discrete random signals and statistical signal processing*. Prentice Hall PTR, 1992.
- [304] R. M. Tobin, J. A. Pologe, and P. B. Batchelder. A characterization of motion affecting pulse oximetry in 350 patients. *Anesthesia and analgesia*, 94(1):S54, 2002.
- [305] H. Tomiyama, A. Yamashina, T. Arai, K. Hirose, Y Koji, T. Chikamori, S. Hori, Y. Yamamoto, N. Doba, and S. Hinohara. Influences of age and gender on results of noninvasive brachial-ankle pulse wave velocity measurement—a survey of 12517 subjects. *Atherosclerosis*, 166(2):303–309, 2003.
- [306] F. Valbusa, C. Labatand P. Salviand M. E. Vivian, O. Hanon, and A. Benetos. Orthostatic hypotension in very old individuals living in nursing homes: the partage study. *Journal of hypertension*, 30(1):53–60, 2012.
- [307] A. van Halteren, R. Bults, K. Wac, N. Dokovsky, G. Koprnikov, I. Widya, D. Konstantas, V. Jones, and R. Herzog. Wireless body area networks for healthcare: the mobihealth project. *Stud Health Technol Inform*, 108:181–93, 2004.
- [308] A. T. van Halteren, R. G. A. Bults, K. E. Wac, D. Konstantas, I. A. Widya, N. T. Dokovski, G. T. Koprnikov, V. M. Jones, and R. Herzog. Mobile patient monitoring: The mobihealth system. 2004.

- [309] Y. Varatharajah, N. Karunathilaka, M. Rismi, S. Kotinkaduwa, and D. Dias. Body area sensor network for evaluating fitness exercise. In *Wireless and Mobile Networking Conference (WMNC), 2013 6th Joint IFIP*, pages 1–8, April 2013.
- [310] Vishay Semiconductors. *Silicon PIN Photodiode Document 81521 [Online Available]*: <http://www.vishay.com/docs/81521/bpw34.pdf>, January 2010. last visited: 2016.03.29.
- [311] Vishay Siliconix. *N-Channel 30-V (D-S) MOSFET Document 65701 [Online Available]*: <http://www.vishay.com/docs/65701/si2300ds.pdf>, August 2011. last visited: 2016.03.29.
- [312] A. Volmer. *Unterdrückung von Bewegungsartefakten beim Langzeitmonitoring zur Anwendung in Personal-Healthcare-Systemen*. PhD thesis, Technical University of Berlin, 2011.
- [313] A. Volmer and R. Orglmeister. Wireless body sensor network for low-power motion-tolerant synchronized vital sign measurement. In *2008 30th Annual International Conference of the IEEE Engineering in Medicine and Biology Society*, pages 3422–3425, Aug 2008.
- [314] A. Volmer and R. Orglmeister. Wireless body sensor network for low-power motion-tolerant synchronized vital sign measurement. In *Engineering in Medicine and Biology Society, 2008. EMBS 2008. 30th Annual International Conference of the IEEE*, pages 3422–3425, Aug 2008.
- [315] E. von Wowern, G. Östling, P. M. Nilsson, and P. Olofsson. Digital photoplethysmography for assessment of arterial stiffness: Repeatability and comparison with applanation tonometry. *PloS one*, 10(8):e0135659, 2015.
- [316] S. Vulliémoz, N. Stergiopoulos, and R. Meuli. Estimation of local aortic elastic properties with mri. *Magnetic resonance in medicine*, 47(4):649–654, 2002.
- [317] K. Wac, R. Bults, B. van Beijnum, I. Widya, V. Jones, D. Konstantas, M. Vollenbroek-Hutten, and H. Hermens. Mobile patient monitoring: The mobihealth system. In *2009 Annual International Conference of the IEEE Engineering in Medicine and Biology Society*, pages 1238–1241, Sept 2009.
- [318] D. R. Wagner, N. Roesch, P. Harpes, H. Körtke, P. Plumer, A. Saberlin, V. Chakoutio, D. Oundjede, C. Delagardelle, and J. Beissel. Relationship between pulse transit time and blood pressure is impaired in patients with chronic heart failure. *Clinical research in cardiology*, 99(10):657–664, 2010.
- [319] J. Wåhslén, I. Orhan, D. Sturm, and T. Lindh. Performance evaluation of time synchronization and clock drift compensation in wireless personal area networks. In *Proceedings of the 7th International Conference on Body Area Networks*, pages 153–158. ICST (Institute for Computer Sciences, Social-Informatics and Telecommunications Engineering), 2012.
- [320] L. Wang, B. P. Lo, and G. Z. Yang. Multichannel reflective ppg earpiece sensor with passive motion cancellation. *IEEE Transactions on Biomedical Circuits and Systems*, 1(4):235–241, Dec 2007.
- [321] Q. Wang, P. Yang, and Y. Zhang. Artifact reduction based on empirical mode decomposition (emd) in photoplethysmography for pulse rate detection. In *2010 Annual International Conference of the IEEE Engineering in Medicine and Biology*, pages 959–962, Aug 2010.
- [322] Z. Wang, C. Zhao, and S. Qiu. A system of human vital signs monitoring and activity recognition based on body sensor network. *Sensor Review*, 34(1):42–50, 2014.
- [323] M. Ward and J. A. Langton. Blood pressure measurement. *Continuing Education in Anaesthesia, Critical Care & Pain*, 7(4):122–126, 2007.
- [324] J. G. Webster. *Design of pulse oximeters*. CRC Press, 1997.

- [325] J. J. Wei, C. J. Chang, N. K. Chou, and G. J. Jan. Ecg data compression using truncated singular value decomposition. *IEEE Transactions on Information Technology in Biomedicine*, 5(4):290–299, Dec 2001.
- [326] P. Wei, R. Guo, J. Zhang, and Y. T. Zhang. A new wristband wearable sensor using adaptive reduction filter to reduce motion artifact. In *Information Technology and Applications in Biomedicine, 2008. ITAB 2008. International Conference on*, pages 278–281, May 2008.
- [327] J. P. Welch, P. J. Ford, R. S. Teplick, and R. M. Rubsamen. The massachusetts general hospital-marquette foundation hemodynamic and electrocardiographic database—comprehensive collection of critical care waveforms. *Clinical Monitoring*, 7(1):96–97, 1991.
- [328] B. E. Westerhof, I. Guelen, N. Westerhof, J. M. Karemaker, and A. P. Avolio. Quantification of wave reflection in the human aorta from pressure alone a proof of principle. *Hypertension*, 48(4):595–601, 2006.
- [329] N. Westerhof, N. Stergiopulos, and M. I. M. Noble. The arterial windkessel. In *Snapshots of Hemodynamics*, pages 173–181. Springer US, 2010.
- [330] N. Westerhof, N. Stergiopulos, and M. I. M. Noble. Compliance. In *Snapshots of Hemodynamics*, pages 57–66. Springer US, 2010.
- [331] N. Westerhof, N. Stergiopulos, and M. I. M. Noble. Elasticity. In *Snapshots of Hemodynamics*, pages 49–56. Springer US, 2010.
- [332] N. Westerhof, N. Stergiopulos, and M. I. M. Noble. Wave travel and reflection. In *Snapshots of Hemodynamics*, pages 147–153. Springer US, 2010.
- [333] N. Westerhof, N. Stergiopulos, and M. I. M. Noble. Wave travel and velocity. In *Snapshots of Hemodynamics*, pages 139–146. Springer US, 2010.
- [334] B. Widrow, J. R. Glover, J. M. McCool, J. Kaunitz, C. S. Williams, R. H. Hearn, J. R. Zeidler, J. Eugene Dong, and R. C. Goodlin. Adaptive noise cancelling: Principles and applications. *Proceedings of the IEEE*, 63(12):1692–1716, Dec 1975.
- [335] J. Wiens and J. Gutttag. Patient-adaptive ectopic beat classification using active learning. In *2010 Computing in Cardiology*, pages 109–112, Sept 2010.
- [336] R. Winker, W. Prager, A. Haider, B. Salameh, and H. W. Rüdiger. Schellong test in orthostatic dysregulation: a comparison with tilt-table testing. *Wiener Klinische Wochenschrift*, 117(1-2):36–41, 2005.
- [337] M. Y. M. Wong, C. C. Y. Poon, and Y. T. Zhang. An evaluation of the cuffless blood pressure estimation based on pulse transit time technique: a half year study on normotensive subjects. *Cardiovascular Engineering*, 9(1):32–38, 2009.
- [338] M. Y. M. Wong and Y. T. Zhang. The relationship between pulse transit time and systolic blood pressure on individual subjects after exercises. In *1st Transdisciplinary Conference on Distributed Diagnosis and Home Healthcare, 2006. D2H2.*, pages 37–38, April 2006.
- [339] L. B. Wood and H. H. Asada. Active motion artifact reduction for wearable sensors using laguerre expansion and signal separation. In *2005 IEEE Engineering in Medicine and Biology 27th Annual Conference*, pages 3571–3574, Jan 2005.
- [340] L. B. Wood and H. H. Asada. Noise cancellation model validation for reduced motion artifact wearable ppg sensors using mems accelerometers. In *2006 International Conference of the IEEE Engineering in Medicine and Biology Society*, pages 3525–3528, Aug 2006.

- [341] L. B. Wood and H. H. Asada. Low variance adaptive filter for cancelling motion artifact in wearable photoplethysmogram sensor signals. In *2007 29th Annual International Conference of the IEEE Engineering in Medicine and Biology Society*, pages 652–655, Aug 2007.
- [342] Y. S. Yan, C. C. Y. Poon, and Y. T. Zhang. Reduction of motion artifact in pulse oximetry by smoothed pseudo wigner-ville distribution. *Journal of NeuroEngineering and Rehabilitation*, 2:3, 2005.
- [343] Y. S. Yan and Y. T. Zhang. Noninvasive estimation of blood pressure using photoplethysmographic signals in the period domain. In *2005 IEEE Engineering in Medicine and Biology 27th Annual Conference*, pages 3583–3584, Jan 2005.
- [344] Y. S. Yan and Y. T. Zhang. An efficient motion-resistant method for wearable pulse oximeter. *IEEE Transactions on Information Technology in Biomedicine*, 12(3):399–405, May 2008.
- [345] B. Yang. Projection approximation subspace tracking. *IEEE Transactions on Signal Processing*, 43(1):95–107, Jan 1995.
- [346] J. Yao and S. Warren. A novel algorithm to separate motion artifacts from photoplethysmographic signals obtained with a reflectance pulse oximeter. In *The 26th Annual International Conference of the IEEE Engineering in Medicine and Biology Society*, volume 1, pages 2153–2156, Sept 2004.
- [347] J. Yao and S. Warren. A short study to assess the potential of independent component analysis for motion artifact separation in wearable pulse oximeter signals. In *2005 IEEE Engineering in Medicine and Biology 27th Annual Conference*, pages 3585–3588, 2005.
- [348] W. Yongbo, S. Xiaodong, and Y. Jianchu. Design of a photoplethysmographic sensor for biometric identification. In *2007 International Conference on Control, Automation and Systems*, pages 1897–1900, Oct 2007.
- [349] R. Yousefi, M. Nourani, S. Ostadabbas, and I. Panahi. A motion-tolerant adaptive algorithm for wearable photoplethysmographic biosensors. *IEEE Journal of Biomedical and Health Informatics*, 18(2):670–681, March 2014.
- [350] C. Yu, Z. Liu, T. McKenna, A. T. Reisner, and J. Reifman. A method for automatic identification of reliable heart rates calculated from ecg and ppg waveforms. *Journal of the American Medical Informatics Association*, 13(3):309–320, 2006.
- [351] G. Zhang, M. Gao, D. Xu, N. B. Olivier, and R. Mukkamala. Pulse arrival time is not an adequate surrogate for pulse transit time as a marker of blood pressure. *Journal of Applied Physiology*, 111(6):1681–1686, 2011.
- [352] J. M. Zhang, P. F. Wei, and Y. Li. A labview based measure system for pulse wave transit time. In *2008 International Conference on Information Technology and Applications in Biomedicine*, pages 477–480, May 2008.
- [353] Xin-Yu Zhang and Yuan-Ting Zhang. The effect of local cold exposure on pulse transit time. In *2005 IEEE Engineering in Medicine and Biology 27th Annual Conference*, pages 3522–3525, Jan 2005.
- [354] C. Zhou, C. Tu, J. Tian, J. Feng, Y. Gao, X. Ye, and C. Loughlin. A low power miniaturized monitoring system of six human physiological parameters based on wearable body sensor network. *Sensor Review*, 35(2), 2015.
- [355] W. Zong, T. Heldt, G. B. Moody, and R. G. Mark. An open-source algorithm to detect onset of arterial blood pressure pulses. In *Computers in Cardiology, 2003*, pages 259–262, Sept 2003.